Theoretical investigation of size effects in multiferroic nanoparticles

by

Marc Alexander Allen
B.Sc., University of British Columbia, 2009
M.Sc., University of Victoria, 2014

A Dissertation Submitted in Partial Fulfillment of the
Requirements for the Degree of

DOCTOR OF PHILOSOPHY

in the Department of Physics and Astronomy

Theoretical investigation of size effects in multiferroic nanoparticles

by

Marc Alexander Allen
B.Sc., University of British Columbia, 2009
M.Sc., University of Victoria, 2014

Supervisory Committee

Dr. Rogério de Sousa, Supervisor
(Department of Physics and Astronomy)

Dr. Byoung-Chul Choi, Departmental Member
(Department of Physics and Astronomy)

Dr. Irina Paci, Outside Member
(Department of Chemistry)

Supervisory Committee

Dr. Rogério de Sousa, Supervisor
(Department of Physics and Astronomy)

Dr. Byoung-Chul Choi, Departmental Member
(Department of Physics and Astronomy)

Dr. Irina Paci, Outside Member
(Department of Chemistry)

ABSTRACT

Over the last two decades, great progress has been made in the understanding of multiferroic materials, ones where multiple long-range orders simultaneously exist. However, much of the research has focused on bulk systems. If these materials are to be incorporated into devices, they would not be in bulk form, but would be miniaturized, such as in nanoparticle form. Accordingly, a better understanding of multiferroic nanoparticles is necessary. This manuscript examines the multiferroic phase diagram of multiferroic nanoparticles related to system size and surface-induced magnetic anisotropy. There is a particular focus on bismuth ferrite, the room-temperature antiferromagnetic-ferroelectric multiferroic. Theoretical results will be presented which show that at certain sizes, a bistability develops in the cycloidal wavevector. This implies bistability in the ferroelectric and magnetic moments of the nanoparticles. This novel magnetoelectric bistability may be of use in the creation of an electrically-written, magnetically-read memory element.

Contents

Supervisory Committee **ii**

Abstract **iii**

Table of Contents **iv**

List of Figures **vii**

Acknowledgements **xxii**

1 Introduction **1**

1.1 Literature review 2
1.2 Research questions 4
1.3 Implications 5
1.4 Agenda 6

2 Background **8**

2.1 Magnetoelectric effect 8
2.2 Multiferroics 10
2.3 Bismuth ferrite 13
2.4 Anisotropy 14
  2.4.1 Spin-orbit coupling 15
  2.4.2 Surface anisotropy 17
2.5 Magnetic nanoparticles 18
2.6 BFO nanoparticles 20
2.7 Depolarization 27
2.8 Demagnetization 28
2.9 Magnons 29
2.10 Temperature effects 34

3 Microscopic Model **39**
3.1 Heisenberg exchange interaction 39
3.2 Dzyaloshinskii-Moriya interaction 42
3.3 Anisotropy 43

4 Methodology for Energy Minimization **48**
4.1 Random search algorithm 49
4.2 Nelder-Mead algorithm 51
4.3 L-BFGS-B algorithm 53

5 Spin Chain **57**
5.1 Long wavelength regime 63
5.2 Edge effect 66
5.3 Bistability 70

6 Spin Plaquette **73**
6.1 Electric field due to spin current 79
6.2 Spin-canting-induced magnetization 83
6.3 Surface anisotropy on side edges 84
6.4 Surface anisotropy on all surfaces 86
6.5 Phase diagrams 91

7 Spin Cube **97**
7.1 Polarization due to spins 102
7.2 Magnetization due to spin canting 104
7.3 Optimization results 104
7.4 Phase diagrams 106

8 Discussion of Results **110**

9 Conclusions **118**

Appendix A Additional Spin Chain Results **121**

Appendix B Additional Spin Plaquette Results **155**

Appendix C Additional Spin Cube Results **174**

Bibliography **181**

List of Figures

Figure 1.1 The electric field applied in certain directions will break the cycloid. Reprinted figure with permission from [9]. Copyright 2013 by the American Physical Society. 3

Figure 1.2 Q/Q_{Bulk} versus spin chain length. $D/J = 0.15708$ and $K_S/J = -0.50$. 5

Figure 2.1 The unit cell of bismuth ferrite. The purple atoms are Bi^{3+}, red O^{2-} and gold Fe^{3+}. The left cell displays the cubic axes for BFO and the right cell shows the rhombohedral axes that it is convenient to use in describing BFO. Reprinted figure with permission from [9]. Copyright 2013 by the American Physical Society. 14

Figure 2.2 Antiferromagnetic cycloid. The blue-green arrows represent the Néel vector **L** and the red arrows represent the local weak ferromagnetism. 15

Figure 2.3 Homogeneous, antiferromagnetic case. The blue-green arrows represent the Néel vector **L** and the red arrows represent the local weak ferromagnetism. 15

Figure 2.4 Model of a magnetic nanoparticle with different core and surface magnetizations. Reprinted from [84], with permission from Elsevier. Copyright 2009. 19

Figure 2.5 Néel temperature as a function of particle size in nanoparticle BFO. The closed markers indicate a heating rate of 1°C min^{-1} and the open markers indicate a heating rate of 10°C min^{-1}. The dashed arrow is indicates the bulk T_N for the 40°C min^{-1} heating rate and the solid arrow indicates a rate of 10°C min^{-1}. The inset shows the differential scanning calorimetry traces used to determine T_N. The plots are for (a) bulk, (b) 72.1 nm, (c) 34.4 nm, (d) 20.4 nm, (e) 15.3 nm, and (f) 13.3 nm. The arrows indicate the maximum and the T_N. Reprinted with permission from [92]. Copyright 2007 American Chemical Society. 21

Figure 2.6 Difference in ion displacement versus particle size for nanoparticle BFO. The difference in ion displacement, $s - t$ is a proxy for the electric polarization. The inset plots $(s - t)^2$ versus the inverse particle size. Reprinted with permission from [92]. Copyright 2007 American Chemical Society. 22

Figure 2.7 Magnetic hysteresis curves (magnetization versus magnetic field) for nanoparticle BFO of various sizes. Insets relate magnetization and particle size. Reprinted with permission from [90]. Copyright 2007 American Chemical Society. 23

Figure 2.8 Magnon spectra from Raman spectroscopy in nanoparticle BFO for various nanoparticle sizes. Reprinted from [105], with the permission of AIP Publishing. 26

Figure 2.9 Electric polarization in a ferroelectric. 27

Figure 2.10 Magnetization in a ferromagnet. 29

Figure 2.11 Ferromagnetic magnon. 30

Figure 2.12 Magnon dispersion for a simple, one-dimensional ferromagnet. . 32

Figure 2.13 AFM magnons in cycloidal BFO. Reprinted figure with permission from [110]. Copyright 2008 by the American Physical Society. 33

Figure 2.14 $\mathbf{M_1}$ and $\mathbf{M_2}$ are spins in BFO in the homogeneous state. The two different homogeneous magnons are depicted in (a) and (b). In (a) the low frequency magnon mode is shown with the spins processing and maintaining a constant angle between themselves. In (b) the high frequency, gapped mode is shown with the spins processing and the canting angle between the spins varying. The blue arrow represents the polarization. Reprinted from [112], with the permission of AIP Publishing. 34

Figure 2.15 Mangetization versus magnetic field at various temperatures. In a) the field is along the polarization direction and in b) the field is perpendicular to it. Reprinted from [113], with permission from Elsevier. Copyright 2015. 35

Figure 3.1 Superexchange model for a Fe-O-Fe bond. The Fe^{3+} cations are too far apart to have any overlap of their wavefunctions. The O^{2-} anion acts as an intermediary. Its $2p$ orbitals overlap with the $3d$ orbitals of the Fe^{3+} cations. 40

Figure 3.2 Examples of different antiferromagnetic spin configurations. . . 42

Figure 5.1 Q/Q_{Bulk} versus nanoparticle size for $K_S = 0, \pm 0.1$, and $\pm\infty$. The inset shows $QL/2\pi$, the winding number, versus nanoparticle size. Only compensated nanoparticles (even N) are shown. Reprinted figure with permission from [141]. Copyright 2019 by the American Physical Society. 57

Figure 5.2 Cycloid of length $\lambda_{\mathrm{Bulk}}/2$. The arrows represent spins of one sublattice. $D/J = 0.15708$. 58

Figure 5.3 Q/Q_{Bulk} and winding number versus spin chain length. $d = 0.15708$ and $k_S = -0.30$. The purple squares are Q/Q_{Bulk} and the green circles represent the winding number. 68

Figure 5.4 Spin chains of various length L with $d = 0.15708$ and $k_S = -0.30$. Spins of the same colour belong to the same sublattice. All spins of unit length. 69

Figure 5.5 Q/Q_{Bulk} and winding number versus spin chain length. $d = 0.31416$ and $k_S = -0.30$. The purple squares are Q/Q_{Bulk} and the green circles represent the winding number. 70

Figure 5.6 Q/Q_{Bulk} and winding number versus spin chain length. $d = 0.04724$ and $k_S = -0.30$. The purple squares are Q/Q_{Bulk} and the green circles represent the winding number. 71
Figure 5.7 Energy per spin versus Qa. $d = 0.15708$, $k_S = 0.10$. The energy at $Qa = 0.08$ and $Qa \approx 0.23$ are equal and minimal. 72
Figure 5.8 Energy versus Qa at various nanoparticle sizes at jump discontinuities in Q. $d = 0.15708$ and $k_S = 0.10$. 72

Figure 6.1 Geometry of the investigated spin plaquette. The plaquette is in the xz plane with a size of $L_x \times L_z$, with L_x being the side length in the x direction and L_z being the side length in the z direction. In the figure, the number of spins in the x direction N_x is three and the number of spins in the z direction N_z is four. The blue spins represent spins belonging to one sublattice and the orange spins belonging to the other. 73
Figure 6.2 Location of various Q's within the plaquette nanoparticle. . . . 84
Figure 6.3 Q/Q_{bulk} versus nanoparticle side length L. $d = 0.15708, k_S^x = -0.30, k_S^z = 0$. 86
Figure 6.4 Q/Q_{bulk} versus nanoparticle side length L. $d = 0.15708, k_S^x = 0.30, k_S^z = 0$. 87
Figure 6.5 Q/Q_{bulk} and spin-canting-induced magnetization versus nanoparticle side length L. $d = 0.15708$, $k_S^x = k_S^z = -0.10$ (easy-plane surface anisotropy). Magnetization is in units of $D'S/J$. 88
Figure 6.6 Nanoparticles of different sizes with the same number of spins in each of the two magnetic sublattice (spins purple and green), with $d = 0.15708$ and $k_S^x = k_S^z = -0.10$. Spins of the same colour belong to the same sublattice. The size of the nanoparticles is $L \times L$. 89
Figure 6.7 Q/Q_{bulk} and spin-canting-induced magnetization versus nanoparticle side length L. $d = 0.15708$, $k_S^x = k_S^z = 0.10$ (easy-axis surface anisotropy). Magnetization is in units of $D'S/J$. 90
Figure 6.8 Nanoparticles of different sizes with $d = 0.15708$ and $k_S^x = k_S^z = 0.10$. Spins of the same colour belong to the same sublattice. The size of the nanoparticles is $L \times L$. 91

Figure 6.9 Q/Q_{bulk} and spin-canting-induced magnetization versus nanoparticle side length L. $d = 0.15708$, $k_S^x = k_S^z = 0$. Magnetization is in units of $D'S/J$. 92

Figure 6.10 Nanoparticles of different sizes with $d = 0.15708$ and $k_S^x = k_S^z = 0$. Spins of the same colour belong to the same sublattice. The size of the nanoparticles is $L \times L$. 93

Figure 6.11 Phase diagram of the magnetically-induced electric polarization $P_{\text{spin},z}$ for a plaquette of size $L \times L$ with equal surface anisotropy on all edges ($K_S^x = K_S^z = K_S$). In units of $D\chi\left(N-1\right)NS^2/\left(Pa^3\right)$. 94

Figure 6.12 Phase diagram of the magnetically-induced electric polarization $|\mathbf{P}_{\text{spin}}|$ for a plaquette of size $L \times L$ with equal surface anisotropy on all edges ($K_S^x = K_S^z = K_S$). In units of $D\chi\left(NS\right)^2/\left(Pa^3\right)$. . 95

Figure 6.13 Phase diagram of the spin-canting-induced magnetization $|\mathbf{M}|$ for a plaquette of size $L \times L$ with equal surface anisotropy on all edges ($K_S^x = K_S^z = K_S$). In units of $D'S/J$. 96

Figure 7.1 Diagram showing the position of the various labelled Q's in the spin cube. 105

Figure 7.2 Q/Q_{Bulk} versus nanoparticle side length L/λ_{bulk} and magnetization versus nanoparticle side length L/λ_{bulk} for spin cube ($L \times L \times L$). The magnetization is in units of $D'S/J$. $d = 0.15708$, $k_S = -0.10$. 106

Figure 7.3 Phase diagram of the spin-induced electric polarization $P_{\text{spin},z}$ in a cubic nanoparticle of side length L. $d = 0.15708$. In units of $D\chi\left(N-1\right)\left(NS\right)^2/\left(Pa^3\right)$. 107

Figure 7.4 Phase diagram of the spin-induced electric polarization $|\mathbf{P}_{\text{spin}}|$ in a cubic nanoparticle of side length L. $d = 0.15708$. In units of $D\chi N^3S^2/\left(Pa^3\right)$. 108

Figure 7.5 Phase diagram of the spin-current-induced magnetization $|\mathbf{M}|$ in a cubic nanoparticle of side length L. $d = 0.15708$. In units of $D'S/J$. 109

Figure A.1 Q/Q_{Bulk} versus spin chain length. $d = 0.15708$ and $k_S = -1.00$, -0.10, 0.10, and 1.00. 122

Figure A.2 Q/Q_{Bulk} and winding number versus spin chain length. $d = 0.15708$ and $k_S = -1.00$. The purple squares are Q/Q_{Bulk} and the green circles represent the winding number. 122

Figure A.3 Q/Q_{Bulk} and winding number versus spin chain length. $d = 0.15708$ and $k_S = -0.90$. The purple squares are Q/Q_{Bulk} and the green circles represent the winding number. 123

Figure A.4 Q/Q_{Bulk} and winding number versus spin chain length. $d = 0.15708$ and $k_S = -0.80$. The purple squares are Q/Q_{Bulk} and the green circles represent the winding number. 123

Figure A.5 Q/Q_{Bulk} and winding number versus spin chain length. $d = 0.15708$ and $k_S = -0.70$. The purple squares are Q/Q_{Bulk} and the green circles represent the winding number. 124

Figure A.6 Q/Q_{Bulk} and winding number versus spin chain length. $d = 0.15708$ and $k_S = -0.60$. The purple squares are Q/Q_{Bulk} and the green circles represent the winding number. 124

Figure A.7 Q/Q_{Bulk} and winding number versus spin chain length. $d = 0.15708$ and $k_S = -0.50$. The purple squares are Q/Q_{Bulk} and the green circles represent the winding number. 125

Figure A.8 Q/Q_{Bulk} and winding number versus spin chain length. $d = 0.15708$ and $k_S = -0.40$. The purple squares are Q/Q_{Bulk} and the green circles represent the winding number. 125

Figure A.9 Q/Q_{Bulk} and winding number versus spin chain length. $d = 0.15708$ and $k_S = -0.20$. The purple squares are Q/Q_{Bulk} and the green circles represent the winding number. 126

Figure A.10 Q/Q_{Bulk} and winding number versus spin chain length. $d = 0.15708$ and $k_S = -0.10$. The purple squares are Q/Q_{Bulk} and the green circles represent the winding number. 126

Figure A.11 Q/Q_{Bulk} and winding number versus spin chain length. $d = 0.15708$ and $k_S = 0$. The purple squares are Q/Q_{Bulk} and the green circles represent the winding number. 127

Figure A.12 Q/Q_{Bulk} and winding number versus spin chain length. $d = 0.15708$ and $k_S = 0.10$. The purple squares are Q/Q_{Bulk} and the green circles represent the winding number. 127

Figure A.13 Q/Q_{Bulk} and winding number versus spin chain length. $d = 0.15708$ and $k_S = 0.20$. The purple squares are Q/Q_{Bulk} and the green circles represent the winding number. 128

Figure A.14 Q/Q_{Bulk} and winding number versus spin chain length. $d = 0.15708$ and $k_S = 0.30$. The purple squares are Q/Q_{Bulk} and the green circles represent the winding number. 128

Figure A.15 Q/Q_{Bulk} and winding number versus spin chain length. $d = 0.15708$ and $k_S = 0.40$. The purple squares are Q/Q_{Bulk} and the green circles represent the winding number. 129

Figure A.16 Q/Q_{Bulk} and winding number versus spin chain length. $d = 0.15708$ and $k_S = 0.50$. The purple squares are Q/Q_{Bulk} and the green circles represent the winding number. 129

Figure A.17 Q/Q_{Bulk} and winding number versus spin chain length. $d = 0.15708$ and $k_S = 0.60$. The purple squares are Q/Q_{Bulk} and the green circles represent the winding number. 130

Figure A.18 Q/Q_{Bulk} and winding number versus spin chain length. $d = 0.15708$ and $k_S = 0.70$. The purple squares are Q/Q_{Bulk} and the green circles represent the winding number. 130

Figure A.19 Q/Q_{Bulk} and winding number versus spin chain length. $d = 0.15708$ and $k_S = 0.80$. The purple squares are Q/Q_{Bulk} and the green circles represent the winding number. 131

Figure A.20 Q/Q_{Bulk} and winding number versus spin chain length. $d = 0.15708$ and $k_S = 0.90$. The purple squares are Q/Q_{Bulk} and the green circles represent the winding number. 131

Figure A.21 Q/Q_{Bulk} and winding number versus spin chain length. $d = 0.15708$ and $k_S = 1.00$. The purple squares are Q/Q_{Bulk} and the green circles represent the winding number. 132

Figure A.22 Q/Q_{Bulk} versus spin chain length. $d = 0.31416$ and $k_S = -1.00$, -0.10, 0.10, and 1.00. 133

Figure A.23 Q/Q_{Bulk} and winding number versus spin chain length. $d = 0.31416$ and $k_S = -1.00$. The purple squares are Q/Q_{Bulk} and the green circles represent the winding number. 134

Figure A.24 Q/Q_{Bulk} and winding number versus spin chain length. $d = 0.31416$ and $k_S = -0.90$. The purple squares are Q/Q_{Bulk} and the green circles represent the winding number. 134

Figure A.25 Q/Q_{Bulk} and winding number versus spin chain length. $d = 0.31416$ and $k_S = -0.80$. The purple squares are Q/Q_{Bulk} and the green circles represent the winding number. 135

Figure A.26 Q/Q_{Bulk} and winding number versus spin chain length. $d = 0.31416$ and $k_S = -0.70$. The purple squares are Q/Q_{Bulk} and the green circles represent the winding number. 135

Figure A.27 Q/Q_{Bulk} and winding number versus spin chain length. $d = 0.31416$ and $k_S = -0.60$. The purple squares are Q/Q_{Bulk} and the green circles represent the winding number. 136

Figure A.28 Q/Q_{Bulk} and winding number versus spin chain length. $d = 0.31416$ and $k_S = -0.50$. The purple squares are Q/Q_{Bulk} and the green circles represent the winding number. 136

Figure A.29 Q/Q_{Bulk} and winding number versus spin chain length. $d = 0.31416$ and $k_S = -0.40$. The purple squares are Q/Q_{Bulk} and the green circles represent the winding number. 137

Figure A.30 Q/Q_{Bulk} and winding number versus spin chain length. $d = 0.31416$ and $k_S = -0.20$. The purple squares are Q/Q_{Bulk} and the green circles represent the winding number. 137

Figure A.31 Q/Q_{Bulk} and winding number versus spin chain length. $d = 0.31416$ and $k_S = -0.10$. The purple squares are Q/Q_{Bulk} and the green circles represent the winding number. 138

Figure A.32 Q/Q_{Bulk} and winding number versus spin chain length. $d = 0.31416$ and $k_S = 0$. The purple squares are Q/Q_{Bulk} and the green circles represent the winding number. 138

Figure A.33 Q/Q_{Bulk} and winding number versus spin chain length. $d = 0.31416$ and $k_S = 0.10$. The purple squares are Q/Q_{Bulk} and the green circles represent the winding number. 139

Figure A.34 Q/Q_{Bulk} and winding number versus spin chain length. $d = 0.31416$ and $k_S = 0.20$. The purple squares are Q/Q_{Bulk} and the green circles represent the winding number. 139

Figure A.35 Q/Q_{Bulk} and winding number versus spin chain length. $d = 0.31416$ and $k_S = 0.30$. The purple squares are Q/Q_{Bulk} and the green circles represent the winding number. 140

Figure A.36 Q/Q_{Bulk} and winding number versus spin chain length. $d = 0.31416$ and $k_S = 0.40$. The purple squares are Q/Q_{Bulk} and the green circles represent the winding number. 140

Figure A.37 Q/Q_{Bulk} and winding number versus spin chain length. $d = 0.31416$ and $k_S = 0.50$. The purple squares are Q/Q_{Bulk} and the green circles represent the winding number. 141

Figure A.38 Q/Q_{Bulk} and winding number versus spin chain length. $d = 0.31416$ and $k_S = 0.60$. The purple squares are Q/Q_{Bulk} and the green circles represent the winding number. 141

Figure A.39 Q/Q_{Bulk} and winding number versus spin chain length. $d = 0.31416$ and $k_S = 0.70$. The purple squares are Q/Q_{Bulk} and the green circles represent the winding number. 142

Figure A.40 Q/Q_{Bulk} and winding number versus spin chain length. $d = 0.31416$ and $k_S = 0.80$. The purple squares are Q/Q_{Bulk} and the green circles represent the winding number. 142

Figure A.41 Q/Q_{Bulk} and winding number versus spin chain length. $d = 0.31416$ and $k_S = 0.90$. The purple squares are Q/Q_{Bulk} and the green circles represent the winding number. 143

Figure A.42 Q/Q_{Bulk} and winding number versus spin chain length. $d = 0.31416$ and $k_S = 1.00$. The purple squares are Q/Q_{Bulk} and the green circles represent the winding number. 143

Figure A.43 Q/Q_{Bulk} versus spin chain length. $d = 0.04724$ and $k_S = -1.00$, -0.10, 0.10, and 1.00. 144

Figure A.44 Q/Q_{Bulk} and winding number versus spin chain length. $d = 0.04724$ and $k_S = -1.00$. The purple squares are Q/Q_{Bulk} and the green circles represent the winding number. 145

Figure A.45 Q/Q_{Bulk} and winding number versus spin chain length. $d = 0.04724$ and $k_S = -0.90$. The purple squares are Q/Q_{Bulk} and the green circles represent the winding number. 145

Figure A.46 Q/Q_{Bulk} and winding number versus spin chain length. $d = 0.04724$ and $k_S = -0.80$. The purple squares are Q/Q_{Bulk} and the green circles represent the winding number. 146

Figure A.47 Q/Q_{Bulk} and winding number versus spin chain length. $d = 0.04724$ and $k_S = -0.70$. The purple squares are Q/Q_{Bulk} and the green circles represent the winding number. 146

Figure A.48 Q/Q_{Bulk} and winding number versus spin chain length. $d = 0.04724$ and $k_S = -0.60$. The purple squares are Q/Q_{Bulk} and the green circles represent the winding number. 147

Figure A.49 Q/Q_{Bulk} and winding number versus spin chain length. $d = 0.04724$ and $k_S = -0.50$. The purple squares are Q/Q_{Bulk} and the green circles represent the winding number. 147
Figure A.50 Q/Q_{Bulk} and winding number versus spin chain length. $d = 0.04724$ and $k_S = -0.40$. The purple squares are Q/Q_{Bulk} and the green circles represent the winding number. 148
Figure A.51 Q/Q_{Bulk} and winding number versus spin chain length. $d = 0.04724$ and $k_S = -0.20$. The purple squares are Q/Q_{Bulk} and the green circles represent the winding number. 148
Figure A.52 Q/Q_{Bulk} and winding number versus spin chain length. $d = 0.04724$ and $k_S = -0.10$. The purple squares are Q/Q_{Bulk} and the green circles represent the winding number. 149
Figure A.53 Q/Q_{Bulk} and winding number versus spin chain length. $d = 0.04724$ and $k_S = 0$. The purple squares are Q/Q_{Bulk} and the green circles represent the winding number. 149
Figure A.54 Q/Q_{Bulk} and winding number versus spin chain length. $d = 0.04724$ and $k_S = 0.10$. The purple squares are Q/Q_{Bulk} and the green circles represent the winding number. 150
Figure A.55 Q/Q_{Bulk} and winding number versus spin chain length. $d = 0.04724$ and $k_S = 0.20$. The purple squares are Q/Q_{Bulk} and the green circles represent the winding number. 150
Figure A.56 Q/Q_{Bulk} and winding number versus spin chain length. $d = 0.04724$ and $k_S = 0.30$. The purple squares are Q/Q_{Bulk} and the green circles represent the winding number. 151
Figure A.57 Q/Q_{Bulk} and winding number versus spin chain length. $d = 0.04724$ and $k_S = 0.40$. The purple squares are Q/Q_{Bulk} and the green circles represent the winding number. 151
Figure A.58 Q/Q_{Bulk} and winding number versus spin chain length. $d = 0.04724$ and $k_S = 0.50$. The purple squares are Q/Q_{Bulk} and the green circles represent the winding number. 152
Figure A.59 Q/Q_{Bulk} and winding number versus spin chain length. $d = 0.04724$ and $k_S = 0.60$. The purple squares are Q/Q_{Bulk} and the green circles represent the winding number. 152

Figure A.60 Q/Q_{Bulk} and winding number versus spin chain length. $d = 0.04724$ and $k_S = 0.70$. The purple squares are Q/Q_{Bulk} and the green circles represent the winding number. 153

Figure A.61 Q/Q_{Bulk} and winding number versus spin chain length. $d = 0.04724$ and $k_S = 0.80$. The purple squares are Q/Q_{Bulk} and the green circles represent the winding number. 153

Figure A.62 Q/Q_{Bulk} and winding number versus spin chain length. $d = 0.04724$ and $k_S = 0.90$. The purple squares are Q/Q_{Bulk} and the green circles represent the winding number. 154

Figure A.63 Q/Q_{Bulk} and winding number versus spin chain length. $d = 0.04724$ and $k_S = 1.00$. The purple squares are Q/Q_{Bulk} and the green circles represent the winding number. 154

Figure B.1 Q/Q_{bulk} and spin-canting-induced magnetization versus nanoparticle length. $d = 0.15708$, $k_S = -1.00$. Magnetization is in units of $D'S/J$. 155

Figure B.2 Nanoparticles of different sizes with $d = 0.15708$ and $k_S = -1.00$. Spins of the same colour belong to the same sublattice. The size of the nanoparticles is $L \times L$. 156

Figure B.3 Q/Q_{bulk} and spin-canting-induced magnetization versus nanoparticle length. $d = 0.15708$, $k_S = -0.90$. Magnetization is in units of $D'S/J$. 156

Figure B.4 Nanoparticles of different sizes with $d = 0.15708$ and $k_S = -0.90$. Spins of the same colour belong to the same sublattice. The size of the nanoparticles is $L \times L$. 157

Figure B.5 Q/Q_{bulk} and spin-canting-induced magnetization versus nanoparticle length. $d = 0.15708$, $k_S = -0.80$. Magnetization is in units of $D'S/J$. 157

Figure B.6 Nanoparticles of different sizes with $d = 0.15708$ and $k_S = -0.80$. Spins of the same colour belong to the same sublattice. The size of the nanoparticles is $L \times L$. 158

Figure B.7 Q/Q_{bulk} and spin-canting-induced magnetization versus nanoparticle length. $d = 0.15708$, $k_S = -0.70$. Magnetization is in units of $D'S/J$. 158

Figure B.8 Nanoparticles of different sizes with $d = 0.15708$ and $k_S = -0.70$. Spins of the same colour belong to the same sublattice. The size of the nanoparticles is $L \times L$. 159

Figure B.9 Q/Q_{bulk} and spin-canting-induced magnetization versus nanoparticle length. $d = 0.15708$, $k_S = -0.60$. Magnetization is in units of $D'S/J$. 159

Figure B.10 Nanoparticles of different sizes with $d = 0.15708$ and $k_S = -0.60$. Spins of the same colour belong to the same sublattice. The size of the nanoparticles is $L \times L$. 160

Figure B.11 Q/Q_{bulk} and spin-canting-induced magnetization versus nanoparticle length. $d = 0.15708$, $k_S = -0.50$. Magnetization is in units of $D'S/J$. 160

Figure B.12 Nanoparticles of different sizes with $d = 0.15708$ and $k_S = -0.50$. Spins of the same colour belong to the same sublattice. The size of the nanoparticles is $L \times L$. 161

Figure B.13 Q/Q_{bulk} and spin-canting-induced magnetization versus nanoparticle length. $d = 0.15708$, $k_S = -0.40$. Magnetization is in units of $D'S/J$. 161

Figure B.14 Nanoparticles of different sizes with $d = 0.15708$ and $k_S = -0.40$. Spins of the same colour belong to the same sublattice. The size of the nanoparticles is $L \times L$. 162

Figure B.15 Q/Q_{bulk} and spin-canting-induced magnetization versus nanoparticle length. $d = 0.15708$, $k_S = -0.30$. Magnetization is in units of $D'S/J$. 162

Figure B.16 Nanoparticles of different sizes with $d = 0.15708$ and $k_S = -0.30$. Spins of the same colour belong to the same sublattice. The size of the nanoparticles is $L \times L$. 163

Figure B.17 Q/Q_{bulk} and spin-canting-induced magnetization versus nanoparticle length. $d = 0.15708$, $k_S = -0.20$. Magnetization is in units of $D'S/J$. 163

Figure B.18 Nanoparticles of different sizes with $d = 0.15708$ and $k_S = -0.20$. Spins of the same colour belong to the same sublattice. The size of the nanoparticles is $L \times L$. 164

Figure B.19 Q/Q_{bulk} and spin-canting-induced magnetization versus nanoparticle length. $d = 0.15708$, $k_S = 0.20$. Magnetization is in units of $D'S/J$. 164
Figure B.20 Nanoparticles of different sizes with $d = 0.15708$ and $k_S = 0.20$. Spins of the same colour belong to the same sublattice. The size of the nanoparticles is $L \times L$. 165
Figure B.21 Q/Q_{bulk} and spin-canting-induced magnetization versus nanoparticle length. $d = 0.15708$, $k_S = 0.30$. Magnetization is in units of $D'S/J$. 165
Figure B.22 Nanoparticles of different sizes with $d = 0.15708$ and $k_S = 0.30$. Spins of the same colour belong to the same sublattice. The size of the nanoparticles is $L \times L$. 166
Figure B.23 Q/Q_{bulk} and spin-canting-induced magnetization versus nanoparticle length. $d = 0.15708$, $k_S = 0.40$. Magnetization is in units of $D'S/J$. 166
Figure B.24 Nanoparticles of different sizes with $d = 0.15708$ and $k_S = 0.40$. Spins of the same colour belong to the same sublattice. The size of the nanoparticles is $L \times L$. 167
Figure B.25 Q/Q_{bulk} and spin-canting-induced magnetization versus nanoparticle length. $d = 0.15708$, $k_S = 0.50$. Magnetization is in units of $D'S/J$. 167
Figure B.26 Nanoparticles of different sizes with $d = 0.15708$ and $k_S = 0.50$. Spins of the same colour belong to the same sublattice. The size of the nanoparticles is $L \times L$. 168
Figure B.27 Q/Q_{bulk} and spin-canting-induced magnetization versus nanoparticle length. $d = 0.15708$, $k_S = 0.60$. Magnetization is in units of $D'S/J$. 168
Figure B.28 Nanoparticles of different sizes with $d = 0.15708$ and $k_S = 0.60$. Spins of the same colour belong to the same sublattice. The size of the nanoparticles is $L \times L$. 169
Figure B.29 Q/Q_{bulk} and spin-canting-induced magnetization versus nanoparticle length. $d = 0.15708$, $k_S = 0.70$. Magnetization is in units of $D'S/J$. 169

Figure B.30 Nanoparticles of different sizes with $d = 0.15708$ and $k_S = 0.70$. Spins of the same colour belong to the same sublattice. The size of the nanoparticles is $L \times L$. 170

Figure B.31 Q/Q_{bulk} and spin-canting-induced magnetization versus nanoparticle length. $d = 0.15708$, $k_S = 0.80$. Magnetization is in units of $D'S/J$. 170

Figure B.32 Nanoparticles of different sizes with $d = 0.15708$ and $k_S = 0.80$. Spins of the same colour belong to the same sublattice. The size of the nanoparticles is $L \times L$. 171

Figure B.33 Q/Q_{bulk} and spin-canting-induced magnetization versus nanoparticle length. $d = 0.15708$, $k_S = 0.90$. Magnetization is in units of $D'S/J$. 171

Figure B.34 Nanoparticles of different sizes with $d = 0.15708$ and $k_S = 0.90$. Spins of the same colour belong to the same sublattice. The size of the nanoparticles is $L \times L$. 172

Figure B.35 Q/Q_{bulk} and spin-canting-induced magnetization versus nanoparticle length. $d = 0.15708$, $k_S = 1.00$. Magnetization is in units of $D'S/J$. 172

Figure B.36 Nanoparticles of different sizes with $d = 0.15708$ and $k_S = 1.00$. Spins of the same colour belong to the same sublattice. The size of the nanoparticles is $L \times L$. 173

Figure C.1 Q/Q_{Bulk} versus nanoparticle side length L/λ_{bulk} and magnetization versus nanoparticle side length L/λ_{bulk} for spin cube $(L \times L \times L)$. The magnetization is in units of $D'S/J$. $d = 0.15708$, $k_S = -1.00$. 175

Figure C.2 Q/Q_{Bulk} versus nanoparticle side length L/λ_{bulk} and magnetization versus nanoparticle side length L/λ_{bulk} for spin cube $(L \times L \times L)$. The magnetization is in units of $D'S/J$. $d = 0.15708$, $k_S = -0.90$. 175

Figure C.3 Q/Q_{Bulk} versus nanoparticle side length L/λ_{bulk} and magnetization versus nanoparticle side length L/λ_{bulk} for spin cube $(L \times L \times L)$. The magnetization is in units of $D'S/J$. $d = 0.15708$, $k_S = -0.80$. 176

Figure C.4 Q/Q_{Bulk} versus nanoparticle side length L/λ_{bulk} and magnetization versus nanoparticle side length L/λ_{bulk} for spin cube $(L \times L \times L)$. The magnetization is in units of $D'S/J$. $d = 0.15708$, $k_S = -0.70$. 176

Figure C.5 Q/Q_{Bulk} versus nanoparticle side length L/λ_{bulk} and magnetization versus nanoparticle side length L/λ_{bulk} for spin cube $(L \times L \times L)$. The magnetization is in units of $D'S/J$. $d = 0.15708$, $k_S = -0.6$ 0.177

Figure C.6 Q/Q_{Bulk} versus nanoparticle side length L/λ_{bulk} and magnetization versus nanoparticle side length L/λ_{bulk} for spin cube $(L \times L \times L)$. The magnetization is in units of $D'S/J$. $d = 0.15708$, $k_S = -0.5$ 0.177

Figure C.7 Q/Q_{Bulk} versus nanoparticle side length L/λ_{bulk} and magnetization versus nanoparticle side length L/λ_{bulk} for spin cube $(L \times L \times L)$. The magnetization is in units of $D'S/J$. $d = 0.15708$, $k_S = -0.4$ 0.178

Figure C.8 Q/Q_{Bulk} versus nanoparticle side length L/λ_{bulk} and magnetization versus nanoparticle side length L/λ_{bulk} for spin cube $(L \times L \times L)$. The magnetization is in units of $D'S/J$. $d = 0.15708$, $k_S = -0.3$ 0.178

Figure C.9 Q/Q_{Bulk} versus nanoparticle side length L/λ_{bulk} and magnetization versus nanoparticle side length L/λ_{bulk} for spin cube $(L \times L \times L)$. The magnetization is in units of $D'S/J$. $d = 0.15708$, $k_S = -0.2$ 0.179

Figure C.10 Q/Q_{Bulk} versus nanoparticle side length L/λ_{bulk} and magnetization versus nanoparticle side length L/λ_{bulk} for spin cube $(L \times L \times L)$. The magnetization is in units of $D'S/J$. $d = 0.15708$, $k_S = 0$. . 180

ACKNOWLEDGEMENTS

I would like to thank my supervisor, **Rogério de Sousa**, for his continued support of me and this project over the years. I must also acknowledge our experimental collaborators **Maximilien Cazayous** and **Ian Aupiais** for their wonderful Raman spectroscopy measurements on bismuth ferrite nanoparticles which were the impetus for much of this research. The **Centre for Advanced Materials & Related Technologies (CAMTEC)** also merits mention for supporting our research by fostering connections in the materials science community at the University of Victoria.

I am grateful to all of the members of the de Sousa research group who over the years have contributed to my understanding and appreciation of physics through our discussions and collaborations. They include **Noah Stemeroff**, **Stephanie LaForest**, **Mattias Le Dall**, **Pramodh Senarath Yapa**, **Seamus Beairsto**, and **Alberto Nava**.

My father and late mother, **Arthur** and **Rosney Allen**, always emphasized the importance of education and for this I thank them. (And for the several decades of free room and board, their unyielding love and support, and birthday parties at Dinotown.) I also thank my sister, **Krista Allen**, for her love and kindness.

Chapter 1

Introduction

Multiferroics are materials where multiple long-range orders are present at the same time [1]. Typically, the orders found in multiferroics are ferroelectricity and antiferromagnetism. Other orders, such as ferromagnetism, ferroelasticity, and ferrotoroidicity, are possible as well. There can be interplay between these orders via what is known as the magnetoelectric effect. If the effect is strong enough, then there is the potential for the material to have its ordering of one of these ferroic orders switched by a stimulus conventionally associated with one of the other orders [2].

The ability to electrically control the magnetic ordering of a material is a highly-desirable property for use such as in memory elements. Switching magnetic memory elements traditionally requires the application of a magnetic field, which is generated by an electric current. Heat loss makes this an inefficient process. Using an electric signal directly to switch the magnetic memory has the potential to reduce energy requirements to write to a memory [3, 4].

As one of the few room temperature multiferroics [1, 5], bismuth ferrite (BFO) has attracted quite a bit of attention. It has the potential to have its electric order controlled magnetically and its magnetic order controlled electrically. An impediment to its ability to be integrated into devices is its spiral antiferromagnetic order. The spins of BFO form a 630 Å long cycloid. This spin structure cancels the local weak ferromagnetism present in the system, which otherwise might be used as a switchable property to be read out.

Over the past two decades, a great deal of effort has been spent trying to understand multiferroics, with BFO as one of the most studied materials. Much of this effort has focused on multiferroics in their bulk form. However, to include these materials into devices they need to be in smaller formats such as thin films or nanoparticles.

Research into nanoparticles has commenced, but they remain less understood than their bulk counterparts.

An understanding of the spin structure of multiferroics in nanoparticle form is necessary to be able to exploit the magnetism in the materials which is of so much interest to researchers. An important difference in nanoparticles from bulk is a loss of symmetry at the surface of the nanoparticle. The reduced symmetry in BFO means that the anisotropy, the desire of materials' spins to point along a certain direction, is altered, and, in fact, increased. This anisotropy ends up having substantial influence on the spin configuration in nanoparticles.

In this dissertation the effects of system size on the cycloid will be analyzed. Using systems of varying size, BFO nanoparticles will be modelled and the lowest energy spin state for each size found. It will be shown that the cycloidal wavevector, a quantity related to the inverse of the wavelength of the cycloid, acquires jump discontinuities as a function of size when the value of the surface anisotropy is different from the bulk.

1.1 Literature review

The last decade has seen much research into the electric control of magnetism in BFO. Some highlights include in 2006 when Zhao *et al.* [6] reported the ability to reorient the direction of antiferromagnetic domains in BFO by switching the polarization. In other experiments BFO was placed within a heterostructure with a ferromagnet. The concept behind this is that exchange bias at the interface between BFO and the ferromagnet will cause the antiferromagnetism of BFO to be linked to the ferromagnetism of the ferromagnet. Chu *et al.* showed that a layer of $Co_{0.9}Fe_{0.1}$ deposited onto BFO had its magnetization change direction when an electric field was applied to the heterostructure [7]. Lebeugle *et al.* found something similar when they deposited $Ni_{78}Fe_{22}$, Permalloy, onto BFO [8]. The Permalloy had a magnetization along the cycloid direction and that magnetization was switched under the application of an electric field.

The above experiments were concerned with changing the ground state of BFO. In 2010, Rovillain *et al.* looked at what happened to the magnons, the magnetic excitations, when an electric field was applied [10]. The experiment saw a significant shift in magnon frequency under the application of an electric field. The magnons linearly shifted by 5 cm^{-1}, a relative shift of 30%. This shift is five orders of magnitude

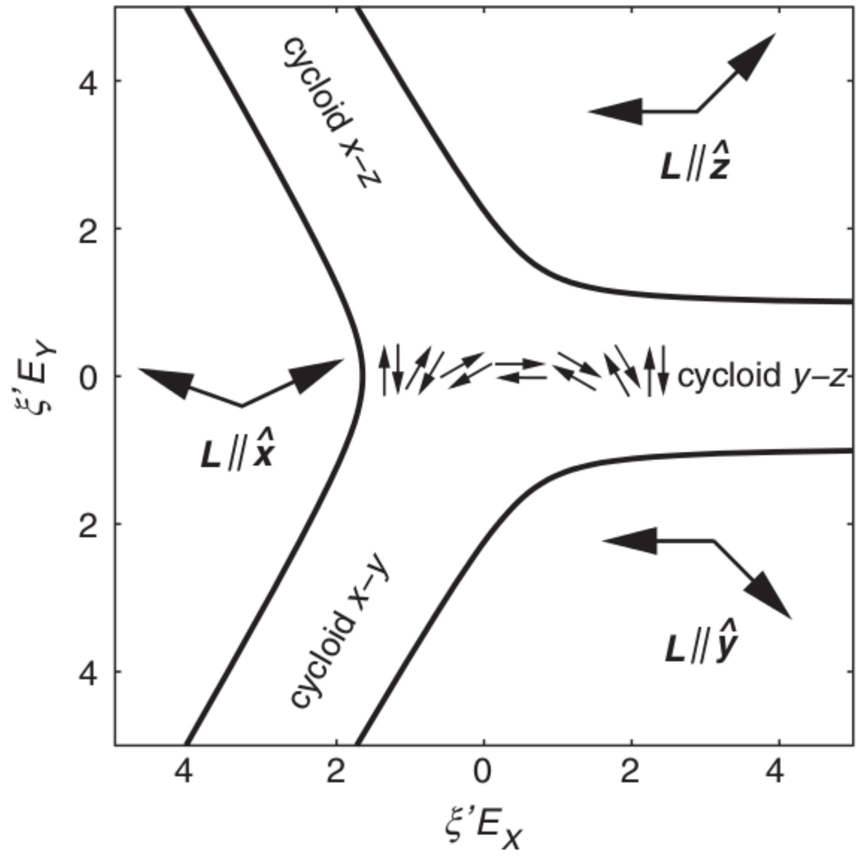

Figure 1.1: The electric field applied in certain directions will break the cycloid. Reprinted figure with permission from [9]. Copyright 2013 by the American Physical Society.

larger than any other known electric-field-induced magnon shift. Using this result, de Sousa *et al.* provided a microscopic theory to explain the shift [9]. The admixture of Bi^{3+} 6p and Fe^{3+} 3d orbitals, combined with the large spin-orbit coupling found in bismuth explain the shift and provide an additional linear magnetoelectric effect in BFO. As seen in Figure 1.1, this effect is also the cause behind the ability to apply an electric field to BFO and compel the cycloidal antiferromagnetic order to transform to homogeneous.

In regards to size effects, Mazumder *et al.* [11] and Annapu Reddy *et al.* [12] found increased magnetization in BFO nanoparticles relative to bulk. This is thought to be due to uncompensated spins at the surface. Huang *et al.* found that BFO nanoparticles comparable in size to the period of the cycloid exhibited an enhanced ferromagnetism versus bulk [13]. As well, they saw that the magnetoelectric coupling in the material was increased. They posited that nanoparticles of this size underwent increased FeO_6 octahedra rotation which increased the Dzyaloshinskii-Moriya interaction responsible for weak ferromagnetism. This led to a suppression of the cycloid and allowed for heightened ferromagnetism. This effect was only seen when the nanoparticles were close in size to the bulk period of the cycloid. Exactly how BFO nanoparticles transform as size is reduced is still not completely understood. Use of the model developed for this research to understand how size effects change the antiferromagnetic order will allow for a better understanding of the properties of BFO nanoparticles.

1.2 Research questions

Because of its status as one of the few room temperature multiferroics, BFO has attracted a great deal of interest for its potential use in industry [14, 15]. Due to this, the question of how to manipulate the weak ferromagnetism looms large in research into the material.

We have data showing Raman spectroscopy of BFO nanoparticles of various sizes (see Figure 2.8). As the nanoparticles become smaller, peaks in the spectroscopy data disappear. The peaks signify the presence of magnons. The spectroscopy data for 31 nm and 61 nm nanoparticles show no peaks, indicating that either the cycloid was destroyed or that the Raman peaks were too broad to be detected.

It is understood that surface anisotropy plays a significant role in nanoparticles. There are two contributions to single-ion anisotropy in bulk BFO which are of opposing sign [16, 17]. The reduced symmetry at the surface of the nanoparticles means that that cancellation which occurs in bulk will not occur in nanoparticles. This means that BFO nanoparticles are quite likely to possess large magnetic surface anisotropy. That anisotropy turns out to greatly influence the spin configuration in nanoparticles as we show below.

Motivated by this finding, we wanted to investigate how system size affects the ground state spin order of BFO. If it is to be incorporated into devices, then it will be in a form similar to these nanoparticles. This makes knowledge of size effects crucial for industrial applications.

A spin Hamiltonian was devised to represent the magnetic system of the nanoparticles. A surface anisotropy energy was included in this Hamiltonian. Nanoparticles of one, two, and three dimensions were studied. Optimization libraries in the computer software programs *Mathematica* and *Python* were used to find the ground state spin configurations.

1.3 Implications

One of the principal discoveries of this work is the bistability of the cycloidal wavevector, $Q = 2\pi/\lambda$, for certain sizes (λ is the period of the cycloid). We found that two different wavevectors, Q_1 and Q_2, can have the same minimal energy. Accompanying the bistability in Q are bistabilities in the spin-induced electric polarization and spin-canting-induced magnetization. As the bistabilities have the same origin, if one could switch either the polarization or the magnetization, then the other would follow. In this way it may be possible to have an electrically-controllable magnetization, and from that an electrically-controllable magnetic memory element.

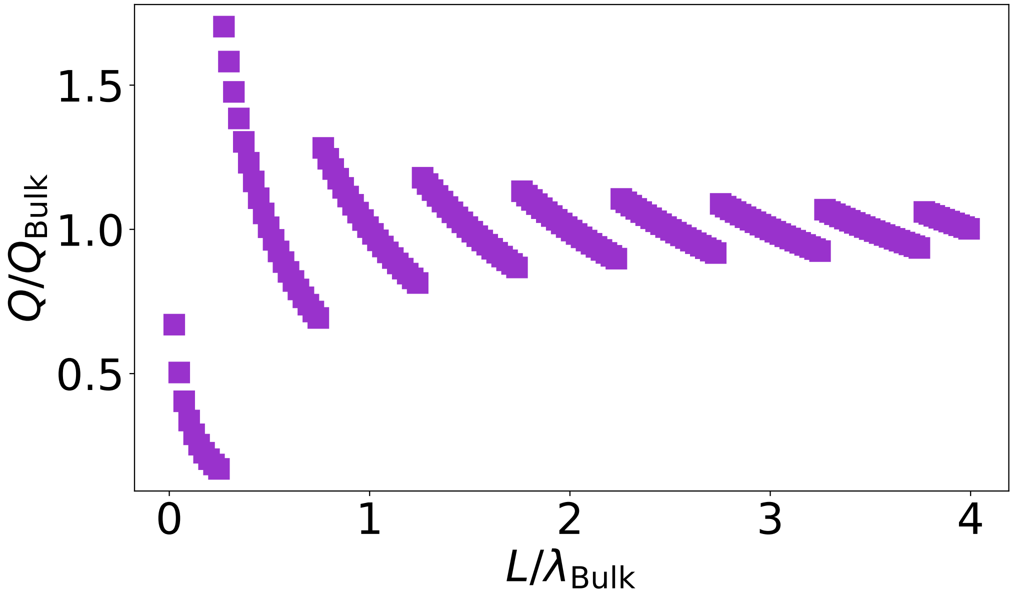

Figure 1.2: Q/Q_{Bulk} versus spin chain length. $D/J = 0.15708$ and $K_S/J = -0.50$.

The jumps and bistability in Q come from an original concept introduced here: the *edge effect*. Surface spins with anisotropy very much want to point perpendicular or parallel to the surface, depending on whether there is easy-axis or easy-plane anisotropy present. To accommodate this, the interior spins in spin chains in the nanoparticle adjust the angle between themselves, and thus, Q. As the size of the nanoparticle changes, the angle between the spins necessarily must change if the surface spins are to maintain their orientation. This leads to variation in Q as the nanoparticle size changes. As the nanoparticle size increases, eventually there becomes a size where it is energetically favourable for there to be a jump and increase in Q. The bistability in Q occurs at this critical size (see Figure 1.2).

Nanoparticles in two and three dimensions can be thought of as composed of ensembles of spin chains parallel to each other. Each spin chain had its own Q. What was found was that spin chains at or near the surface had reduced Q values relative to spin chains deeper inside the nanoparticle. This phenomenon was dubbed the *proximity effect*. Spin chains on the surface of higher-dimensional nanoparticles have surface anisotropy on all spins. Thus, surface spin chains want to have a reduced Q so that all of its spins can point along or against the surface normal to minimize the anisotropy energy. Interior spin chains only have surface anisotropy on the end spins of their chains. However, they are coupled to the surface spin chains through the exchange interaction. This leads to interior spin chains lowering the angle between spins, just as the surface spin chains do, but to a lesser degree. The reduction propagates into the nanoparticle, leaving spin chains in the centre of the nanoparticle with the largest cycloidal wavevector.

1.4 Agenda

Below is a description of the layout of the dissertation:

Chapter 1 introduces the work and its relevance. It also includes a listing of the proceeding chapters.

Chapter 2 describes background information on relevant topics such as magnetoelectric materials, multiferroics, bismuth ferrite, and magnetic nanoparticles.

Chapter 3 goes into detail describing the model used to describe the multiferroic nanoparticles.

Chapter 4 describes the energy minimization methods used to obtain results.

Chapter 5 contains results for one-dimensional spin chains. It also describes a phenomenon discovered in the work, the edge effect. There is also a discussion on the origin of the jump discontinuities found in the chains as the size of the nanoparticles is varied.

Chapter 6 has two-dimensional results for spin plaquettes. The proximity effect is described here.

Chapter 7 contains three-dimensional results for spin cubes.

Chapter 8 is a discussion of the results from earlier chapters.

Chapter 9 offers concluding remarks on the work.

Appendix A contains additional one-dimensional results.

Appendix B is a detailing of more two-dimensional results.

Appendix C has supplemental three-dimensional results not found in **Chapter 7**.

Chapter 2

Background

Bismuth ferrite has been a leading material of fascination in the 21^{st} century revival of multiferroics research. Primarily, because it is multiferroic at room temperature and has the potential to allow for electric (magnetic) control of magnetism (electricity). This interplay of orders is unique at room temperature. To understand the material better and reason for its place in materials research today, this chapter will go over some of the background information related to bismuth ferrite, including the magnetoelectric effect and multiferroics.

2.1 Magnetoelectric effect

The manipulation of the magnetic order in a material by an electric field and vice versa is known as the magnetoelectric (ME) effect [18]. If the material in question exhibits an ME effect, then an electric field can affect the material's magnetization or a magnetic field can alter the polarization:

$$M_i = M_{i,0} + \mu_0 \mu_{ij} H_j + \alpha_{ji} E_j + \dots, \tag{2.1}$$

$$P_i = P_{i,0} + \epsilon_0 \epsilon_{ij} E_j + \alpha_{ij} H_j + \dots. \tag{2.2}$$

Here μ_0 is the permeability of free space, ϵ_0 is permittivity of free space, μ_{ij} is magnetic susceptibility tensor, ϵ_{ij} is the electric susceptibility tensor, and α_{ij} is the linear ME tensor. It describes how a magnetization is induced by an electric field and how a electric polarization is induced by a magnetic field [19, §51. Piezomagnetism and the magnetoelectric effect].

This interplay suggests the ability to create devices which use the relationship between the magnetism and electricity. For instance, a magnetoelectric device might be able to be constructed so one could electrically write to a magnetic memory. This has potential energy savings versus magnetic writing [4].

Interest in this interconnectedness between the electric and magnetic realms in materials dates at least back to the late 19th century when Wilhelm Röntgen found that moving a dielectric through an electric field caused it to become magnetized [20]. Several years later Pierre Curie used symmetry arguments to suggest that certain materials might be able to exhibit an ME effect [21]. Experimental attempts in the 1920s to prove Curie's assertion correct were unable to do so [22]. The problem was that the tested materials were time-reversal invariant [18]. Time-reversal symmetry can be violated via application of a magnetic field or by moving the substance as Röntgen did [20]. It can also be violated if the material itself has long-range magnetic ordering. Landau and Lifshitz showed that for a material to possess the ME effect it must belong to certain magnetic symmetry classes and not contain an inversion centre [19]. In 1959 Dzyaloshinskii analyzed the symmetry of Cr_2O_3 and proposed it as a material that should show an ME effect [23]. In 1960 Astrov subjected a Cr_2O_3 sample to an electric field and measured a magnetic moment which linearly changed in magnitude with an alteration in the electric field strength [24].

Astrov's discovery set off a period where the effect was found in several more materials [18, 22]. However, in all of these cases the strength of the effect was found to be too low to be exploited in any device one might conceive. The unsuitability of discovered materials with ME effects to be used in devices contributed to reduced interest in topic after the early 1970s, along with the facts that relatively few materials were found possessing an ME effect and those that did often were unable to express the effect at room temperature [18].

It turns out that [25]

$$\alpha_{ij}^2 < \epsilon_{ii}\mu_{jj}. \tag{2.3}$$

This means that for a material to have a large magnetoelectric effect the material should be ferroelectric or ferromagnetic. Ideally, it would be both. That suggests that materials which have both of those ferroic orders are the prime ones to investigate in search for a large ME effect. Materials possessing multiple ferroic orders in the same phase are called multiferroics.

2.2 Multiferroics

That a material is a multiferroic does not guarantee that it will exhibit the ME effect, or, even if it does, possess one larger than those found in the initial search for ME materials. But multiferroics do provide a rich search area for strong ME effects.

A multiferroic is a material that has, in the same phase, two or more ferroic orders. Usually when referring to multiferroics this means ferromagnetism, a switchable magnetization in the absence of an applied magnetic field, and ferroelectricity, a switchable electric polarization in the absence of an applied electric field. But there are other ferroic orders that may be included: ferroelasticity is when a material spontaneously develops a switchable strain when the temperature is changed; and ferrotoroidicty is a proposed ferroic order where a spontaneous toroidal moment is formed and can be switched by the application of both electric and magnetic fields ($\mathbf{E} \times \mathbf{B}$). A toroidal moment is generated by certain spin arrangements, such as vortices, in materials. Antiferromagnetism, also considered a ferroic order, occurs when the difference in sublattice magnetizations of a material is non-zero [26].

For each ferroic order there is an associated order parameter, a property of the system that is zero at temperatures above which the ferroic order is not realized and non-zero at temperatures when the ferroic order is realized. For ferromagnetism the order parameter is $\mathbf{M}$, the magnetization. A magnetic lattice can be divided into sublattices and the sum of the magnetizations of these is the magnetization of the entire system:

$$\mathbf{M} = \mathbf{M}_1 + \mathbf{M}_2. \tag{2.4}$$

For ferroelectricity, the order parameter is $\mathbf{P}$, the electric polarization. For ferroelasticity, strain is the order parameter. The difference of the sublattice magnetizations, $\mathbf{L}$, known as the Néel vector, is the order parameter for antiferromagnetism:

$$\mathbf{L} = \mathbf{M}_1 - \mathbf{M}_2. \tag{2.5}$$

An impediment to the formation of some ferroelectric (anti)ferromagnets is that many materials that are ferroelectric are transition metal oxides and they are ferroelectric because the transition metal cations covalently bond with oxygen ions which causes the ions to move to non-centrosymmetric positions. For this bonding to occur, the transition metal ions are required to have empty d orbitals. Magnetism requires partially-filled d orbitals as empty or filled orbitals have zero magnetic moment so do not participate in magnetism [27]. This means that any ferroelectric (anti)ferromagnet needs to traverse an unconventional path to incorporate both ferroic orders into the same phase. (There are known ferroelectric ferromagnets such as strained $EuTiO_3$ [28]. Spin-phonon coupling in the system transforms the usual paraelectric and antiferromagnetic material into a ferroelectric ferromagnet via strain.)

Some multiferroics manage to allow for the coexistence of both orders by having one ion be responsible for the ferroelectricity and the another the magnetism. In materials such as the perovskites $BiFeO_3$ and $BiMnO_3$, the A-site Bi^{3+} contains an electron lone pair which is primarily responsible for the ferroelectricity. A-site refers to the generic formula for perovskite, ABO_3. The A-site ions are at the corners of the cubic unit cell, the B-site ion is in the centre of the cell surrounded by oxygen ions (see Figure 2.1). The B-site Fe^{3+} or Mn^{3+} is responsible for the magnetic ordering. Another means by which both orders might appear in the same phase is through ferroelectricity generated by a magnetic spiral [29–31]. All magnetic structures break time-reversal symmetry: spins flip under time reversal. Magnetic structures, however, do not necessarily break inversion symmetry. If all coordinates are negated, a homogeneous magnetic structure remains unchanged. A magnetic spiral is different, it does break inversion symmetry as the spiral has a definite direction which is reversed under inversion. This means an interaction of the form $P_i M_j \partial_k M_\ell$ can appear in the free energy of the system where P_i and M_j are components of the polarization and magnetization, respectively. The term is unchanged by inversion and time-reversal, requisite for inclusion in the free energy. If a magnetic spiral develops in a material, $\partial_k M_\ell$ becomes non-zero and and $M_j \partial_k M_\ell$ acts like an effective electric field induced by the magnetic texture. This results in a non-zero P_i in the lowest energy phase.

Other means in achieving multiferroicity include via geometric ferroelectricity, where geometric constraints cause polar ordering to occur [32, 33]. RMnO$_3$ (where R = Sc, Y, In, or Dy-Lu), $LuFeO_3$, $BaNiF_4$, and $Ca_3Mn_2O_7$ become multiferroic through this means. The materials are already magnetic and the geometric ferroelectricity means that they are then multiferroic. Magnetic ordering can also give rise to ferroelectricity [29, 34]. Cr_2BrO_4, $TbMnO_3$, and $YBaCuFeO_5$ are some of the materials which gain multiferroicity via this pathway [32, 33]. Fe_3O_4 [35] and an organic salt [36] use charge ordering, where the non-symmetric distribution of electrons about cations leads to the formation of an electric polarization, to achieve multiferroicity [32]. Composite multiferroics, with one component providing the magnetism and the other the ferroelectricity, have also been devised [32, 33].

Room-temperature multiferroics have been of interest due to their ability to be used in devices at ambient temperatures [37]. Reports of room-temperature multiferroicity appears for a variety of systems [38–64]. Several types of materials have been identified [37] as holding promise for room-temperature multiferroicity.

The lead-iron mixed perovskites $PbFe_{1/2}Nb_{1/2}O_3$ (PFN), $PbFe_{1/2}Ta_{1/2}O_3$ (PFT), $PbFe_{2/3}W_{1/3}O_3$ (PFW) combined with $PbZr_{1-x}Ti_xO_3$ (PZT) have drawn interest as room-temperature multiferroics [37]. PFN, PFT, and PFW are all ferroelectric and possess room-temperature or near-room-temperature weak ferromagnetism. PZT is the most studied room-temperature ferroelectric material, due in particular to its excellent piezoelectric properties. The idea is that combining these materials may be able to give rise to robust room-temperature multiferroicity [37, 51]. Solid solution PZTFT thin films, a combination of PZT and PFT (approximately $[\mathrm{Pb}\,(\mathrm{Zr}_{0.53}\mathrm{Ti}_{0.47})\,\mathrm{O}_3]_{0.6} - [\mathrm{Pb}\,(\mathrm{Fe}_{0.50}\mathrm{Ta}_{0.50})\,\mathrm{O}_3]_{0.4}$), have been shown to be multiferroic at room temperature [50].

Aurivillius-phase ferroelectrics such as $Bi_5Ti_3Fe_{0.7}Co_{0.3}O_{15}$ thin films [47] have been shown to be multiferroic at room temperature. These ferroelectrics have n number of perovskite units separated by Bi_2O_2 layers.

Additionally, there are claims that thin films of $Ga_xFe_{1-x}O_3$ [61, 64] have been made to be multiferroic (ferroelectric and ferrimagnetic) at room temperature. $Bi_{0.8}Ca_{0.2}MnO_3$ [55], $SmFeO_3$ [59], and $PbTi_{1-x}Pd_xO_3$ [60] all have reports of room-temperature multiferroicity. The double perovskite Bi_2FeCrO_6 (BFCO) is also known to be multiferroic at room temperature [38, 44].

With multiferroics we can return to the notion of controlling different ferroic orders with stimuli generally associated with other orders. For instance, in a ferroelectric ferroelastic it can be imagined that a mechanical stress would affect the electric polarization or that an applied electric field would change the strain in the material. In multiferroics, much of the research is focused on ferroelectric (anti)ferromagnets, as these systems are seen as the most promising area within multiferroics for potential device applications.

Ideally, there would be a multiferroic which was ferroelectric and ferromagnetic at room temperature while also possessing a large ME effect. Ferromagnetic materials comprise memory elements in many devices. The ferromagnet can be used as a memory as it holds its current magnetization direction after the applied field is turned off after any switching has occurred. But if the ferromagnet was also ferroelectric then its magnetization could be switched by an electric field. Switching a magnetization via an electric, rather than magnetic, field is desirable because to generate a magnetic field one needs a current and then that current is sent through a device to produce the magnetic field. There are losses due to heat in the generation of the magnetic field. Instead of this, it would be favourable to simply have an applied electric field reverse the magnetization. Nature, to date, has not been so kind.

There is no known room temperature ferroelectric ferromagnet. What there is is a room temperature ferroelectric antiferromagnet: bismuth ferrite.

2.3 Bismuth ferrite

Bismuth ferrite (BFO), $BiFeO_3$, as mentioned above, is a room temperature ferroelectric antiferromagnet. Its Curie temperature, the temperature below which it is ferroelectric is approximately 1100 K. The temperature below which it is antiferromagnetic, its Néel temperature, is approximately 650 K [5]. Its unit cell has a perovskite structure with a Bi^{3+} ion at the A-site and a Fe^{3+} ion at the B-site. At room temperature it has a pseudocubic rhombohedral structure and its space group is R3c. The rhombohedral lattice parameter a is equal to 3.965 Å and the rhombohedral angle is approximately 89.3° [1]. See Figure 2.1 for a visual representation of BFO.

BFO has a large electric polarization near 100 μC·cm^{-2} [65]. It points along one of the eight pseudocubic diagonals, $(\pm 1, \pm 1, \pm 1)$. The application of an electric field can switch along which diagonal the polarization points. The polarization is usually taken to be pointing along the [111] direction. A rhombohedral coordinate system can be introduced to describe the special directions in BFO as seen in Figure 2.1. The X direction points along the $\left[\bar{2}11\right]$ direction, the Y direction is along $\left[0\bar{1}1\right]$, and the Z direction is along [111].

In its ground state, the spins of BFO are not homogeneously antialigned. They form a spiral due to a spin-orbit effect known as the Dzyaloshinskii-Moriya interaction. The spiral is incommensurate, meaning that the crystal's lattice parameter is not a rational fraction of the spiral's wavelength [66, 67]. The type of spiral that the spins make is a cycloid, as shown in Figure 2.2. The length of the cycloid is $\lambda_{\text{bulk}} = 630$ Å. A second Dzyaloshinskii-Moriya interaction gives rise to a weak ferromagnetic moment (the red arrows in Figure 2.2). Because of the cycloid, the weak ferromagnetic moment averages to zero over the period of the cycloid.

Unwinding the cycloid would allow for the weak ferromagnetism to be homogeneous and not average to zero (see Figure 2.3). This ferromagnetism could then be

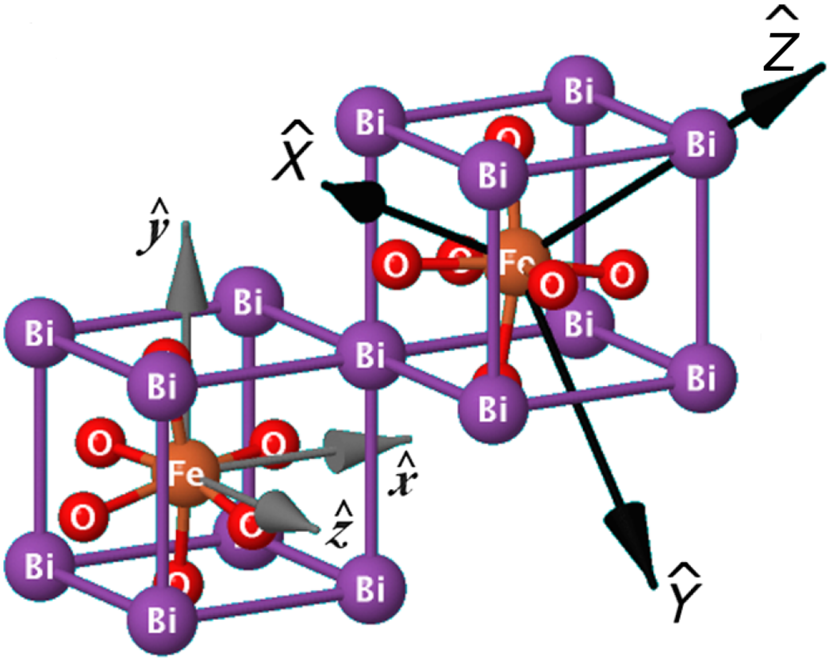

Figure 2.1: The unit cell of bismuth ferrite. The purple atoms are Bi^{3+}, red O^{2-} and gold Fe^{3+}. The left cell displays the cubic axes for BFO and the right cell shows the rhombohedral axes that it is convenient to use in describing BFO. Reprinted figure with permission from [9]. Copyright 2013 by the American Physical Society.

measured. It is known that the cycloid can be unwound in thin films [68], through chemical doping [69], with the application of a magnetic field [70], or an electric field [9].

The direction of the cycloid, represented by the vector $\mathbf{Q}$, is orthogonal to that of the polarization and is along one of the $\langle 1\bar{1}0 \rangle$ directions. Because of this, and the fact that the polarization direction can be switched, there have been successful schemes where the direction of the cycloid has been switched via the application of an electric field [8, 71, 72].

2.4 Anisotropy

One question which needs to be answered if BFO is to be used in devices is what happens to the cycloid for different nanoparticle sizes? The magnetization of the material depends on the nature of the antiferromagnetic ordering: If there remains a cycloid, then the weak ferromagnetism averages to zero over the sample; if the cycloid is absent, what takes its place? Standard G-type antiferromagnetism (nearest

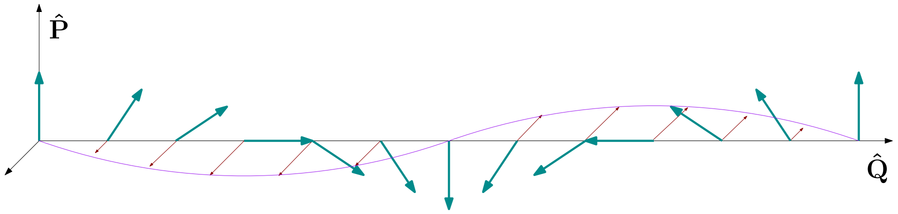

Figure 2.2: Antiferromagnetic cycloid. The blue-green arrows represent the Néel vector **L** and the red arrows represent the local weak ferromagnetism.

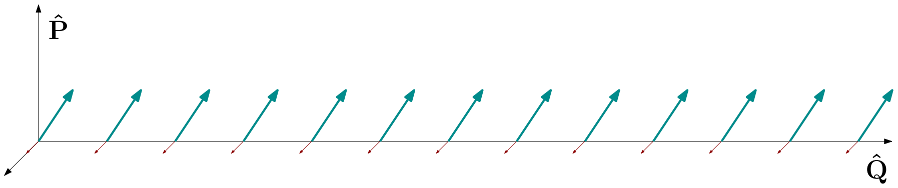

Figure 2.3: Homogeneous, antiferromagnetic case. The blue-green arrows represent the Néel vector **L** and the red arrows represent the local weak ferromagnetism.

neighbour spins antiparallel) with canting or something else altogether? It is obvious that for small particles there must be deviation from the bulk system. In the bulk BFO has a cycloid wavelength of ~ 63 nm. Any particle smaller than that size cannot complete a full twist of the spins.

One significant difference in nanoparticles compared to bulk samples is the contribution of surface anisotropy. Magnetic ions located at low-symmetry sites have greater anisotropy than ions at higher symmetry sites [73]. A nanoparticle, with a larger surface-to-volume ratio than a bulk sample, will have a significant fraction of its ions subject to surface anisotropy. This necessitates an understanding of anisotropy in magnetic materials.

2.4.1 Spin-orbit coupling

Magnetic anisotropy originates from spin-orbit coupling [73–75]. This is the coupling that occurs when an electron in an atom orbiting a charged nucleus experiences a magnetic field. From the frame of reference of the electron, it is the nucleus which is moving. As a charged object moving in a loop, the nucleus creates a magnetic field. The magnetic field is dependent on the orbital angular momentum of the electron, **L**. That field couples to the magnetic moment of the electron, which is proportional to the electron spin, **S**.

An electron in an atom experiences a potential, $V(r)$, from the positively-charged nucleus and from other electrons in the atom [76]. It is assumed that the potential is spherically symmetric. $\mathbf{r}$ is the position vector of the electron with the nucleus as the origin. $V(r)$ gives rise to an electric field:

$$\mathbf{E} = -\frac{1}{e}\nabla V = -\frac{1}{e}\frac{\mathbf{r}}{r}\frac{\partial V}{\partial r}, \tag{2.6}$$

where e is the electron's charge. The magnetic field in the rest frame of the nucleus is zero, which means that in the frame of the electron,

$$\mathbf{B} = -\frac{1}{c^2}\left(\mathbf{v} \times \mathbf{E}\right) = \frac{1}{ec^2}\frac{1}{r}\left(\mathbf{v} \times \mathbf{r}\frac{\partial V}{\partial r}\right), \tag{2.7}$$

where c is the speed of light and $\mathbf{v}$ is the velocity with which the electron is moving. (2.7) is not quite correct as the electron is not in an inertial frame. The argument will continue, for now, but the point will be re-evaluated shortly. The angular orbital momentum is equal to $\mathbf{L} = \mathbf{r} \times \mathbf{p}$. Setting $\mathbf{v} = \mathbf{p}/m$, where m is the electron mass, the magnetic field can be re-written as

$$\begin{aligned}\mathbf{B} &= \frac{1}{ec^2}\frac{1}{r}\left(\mathbf{v} \times \mathbf{r}\frac{\partial V}{\partial r}\right)\\ &= \frac{1}{mec^2}\frac{1}{r}\left(\mathbf{p} \times \mathbf{r}\frac{\partial V}{\partial r}\right)\\ &= -\frac{1}{mec^2}\frac{1}{r}\frac{\partial V}{\partial r}\mathbf{L}.\end{aligned} \tag{2.8}$$

The magnetic moment of the electron is

$$\boldsymbol{\mu} = \frac{e\,\mathbf{S}}{m}. \tag{2.9}$$

The potential energy of the spin in the magnetic field is then

$$\begin{aligned}U'_{\mathrm{SO}} &= -\boldsymbol{\mu} \cdot \mathbf{B}\\ &= \frac{e\mathbf{S}}{m} \cdot \frac{1}{mec^2}\frac{1}{r}\frac{\partial V}{\partial r}\mathbf{L}\\ &= \frac{1}{m^2c^2}\frac{1}{r}\frac{\partial V}{\partial r}\left(\mathbf{L} \cdot \mathbf{S}\right).\end{aligned} \tag{2.10}$$

Experimental evidence shows that (2.10) is two times larger than the actual spin-orbit energy [73, 74, 76, 77]. This can be attributed to the inappropriate use of the

Lorentz transformation for the magnetic field in a non-inertial frame. The corrected spin-orbit energy is

$$U_{\mathrm{SO}} = \frac{1}{2m^2c^2}\frac{1}{r}\frac{\partial V}{\partial r}\left(\mathbf{L}\cdot\mathbf{S}\right). \tag{2.11}$$

It can be seen how spin-orbit coupling contributes to anisotropy. The symmetry of a crystal favours a certain orbital arrangement, which, in turn, favours a certain spin arrangement. An attempt to change the direction that spins point would have to overcome the orbitals that relish the spin alignment as is. Changing the orbital orientation would mean overcoming the crystal lattice that prefers the present orbital configuration [75]. Anisotropy of this kind is known as magnetocrystalline anisotropy.

2.4.2 Surface anisotropy

The interface between the nanoparticle and vacuum allows for the emergence and strengthening of effects unseen in bulk samples [75, 78]. The sudden change between crystal and vacuum brings about a reduction in symmetry in nanoparticles as compared to their bulk counterparts. Néel first raised this point in an article from 1954 where he developed the idea of surface anisotropy [79]. Surfaces also tend to be rough with defects, have missing or broken bonds, and have variation in interatomic distances [78, 80, 81].

Weingart *et al.* [16] used density functional theory to calculate the single-ion anisotropy for $\mathrm{LaFeO_3}$ and BFO for different crystal structures. Single-ion anisotropy is attributable to only one spin site, unlike other interactions, like the exchange interaction, which depend on two spins. The single-ion anisotropy in BFO with cubic symmetry was found to be on the order of several μeV, which is relatively small for anisotropy energies. This is not the symmetry of standard BFO. The normal symmetry is rhombohedral R3c. For a tetragonal configuration with multiple antiferrodistortive rotations of the $\mathrm{FeO_6}$ octahedra (adjacent octahedra alternate rotation directions [82]), the single-ion anisotropy increased by two orders of magnitude. Also, there was a large anisotropy of -400 μeV reported with just the antiferrodistortive rotations and no ferroelectric distortion, responsible for the polarization in BFO. This is R$\bar{3}$c symmetry. With the introduction of the ferroelectric distortion to that system, the symmetry becomes the correct R3c of BFO. With both the antiferrodistortive rotations and ferroelectric distortion, the authors reported an anisotropy energy of just -1.3 μeV. Therefore, the authors concluded that BFO's anisotropy results from the addition of two large energy scales with opposite sign. It should be noted that a negative anisotropy energy would indicate an easy-plane anisotropy. In contrast, experimental results [83] report a positive anisotropy value of 7 μeV.

These results suggest that BFO is highly sensitive to the symmetry of the system and with reduced symmetry the conventionally small anisotropy in BFO could very well increase by significant amounts. As mentioned above, the point group symmetry at a surface site is generally lower than at a bulk one. For BFO nanoparticles this has the potential to significantly raise the anisotropy energy and open pathways to new spin structures unseen in bulk.

2.5 Magnetic nanoparticles

The integration of magnetic materials into devices requires that the said materials be in miniature form, be that thin films or nanoparticles. Materials in these different architectures end up having different properties than in bulk [84]. One of the primary reasons for deviation from bulk properties is the increase in surface anisotropy. Surface roughness and strain combine to allow the anisotropy in nanoparticles to be much larger than what is in bulk. There are reports that the anisotropy in nanoparticles can be up to two orders of magnitude larger in nanoparticles than in bulk [85, 86].

Another feature which can alter the spin configuration of magnetic nanoparticles is the absence of magnetic domains [84]. The small size of the particles makes the formation of domain walls energetically unfavourable. O'Handley [74] reports the critical size of a spherical, single-domain nanparticle to be

$$R_{\mathrm{SD}} = \frac{6\sqrt{AK}}{\mu_0 M_S^2}. \tag{2.12}$$

A is the exchange stiffness, a measure related to the temperature at which magnetic ordering sets in. K is the magnetic anisotropy, μ_0 is the permeability of free space, and M_S is the saturation magnetization, the magnetization the material experiences in a high magnetic field. The nanoparticle acts with a single magnetization for sizes smaller than R_{SD}. The bulk system has domains with magnetizations in different directions and responds to the application of an applied magnetic field primarily by the movement of domain walls [84].

In the single-magnetic-domain regime, the coercivity, the strength of magnetic field necessary to reverse the magnetization is usually larger than for the multiple domain regime. Only at very small nanoparticle sizes does the coercivity drop off. This occurs due to thermal fluctuations. There is a competiton between the anisotropy energy, KV, where V is the volume of the nanoparticle, and the thermal energy, k_BT, where k_B is the Boltzmann constant and T is the temperature. As the size of the nanoparticle reduces, the thermal energy becomes comparable to the anisotropy energy, which introduces thermal fluctuations. The magnetization rapidly switches in these nanoparticles. This state is known as superparamagnetism [75, 84]. The thermal fluctuations that can cause the magnetization of the nanoparticle to rapidly switch orientations means that on average the magnetization is zero. As the Néel vector $\mathbf{L}$ is the difference of magnetization in the sublattices, it too would average zero in the superparamagnetic regime.

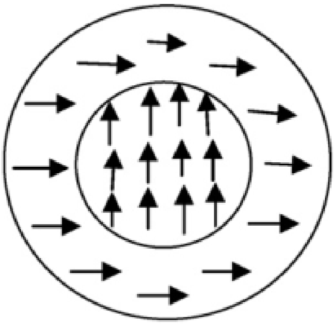

Figure 2.4: Model of a magnetic nanoparticle with different core and surface magnetizations. Reprinted from [84], with permission from Elsevier. Copyright 2009.

Looking further into the reasons that nanoparticles have differing characteristics to bulk systems, the surface is a sudden change in the spin and lattice structure of the material. This can cause reduced symmetry, changing interaction strength. Another possibility is that a lattice distortion at the surface traps an atom in an excited state. The large surface-to-volume ratio of nanoparticles relative bulk means that many of these excited states can occur, introducing effects unseen in the bulk [84].

Experimental research [85, 87–89] has found that the anisotropy in spherical nanoparticles goes as

$$K = K_c + \frac{6K_S}{D}. \tag{2.13}$$

K_c is the magnetocrystalline anisotropy associated with the core of nanoparticle. There is some axis along which it is favourable for the spins in a particle to point in relation to their orbitals [75]. K_S is the surface anisotropy which is seemingly size-independent and D is the diameter of the nanoparticle. This formula shows that the anisotropy of a nanoparticle is highly size-dependent.

The notion of the core and surface of a nanoparticle having different anisotropies leads to a model as depicted in Figure 2.4. The interior of the nanoparticle behaves much like the bulk crystal, but the surface behaves like a disordered layer with broken bonds, vacancies, and strain contributing to the disorder [84]. Theoretical work with such models has agreed with results from experiments. In such models, the saturation magnetization is lowered and magnetic saturation, where the application of a stronger external magnetic field does not increase the magnetization, is never achieved. There is a shifting of hysteresis loops in antiferromagnetic nanoparticles due to exchange bias between the core and the surface [90].

2.6 BFO nanoparticles

The first question one might ask about BFO nanoparticles is whether they remain multiferroic at room temperature. The answer turns out be yes. In recent years, several studies [11–13, 90–98] have examined BFO in nanoparticle form. Mazumder *et al.* [11] and Selbach *et al.* [92] found that while the Néel temperature reduced with particle size, the drop in T_N from bulk was only approximately 30 K for the smallest measured nanoparticles. Selbach *et al.* also found evidence that the ferroelectric moment was still present in 13 nm nanoparticles.

Both Mazumder *et al.* and Selbach *et al.* conducted calorimetry measurements to determine the Néel temperature as a function of the particle size, d. Figure 2.5 shows the results from the Selbach *et al.* paper. X-ray diffraction was performed to determine the size of the nanoparticles. For the calorimetry, a function of the heat capacity is plotted against temperature. Where the maximum in the resulting curve occurs is determined to be T_N. A phonon anomaly and a change in the dielectric response due to the magnetoelectric effect at T_N explains why the maximum of the curve corresponds to T_N [11]. Mazumder *et al.* and Selbach *et al.* report different changes to T_N, but this was thought to be due to differences in nanoparticle fabrication [92].

In Figure 2.5 there is approximately a difference of 25°C between the bulk Néel temperature and the value for 13.3 nm nanoparticles. From the progression of T_N, a formula [99, 100] can be fitted for $T_N(d)$:

$$\frac{T_N(d) - T_N(\infty)}{T_N(\infty)} = \pm \left(\frac{d}{d_0}\right)^{-1/\nu}. \tag{2.14}$$

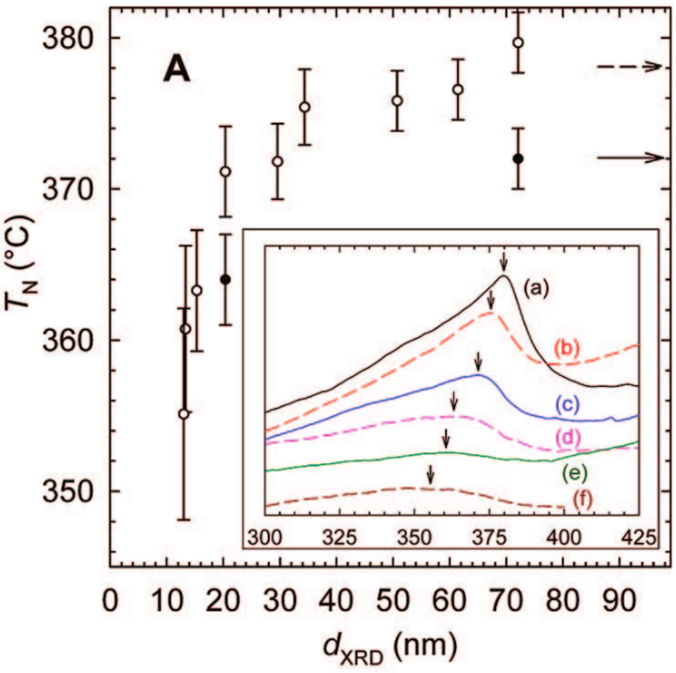

Figure 2.5: Néel temperature as a function of particle size in nanoparticle BFO. The closed markers indicate a heating rate of 1°C min^{-1} and the open markers indicate a heating rate of 10°C min^{-1}. The dashed arrow is indicates the bulk T_N for the 40°C min^{-1} heating rate and the solid arrow indicates a rate of 10°C min^{-1}. The inset shows the differential scanning calorimetry traces used to determine T_N. The plots are for (a) bulk, (b) 72.1 nm, (c) 34.4 nm, (d) 20.4 nm, (e) 15.3 nm, and (f) 13.3 nm. The arrows indicate the maximum and the T_N. Reprinted with permission from [92]. Copyright 2007 American Chemical Society.

$T_N(\infty)$ is the bulk Néel temperature, d_0 is a characteristic length in the nanoparticle, and ν is an exponent related to the correlation length. Selbach *et al.* [92] found values of $d_0 = (1.7 \pm 0.5)$ nm and $\nu = 0.5 \pm 0.1$.

Regarding the ferroelectric polarization in nanoparticle BFO, Selbach *et al.* [92] found evidence that for nanoparticles larger than 30 nm the polarization is near its bulk value. The polarization decreased for nanoparticles below 30 nm, but was still 75% of its bulk value for 13-nm-sized nanoparticles. To probe the polarization strength of BFO nanoparticles the authors adopted a representation of the BFO unit cell as being hexagonal. Two variables were then introduced, s and t. With the Z position of the O^{2-} ions held fixed, s describes the Z position of the Fe^{3+} ion and t is dependent on the Z position of the Bi^{3+} ion [101]. X-ray diffraction and Rietveld refinement [102, 103], optimizing the atomic positions to best match the diffraction spectra, was used to find s and t. The difference of the two, $s - t$, is proportional

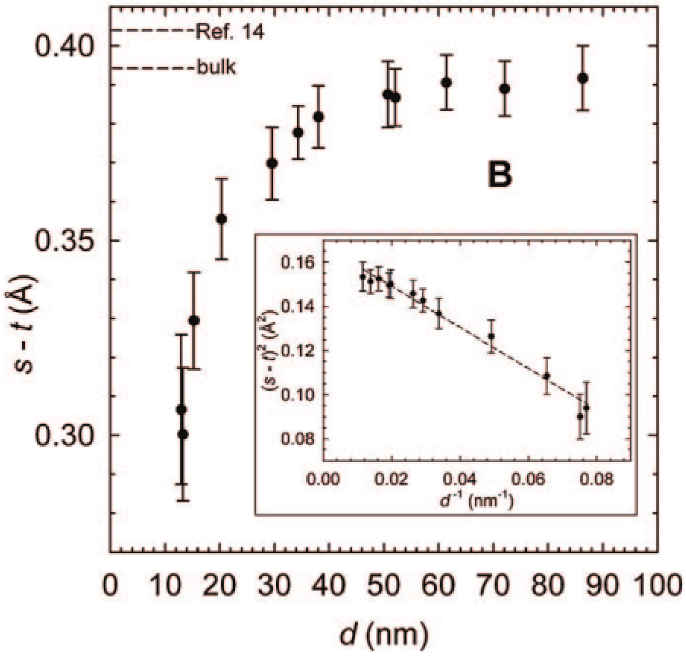

Figure 2.6: Difference in ion displacement versus particle size for nanoparticle BFO. The difference in ion displacement, $s - t$ is a proxy for the electric polarization. The inset plots $(s - t)^2$ versus the inverse particle size. Reprinted with permission from [92]. Copyright 2007 American Chemical Society.

to the polarization. s and t are displacements for the ions in the hexagonal unit cell. If they are both equal to zero then there is no spontaneous polarization in the nanoparticle [101].

Figure 2.6 shows a plot of $s-t$ versus the nanoparticle size, d. Its value is relatively flat for $d \geq 30$ nm. For nanoparticles below 30 nm, $s - t$ begins to drop off. However, at 13 nm, the smallest value measured, the $s - t$ is three quarters of what is was at and above 30 nm, so while the decline in $s - t$, and accordingly the polarization, is substantial, it retains much of its magnitude.

Park *et al.* [90] reported on the magnetization in a BFO nanoparticle as a function of size. The insets of Figure 2.7 shows this. In Figure 2.7b, it can be seen that there is a $1/d$ relationship for the magnetization except for the 14 nm nanoparticle. A magnetic field was applied to the nanoparticles and their magnetization was measured using a superconducting quantum interference device (SQUID) magnetometer. The results are for the magnetization measured under a 50 kOe field. Magnetization being proportional to $1/d$ suggests that the surface-to-volume ratio is driving the magnetization. The weak ferromagnetism present in bulk BFO cannot be cancelled

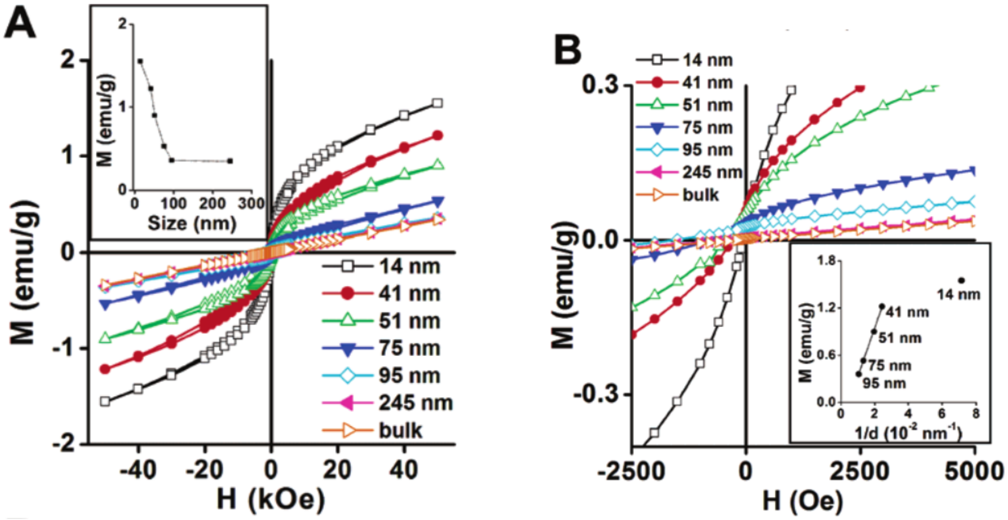

(a) From -50 kOe to 50 kOe. Inset shows magnetization versus particle size under a 50 kOe field.

(b) From -2500 Oe to 5000 Oe. The return branches of the hysteresis curves have been omitted. Inset shows magnetization versus inverse particle size under a 50 kOe field.

Figure 2.7: Magnetic hysteresis curves (magnetization versus magnetic field) for nanoparticle BFO of various sizes. Insets relate magnetization and particle size. Reprinted with permission from [90]. Copyright 2007 American Chemical Society.

in nanoparticles smaller than λ_{bulk}. As the nanoparticles become smaller, less of the weak ferromagnetism is cancelled and the magnetization grows. The authors suggest that the 14 nm nanoparticles not continuing the trend of the others in regards to magnetization strength may be due surface strain and lattice disorder being introduced into the interiors of the particles. That would lead to novel magnetic structures being formed, which would overall frustrate the magnetism and reduce the magnetization relative to the $1/d$ trend. The magnetization found at 50 kOe for the 14 nm nanoparticles was 1.55 emu/g = 0.093 μ_{B}/Fe.

To ensure that studied BFO nanoparticles are not in the superparamagnetic regime, it is necessary to determine the critical size for superparamagnetism. As discussed in Section 2.5, superparamagnetism arises when the thermal energy is close in magnitude to that of the anisotropy energy. Specifically, the relaxation time of the spin [73, 74] is given by the Néel-Arrhenius equation,

$$\tau = \tau_0 \exp\left(\frac{KV}{k_B T}\right). \tag{2.15}$$

τ_0 is the characteristic relaxation time for a material. It is usually on the order of a nanosecond [73]. From this relation, the critical size for superparamagnetism can be determined. Superparamagnetism occurs when $KV < k_BT$. The predominant anisotropy energy in antiferromagnets is the single-ion one. For the anisotropy energy, we will take the bulk single-ion anisotropy reported for BFO as 6.8 μeV [83]. $KV = NS^2K_{\text{bulk}}v_0$, where N is the number of unit cells comprising the nanoparticle and $v_0 = a^3$ is the volume of the unit cell.

This means that superparamagnetism will occur when $V < V_c$ for

$$V_c = Nv_0 = \frac{k_BTv_0}{K_{\text{bulk}}S^2}. \tag{2.16}$$

From (2.16), the critical radius for a spherical nanoparticle at room temperature is

$$\begin{aligned} r_c &= \left(\frac{3V_c}{4\pi}\right)^{1/3} \\ &= \left(\frac{3k_BT}{4\pi K_{\text{bulk}}S^2}\right)^{1/3} a \\ &= \left(\frac{3\,[86.17\ \mu\text{eV}\cdot\text{K}^{-1}]\,[300\ \text{K}]}{4\pi\,[6.8\ \mu\text{eV}]\,[5/2]^2}\right)^{1/3} (0.396\ \text{nm}) \\ &= 2.1\ \text{nm}. \end{aligned} \tag{2.17}$$

To be certain that the nanoparticle is not superparamagnetic it must be of a size such that $r \gg r_c$. However, the value of r_c in (2.17) is only an upper bound for the superparamagnetic regime. The estimate does not take into account the other contributing sources to anisotropy, such as the surface anisotropy. The surface anisotropy can exceed the bulk single-ion anisotropy and adding this contribution would lower the critical radius.

Alternatively, one can invert (2.15) and define [74] a probability per unit time of a spin reversing:

$$P_{\text{relax}} = \nu_0 \exp\left(-\frac{KV}{k_BT}\right). \tag{2.18}$$

$\nu_0 = 1/\tau_0$ is known as the attempt frequency factor. We can define stability of the spin as having a less than 10% probability of flipping for a given time interval. We can assume $\nu_0 = 10^9\ \text{s}^{-1}$. If we want the particle to be stable for one second at room temperature then

$$\begin{aligned}
0.1\ \mathrm{s}^{-1} &= 10^{9}\ \mathrm{s}^{-1} \exp\left(-\frac{KV}{k_B T}\right) \\
10^{-10} &= \exp\left(-\frac{K_{\mathrm{bulk}} S^2 V_c}{k_B T V_0}\right) \\
10 \ln 10 &= \frac{K_{\mathrm{bulk}} S^2 V_c}{k_B T V_0} \\
V_c &= \frac{10 \ln 10 k_B T V_0}{K_{\mathrm{bulk}} S^2}. \qquad (2.19)
\end{aligned}$$

Solving for the radius leads to

$$\begin{aligned}
r_c &= \left(\frac{30 \ln 10 k_B T}{4\pi K_{\mathrm{bulk}} S^2}\right)^{1/3} a \\
&= \left(\frac{30 \ln 10\, [86.17\ \mu\mathrm{eV} \cdot \mathrm{K}^{-1}]\, [300\ \mathrm{K}]}{4\pi\, [6.8\ \mu\mathrm{eV}]\, [5/2]^2}\right)^{1/3} (0.396\ \mathrm{nm}) \\
&= 5.9\ \mathrm{nm}. \qquad (2.20)
\end{aligned}$$

In general we have

$$r_c = \left(\frac{3 \ln \left[t_{\mathrm{stable}} \times 10^{10}\ \mathrm{s}^{-1}\right] k_B T}{4\pi K_{\mathrm{bulk}} S^2}\right)^{1/3} a, \qquad (2.21)$$

where t_{stable} is the time interval for stability. For $t_{\mathrm{stable}} = 100$ s, the critical radius is 6.3 nm. For $t_{\mathrm{stable}} = 1\ \mathrm{yr} = 3.1536 \times 10^7$ s, the critical radius is 7.1 nm. As mentioned previously, these estimates disregard all other sources of anisotropy other than the bulk single-ion anisotropy. Accordingly, the actual critical radii should be smaller than the provided estimates.

This discussion illustrates that BFO nanoparticles at 13 nm should still be magnetic and not superparamagnetic, assuming that the characteristic relaxation time for BFO is close to the common value of 10^{-9} s. In fact, using $\nu_0 = 10^9\ \mathrm{s}^{-1}$ and rearranging (2.21) with $r_c = 13$ nm gives $t_{\mathrm{stable}} \approx 10^{96}$ s. The time that a 13 nm BFO nanoparticle should be stable is therefore significantly longer than the age of the universe, estimated to be $13.8 \times 10^9\ \mathrm{yr} = 4.35 \times 10^{17}$ s [104].

Recent work [105] has investigated the magnon spectra of BFO nanoparticles. Magnons are magnetic excitations and Section 2.9 goes into more detail about them. In the work, it is shown that there is a loss of signal for small BFO nanoparticles in

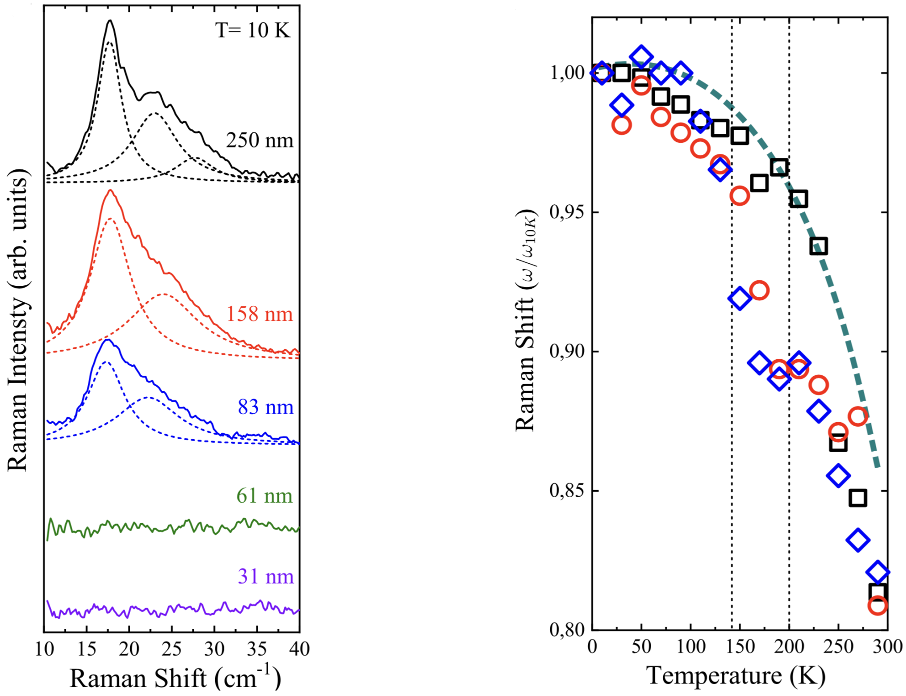

(a) The magnon modes for various sizes listed in the figure. Solid curves are the Raman spectra. Dotted curves are the fitted curves to the measured spectrum.

(b) The magnon frequency from Raman spectroscopy in nanoparticle BFO as a function of temperature. The green trendline is the bulk value for the magnon. The sizes plotted 250 nm (square), 158 nm (circle), and 83 nm (diamond). The vertical lines is the temperature range where surface expansion is expected to play a role.

Figure 2.8: Magnon spectra from Raman spectroscopy in nanoparticle BFO for various nanoparticle sizes. Reprinted from [105], with the permission of AIP Publishing.

Raman spectroscopy – see Figure 2.8a. The low frequency Raman spectrum measures the magnons in BFO. In bulk BFO, a series of peaks can be fit to the Raman spectrum and those peaks indicate that there is cycloidal ordering in BFO. Three peaks were fit for the nanoparticle at 250 nm. Only two could be fit for 83 nm and 158 nm. At 31 nm and 61 nm, there was no discernible signal and no peaks could be fit. A potential explanation for this loss of signal will be explored later in the dissertation.

In Figure 2.8b the magnon frequency for several sizes of nanoparticles is plotted against the temperature. The dashed line in the plot is the magnon frequency in bulk BFO. There is an expected expansion of the surface between 140 K and 200 K where the lattice parameter at the surface undergoes a significant change [106]. The frequency of the magnons fell off dramatically from the bulk line in this temperature range. The fall is particularly large for the 83 nm nanoparticles. These findings suggest that the surface plays a crucial role in the magnetism for nanoparticles close in size to that of the bulk cycloidal wavelength.

2.7 Depolarization

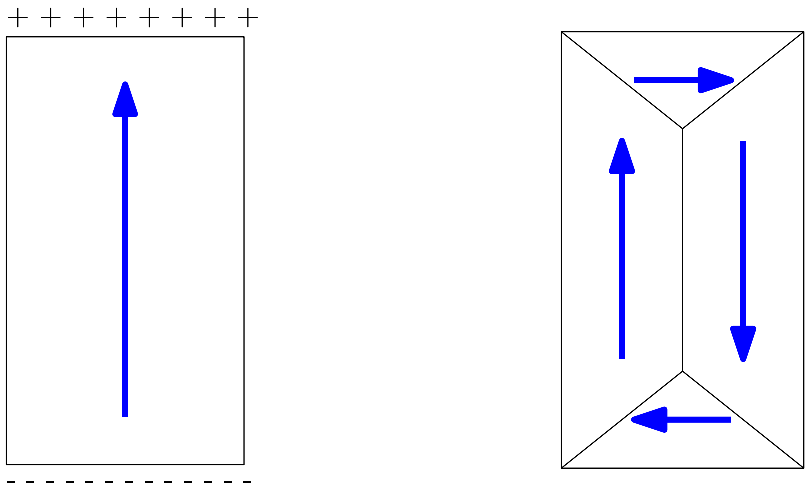

(a) A single-domain ferroelectric with an electric polarization in blue. The positive signs indicate a surface which contains positive charge and the negative signs represent negative charge on the surface.

(b) The same ferroelectric with a domain structure. The depolarizing energy is reduced in this configuration.

Figure 2.9: Electric polarization in a ferroelectric.

There will be charge accumulation at the surfaces of a finite ferroelectric material. See Figure 2.9a for an example of this. The electric polarization in the ferroelectric will cause the surfaces to become polarized. This, in turn, causes the development of a counteracting depolarization field, $\mathbf{E}_d$ [107, 108]. The depolarization field gives rise to a depolarization energy. The energy is proportional to the square of the electric polarization. The ferroelectric may form domains (see Figure 2.9b) to reduce the depolarization energy. The reduction occurs because the changing polarization throughout the material means that there is less charge accumulation on the surfaces, resulting in a weaker depolarization field.

In nanoparticles it may not be favourable to form domains. This means that the depolarization field may be quite large and can significantly reduce the polarization.

There is a size for ferroelectric nanoparticles below which they no longer exhibit ferroelectricity [93, 107]. For well-known ferroelectrics $PbTiO_3$ and $BaTiO_3$, it has been reported that ferroelectricity disappears below 7–15 nm for $PbTiO_3$ and 70–120 nm for $BaTiO_3$ [92]. The effect of reduced nanoparticle size on the polarization has also been studied in BFO. Minimal change has been seen for particles down to 30 nm. At 13 nm, the polarization is roughly 75% of its bulk value. Selbach *et al.* extrapolate these results to claim that the critical size for ferroelectricity in BFO is around 9 nm. Below that size nanoparticles would not be ferroelectric.

In the research conducted for this dissertation, effects due to depolarization were ignored. The justification for this was that the effects for depolarization in BFO were reported to be negligible for nanoparticles of size greater than $\lambda_{\text{bulk}}/2$. From 30 nm down to 13 nm there is, roughly, only a 25% decrease in the polarization. Whilst that reduction in polarization would affect the spin configuration of a BFO nanoparticle, it would still have a great deal of resemblance to the case with the full bulk value. Below 13 nm the polarization rapidly falls off, but this is approximately equal to $0.2\lambda_{\text{bulk}}$. So there is only a small range between 0 and 13 nm $\approx 0.2\,\lambda_{\text{bulk}}$ where the polarization would be substantially reduced. Instead of omitting results from this range, they have been included to help detect patterns in results, even though the theoretical results are unlikely to match the spin configurations in BFO nanoparticles of such size.

2.8 Demagnetization

One can imagine a single-domain ferromagnet with a magnetization pointing along one of its axes (see Figure 2.10a). At the surfaces orthogonal to the magnetization, there will be an accumulation of magnetic polarity. On its opposite surface the magnetic "charge" will be of opposite polarity [73, 75]. This, in turn, induces a magnetic field in a direction opposite to the magnetization. This magnetic field is known as the demagnetizing field, $\mathbf{H}_d$. There is an energy, E_{demag}, associated with the demagnetizing field,

$$E_{\text{demag}} = \frac{\mu_0}{2} \int_V \mathbf{M} \cdot \mathbf{H}_d \, \mathrm{d}\tau. \tag{2.22}$$

μ_0 is the permeability of free space, $\mathbf{M}$ is the magnetization of the material, $\mathrm{d}\tau$ is a volume element of the space in which the material is in, and V indicates that the integral is taken over the volume of the material.

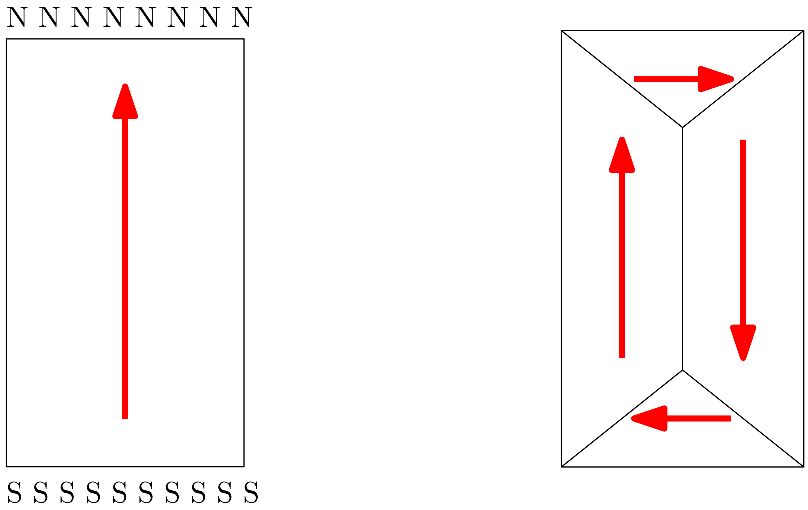

(a) A single-domain ferromagnetic with a magnetization in red. The N's indicate a surface which contains north magnetic poles and the S's represent south poles.

(b) Domain formation in a ferromagnetic with reduced depolarizing energy. The magnetization in red changes orientation throughout the material, forming a vortex-like state.

Figure 2.10: Magnetization in a ferromagnet.

This energy, known as the magnetostatic, dipolar, or demagnetization energy, plays a role in domain creation. The formation of domains lowers E_{demag}, making their presence desirable. The demagnetization energy can also lead to vortex states in ferromagnetic nanoparticles [109].

Because the demagnetizing field opposes the magnetization, it reduces the effective magnetization of the material. However, in antiferromagnets there is no demagnetization because there is no net magnetization to terminate at the surface and induce an opposing field. Even for the case of weak ferromagnetism, the demagnetizing energy is so weak as to be readily neglected.

2.9 Magnons

In a simple, one-dimensional ferromagnet the ground state spin configuration is with all spins parallel (see Figure 2.11). The first excited state would have a total of one spin reversed. One way to implement the reversal would be to flip a single spin. That turns out to be of higher energy than allowing all spins to share the spin reversal. All spins form a spin wave where the spins vary position in time with the frequency related to the lattice parameter and the wavenumber. When quantized, the spin wave is referred to as a magnon [73, 108].

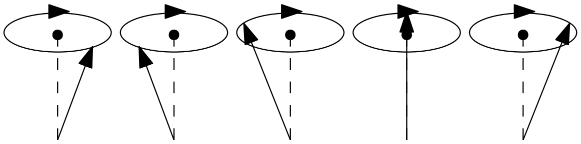

Figure 2.11: Ferromagnetic magnon.

We can represent the simple ferromagnet with merely a nearest-neighbour exchange interaction:

$$H = -J \sum_i \mathbf{S}_i \cdot \mathbf{S}_{i+1}, \tag{2.23}$$

where $J > 0$ is the nearest-neighbour exchange integral. Looking at the r^{th} spin in the chain, the terms in the Hamiltonian including it are

$$-J\mathbf{S}_r \cdot \left(\mathbf{S}_{r-1} + \mathbf{S}_{r+1}\right). \tag{2.24}$$

To analyze the spin dynamics we look at how the operator changes in time. It has no explicit time dependence, so it varies in time as

$$\begin{aligned}
\frac{d\left\langle \mathbf{S}_r \right\rangle}{dt} =& \frac{1}{i\hbar}\left\langle \left[\mathbf{S}_r, H\right]\right\rangle \\
=& -\frac{J}{i\hbar}\left\langle \left[\mathbf{S}_r, \ldots + \mathbf{S}_{r-1}\cdot\mathbf{S}_r + \mathbf{S}_r\cdot\mathbf{S}_{r+1} + \ldots\right]\right\rangle \\
=& -\frac{J}{i\hbar}\left\langle \left[\mathbf{S}_r, \mathbf{S}_{r-1}\cdot\mathbf{S}_r\right] + \left[\mathbf{S}_r, \mathbf{S}_r\cdot\mathbf{S}_{r+1}\right]\right\rangle \\
=& -\frac{J}{i\hbar}\Big\langle \left[S_r^x\hat{\mathbf{x}} + S_r^y\hat{\mathbf{y}} + S_r^z\hat{\mathbf{z}}, S_{r-1}^x S_r^x + S_{r-1}^y S_r^y + S_{r-1}^z S_r^z\right] \\
&+ \left[S_r^x\hat{\mathbf{x}} + S_r^y\hat{\mathbf{y}} + S_r^z\hat{\mathbf{z}}, S_r^x S_{r+1}^x + S_r^y S_{r+1}^y + S_r^z S_{r+1}^z\right]\Big\rangle \\
=& -\frac{J}{i\hbar}\Big\langle \left(\left[S_r^x, S_{r-1}^x S_r^x\right] + \left[S_r^x, S_{r-1}^y S_r^y\right] + \left[S_r^x, S_{r-1}^z S_r^z\right]\right)\hat{\mathbf{x}} \\
&+ \left(\left[S_r^y, S_{r-1}^x S_r^x\right] + \left[S_r^y, S_{r-1}^y S_r^y\right] + \left[S_r^y, S_{r-1}^z S_r^z\right]\right)\hat{\mathbf{y}} \\
&+ \left(\left[S_r^z, S_{r-1}^x S_r^x\right] + \left[S_r^z, S_{r-1}^y S_r^y\right] + \left[S_r^z, S_{r-1}^z S_r^z\right]\right)\hat{\mathbf{z}} \\
&+ \left(\left[S_r^x, S_r^x S_{r+1}^x\right] + \left[S_r^x, S_r^y S_{r+1}^y\right] + \left[S_r^x, S_r^z S_{r+1}^z\right]\right)\hat{\mathbf{x}} \\
&+ \left(\left[S_r^y, S_r^x S_{r+1}^x\right] + \left[S_r^y, S_r^y S_{r+1}^y\right] + \left[S_r^y, S_r^z S_{r+1}^z\right]\right)\hat{\mathbf{y}} \\
&+ \left(\left[S_r^z, S_r^x S_{r+1}^x\right] + \left[S_r^z, S_r^y S_{r+1}^y\right] + \left[S_r^z, S_r^z S_{r+1}^z\right]\right)\hat{\mathbf{z}}\Big] \\
=& -\frac{J}{\hbar}\Big\langle \left(S_r^z\left[S_{r-1}^y + S_{r+1}^y\right] - S_r^y\left[S_{r-1}^z + S_{r+1}^z\right]\right)\hat{\mathbf{x}}
\end{aligned}$$

$$
\begin{aligned}
&+\left(S_r^x\left[S_{r-1}^z+S_{r+1}^z\right]-S_r^z\left[S_{r-1}^x+S_{r+1}^x\right]\right)\hat{\mathbf{y}}\\
&+\left(S_r^y\left[S_{r-1}^x+S_{r+1}^x\right]-S_r^x\left[S_{r-1}^y+S_{r+1}^y\right]\right)\hat{\mathbf{z}}\rangle\\
=&\frac{J}{\hbar}\left\langle\mathbf{S}_r\times\left(\mathbf{S}_{r-1}+\mathbf{S}_{r+1}\right)\right\rangle. \qquad (2.25)
\end{aligned}
$$

Above we have used the relations $\left[S_r^a, S_p^b\right]=i\delta_{rp}\epsilon_{abc}S_r^c$ where δ_{rp} is the Kronecker delta and ϵ_{abc} is the Levi-Civita tensor. There is no $\hbar$ in the equations as the spins are treated as being unitless.

We then treat the spins as classical vectors and look at their components. Without loss of generality, we take the ground state system as $S_r^z=S$ and $S_r^x=S_r^y=0$. For the excited states we consider small deviations from the ground state with $S_r^z\approx S$ and $S_r^x, S_r^y\ll S$. This leads to

$$
\begin{aligned}
\frac{dS_r^x}{dt}=&\frac{J}{\hbar}\left(S_r^y\left[S_{r-1}^z+S_{r+1}^z\right]-S_r^z\left[S_{r-1}^y+S_{r+1}^y\right]\right)\\
\approx&\frac{JS}{\hbar}\left(2S_r^y-S_{r-1}^y-S_{r+1}^y\right), \qquad (2.26)
\end{aligned}
$$

$$
\begin{aligned}
\frac{dS_r^y}{dt}=&\frac{J}{\hbar}\left(S_r^z\left[S_{r-1}^x+S_{r+1}^x\right]-S_r^x\left[S_{r-1}^z+S_{r+1}^z\right]\right)\\
\approx&\frac{JS}{\hbar}\left(S_{r-1}^x+S_{r+1}^x-2S_r^x\right), \qquad (2.27)
\end{aligned}
$$

and

$$
\begin{aligned}
\frac{dS_r^z}{dt}=&\frac{J}{\hbar}\left(S_r^x\left[S_{r-1}^y+S_{r+1}^y\right]-S_r^y\left[S_{r-1}^x+S_{r+1}^x\right]\right)\\
\approx&0. \qquad (2.28)
\end{aligned}
$$

From here we can look for solutions for S_r^x and S_r^y in the form of

$$S_r^x=A\exp\left(i\left[rka-\omega t\right]\right), \qquad (2.29)$$

$$S_r^x=B\exp\left(i\left[rka-\omega t\right]\right). \qquad (2.30)$$

k is the wavenumber, a is the lattice parameter for the ferromagnet and ω is the angular frequency. Inserting these into (2.26) and (2.27) leads to

$$-i\omega A=\frac{2JSB}{\hbar}\left(1-\cos\left[ka\right]\right) \qquad (2.31)$$

and

$$-i\omega B = -\frac{2JSA}{\hbar}\left(1 - \cos\left[ka\right]\right). \tag{2.32}$$

The below determinant must be zero if the system of equations is to have a solution:

$$\begin{vmatrix} i\omega & \frac{2JS}{\hbar}\left(1 - \cos\left[ka\right]\right) \\ -\frac{2JS}{\hbar}\left(1 - \cos\left[ka\right]\right) & i\omega \end{vmatrix} = 0. \tag{2.33}$$

From that one finds

$$\hbar\omega = 2JS\left(1 - \cos\left[ka\right]\right). \tag{2.34}$$

This is the dispersion relation for a magnon in a one-dimensional ferromagnet. Figure 2.12 illustrates the dispersion relation. For $ka \ll 1$ the relationship is approximately quadratic. Inserting (2.34) into (2.31) allows for a relationship between the coefficients A and B to be determined:

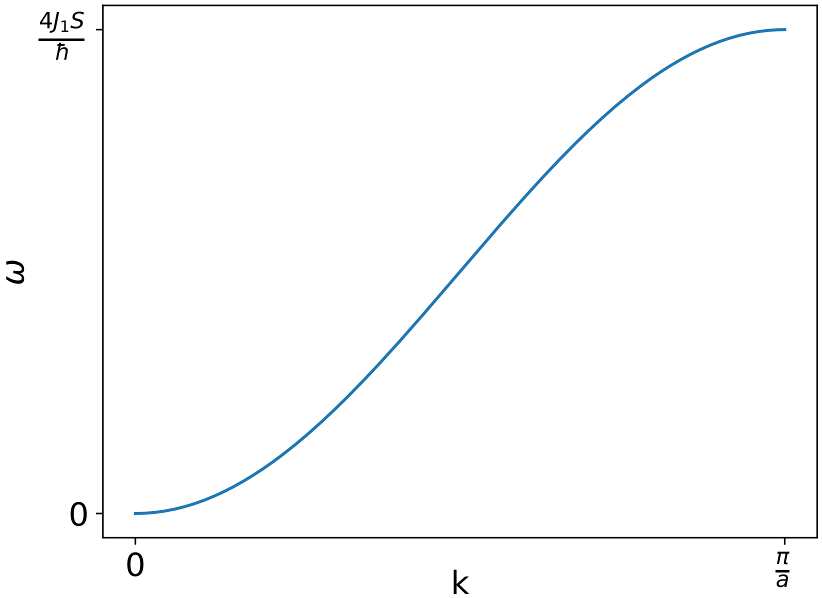

Figure 2.12: Magnon dispersion for a simple, one-dimensional ferromagnet.

$$-i\omega A = -\frac{2iJSA}{\hbar}\left(1 - \cos\left[ka\right]\right) = \frac{2JSB}{\hbar}\left(1 - \cos\left[ka\right]\right) \implies B = -iA. \tag{2.35}$$

It turns out the x and y components of the spin deviations are of equal magnitude

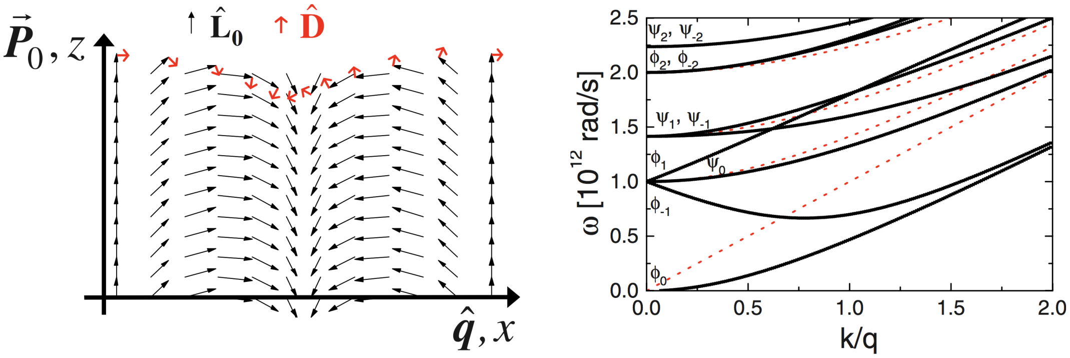

(a) Antiferromagnetic lattice with cycloidal order. The black arrows represent local Néel moments and the red arrows represent displacement of the moments from their ground state configurations. This is a cyclon mode.

(b) Magnon spectra for BFO in the cycloidal state. ϕ_n are cyclon modes and ψ_n are extra-cyclon modes. The red dashed lines represent modes along the polarization direction.

Figure 2.13: AFM magnons in cycloidal BFO. Reprinted figure with permission from [110]. Copyright 2008 by the American Physical Society.

but 90° out of phase. Using this information and taking the real parts of the spin components S_r^x and S_r^y can be rewritten as

$$S_r^x = A\cos\left(rka - \omega t\right) \tag{2.36}$$

and

$$S_r^y = A\sin\left(rka - \omega t\right). \tag{2.37}$$

What can be seen here is that the x and y components of the spin process in time in a circle about the z axis.

There can be magnons in an antiferromagnet as well. Treating it like the ferromagnet, but with odd spins antiparallel to even ones and with $J < 0$, one can derive dispersion relations for magnons in a simple, one-dimensional antiferromagnet in the same manner as was done for the ferromagnetic case.

In BFO there are magnons which appear both in the cycloidal and homogeneous states. In the cycloidal case there is an infinite set of magnon modes which arise [110, 111]. The excitations along the direction of the cycloid (see Figure 2.13a), known as the cyclon modes, represented by ϕ_n, are soft (as $k \to 0$, $\omega \to 0$). The excitations perpendicular to the cycloid direction are known as extra-cyclon modes and they are gapped (as $k \to 0$, $\omega \to \omega_0 > 0$) (see Figure 2.13b).

For the homogeneous case, BFO has two magnons. One a low frequency, soft mode where the angle between spins remains constant as the spins rotate and the other a high frequency, gapped mode where the angle between spins changes as the spins revolve (see Figure 2.14).

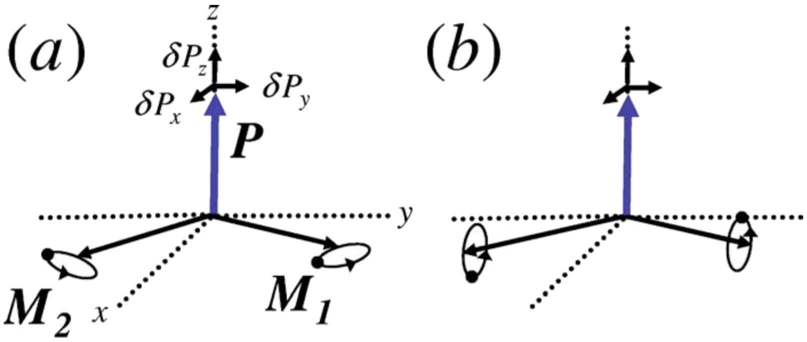

Figure 2.14: $\mathbf{M_1}$ and $\mathbf{M_2}$ are spins in BFO in the homogeneous state. The two different homogeneous magnons are depicted in (a) and (b). In (a) the low frequency magnon mode is shown with the spins processing and maintaining a constant angle between themselves. In (b) the high frequency, gapped mode is shown with the spins processing and the canting angle between the spins varying. The blue arrow represents the polarization. Reprinted from [112], with the permission of AIP Publishing.

2.10 Temperature effects

BFO is ferroelectric up to approximately 1100 K and antiferromagnetic up to approximately 650 K. For those reasons we expect experimental and theoretical results at 0 K to be similar to those found at room temperature, near 300 K. Room temperature is far below the temperature at which BFO ceases to be antiferromagnetic or ferroelectric. As such, calculations performed on 0 K systems, like the ones in this dissertation, have significance in comparison to room temperature experimental results.

Some BFO experiments have been conducted over a broad range of temperatures. They show how properties of the material change with temperature. For the transition from cycloidal to homogeneous order under a magnetic field, Tokunaga *et al.* [113] took measurements at temperatures between 4.2 K and 300 K. The kink in the magnetization versus magnetic field curves indicates a transition from cycloidal order to homogeneous. While the kink becomes broader with increasing temperature, its location is barely changed between 4.2 K and 300 K (see Figure 2.15).

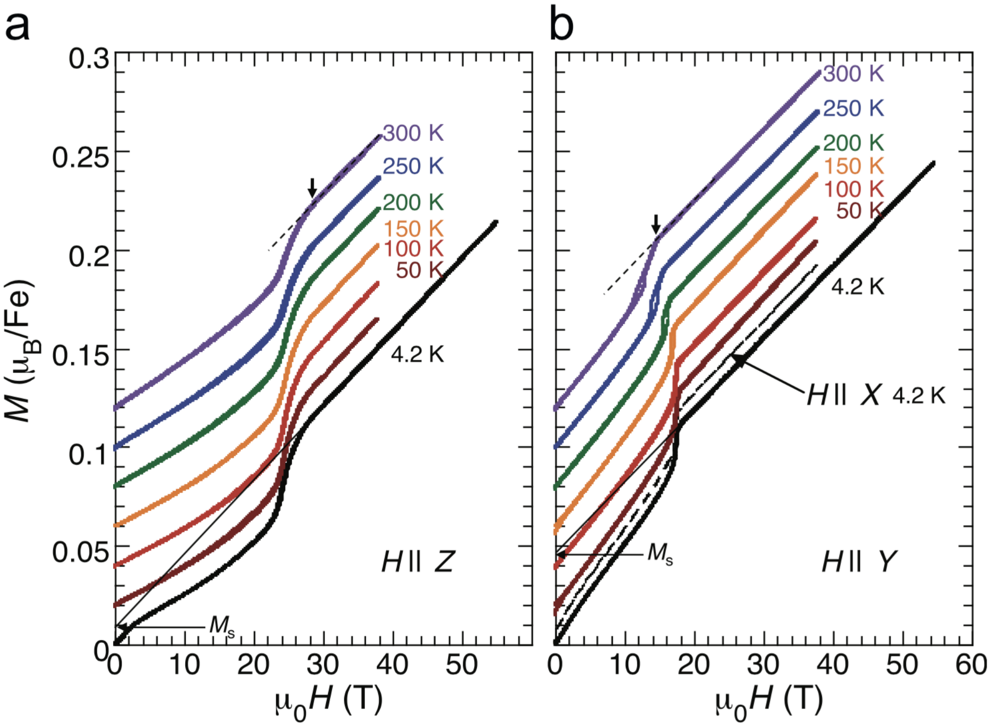

Figure 2.15: Mangetization versus magnetic field at various temperatures. In a) the field is along the polarization direction and in b) the field is perpendicular to it. Reprinted from [113], with permission from Elsevier. Copyright 2015.

Ramazanoglu *et al.* looked at the temperature evolution of several properties of BFO [114]. They found that the period of the cycloid expanded from (629 ± 5) Å at 5 K to (780 ± 30) Å at 615 K. From the data, the cycloid length would be near 660 Å at room temperature. This is in disagreement with Sosnowska *et al.* who took measurements of the cycloid length between 78 K and 463 K and saw little deviation from the value of 620 Å [115]. If it is true that the cycloid length varies with temperature, the increasing cycloid length would suggest that the value of D, the Dzyaloshinskii-Moriya spin-current energy term, decreases with temperature. Ramazanoglu *et al.* also reported that a minuscule amount of anharmonicity was found at 5 K, while at room temperature none was discernible.

These changes in properties as the temperature increases will affect the location of critical points for transition from cycloidal to homogeneous order. However, as we see with the critical point for when a magnetic field is applied, the difference between 0 K and 300 K should not be large. The data from Ramazanoglu *et al.* suggest that there is a 5% difference in the cycloid length at 5 K and 300 K. The anharmonicity is a function of the single-ion anisotropy, so with increasing temperature that energy will decrease as well. The findings of Ramazanoglu *et al.* suggests that the single-ion anisotropy in all cases is small, so its temperature dependence should not greatly affect the location of critical points. While there are differences in BFO structure between 5 K and 300 K, those differences are small enough that results at 0 K will be similar to those found at room temperature.

Another argument for why results at room temperature are similar to those at 0 K is the thermal energy. At room temperature the thermal energy is $k_B T_{RT} = \left(8.617 \times 10^{-2}\ \mathrm{meV} \cdot \mathrm{K}^{-1}\right)(300\ \mathrm{K}) = 25.85\ \mathrm{meV}$. To evaluate the energies, a spin Hamiltonian is introduced:

$$\begin{aligned}\mathcal{H} = &\sum_i \sum_{\boldsymbol{\delta}} \Bigg(J\mathbf{S}_{1,i} \cdot \mathbf{S}_{2,i+\boldsymbol{\delta}} \\ &+ D\left[\hat{\mathbf{Z}} \times \frac{\boldsymbol{\tau}+\boldsymbol{\delta}}{a}\right] \cdot \left[\mathbf{S}_{1,i} \times \mathbf{S}_{2,i+\boldsymbol{\delta}}\right]\Bigg) \\ &- \frac{K}{2} \sum_i \sum_{\alpha=1,2} \left(\mathbf{S}_{\alpha,i} \cdot \hat{\mathbf{Z}}\right)^2 .\end{aligned} \tag{2.38}$$

i represents a specific sublattice position. Each spin belongs to a sublattice α, which is equal to either one or two. The spin $\mathbf{S}_{\alpha,i}$ is located at $\mathbf{R}_{\alpha,i}$ with $\mathbf{R}_{2,i} = \mathbf{R}_{1,i} + \boldsymbol{\tau}$. $\boldsymbol{\tau} = a\left(\hat{\mathbf{x}} + \hat{\mathbf{y}} + \hat{\mathbf{z}}\right)$. a is the rhombohedral lattice parameter of BFO. The vector $\boldsymbol{\tau} + \boldsymbol{\delta}$ connects spins to nearest neighbours:

$$\boldsymbol{\delta} = a \times \left\{-\hat{\mathbf{y}} - \hat{\mathbf{z}}, -2\hat{\mathbf{x}} - \hat{\mathbf{y}} - \hat{\mathbf{z}}, -\hat{\mathbf{x}} - \hat{\mathbf{z}}, \hat{\mathbf{x}} - 2\hat{\mathbf{y}} - \hat{\mathbf{z}}, -\hat{\mathbf{x}} - \hat{\mathbf{y}}, -\hat{\mathbf{x}} - \hat{\mathbf{y}} - 2\hat{\mathbf{z}}\right\}. \tag{2.39}$$

$\boldsymbol{\tau} + \boldsymbol{\delta} = \pm a\left(1, 0, 0\right)$ and cyclic permutations. J is the nearest-neighbour exchange energy, D is the Dzyaloshinskii-Moriya interaction energy, and K is the bulk single-ion anisotropy. Chapter 3 will go into more detail about these interactions.

From References [5] and [116] the energy for the homogeneous state $\mathbf{S}_{1,i} = -\mathbf{S}_{2,i} = S\,\hat{\mathbf{Z}}$ is

$$E_{\text{homogeneous}} = -NS^2\left(3J + K\right), \tag{2.40}$$

and energy for the cyloid state

$$\mathbf{S}_{1,i} = S\left(\sin\left[\mathbf{Q} \cdot \mathbf{R}_{1,i}\right]\hat{\mathbf{Y}} + \cos\left[\mathbf{Q} \cdot \mathbf{R}_{1,i}\right]\hat{\mathbf{Z}}\right), \tag{2.41}$$

$$\mathbf{S}_{2,i} = -S\left(\sin\left[\mathbf{Q} \cdot \mathbf{R}_{2,i}\right]\hat{\mathbf{Y}} + \cos\left[\mathbf{Q} \cdot \mathbf{R}_{2,i}\right]\hat{\mathbf{Z}}\right) \tag{2.42}$$

is

$$E_{\text{cycloid}}\left(Q\right) \approx -NS^2\left(3J - \frac{J\left[Qa\right]^2}{2} + D\left[Qa\right] + \frac{K}{2}\right). \tag{2.43}$$

This comes from minimizing the state with respect to Q. Taking $J = 4.88$ meV, $D = 0.20$ meV, $K = 0.054$ meV and $Qa = 2\pi/111$, as in bulk BFO, leads to both $E_{\text{homogeneous}}/N$ and E_{cycloid}/N being approximately equal to -92 meV. The thermal energy at room temperature is approximately a quarter of this in magnitude, making it not large enough to expect thermal fluctuations to influence results.

What thermal fluctuations will do is vary the number of magnons in BFO. The average number of magnons for a mode k as a function of temperature [108] is

$$\langle n_k \rangle = \frac{1}{\exp\left(\hbar\omega_k/k_B T\right) - 1}. \tag{2.44}$$

ω_k is the frequency of the mode k. The total number of magnon modes excited at a certain temperature [108] is

$$N = \sum_{\mathbf{k}} n_{\mathbf{k}} = \int \mathrm{d}\omega\ D(\omega)\left\langle n(\omega)\right\rangle = 0.0587\left(\frac{k_B T}{2JSa^2}\right)^{3/2}. \tag{2.45}$$

$D(\omega)$ is the number of states per unit frequency range, J is the exchange integral, S is the spin of the particles of the system with the magnons in it, and a is the lattice constant. The generation of magnons leads to the loss of magnetization. As such, temperature fluctuations will cause fluctuations in the magnetization. The change in the magnetization [73, 108] for a simple cubic lattice is

$$\frac{M(0) - M(T)}{M(0)} = \frac{0.0587}{S}\left(\frac{k_B T}{2JS}\right)^{3/2}. \tag{2.46}$$

This is known as the Bloch $T^{3/2}$ law. By the law, the magnetization drops off as temperature increases. For an antiferromagnet the analogous result is

$$\frac{L(0) - L(T)}{L(0)} = \frac{0.0587\left(S+1\right)^{3/2}}{S}\left(\frac{T}{T_N}\right)^{3/2}, \tag{2.47}$$

where we used the mean-field critical Néel temperature $k_B T_N = \frac{S\left(S+1\right)}{3}\gamma J$, with $\gamma = 6$ the number of nearest neighbours for each spin in the cubic lattice. It should be noted that (2.47) only holds for $T \ll T_N$ [73]. We estimate (2.47) for BFO using

$T_N = 640$ K and $S = 5/2$ leading to

$$\frac{L(0) - L(300\text{ K})}{L(0)} = \frac{0.0587\,(5/2+1)^{3/2}}{5/2}\left(\frac{300\text{ K}}{640\text{ K}}\right)^{3/2} = 0.0493, \tag{2.48}$$

so that at room temperature there is only a 5% deviation from the saturated sublattice magnetization.

Chapter 3

Microscopic Model

There are two principal spin-spin interactions in BFO and BFO-like materials: the Heisenberg exchange interaction, which causes neighbouring spins to be antiparallel (G-type antiferromagnetism – see Figure 3.2), and the Dzyaloshinskii-Moriya interaction, which is due to spin-orbit coupling and responsible for the cycloid in BFO [29, 83, 117–119]. The proceeding equation describes both of these interactions in a cubic lattice:

$$\mathcal{H}_0 = \frac{1}{2}\sum_{i,\hat{\mathbf{v}}}\left(J\mathbf{S}_i\cdot\mathbf{S}_{i+\hat{\mathbf{v}}} + D\hat{\mathbf{P}}\cdot\hat{\mathbf{v}}\times\left[\mathbf{S}_i\times\mathbf{S}_{i+\hat{\mathbf{v}}}\right]\right). \tag{3.1}$$

i represents each spin site, while $\hat{\mathbf{v}}$ is the nearest-neighbour vector taking possible values of $\pm\hat{\mathbf{x}}, \pm\hat{\mathbf{y}}, \pm\hat{\mathbf{z}}$.

3.1 Heisenberg exchange interaction

The Heisenberg exchange interaction, the first interaction in (3.1), is primarily responsible for the magnetic nature of the material. If the nearest-neighbour exchange integral, J, is positive then the material will be antiferromagnetic. If it is negative then the ordering will be ferromagnetic.

The exchange interaction is due to the Coulomb interaction of neighbouring electrons and the requirements of exchange symmetry for the wavefunction of the system [73]. In BFO the exchange interaction is O^{2-}-mediated in what is known as superexchange. Superexchange favours antiferromagnetic bonding and that is what we find in BFO [5].

Neighbouring Fe^{3+} spins are not directly linked as their orbitals do not overlap

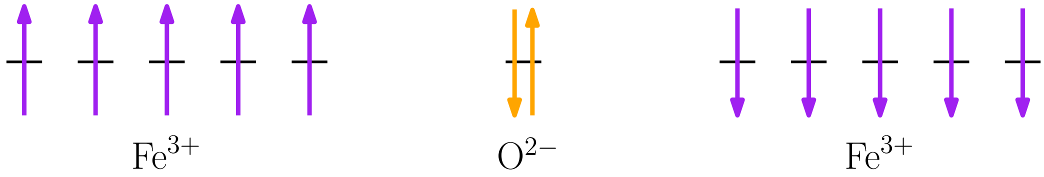

(a) Ground state with filled $2p$ orbital for O^{2-} and five electrons in each set of $3d$ orbitals of Fe^{3+}.

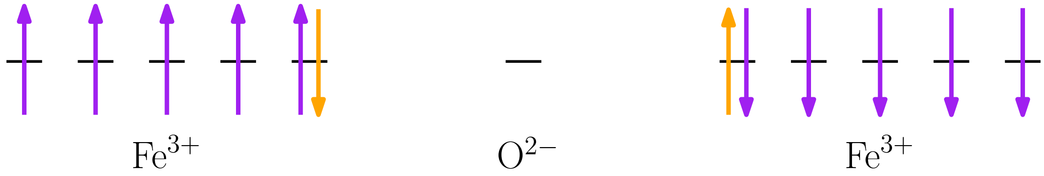

(b) An excited state with electrons hopping to $3d$ orbitals of Fe^{3+}.

Figure 3.1: Superexchange model for a Fe-O-Fe bond. The Fe^{3+} cations are too far apart to have any overlap of their wavefunctions. The O^{2-} anion acts as an intermediary. Its $2p$ orbitals overlap with the $3d$ orbitals of the Fe^{3+} cations.

– they are too far apart. It thus requires an intermediary to couple the spins. O^{2-} assumes that role in BFO. See Figure 3.1 for an illustration of this. The Fe^{3+} cations have a d^5 configuration. There is a single electron each of their five $3d$ orbitals. A $2p$ orbital of O^{2-} is filled with two electrons of opposite spin by the Pauli exclusion principle. Those electrons can then be shared with the neighbouring Fe^{3+} ions and their $3d$ orbitals via covalent bonding. The O^{2-} anion is amenable to sharing its $2p$ electrons because it allows the electrons to become delocalized. Excited states with the oxygen ion donating its electrons to the iron ions mixing with the ground state allows for a reduction in kinetic energy. As all of the Fe^{3+} $3d$ orbitals have an electron in them, the spins in the orbitals of one Fe^{3+} ion will all be the same, either spin up or spin down. The electron from the oxygen that goes into one of the $3d$ orbitals then must have the opposite spin. On the other side of the oxygen, the same argument holds for the other Fe^{3+}, but as the second O^{2-} electron must have opposite spin to the first, the spins of the second Fe^{3+} must be opposite to those of the first Fe^{3+}. In this way, there is an effective antiferromagnetic coupling between adjacent Fe^{3+} ions [73–75].

Whilst O^{2-} is a common ligand in superexchange, other ions are capable of serving in its role. For instance, in MnF$_2$, F$^-$ is the linking ion [73] and in MnS, S^{2-} is the ligand [120]. The electronegativity of oxygen (it is the second most electronegative atom after fluorine with a Pauling scale value of 3.44 [121]) means that it has a strong desire to have electron density near it. That desire means that oxygen will have more of the electron density in the bond than iron (Pauling scale value of 1.83 [121]).

Sulphur (Pauling scale value of 2.58 [121]) is below oxygen in the periodic table of the elements. With its lower electronegativity, it is more willing to share electron density in covalent bonding than oxygen. It has an electron configuration of $[\mathrm{Ne}]\,3s^2 3p^4$, so it has an empty p orbital just as oxygen does (the electron configuration of oxygen is $[\mathrm{He}]\,2s^2 2p^4$) that can be used in bonding. There are reports [122–125] of sulphur-containing materials that have magnetic properties due in part to superexchange. Some of these materials are also thought to be multiferroic. There is no literature citing the material $\mathrm{BiFeS_3}$, but were it to be synthesized, superexchange would no doubt play a significant role in its magnetism. Sulphur is a larger atom than oxygen ($Z = 16$ versus $Z = 8$) and this would affect the exchange coupling. Firstly, the Fe^{3+} would be farther apart from each other which would weaken the interaction. Also, the Fe-S-Fe bond angle might be different than that of the Fe-O-Fe bond angle. It is known that the bond angle affects the nature of the exchange interaction – whether it is ferromagnetic or antiferromagnetic [73, 74, 124].

The strength of the exchange interaction is dependent on the Coulomb energy, U, and the transition matrix element or hopping integral, t, which determines the likelihood of an electron hopping between the oxygen and iron ions. The exchange integral J is related to these entities by $J \sim -t^2/U$ [73]. Some models include a next-nearest-neighbour exchange interaction [5, 119]. It is an order of magnitude less than the nearest-neighbour interaction. Because of this and the desire to establish the overarching behaviour of spin structures in nanoparticles with surface anisotropy before exploring finer details, the next-nearest-neighbour interaction was not included in the model used in this study.

There are various types of spin ordering in antiferromagnetic materials. Figure 3.2 displays some of the more common ones. Planes all have spins pointing in the same direction in A-type antiferromagnetism, as seen in Figure 3.2a. The neighbouring planes are then of opposite spin. For C-type, chains of spins in a certain direction are all pointing in the same direction. Neighbouring chains are of opposite spin. This can be seen in Figure 3.2b. Figure 3.2c illustrates G-type antiferromagnetism. In this type, all nearest neighbours of all spins point in the opposite direction [126]. The exchange interaction in (3.1) depicts this type of ordering as it is the ordering in BFO.

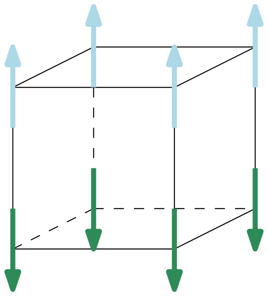

(a) A-type.

(b) C-type.

(c) G-type.

Figure 3.2: Examples of different antiferromagnetic spin configurations.

3.2 Dzyaloshinskii-Moriya interaction

There are two Dzyaloshinskii-Moriya interactions. The first is the second term in (3.1). The interaction is a type of anisotropic exchange interaction that arises due to spin-orbit coupling [127–129]. The cycloid in BFO is thought to be mainly due to this interaction and its competition with the exchange interaction [5]. Dzyaloshinskii [127] noted in the late 1950's that some antiferromagnets, such as α-Fe_2O_3, $MnCO_3$, and $CoCO_3$, had small magnetizations and that these could be explained by an exchange interaction for materials lacking inversion symmetry. Moriya [128, 129] used the superexchange formalism to describe this phenomenon by including spin-orbit coupling to linear order in perturbation theory. He showed that the energy for the interaction could be written as $\mathbf{D} \cdot (\mathbf{S}_i \times \mathbf{S}_j)$, where $\mathbf{D}$ is the interaction strength and $\mathbf{S}_i$ and $\mathbf{S}_j$ are neighbouring spins.

This interaction is broken into two parts here, with the first in (3.1) representing a Dzyaloshinskii-Moriya interaction with $\mathbf{D} = \hat{\mathbf{P}} \times \hat{\mathbf{v}}$ and the second with $\mathbf{D} = D'\,\hat{\mathbf{z}}$,

$$H_{\mathrm{wFM}} = D'\,\hat{\mathbf{z}} \cdot \sum_{i,\hat{\mathbf{v}}} (\mathbf{S}_i \times \mathbf{S}_{i+\hat{\mathbf{v}}})\,. \tag{3.2}$$

This interaction is for the component of $\mathbf{S}_i \times \mathbf{S}_{i+\hat{\mathbf{v}}}$ orthogonal to that in (3.1). While the Dzyaloshinskii-Moriya interaction in (3.1) induces a spiral spin state, (3.2) causes a quite different effect: D' favours a canting between spins and leads to weak ferromagnetism. The larger this is, the greater the canting and weak ferromagnetism. The weak ferromagnetism also acts to raise the cycloid out of the PQ plane. The weak ferromagnetism in BFO averages to zero over a full revolution of the cycloid.

Because $D' \ll D$ [119], (3.2) is not included in the modelling of nanoparticle spin texture below. However, we do incorporate D' when calculating the spin-canting magnetization generated by the nanoparticle. This is equivalent to treating D' as a small perturbation to the state obtained with $D' = 0$.

3.3 Anisotropy

Single-ion anisotropy, anisotropy due to a single magnetic ion and not to exchange between two spins [74], dominates the magnetic anisotropy in antiferromagnets. Many of the mechanisms available for anisotropy in ferromagnets are weaker in antiferromagnets. For instance, because of the weakness of dipolar or demagnetizing energy in an antiferromagnet, shape anisotropy, anisotropy where, due to the demagnetizing energy, the shape of particle determines the preferred spin direction, is not a significant contributor to the total anisotropy. The spin has a preferred (or disfavoured) direction to orient itself due to its interaction with the crystal lattice through spin-orbit coupling. The spin couples to the atomic orbit through spin-orbit coupling and the orbit couples to the lattice through the crystal field, the local electric environment provided by the location of atoms throughout the crystal [74, 130]. As seen in (2.11), the angular momentum must be non-zero for the spin-orbit energy to be non-zero. Additionally, the lattice, and consequently the crystal field needs to have low symmetry for there to be a preferred, energetically-favourable direction for the spins to point. The orbitals must have some non-symmetric relationship with the lattice for there to be anisotropy. The orbitals cannot be spherically symmetric and the lattice needs to be of low symmetry.

In BFO, the $3d$ electrons of the Fe^{3+} atoms are responsible for the magnetic properties of the material. They admix with the $6s$ electrons of the Bi^{3+} atoms via spin-orbit coupling to bring about the single-ion anisotropy in the system. The low symmetry of the crystal is provided by the elongated axis along the polarization direction. Without this, there would be no single-ion anisotropy [9].

Anisotropy is quadratic in spin-orbit coupling [9]. The anisotropy causes the cycloid to be anharmonic. Also, the single-ion anisotropy strength controls the amount of anharmonicity [131]. The spin-orbit coupling in BFO is predominantly in the Bi^{3+} ion. The coupling causes the ion's $6p$ energy level to split, and since the Bi^{3+} orbitals are admixed with the Fe^{3+} orbitals, this results in magnetic anisotropy at the Fe site [9, 17].

The model to isolate the anisotropy energy is a Hamilton containing three parts:

$$\mathcal{H} = \mathcal{H}_{\text{latt}} + \mathcal{H}_{\text{elec}} + \mathcal{H}_{\text{SO}}, \tag{3.3}$$

with

$$\mathcal{H}_{\text{latt}} = -\frac{\hbar^2\nabla^2}{2m_e} + V_{\text{crystal}}(\mathbf{r}), \tag{3.4}$$

$$\mathcal{H}_{\text{elec}} = -e\,\mathbf{r}\cdot\mathbf{E}, \tag{3.5}$$

$$\mathcal{H}_{\text{SO}} = \zeta\boldsymbol{\ell}\cdot\boldsymbol{\sigma}. \tag{3.6}$$

$\mathcal{H}_{\text{latt}}$ is the energy due to the lattice, $\mathcal{H}_{\text{elec}}$ is the electronic energy, and $\mathcal{H}_{\text{SO}}$ is the spin-orbit energy. $V_{\text{crystal}}(\mathbf{r})$ the potential energy due to the crystal, m_e is the electron mass, $\mathbf{r}$ is the electron position vector, and $e < 0$ is the electron charge. The electron orbital angular momentum is $\boldsymbol{\ell} = -i\mathbf{r}\times\nabla$ and $\boldsymbol{\sigma}/2$ represents the electron spin operator [9].

The single-ion anisotropy here is a fourth order perturbation, that is second-order in spin-orbit coupling and second-order in either the lattice or the electronic energy. The resulting single-ion anisotropy energy is

$$\mathcal{H}_{\text{SIA}} = -\frac{1}{(2S)^2}\mathbf{S}\cdot\left[\sum_{m,n}\frac{V_{mn}\otimes V_{nm}}{E_{6p}-E_{3d_m}}\right]\cdot\mathbf{S}. \tag{3.7}$$

$\mathbf{S} = \sum_{i=1}^{5}\boldsymbol{\sigma}_i/2$ for the five electrons in the $3d$ orbital of Fe^{3+}. E_{6p} is the energy of an electron in a $6p$ orbital of Bi^{3+} and E_{3d_m} is the energy of an electron in a $3d$ orbital of Fe^{3+}. V_{mn} is the coupling between the spin-orbit coupling and either the lattice or electronic energy:

$$V_{mn} = -\sum_{n',\mathbf{R}_{\text{Bi}}}\frac{\langle 3d_m\left|\mathcal{H}_{\text{latt,elec}}\right|6p_{n'}\rangle\,\langle 6p_{n'}\left|\zeta\boldsymbol{\ell}\right|6p_n\rangle}{E_{6p}-E_{3d_m}}. \tag{3.8}$$

This sums over the $6p$ Bi and $3d$ Fe orbitals. $\mathbf{R}_{\mathrm{Bi}}$ is a vector linking the Fe site being evaluated to its eight neighbour Bi atoms (see Figure 2.1). The $|6p_x\rangle$, $|6p_y\rangle$, and $|6p_z\rangle$ Bi orbitals are used in the calculation for (3.8), as well as the $|3d_{3z^2-r^2}\rangle$ and $|3d_{x^2-y^2}\rangle$ Fe orbitals. The other three $3d$ Fe orbitals are not used in the calculation because they are 2 eV lower in energy than the two listed orbitals, and would have minimal impact on the results.

The $6p$ matrix element equals

$$\langle 6p_{n'} | \zeta \boldsymbol{\ell} | 6p_n \rangle = -i\eta\, \hat{\mathbf{n}}' \times \hat{\mathbf{n}}, \tag{3.9}$$

with $\eta = 0.86$ eV. For the sum of the matrix elements with the $3d$ orbital, a conversion to an angular integral can be made:

$$\sum_{\mathbf{R}_{\mathrm{Bi}}} \langle 3d_m | \mathcal{H}_{\mathrm{latt,elec}} | 6p_{n'} \rangle \approx \frac{8}{4\pi} \int \mathrm{d}\Omega_R \left[1 + \delta\mathbf{R} \cdot \nabla_{\mathbf{R}}\right] \times \langle 3d_m | \mathcal{H}_{\mathrm{latt,elec}} | 6p_{n'} \rangle . \tag{3.10}$$

$\delta\mathbf{R}$ is a term that comes from the deviation of the Bi ions from the centrosymmetric position which is the cause of ferroelectricity in BFO. $\delta\mathbf{R} = R_{\parallel}\hat{\mathbf{P}} + u_{\perp}\mathbf{E}_{\perp}$. $R_{\parallel} = 0.116 R_{\mathrm{Bi}} = 0.57$ Å. $\mathbf{E}_{\perp}$ is an applied electric field in the direction orthogonal to the polarization direction. $u_{\perp}E_{\perp}/R_{\mathrm{Bi}} = 2.4 \times 10^{-4} E_{\perp}/(10^5\ \mathrm{V/cm})$ [9].

Inserting all of these values into (3.7) and doing all of the sums leads to the energies,

$$\mathcal{H}_2 = -K_{\mathrm{Bi}} \left(\mathbf{S} \cdot \hat{\mathbf{P}}\right)^2, \tag{3.11}$$

and

$$\mathcal{H}_E = \frac{\xi E_{\perp}}{2} \left[\cos(\Psi) S_x^2 + \cos\left(\Psi - \frac{2\pi}{3}\right) S_y^2 + \cos\left(\Psi - \frac{4\pi}{3}\right) S_z^2\right]. \tag{3.12}$$

$\mathcal{H}_2$ is an anisotropy interaction dependent on the inherent polarization of BFO. $\mathcal{H}_E$ is another anisotropy interaction, but it only comes about when there is an electric field applied perpendicular to the the polarization, $\mathbf{P}$, of the multiferroic. It has a linear dependence on the electric field, and is thus, a linear magnetoelectric effect in BFO [9]. As for the terms above,

$$K_{\mathrm{Bi}} = \frac{1792\zeta^2}{18(2S)^2} \frac{V_{\parallel}^2}{(E_{6p} - E_{3p})^3}, \tag{3.13}$$

where

$$V_{pd\sigma} = \left\langle 3d_{3z'^2-r^2} \left| \mathcal{H}_{\text{latt}} \right| 6p_{z'} \right\rangle , \tag{3.14}$$

$$V_{pd\pi} = \left\langle 3d_{x'z'} \left| \mathcal{H}_{\text{latt}} \right| 6p_{x'} \right\rangle , \tag{3.15}$$

and

$$V_{\parallel} = \frac{R_{\parallel}}{R_{\text{Bi}}} \left(V_{pd\sigma} + \frac{V_{pd\pi}}{\sqrt{3}} \right) . \tag{3.16}$$

z' points in the same direction as $\mathbf{R}_{\text{Bi}}$. For $\mathcal{H}_E$, the perpendicular electric field can be described as $\mathbf{E}_{\perp} = E_{\perp} \left[\cos\left(\Psi\right) \hat{\mathbf{X}} + \sin\left(\Psi\right) \hat{\mathbf{Y}} \right]$. This is with the polarization along the Z direction.

Using the known values of $V_{pd\sigma}$ and $V_{pd\pi}$, -71 meV and -41 meV respectively [132], $V_{\parallel} = 11$ meV and $K_{\text{Bi}} = 16$ μeV. With no applied field, the anisotropy in bulk comes from K_{Bi} and from the FeO_6 antiferrodistortive rotations which lead to weak ferromagnetism in the Dzyaloshinksii-Moriya interaction. The anisotropy from the weak ferromagnetism has an energy of -5 μeV for a total effective anisotropy of 11 μeV [17]. This is of the same sign and order of the anisotropy found experimentally of 7 μeV [83].

For $\mathcal{H}_E$, the ξ term can be broken up into lattice and electronic components and solved using (3.7). ξ_{latt} turns out to be -5×10^{-2} $\mu\text{eV}/\left(10^5 \text{ V/cm}\right)$ and ξ_{elec} is in the range of 3 to 30 $\mu\text{eV}/\left(10^5 \text{ V/cm}\right)$.

(3.12) can be re-written in the rhombohedral basis to get

$$\begin{aligned} H_E = -\frac{\xi}{4} \sum_i \Big(\mathbf{E}_{\perp} \cdot \Big[\Big\{ \left(S_i^Y\right)^2 - \left(S_i^X\right)^2 \Big\} \hat{\mathbf{X}} + 2 S_i^X S_i^Y \hat{\mathbf{Y}} \Big] \\ + 2\sqrt{2} \mathbf{E}_{\perp} \cdot \Big[S_i^X \hat{\mathbf{X}} + S_i^Y \hat{\mathbf{Y}} \Big] S_i^Z \Big) . \end{aligned} \tag{3.17}$$

The strength of the interaction relies on the fact that bismuth (Z = 83) is a heavy atom [9]. Spin-orbit coupling is proportional to Z^4 [133]. No applied field was used in the modelling for this research, so (3.17) was omitted from the model.

The transition from bulk to nanoscale means that the anisotropy changes as was discussed in Section 2.4. The lower symmetry of the nanoparticle should mean that there is greater anisotropy. As the asymmetry is mostly due to the sudden change at the surface between the lattice and vacuum, that strengthened anisotropy should lie mostly in the atoms at the surface. This anisotropy is referred to as surface anisotropy. It is assumed that the surface anisotropy is of significantly greater magnitude than the bulk anisotropy and, for that reason, the bulk single-ion anisotropy was left out of the model explored.

The surface anisotropy interaction is then only applied to spins at the surface. It is assumed that the surface that causes the anisotropy will then drive spins to either want to lie normal to the surface or in-plane. That is, the easy axis or easy plane is due to the surface, so a spin $\mathbf{S}_i$ will couple to the normal of the surface, $\hat{\mathbf{n}}$, in the anisotropy energy:

$$\mathcal{H}_{\mathrm{SA}} = -K_S \sum_{i \in \mathrm{surfaces}} \left(\mathbf{S}_i \cdot \hat{\mathbf{n}}\right)^2 .$$

If the anisotropy is easy-axis, then K_S, the surface anisotropy energy, is greater than zero; if it is easy-plane, then $K_S < 0$. Spins at the intersection of multiple surfaces will appear multiple times in the sum. For surfaces with $\hat{\mathbf{n}} \perp \mathbf{P}$, only spins at the edges of spin chains will experience surface anisotropy. The subsequent modification of Q to accommodate the anisotropy will be referred to as the edge effect. For surfaces with $\hat{\mathbf{n}} \parallel \pm \mathbf{P}$, all spins in the spin chain will have surface anisotropy. This will reduce Q relative to chains that only have the edge spins with surface anisotropy. Chains near ones with surface anisotropy on all spins will also see the Q in their chain reduced. This is known as the proximity effect.

Chapter 4

Methodology for Energy Minimization

The investigation into multiferroic nanoparticle spin structures relied on analysis of Hamiltonians modelling the system of spins. Minimization algorithms were used to find the ground state energies. It was found that different methods worked best for different dimensionality. In one dimension, random search methods were used. Nelder-Mead optimization was used for two dimensions. Finally, for three dimensions, the quasi-Newton L-BFGS-B algorithm was employed.

In the approach used, the spins were treated classically. Each spin was of unit length and was characterized by a phase angle, ϕ, common for all spins in the row, and by the cycloidal wavevector, $\mathbf{Q}$, which sets the angular difference between two spins located at $\mathbf{x}_i$ and $\mathbf{x}_j$ as $\mathbf{Q} \cdot (\mathbf{x}_i - \mathbf{x}_j)$. These variables were varied for the optimization.

In general, the optimization of a function $f(\mathbf{x})$ is done by making an initial guess of the minimum value, $\mathbf{x}_0$. That guess is tested to see if it satisfies the criterion for finding a minimum value for the function (often something such as the gradient of the function being less than some arbitrarily small, positive value: $\|\nabla f(\mathbf{x})\| < \epsilon$, where ϵ is the arbitrarily small, positive value). If the guess does not satisfy the exit condition, then the guess is improved by some means dependent on the optimization method employed. That improved guess, $\mathbf{x}_1$, is then tested by the exit condition. Again, if it meets the condition, then $\mathbf{x}_1$ is taken as the minimal value of $f(\mathbf{x})$. If it does not, the algorithm continues iteratively finding $\mathbf{x}_n$, where $n = 2, 3, 4, \ldots$, until the exit condition is met.

4.1 Random search algorithm

In *Mathematica*, the NMinimize function was used with the random search algorithm to determine the minima. The random search algorithm uses multiple starting points and performs minimization on those points. Whichever point's energy is the least from this process is assigned as the true minimum.

The minimization was done with constraints on the energy, and under such conditions, *Mathematica* performs the minimization using what is known as interior-point methods [134].

With the methods there is a function $f(\mathbf{x})$ that is to be minimized. It may have the constraints $c_i(\mathbf{x}) = 0$ for $i = 1, 2, \ldots, M$, where M is a positive integer and $d_j(\mathbf{x}) \geq 0$ for $j = 1, 2, \ldots, N$, where N is a positive integer [135].

The above optimization problem is then reformulated as

$$\underset{\mathbf{x},\, s_j}{\text{minimize}}\ f(\mathbf{x}) - \mu \sum_{j}^{N} \ln s_j, \tag{4.1a}$$

$$\text{subject to } c_i(\mathbf{x}) = 0\ \forall\ i = 1, 2, \ldots, M, \tag{4.1b}$$

$$d_j(\mathbf{x}) - s_j = 0\ \forall\ j = 1, 2, \ldots, N. \tag{4.1c}$$

μ is a positive value and $s_j \geq 0$ are slack variables introduced in place of the inequalities. The term to minimize now includes $-\mu \sum_{j}^{N} \ln s_j$. It is known as the barrier term. It does not admit solutions with $s_j < 0$, ensuring that the inequalities hold. The solution to (4.1) does not match that of the original problem of minimizing $f(\mathbf{x})$ as long as $\mu > 0$. But the goal is to find solutions to (4.1) for a sequence of positive μ values, $\{\mu_k\}$, as the sequence converges to zero. As $\mu \to 0$, (4.1) converges to the initial problem and the solution for (4.1) functions as a solution to the original problem [135].

The Karush-Kuhn-Tucker conditions relate to Lagrange multipliers and require that constraints be active or that the Lagrange multipliers of the constraints be equal to zero. For (4.1), this amounts to

$$\nabla f(\mathbf{x}) - A_E^T(\mathbf{x})\,\mathbf{y} - A_I^T(\mathbf{x})\,\mathbf{z} = 0, \tag{4.2a}$$

$$S\mathbf{z} - \mu\mathbf{e} = 0, \tag{4.2b}$$

$$\mathbf{c}(\mathbf{x}) = 0, \tag{4.2c}$$

$$\mathbf{d}\left(\mathbf{x}\right) - \mathbf{s} = 0. \tag{4.2d}$$

A_E and A_I are the Jacobian matrices for the equality and inequality constraints respectively. Jacobian matrices are comprised of the entries of all of the first partial derivatives for a given function (in this case, all of the (in)equality constraints are thought of as comprising components of a vector function). $\mathbf{y}$ and $\mathbf{z}$ are vectors containing the Lagrange multipliers $\{y_i\}$ and $\{z_j\}$ respectively. $\mathbf{c}\left(\mathbf{x}\right)$ and $\mathbf{d}\left(\mathbf{x}\right)$ are the vector forms of the equality and inequality constraints. S is a diagonal $N \times N$ matrix whose diagonal entries are given by $\{s_j\}$. $\mathbf{e}$ is an N-dimensional vector equal to $\left(1, 1, \ldots, 1\right)^T$.

Newton's method is then applied for $\mathbf{x}$, $\mathbf{s}$, $\mathbf{y}$, and $\mathbf{z}$. In Newton's method, for a given function $g(r)$, the minimum is found by iteratively searching along the $-\left[\nabla^2 g\left(r\right)\right]^{-1} \nabla g\left(r\right)$ direction. The k^{th} guess of the minimum value, r_k is updated via Newton's method by

$$r_{k+1} = r_k - \left[\nabla^2 g\left(r_k\right)\right]^{-1} \nabla g\left(r_k\right). \tag{4.3}$$

Eventually this should satisfy whatever termination condition was assigned and the minimum of $g(r)$ will be found. Returning to the interior-point methods, using Newton's method on (4.2) results in

$$\begin{bmatrix} \nabla^2_{xx}\mathcal{L} & 0 & -A_E^T\left(\mathbf{x}\right) & -A_I^T\left(\mathbf{x}\right) \\ 0 & Z & 0 & S \\ A_E\left(\mathbf{x}\right) & 0 & 0 & 0 \\ A_I\left(\mathbf{x}\right) & -I & 0 & 0 \end{bmatrix} \begin{bmatrix} p_x \\ p_s \\ p_y \\ p_z \end{bmatrix} = - \begin{bmatrix} \nabla f\left(\mathbf{x}\right) - A_E^T\left(\mathbf{x}\right)\mathbf{y} - A_I^T\left(\mathbf{x}\right)\mathbf{z} \\ S\mathbf{z} - \mu\mathbf{e} \\ \mathbf{c}\left(\mathbf{x}\right) \\ \mathbf{d}\left(\mathbf{x}\right) - \mathbf{s} \end{bmatrix}. \tag{4.4}$$

Here Z is a diagonal $N \times N$ matrix whose diagonal entries are given by $\{z_j\}$. I is the identity matrix. $\mathbf{p} = \left(p_x, p_s, p_y, p_z\right)^T$ is the step direction vector – it determines in which direction of the variable space the search proceeds. Also, $\mathcal{L}\left(\mathbf{x}, \mathbf{s}, \mathbf{y}, \mathbf{z}\right) = f\left(\mathbf{x}\right) - \mathbf{y} \cdot \mathbf{c}\left(\mathbf{x}\right) - \mathbf{z} \cdot \left(\mathbf{d}\left[\mathbf{x}\right] - \mathbf{s}\right)$.

The variables are updated as follows:

$$\mathbf{x}^+ = \mathbf{x} + \alpha_s p_x, \tag{4.5a}$$

$$\mathbf{s}^+ = \mathbf{s} + \alpha_s p_s, \tag{4.5b}$$

$$\mathbf{y}^+ = \mathbf{y} + \alpha_z p_y, \tag{4.5c}$$

$$\mathbf{z}^{+} = \mathbf{z} + \alpha_z p_z, \tag{4.5d}$$

where

$$\alpha_s = \max\left\{\alpha \in (0,1] : s + \alpha p_s \geq (1-\tau)\, s\right\}, \tag{4.6a}$$

$$\alpha_z = \max\left\{\alpha \in (0,1] : z + \alpha p_z \geq (1-\tau)\, z\right\}. \tag{4.6b}$$

τ is chosen to be between zero and one and usually takes the value 0.995.

A typical minimization scheme entails starting with initial values for $\mathbf{x}$, $\mathbf{s}$, and μ. From there, (4.4) is used to find $\mathbf{p}$. (4.5) and (4.6) provide the means of updating the guesses. This procedure is then repeated until the conditions from (4.2) are met to a certain degree of accuracy (for instance, until the norm of all of the subequations of (4.2) is less than the present μ). μ is then reduced by an amount chosen to optimize the number of iterations needed for convergence. These procedures are repeated until $\mu \to 0$ and the established termination conditions are met [135].

4.2 Nelder-Mead algorithm

The Nelder-Mead algorithm is a derivative-free optimization method. In the method, a simplex, whose vertices are comprised of initial guesses of the value of the function that one is trying to minimize, is constructed. A simplex in a n-dimensional space is a generalization of a line segment in one dimension, an equilateral triangle in two dimensions, and a tetrahedron in three dimensions [136]. Through testing of the vertices of the simplex, via the progressive elimination of the worst vertex, the one where the function evaluates to the highest value, a minimum of the function is found [135, 137].

To minimize a function $f : \mathbb{R}^n \to \mathbb{R}$ via the Nelder-Mead algorithm $n+1$ points in $\mathbb{R}^n$ are chosen to form the vertices of the initial simplex.The function is then evaluated at the $n+1$ points. The points form a set $\{\mathbf{x}_i\}$ for $i = 1, 2, \ldots, n+1$, and can be labelled in such a manner that

$$f(\mathbf{x}_1) \leq f(\mathbf{x}_2) \leq \ldots \leq f(\mathbf{x}_{n+1})\,.$$

A centroid, the midpoint between the vertices, for $\{\mathbf{x}_i\}$, but omitting $\mathbf{x}_{n+1}$, can then be determined:

$$\bar{\mathbf{x}} = \sum_{i=1}^{n} \mathbf{x}_i. \tag{4.7}$$

$\mathbf{x}_{n+1}$ is then reflected through the centroid,

$$\mathbf{x}_{\text{reflected}} = \bar{\mathbf{x}} - \delta\left(\mathbf{x}_{n+1} - \bar{\mathbf{x}}\right), \tag{4.8}$$

where δ often equals 1 [138]. If $f(\mathbf{x}_1) \leq f(\mathbf{x}_{\text{reflected}}) < f(\mathbf{x}_{n+1})$ then the reflected point is accepted as the replacement of $\mathbf{x}_{n+1}$ and another iteration is performed with the simplex to find the vertex which supplies the largest function value and that is replaced.

If $f(\mathbf{x}_{\text{reflected}}) < f(\mathbf{x}_1)$ then the reflection is expanded to see if an even lower function value can be found:

$$\mathbf{x}_{\text{expanded}} = \bar{\mathbf{x}} - \alpha\left(\mathbf{x}_{n+1} - \bar{\mathbf{x}}\right), \tag{4.9}$$

where α often equals 2. If $f(\mathbf{x}_{\text{expanded}}) < f(\mathbf{x}_{\text{reflected}})$ then $\mathbf{x}_{\text{expanded}}$ replaces $\mathbf{x}_{n+1}$. Otherwise, $\mathbf{x}_{\text{reflected}}$ takes the place of $\mathbf{x}_{n+1}$.

If $f(\mathbf{x}_{\text{reflected}}) \geq f(\mathbf{x}_{n+1})$ then a contracted reflection is performed:

$$\mathbf{x}_{\text{contracted}} = \bar{\mathbf{x}} - \beta\left(\mathbf{x}_{n+1} - \bar{\mathbf{x}}\right). \tag{4.10}$$

Frequently, $\beta = 1/2$. Assuming that the function evaluated at the contracted reflection returns a lesser value than the function evaluated at $\mathbf{x}_{n+1}$, $\mathbf{x}_{\text{contracted}}$ replaces $\mathbf{x}_{n+1}$. If that assumption is invalid, then a point between the centroid and $\mathbf{x}_{n+1}$ is tested:

$$\mathbf{x}_{\text{inside contracted}} = \bar{\mathbf{x}} + \sigma\left(\mathbf{x}_{n+1} - \bar{\mathbf{x}}\right), \tag{4.11}$$

where σ usually equals $1/2$. If the function value at that point is less than the function value at $\mathbf{x}_{n+1}$, then the point takes the place of $\mathbf{x}_{n+1}$.

If the function f is greater than $f(\mathbf{x}_{n+1})$ at all of the reflected, expanded reflected, contracted reflected, and inside contracted points then the original simplex is shrunken. All other points are drawn nearer to $\mathbf{x}_1$:

$$\mathbf{x}_i' = \frac{1}{2}\left(\mathbf{x}_1 + \mathbf{x}_i\right), \quad i = 2, 3, \ldots, n+1. \tag{4.12}$$

The procedure of ordering the $n+1$ vertices based on function value and trying to improve upon the one with the highest value is then repeated.

Termination is often achieved when the spread of the $n + 1$ values falls below a threshold value [137, 138]. For instance, let

$$\rho = \max_{2 \leq i \leq n+1} \left\| \mathbf{x}_1 - \mathbf{x}_i \right\| . \tag{4.13}$$

If $\rho < \varepsilon$, where ε is a small, positive value, then the Nelder-Mead method terminates.

It should be noted that the algorithm is not a global optimization method. However, for functions with few local minima, it works well to find the global minimum [139]. The implementation of the Nelder-Mead algorithm in *Mathematica* allows constraints that the general method usually does not. Constraints are realized through penalty functions [139].

4.3 L-BFGS-B algorithm

The BFGS method is a quasi-Newton optimization method. Newton's method to optimize a function f uses the Hessian, $\nabla^2 f$, the matrix containing all of the partial second derivatives of f. Convergence is often very fast (in terms of the number of iterations), however calculating the Hessian at every step can be quite costly. Quasi-Newton methods try to capture the fast convergence of Newton's method while eschewing the calculation of the actual Hessian. Instead, an approximate Hessian is calculated [135]. The BFGS method takes its name from its originators Broyden, Fletcher, Goldfarb, and Shanno.

An initial guess of the minimum of the function f is made. Then steps determined by the approximate Hessian are used to improve upon the initial guess. This iterative process continues until the termination condition, such as $\|\nabla f\| < \varepsilon$, where ε is a small, positive value. The steps are

$$\mathbf{x}_{k+1} = \mathbf{x}_k + \alpha_k \mathbf{p}_k, \tag{4.14}$$

where $\mathbf{x}_k$ is the k^{th} iteration of the algorithm, $\mathbf{p}_k$ is the step direction vector, and α_k is the step size. α_k is determined in part by the Wolfe conditions, which ensure that f sufficiently decreases during a step and that the step size used is not too small:

$$f(\mathbf{x}_k + \alpha_k \mathbf{p}_k) \leq f(\mathbf{x}_k) + c_1 \alpha_k \nabla f_k \cdot \mathbf{p}_k, \tag{4.15a}$$

$$\nabla f(\mathbf{x}_k + \alpha_k \mathbf{p}_k) \cdot \mathbf{p}_k \geq c_2 \nabla f_k \cdot \mathbf{p}_k, \tag{4.15b}$$

where $0 < c_1 < c_2 < 1$.

A quadratic representation of the objective function at the k^{th} step is

$$m_k(\mathbf{p}) = f_k + \nabla f_k \cdot \mathbf{p} + \frac{1}{2}\mathbf{p}^T B_k \mathbf{p}, \tag{4.16}$$

where $f_k = f(\mathbf{x}_k)$, $\mathbf{p}$ is the step direction vector, and B_k is the approximate Hessian matrix. Minimizing $\mathbf{p}$ for the k^{th} step leads to

$$\mathbf{p}_k = -B_k^{-1} \nabla f_k. \tag{4.17}$$

A condition is imposed to update B_k instead of recalculating it for every step. The gradient of the quadratic representation of f is required to equal the gradient at the last two steps. That is, $\nabla m_{k+1}(0) = \nabla f_{k+1}$ and $\nabla m_{k+1}(-\alpha_k \mathbf{p}_k) = \nabla f_k$. The first of these is automatically satisfied from (4.16). As for the second,

$$\nabla m_{k+1}(-\alpha_k \mathbf{p}_k) = \nabla f_{k+1} - \alpha_k B_{k+1} \mathbf{p}_k = \nabla f_k. \tag{4.18}$$

Substituting $\mathbf{s}_k = \mathbf{x}_{k+1} - \mathbf{x}_k = \alpha_k \mathbf{p}_k$ and $\mathbf{y}_k = \nabla f_{k+1} - \nabla f_k$, as well as rearranging terms in (4.18) leads to

$$B_{k+1} \mathbf{s}_k = \mathbf{y}_k. \tag{4.19}$$

This equation is known as the secant equation. To uniquely find B_{k+1}, it is required that B_{k+1} be the "closest" appropriate matrix to B_k. That is,

$$\underset{B}{\text{minimize}} \quad \|B_{k+1} - B_k\| \tag{4.20a}$$

$$\text{subject to} \quad B_{k+1} = B_{k+1}^T, \quad B_{k+1}\mathbf{s}_k = \mathbf{y}_k. \tag{4.20b}$$

It is actually the inverse of B_k, $H_k = B_k^{-1}$, that is modified in the BFGS method:

$$\underset{H}{\text{minimize}} \quad \|H_{k+1} - H_k\| \tag{4.21a}$$

$$\text{subject to} \quad H_{k+1} = H_{k+1}^T, \quad H_{k+1}\mathbf{y}_k = \mathbf{s}_k. \tag{4.21b}$$

The weighted Frobenius norm can be used as the norm in the minimization [135],

$$\|A\|_W = \left\|W^{1/2} A W^{1/2}\right\|_F, \tag{4.22}$$

where

$$\|C\|_F^2 = \sum_{i=1}^{n} \sum_{j=1}^{n} c_{ij}^2. \tag{4.23}$$

For (4.20), W is any matrix that satisfies $W\mathbf{y}_k = \mathbf{s}_k$ and for (4.21), W is any matrix that satisfies $W\mathbf{s}_k = \mathbf{y}_k$. W can be assumed to equal $\bar{G}_k^{-1}$ for (4.20) and $\bar{G}_k$ for (4.21), where $\bar{G}_k$ is the average Hessian,

$$\bar{G}_k = \int_0^1 \nabla^2 f\left(\mathbf{x}_k + \tau \alpha_k \mathbf{p}_k\right) \mathrm{d}\tau. \tag{4.24}$$

These steps lead to the formula to update H_k:

$$H_{k+1} = \left(I - \frac{\mathbf{s}_k \mathbf{y}_k^T}{\mathbf{y}_k^T \mathbf{s}_k}\right) H_k \left(I - \frac{\mathbf{y}_k \mathbf{s}_k^T}{\mathbf{y}_k^T \mathbf{s}_k}\right) + \frac{\mathbf{s}_k \mathbf{s}_k^T}{\mathbf{y}_k^T \mathbf{s}_k}. \tag{4.25}$$

I is the identity matrix. In sum, the procedure in a BFGS step is to find a search direction using (4.17), find $\mathbf{x}_{k+1}$ by satisfying (4.15), the Wolfe conditions, and then use (4.25) to find H_{k+1}. This procedure is continued until the termination conditions are reached. The initial inverse Hessian approximation, H_0, can either be determined by using the finite differences in $\mathbf{x}_0$ or be a multiple of the identity matrix [135].

Calculating H_k in a large vector space can be quite challenging. There are methods which use limited information for H_k to circumvent the issue. These are known as limited-memory methods. In the limited-memory BFGS, or L-BFGS, method only the last r pairs of $\{\mathbf{s}_i, \mathbf{y}_i\}$ are retained. $r \approx 20$ is often large enough for good results. This can speed up the algorithm considerably and although the actual H_k is not calculated, the method has been shown to optimize functions quite well [135].

Conventional BFGS and L-BFGS methods only optimize unconstrained functions. L-BFGS-B methods can deal with constraints. $m_k\left(\mathbf{x}_k - t\,\nabla f_k\right)$ is minimized for some $t > 0$. Any variable which falls outside of its bounds from that minimization is then held fixed at the bound whilst a L-BFGS minimization of $m_k\left(\mathbf{x}\right)$ is done on the free variables. The solution to this is the tentative new step, $\bar{\mathbf{x}}_{k+1}$. It is then checked that none of the free variables violated its bounds. If some did, then the solution is scaled along the line $\bar{\mathbf{x}}_{k+1} - \mathbf{x}_k$ to find a feasible new step. Once $\mathbf{x}_{k+1}$ is found, the procedure returns to the usual L-BFGS steps [140].

Chapter 5

Spin Chain

Modelling done in one dimension illustrated two striking effects in BFO: (a) the Q value varied with nanoparticle size and had discontinuous jumps; and (b) at the asymptotes the energy for the system was bistable – two different Q values were of the same minimum energy.

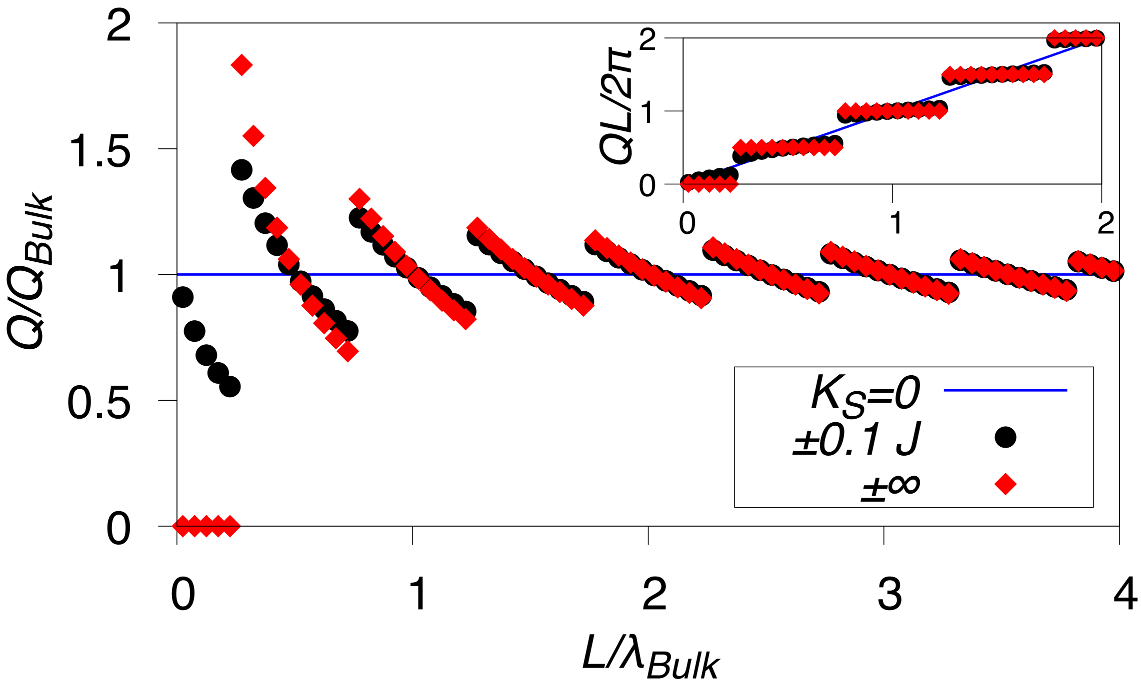

Figure 5.1: Q/Q_{Bulk} versus nanoparticle size for $K_S = 0, \pm 0.1$, and $\pm \infty$. The inset shows $QL/2\pi$, the winding number, versus nanoparticle size. Only compensated nanoparticles (even N) are shown. Reprinted figure with permission from [141]. Copyright 2019 by the American Physical Society.

Strain has previously been shown to affect the value of Q [142, 143]. However, there are no known reports of sudden jumps in Q. The drastic change in the cycloidal wavevector seen in Figure 5.1 is attributable to the competition between the surface anisotropy and the cycloid energy. Imagine a spin chain of length $\lambda_{\text{bulk}}/2$ with easy-axis anisotropy (see Figure 5.2). At this size, the nanoparticle is perfectly content to have the surface spins pointing outwards and the spins in the interior angled with respect to each other as they would be in the bulk system. Q_{bulk} perfectly satisfies the conditions for this nanoparticle. However, in a slightly longer or shorter nanoparticle a conflict arises. If the surface spins are to be normal, then Q must change to accommodate this, either increasing for a smaller nanoparticle or decreasing for a larger nanoparticle. L is the length of the spin chain. The inset of Figure 5.1 illustrates this. It plots $QL/2\pi$, or the winding number – the number of cycloid revolutions made within the nanoparticle. The value of the winding number changes in half-integer steps. In most instances of changing nanoparticle size it is advantageous to slightly change Q so that the winding number remains near constant. At critical sizes, $L = (2n + 1)\lambda_{\text{bulk}}/4$, where n is a non-negative integer, this is not the case and the nanoparticle finds its lowest energy state by dramatically changing the angle between the spins and moving to an adjacent winding number level.

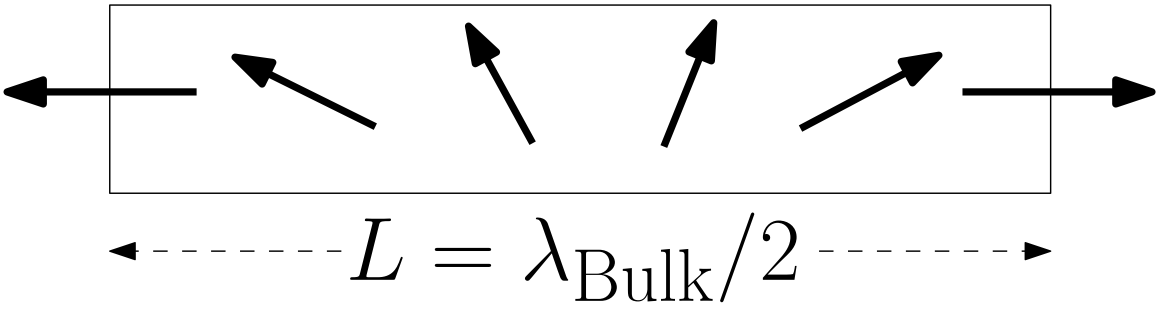

Figure 5.2: Cycloid of length $\lambda_{\text{Bulk}}/2$. The arrows represent spins of one sublattice. $D/J = 0.15708$.

In Figure 5.1 the blue line represents the case for no surface anisotropy. Q is independent of nanoparticle size and takes its bulk value, as would be expected. With the addition of surface anisotropy, Q acquires a significant size dependence. For $K_S = \pm 0.1$ starting at the left-hand side of Figure 5.1, Q decreases with increasing nanoparticle size with the winding number being zero, until, as the spin chain continues to lengthen, it becomes favourable for the chain to move into the half-cycloid level, which causes Q to jump dramatically.

As the chain continues to increase in size Q decreases once more until the jumps into the one-complete-cycloid level and Q sharply rises. Figure 5.1 also shows that as the length of the cycloid increases over several cycloid lengths, Q tends toward its bulk value. The tending of Q towards its bulk value as size increases makes sense considering that the longer the spin chain, the less the effect of the surface anisotropy would expected to be. With minimal impact from the surface anisotropy (just as if $K_S \approx 0$) the system behaves as it does in the bulk case.

To determine the bulk value of Q we can look at the Hamiltonian in (3.1) and introduce periodic boundary conditions. Then we write $\mathbf{S}_i$ as

$$\frac{\mathbf{S}_i}{S} = \mathbf{s}_i = (-1)^i \left(\sin\theta_i \sin\phi_i\, \hat{\mathbf{x}} + \cos\theta_i\, \hat{\mathbf{y}} + \sin\theta_i \cos\phi_i\, \hat{\mathbf{z}}\right). \tag{5.1}$$

θ_i can be set to be equal to $\pi/2$ as all directions orthogonal to the $\hat{\mathbf{P}} = \hat{\mathbf{z}}$ are equivalent. Inserting (5.1) into (3.1) with $\hat{\mathbf{P}} = \hat{\mathbf{z}}$ gives

$$\begin{aligned}\mathcal{H} = &-\frac{S^2}{2}\sum_{i,\hat{\mathbf{v}}}\Big(J\left[\sin\phi_i \sin\phi_{i+1} + \cos\phi_i \cos\phi_{i+1}\right] \\ &+ D\left[\hat{\mathbf{z}} \times \hat{\mathbf{x}}\right] \cdot \left[\cos\phi_i \sin\phi_{i+1} - \sin\phi_i \cos\phi_{i+1}\right]\hat{\mathbf{y}}\Big) \\ = &-\frac{S^2}{2}\sum_{i,\hat{\mathbf{v}}}\Big(J\cos\left[\phi_{i+1} - \phi_i\right] + D\sin\left[\phi_{i+1} - \phi_i\right]\Big).\end{aligned} \tag{5.2}$$

$\phi_i = \mathbf{Q} \cdot \mathbf{R}_i + \phi_0$, where ϕ_0 is an arbitrary phase universal for all spins in the chain, and $\mathbf{R}_i$ is the location of the i^{th} spin with $\mathbf{R}_{i+1} - \mathbf{R}_i = a\,\hat{\mathbf{v}}$. Using this information (5.2) reduces to

$$\mathcal{H} = -\frac{N^d S^2}{2}\sum_{\hat{\mathbf{v}}}\Big(J\cos\left[\mathbf{Q} \cdot a\,\hat{\mathbf{v}}\right] + D\sin\left[\mathbf{Q} \cdot a\,\hat{\mathbf{v}}\right]\Big). \tag{5.3}$$

In one dimension $d = 1$, $\mathbf{Q} = Q\,\hat{\mathbf{x}}$, and $\hat{\mathbf{v}} = \pm\hat{\mathbf{x}}$. From this,

$$\mathcal{H} = -NS^2\Big(J\cos\left[Qa\right] + D\sin\left[Qa\right]\Big). \tag{5.4}$$

(5.4) can be differentiated with respect to Q to find the Q value which gives the minimum energy:

$$\frac{\mathrm{d}\mathcal{H}}{\mathrm{d}Q} = -NS^2 a\Big(-J\sin\left[Qa\right] + D\cos\left[Qa\right]\Big) = 0$$

$$\implies Q_{\text{bulk}} = \frac{1}{a}\arctan\left(\frac{D}{J}\right). \tag{5.5}$$

This result remains the same for higher dimensions and $\hat{\mathbf{P}} = \hat{\mathbf{z}}$, since Q can remain along x as $\mathbf{Q} \perp \hat{\mathbf{v}}$ for interactions along other directions, and those interactions will not affect the energy.

For general $\mathbf{P}$ not along a cubic direction then $\mathbf{Q}$, always orthogonal to $\mathbf{P}$, is not along one of the cubic directions, but the magnitude of Q remains approximately the same as in (5.5), if $D \ll J$. We can see this with the following calculations. Returning to (5.2), if we have $d = 3$ and $\mathbf{Q}$ along an arbitrary direction, we end up with

$$\frac{\mathbf{S}_i}{S} = \mathbf{s}_i = (-1)^i\left(\sin\left[\mathbf{Q}\cdot\mathbf{R}_i + \phi_0\right]\hat{\mathbf{Q}} + \cos\left[\mathbf{Q}\cdot\mathbf{R}_i + \phi_0\right]\hat{\mathbf{P}}\right). \tag{5.6}$$

Inserting (5.6) into (3.1) gives

$$\begin{aligned}
\mathcal{H} =& \frac{1}{2}\sum_{i,\hat{\mathbf{v}}}\left(J\mathbf{S}_i\cdot\mathbf{S}_{i+1} + D\left[\hat{\mathbf{P}}\times\hat{\mathbf{v}}\right]\cdot\left[\mathbf{S}_i\times\mathbf{S}_{i+1}\right]\right)\\
=& -\frac{S^2}{2}\sum_{i,\hat{\mathbf{v}}}\left(J\left[\sin\left\{\mathbf{Q}\cdot\mathbf{R}_i+\phi_0\right\}\sin\left\{\mathbf{Q}\cdot\mathbf{R}_{i+1}+\phi_0\right\}\right.\right.\\
&+ \left.\cos\left\{\mathbf{Q}\cdot\mathbf{R}_i+\phi_0\right\}\cos\left\{\mathbf{Q}\cdot\mathbf{R}_{i+1}+\phi_0\right\}\right]\\
&+ D\left[\hat{\mathbf{P}}\times\hat{\mathbf{v}}\right]\cdot\left[\sin\left\{\mathbf{Q}\cdot\mathbf{R}_i+\phi_0\right\}\cos\left\{\mathbf{Q}\cdot\mathbf{R}_{i+1}+\phi_0\right\}\right.\\
&- \left.\left.\cos\left\{\mathbf{Q}\cdot\mathbf{R}_i+\phi_0\right\}\sin\left\{\mathbf{Q}\cdot\mathbf{R}_{i+1}+\phi_0\right\}\right]\hat{\mathbf{Q}}\times\hat{\mathbf{P}}\right)\\
=& -\frac{S^2}{2}\sum_{i,\hat{\mathbf{v}}}\left(J\cos\left[\mathbf{Q}\cdot\left\{\mathbf{R}_{i+1}-\mathbf{R}_i\right\}\right]\right.\\
&- \left.D\sin\left[\mathbf{Q}\cdot\left\{\mathbf{R}_{i+1}-\mathbf{R}_i\right\}\right]\left[\hat{\mathbf{P}}\times\hat{\mathbf{v}}\right]\cdot\left[\hat{\mathbf{Q}}\times\hat{\mathbf{P}}\right]\right)\\
=& -\frac{S^2}{2}\sum_{i,\hat{\mathbf{v}}}\left(J\cos\left[\mathbf{Q}\cdot a\,\hat{\mathbf{v}}\right]\right.\\
&- \left.D\sin\left[\mathbf{Q}\cdot a\,\hat{\mathbf{v}}\right]\left[\left\{\hat{\mathbf{P}}\cdot\hat{\mathbf{Q}}\right\}\left\{\hat{\mathbf{v}}\cdot\hat{\mathbf{P}}\right\} - \left\{\hat{\mathbf{P}}\cdot\hat{\mathbf{P}}\right\}\left\{\hat{\mathbf{v}}\cdot\hat{\mathbf{Q}}\right\}\right]\right)\\
=& -\frac{S^2}{2}\sum_{i,\hat{\mathbf{v}}}\left(J\cos\left[\mathbf{Q}\cdot a\,\hat{\mathbf{v}}\right] + D\sin\left[\mathbf{Q}\cdot a\,\hat{\mathbf{v}}\right]\hat{\mathbf{v}}\cdot\hat{\mathbf{Q}}\right)\\
=& -\frac{N^3S^2}{2}\sum_{\hat{\mathbf{v}}}\left(J\cos\left[\mathbf{Q}\cdot a\,\hat{\mathbf{v}}\right] + D\sin\left[\mathbf{Q}\cdot a\,\hat{\mathbf{v}}\right]\hat{\mathbf{v}}\cdot\hat{\mathbf{Q}}\right)\\
=& -N^3S^2\left(J\left[\cos\left\{Q_xa\right\} + \cos\left\{Q_ya\right\} + \cos\left\{Q_za\right\}\right]\right.
\end{aligned}$$

$$+\frac{D}{Q}\left[Q_x \sin\{Q_x a\} + Q_y \sin\{Q_y a\} + Q_z \sin\{Q_z a\}\right]). \tag{5.7}$$

Taking the derivative with respect to Q_x gives

$$\begin{aligned}\frac{\mathrm{d}\mathcal{H}}{\mathrm{d}Q_x} &= -N^3 S^2 \left(-Ja\sin\left[Q_x a\right] + \frac{DQ_x a}{Q}\cos\left[Q_x a\right]\right) = 0\\ \implies Q_x &= \frac{1}{a}\arctan\left(\frac{DQ_x}{JQ}\right).\end{aligned} \tag{5.8}$$

The fraction Q_x/Q is fixed by the direction of the cycloid, and thus is constant in (5.8). Similarly for Q_y and Q_z, we have

$$Q_y = \frac{1}{a}\arctan\left(\frac{DQ_y}{JQ}\right) \tag{5.9}$$

and

$$Q_z = \frac{1}{a}\arctan\left(\frac{DQ_z}{JQ}\right). \tag{5.10}$$

For $D \ll J$ we get

$$Qa \approx \frac{D}{J}. \tag{5.11}$$

Indeed Q is roughly independent of direction when the Dzyaloshinskii-Moriya interaction strength is much less than that of the exchange interaction.

For the spin chain results, we started with the following Hamiltonian:

$$\begin{aligned}\mathcal{H} = &\sum_{i=1}^{N-1}\left(J\mathbf{S}_i\cdot\mathbf{S}_{i+1} + \left[D\left\{\hat{\mathbf{z}}\times\hat{\mathbf{x}}\right\} + D'\left\{-1\right\}^i\hat{\mathbf{z}}\right]\cdot\left[\mathbf{S}_i\times\mathbf{S}_{i+1}\right]\right)\\ &-K\sum_{i=1}^{N}\left(\mathbf{S}_i\cdot\hat{\mathbf{z}}\right)^2 - K_S\left(\left[\mathbf{S}_1\cdot\hat{\mathbf{n}}\right]^2 + \left[\mathbf{S}_N\cdot\hat{\mathbf{n}}\right]^2\right).\end{aligned} \tag{5.12}$$

The first term is the exchange interaction with J as the exchange integral. The second and third terms are the Dzyaloshinskii-Moriya interaction terms. The second term, with D, is responsible for the cycloid of the system. The third, with D', is the weak ferromagnetic component, and K is the bulk single-ion anisotropy. Dividing (5.12) by JS^2 gives

$$\frac{\mathcal{H}}{JS^2} = \sum_{i=1}^{N-1}\left(\mathbf{s}_i\cdot\mathbf{s}_{i+1} + \left[d\,\hat{\mathbf{y}} + d'\left\{-1\right\}^i\hat{\mathbf{z}}\right]\cdot\left[\mathbf{s}_i\times\mathbf{s}_{i+1}\right]\right)$$

$$-k\sum_{i=1}^{N}s_{i,z}^{2}-k_{S}\left(s_{1,z}^{2}+s_{N,z}^{2}\right). \tag{5.13}$$

Here $d=D/J, d'=D'/J, k=K/J, k_S=K_S/J$, and $\mathbf{s}_i=\mathbf{S}/S$. d' and k were both taken to be equal to zero in the modelling.

The idealized Q for a particular spin chain was found using the NMinimize function in *Mathematica* with the random search algorithm. The spin vector was characterized as in (5.1). Expanding the spin terms, we can examine the components of the Hamiltonian separately. Starting with the exchange interaction, we have

$$\begin{aligned}\mathbf{s}_i\cdot\mathbf{s}_{i+1}&=-\left(\sin\theta_i\sin\phi_i\sin\theta_{i+1}\sin\phi_{i+1}+\cos\theta_i\cos\theta_{i+1}+\sin\theta_i\cos\phi_i\sin\theta_{i+1}\cos\phi_{i+1}\right)\\&=-\left(\cos\left[\phi_{i+1}-\phi_i\right]\sin\theta_i\sin\theta_{i+1}+\cos\theta_i\cos\theta_{i+1}\right)\\&=-\frac{1}{2}\Big(\left[\cos\left\{\theta_{i+1}-\theta_i\right\}-\cos\left\{\theta_{i+1}+\theta_i\right\}\right]\cos\left[\phi_{i+1}-\phi_i\right]\\&\quad+\cos\left[\theta_{i+1}+\theta_i\right]+\cos\left[\theta_{i+1}-\theta_i\right]\Big).\end{aligned}\tag{5.14}$$

Next, we can look at the components of the cross product in the Dzyaloshinskii-Moriya interaction. The y component provides

$$\begin{aligned}\left(\mathbf{s}_i\times\mathbf{s}_{i+1}\right)_y&=-\sin\theta_i\sin\theta_{i+1}\sin\left(\phi_{i+1}-\phi_i\right)\\&=\frac{\cos\left(\theta_{i+1}+\theta_i\right)-\cos\left(\theta_{i+1}-\theta_i\right)}{2}\sin\left(\phi_{i+1}-\phi_i\right).\end{aligned}\tag{5.15}$$

The z component leads to

$$\begin{aligned}\left(\mathbf{s}_i\times\mathbf{s}_{i+1}\right)_z&=\cos\theta_i\sin\theta_{i+1}\sin\phi_{i+1}-\sin\theta_i\cos\theta_{i+1}\sin\phi_i\\&=\frac{1}{2}\left(\left[\sin\left\{\theta_{i+1}+\theta_i\right\}+\sin\left\{\theta_{i+1}-\theta_i\right\}\right]\sin\phi_{i+1}\right.\\&\quad\left.-\left[\sin\left\{\theta_{i+1}+\theta_i\right\}-\sin\left\{\theta_{i+1}-\theta_i\right\}\right]\sin\phi_i\right)\\&=\frac{1}{2}\left(\sin\left[\theta_{i+1}-\theta_i\right]\left[\sin\phi_i+\sin\phi_{i+1}\right]-\sin\left[\theta_{i+1}+\theta_i\right]\left[\sin\phi_i-\sin\phi_{i+1}\right]\right)\\&=\sin\left(\theta_{i+1}-\theta_i\right)\sin\left(\frac{\phi_{i+1}+\phi_i}{2}\right)\cos\left(\frac{\phi_{i+1}-\phi_i}{2}\right)\\&\quad+\sin\left(\theta_{i+1}+\theta_i\right)\cos\left(\frac{\phi_{i+1}+\phi_i}{2}\right)\sin\left(\frac{\phi_{i+1}-\phi_i}{2}\right).\end{aligned}\tag{5.16}$$

From here, we will investigate the case with $d'=k=0$. θ_i can again be set to $\pi/2$ for all i as there is no gain in energy if the spins are in the xz-plane. These conditions lead to the Hamiltonian

$$\frac{\mathcal{H}}{JS^2} = -\sum_{i=1}^{N-1} \left(\cos\left[\phi_{i+1}-\phi_i\right] + d\sin\left[\phi_{i+1}-\phi_i\right]\right) - k_S\left(\sin^2\phi_1 + \sin^2\phi_N\right). \tag{5.17}$$

The term in the summation can be rewritten as

$$\begin{aligned}\cos\left(\phi_{i+1}-\phi_i\right) + d\sin\left(\phi_{i+1}-\phi_i\right) =& \sqrt{1+d^2}\left(\frac{1}{\sqrt{1+d^2}}\cos\left[\phi_{i+1}-\phi_i\right]\right.\\ &\left.+\frac{d}{\sqrt{1+d^2}}\sin\left[\phi_{i+1}-\phi_i\right]\right)\\ =&\sqrt{1+d^2}\left(\cos\tilde{d}\cos\left[\phi_{i+1}-\phi_i\right]\right.\\ &\left.+\sin\tilde{d}\sin\left[\phi_{i+1}-\phi_i\right]\right)\\ =&\sqrt{1+d^2}\cos\left(\phi_{i+1}-\phi_i-\tilde{d}\right),\end{aligned} \tag{5.18}$$

where $\tilde{d} = \arctan(d)$. (5.17) can then be reformulated as

$$\frac{\mathcal{H}}{JS^2} = -\sqrt{1+d^2}\sum_{i=1}^{N-1}\cos\left(\phi_{i+1}-\phi_i+\tilde{d}\right) - k_S\left(\sin^2\phi_1+\sin^2\phi_N\right). \tag{5.19}$$

5.1 Long wavelength regime

If the relative angle between spins of the same sublattice is small then it is said that the spin chain is in the long wavelength regime. The chain can then be analyzed not as a system of discrete spins, but as a continuous object. The transition from discrete to continuous analysis can be done by setting

$$\sum_{i=1}^{N-1} \to \frac{1}{a}\int_{-\frac{L}{2}}^{\frac{L}{2}} \mathrm{d}x, \tag{5.20}$$

$$\phi_i \to \phi(x), \tag{5.21}$$

and

$$\frac{\phi_{i+1}-\phi_i}{a} \to \phi'(x). \tag{5.22}$$

Using the above conversions on the Hamiltonian of (5.17) we arrive at

$$\begin{aligned}\frac{\mathcal{H}}{JS^2} =& -\frac{1}{a}\int_{-\frac{L}{2}}^{\frac{L}{2}}\big(\cos\left[a\phi'\right] + d\sin\left[a\phi'\right]\big)\mathrm{d}x \\ & -\frac{k_S}{a}\left(\sin^2\left[\phi\left\{x=-\frac{L}{2}\right\}\right] + \sin^2\left[\phi\left\{x=\frac{L}{2}\right\}\right]\right).\end{aligned} \tag{5.23}$$

A harmonic solution to (5.23) is valid when $a\phi'(x) \ll 1$ and $d \ll 1$. Such a solution has the form of $\phi(x) = \phi_0 + Qx$ where ϕ_0 is a phase angle. Inserting this into (5.23) and working in the regime where the harmonic solution is valid leads to

$$\begin{aligned}\frac{\mathcal{H}}{JS^2} =& -\frac{1}{a}\int_{-\frac{L}{2}}^{\frac{L}{2}}\left(1 - \frac{\left[a\phi'\right]^2}{2} + d\,a\,\phi'\right)\mathrm{d}x \\ & -\frac{k_S}{a}\left(\sin^2\left[\phi_0 - \frac{QL}{2}\right] + \sin^2\left[\phi_0 + \frac{QL}{2}\right]\right) \\ =& -\frac{L}{a} + \int_{-\frac{L}{2}}^{\frac{L}{2}}\left(\frac{a\,Q^2}{2} - d\,Q\right)\mathrm{d}x \\ & - k_S\left(\sin^2\phi_0\cos^2\left[\frac{QL}{2}\right] - 2\sin\phi_0\cos\left[\frac{QL}{2}\right]\sin\left[\frac{QL}{2}\right]\cos\phi_0\right. \\ & + \sin^2\left[\frac{QL}{2}\right]\cos^2\phi_0 + \sin^2\phi_0\cos^2\left[\frac{QL}{2}\right] \\ & \left. + 2\sin\phi_0\cos\left[\frac{QL}{2}\right]\sin\left[\frac{QL}{2}\right]\cos\phi_0 + \sin^2\left[\frac{QL}{2}\right]\cos^2\phi_0\right) \\ =& -L\left(\frac{1}{a} - \frac{a\,Q^2}{2} + d\,Q\right) - 2k_S\left(\sin^2\phi_0\cos^2\left[\frac{QL}{2}\right] + \sin^2\left[\frac{QL}{2}\right]\cos^2\phi_0\right) \\ =& -L\left(\frac{1}{a} + \frac{d^2}{2a} - \frac{a}{2}\left[Q - \frac{d}{a}\right]^2\right) \\ & - 2k_S\left(\sin^2\phi_0\left[\frac{1+\cos\{QL\}}{2}\right] + \left[\frac{1-\cos\{QL\}}{2}\right]\cos^2\phi_0\right) \\ =& -L\left(\frac{1}{a} + \frac{d^2}{2a} - \frac{a}{2}\left[Q - \frac{d}{a}\right]^2\right) \\ & - k_S\left(\sin^2\phi_0 + \sin^2\phi_0\cos\left[QL\right] + \cos^2\phi_0 - \cos\left[QL\right]\cos^2\phi_0\right) \\ =& -L\left(\frac{1}{a} + \frac{d^2}{2a} - \frac{a}{2}\left[Q - \frac{d}{a}\right]^2\right) + k_S\big(\cos\left[2\phi_0\right]\cos\left[QL\right] - 1\big).\end{aligned} \tag{5.24}$$

Using (5.24), an exact solution for the case when $k_S \to -\infty$ can be examined.

When the surface anisotropy approaches infinite easy-axis anisotropy, the edge spins are fixed. The edge spins will point along the z axis to avoid the energy penalty of having a component along the x direction. (5.24) informs on the requirements such that the anisotropy energy is zero. $\cos(2\phi_0)\cos(QL)$ must equal one for there to be no anisotropy energy. Thus, $\cos(2\phi_0) = \cos(QL) = \pm 1$. From these requirements, the winding angle QL must be

$$QL = \begin{cases} 2n'\pi & \text{for } \phi_0 = 0, \\ (2n'+1)\,\pi & \text{for } \phi_0 = \pi/2. \end{cases} \tag{5.25}$$

Here n' is a non-negative integer. Rearranging (5.25) leads to $Q = n\pi/L$, where n is a non-negative integer. This can be inserted into (5.24) to find the energy for the infinite easy-axis anisotropy case and find the Q which minimizes the energy:

$$\begin{aligned} \frac{\mathcal{H}}{JS^2} = E_n &= -\,L\left(\frac{1}{a} + \frac{d^2}{2a} - \frac{a}{2}\left[\frac{n\pi}{L} - \frac{d}{a}\right]^2\right) + 0 \\ &= -\,L\left(\frac{1}{a} + \frac{d^2}{2a} - \frac{\pi^2 a}{2L^2}\left[n - \frac{dL}{\pi a}\right]^2\right). \end{aligned} \tag{5.26}$$

All of the values in (5.26) are fixed, save for n. As L is the length of the spin chain and a is the lattice parameter, they are always positive numbers, and, as such, the term $\frac{\pi^2 a}{2L}\left(n - \frac{dL}{\pi a}\right)^2$ is always positive. Therefore, choosing n such that the preceding term is as small as possible will minimize the energy of the chain. To do that n should be as close to $\frac{dL}{\pi a}$ as possible. Given that n must be an integer,

$$n_{\min} = \text{Round}\left(\frac{dL}{\pi a}\right), \tag{5.27}$$

where Round(x) is a function which rounds x to the nearest integer. Inserting this into the equation for Q gives

$$Q_{\min} = \frac{n_{\min}\pi}{L} = \frac{\pi}{L}\,\text{Round}\left(\frac{dL}{\pi a}\right). \tag{5.28}$$

The relationship between the length of the spin chain, L, and the number of spins,

N, is $L = (N-1)\,a$. Substituting this into (5.28) provides

$$Q_{\min} = \frac{\pi}{L}\,\mathrm{Round}\left(\frac{dL}{\pi a}\right) = \frac{\pi}{(N-1)\,a}\,\mathrm{Round}\left(\frac{d\,[N-1]}{\pi}\right). \tag{5.29}$$

From this equation it can be seen why there is a jump discontinuity in $Q_{\min}$. Within a half-integer winding number level, the value of $\mathrm{Round}\left(\frac{d\,[N-1]}{\pi}\right)$ is unchanged and therefore $Q_{\min} \sim \frac{1}{N}$. However, when N increases to the extent as to increase $\mathrm{Round}\left(\frac{d\,[N-1]}{\pi}\right)$, then Q suddenly rises in value.

Analyzing the problem of $k_S \to \infty$ (infinite easy-axis surface anisotropy) and looking at (5.24), the energy is minimized when $\cos(2\phi_0)\cos(QL) = -1$. That means that the winding angle is

$$QL = \begin{cases} (2n'+1)\,\pi & \text{for } \phi_0 = 0, \\ 2n'\pi & \text{for } \phi_0 = \pi/2. \end{cases} \tag{5.30}$$

Here again n' is a non-negative integer. The same arguments follow from before, resulting in (5.29) being valid for the infinite easy-axis surface anisotropy case as well.

The cases for when $k_S \to \pm\infty$ provide insight as to what happens for finite k_S. In the easy-axis (easy-plane) case, the edge spins desire to point along (out of) the x axis. Because of the harmonic approximation, neighbouring spins have a consistent relative angle to each other. If k_S is large enough such that the energy of the system will benefit from minimizing, or nearly minimizing, the surface anisotropy component then (5.25) or (5.30) will be near the winding angle with $Q \approx n\pi/L$, with n as a non-negative integer. The minimum Q will, like (5.29), have jumps as the winding angle increases by π when the length of the chain increases sufficiently.

5.2 Edge effect

Informed by the discussion in Section 5.1, the locations of the spins, x_i can be defined by

$$x_i = -\frac{L}{2} + \frac{(i-1)\,L}{N-1} = \frac{-(N-1)\,a + 2\,(i-1)\,a}{2} = \frac{(2i-N-1)\,a}{2}, \tag{5.31}$$

where $i = 1, 2, \ldots, N$. The chain has length L and has evenly spaced spins along $-L/2 \leq x \leq L/2$. The angle, ϕ_i, of each spin is then

$$\phi_i = \phi_0 + Qx_i. \tag{5.32}$$

If we analyze the difference between two adjacent spins, we get

$$\begin{aligned}\phi_{i+1} - \phi_i &= \phi_0 + Qx_{i+1} - \phi_0 - Qx_i \\ &= Q\left(x_{i+1} - x_i\right) \\ &= Qa\left(\frac{2\left[i+1\right] - N - 1 - 2i + N + 1}{2}\right) \\ &= Qa.\end{aligned} \tag{5.33}$$

Using (5.24) and (5.33), (5.19) can be rewritten as

$$\begin{aligned}\frac{\mathcal{H}}{JS^2} &= -\sqrt{1+d^2}\sum_{i=1}^{N-1}\cos\left(\phi_{i+1} - \phi_i + \tilde{d}\right) - k_S\left(\sin^2\phi_1 + \sin^2\phi_N\right) \\ &= -\sqrt{1+d^2}\sum_{i=1}^{N-1}\cos\left(Qa + \tilde{d}\right) + k_S\big(\cos\left[2\phi_0\right]\cos\left[QL\right] - 1\big) \\ &= -\sqrt{1+d^2}\sum_{i=1}^{N-1}\cos\left(Qa + \tilde{d}\right) + k_S\big(\cos\left[2\phi_0\right]\cos\left[Qa\left\{N-1\right\}\right] - 1\big).\end{aligned} \tag{5.34}$$

This equation was used in *Mathematica* to find the Q and ϕ_0 values which corresponded with lowest energy. (5.29) was also used to plot Q for the $k_S \to \pm\infty$ cases.

The constraints $0 \leq Q < 2d$ and $0 \leq \phi_0 < 2\pi$ were used. The rationale for the constraint on Q was that $Q_{\text{bulk}} = \arctan(d) \approx d$ for small d, and having a Q which was more than double that of the bulk value appeared unrealistic. a was taken to be equal to unity. Most minimizations were done with $d = 2\pi/40 = 0.15708$, but the results appear to be independent of d. Minimizations were performed for $k_S \in [-1.0, 1.0]$ in 0.10 intervals. As illustrated in Figure 5.1, there are quite a few similarities between the plots of different non-zero k_S. As long as there is a non-zero surface anisotropy, the behaviour of Q seems to vary little.

Another aspect of the results of which to take note is that they were, in terms of Q, identical for easy-axis and easy-plane anisotropy of the same magnitude. In Section 5.1, it was seen that in the infinite k_S case Q was unchanged for easy-axis and easy-plane surface anisotropy. The same behaviour materializes for finite k_S. The reason this happens both in the infinite and finite cases can be seen in (5.24). ϕ_0 changes so that $\cos(2\phi_0)$ changes sign to maintain minimum energy, but beyond that, no change is necessary for the (new) system to be at a minimum. This happens between 0 and $\pi/2$ when $|k_S| \to \infty$. The spacing between the spins remains constant, all of the spins merely rotate by some angle when going between easy-axis and easy-plane anisotropy.

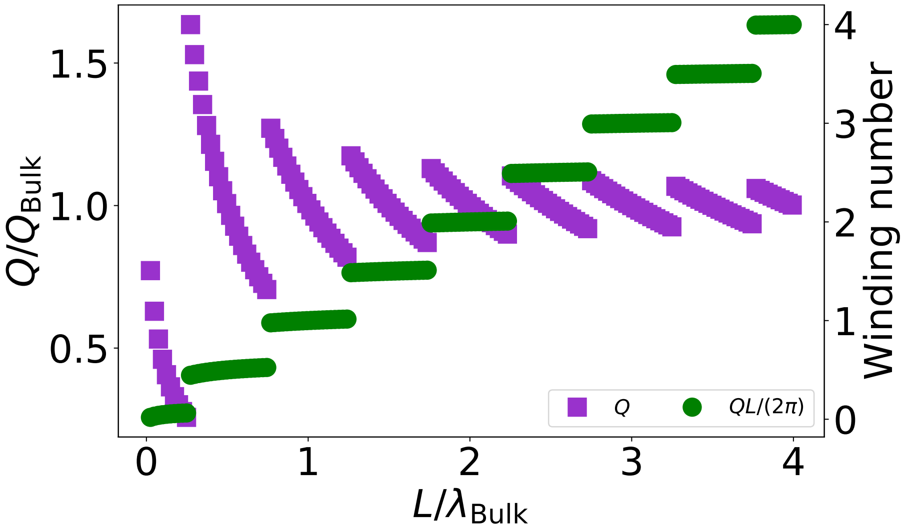

Figure 5.3: Q/Q_{Bulk} and winding number versus spin chain length. $d = 0.15708$ and $k_S = -0.30$. The purple squares are Q/Q_{Bulk} and the green circles represent the winding number.

In Figure 5.3, Q/Q_{bulk} and the winding number are plotted against the spin chain length for $k_S = -0.30$. For smaller chains, there is significant variability in Q, with it varying between $\sim 0.7Q_{\text{bulk}}$ and $\sim 1.6Q_{\text{bulk}}$ in the second segment of spin chain sizes. Also, the winding numbers do exhibit some variance for the first few winding number levels. The levels flatten at larger spin chain lengths.

Figure 5.4 shows how the spins on the spin chain progress as N is increased. In the figure, the chain for $k_S = -0.30$ is shown. Here it should be noted that λ_{bulk} is

$$\lambda_{\text{bulk}} = \frac{2\pi}{Q_{\text{bulk}}} = \frac{2\pi a}{\arctan(d)}. \tag{5.35}$$

For $L = 0.17\lambda_{\text{bulk}}\,(N = 8)$, the chain is of length less than $\lambda_{\text{bulk}}/4$. By Figure 5.3, that means the spin chain is in the zero winding number level. Figure 5.4a shows that this is indeed the case. In Figure 5.4b the chain is now longer than $\lambda_{\text{bulk}}/4$ and, as such, the chain is in the one-half winding number level. The increased angle between the spins can be noted compared to Figure 5.4a. Figures 5.4c and 5.4d show similar progression with the $L = 0.97\lambda_{\text{bulk}}$ $(N = 40)$ chain being in the one winding number level and $L = 1.47\lambda_{\text{bulk}}$ $(N = 60)$ chain being in the three-halves level. Additonal spin chain optimization results can be found in Appendix A.

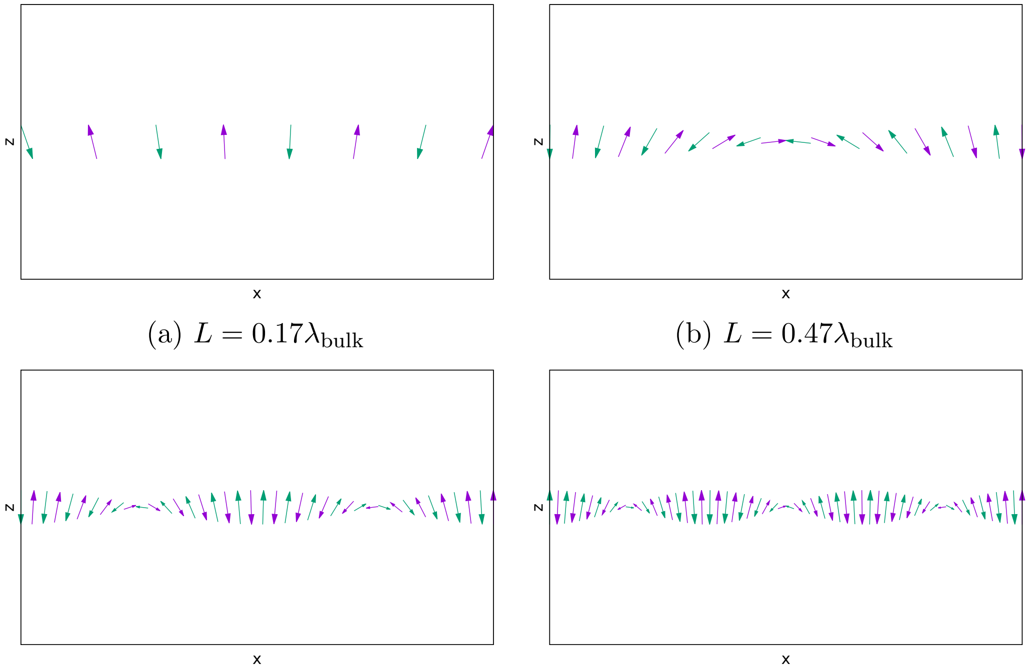

(a) $L = 0.17\lambda_{\text{bulk}}$

(b) $L = 0.47\lambda_{\text{bulk}}$

(c) $L = 0.97\lambda_{\text{bulk}}$

(d) $L = 1.47\lambda_{\text{bulk}}$

Figure 5.4: Spin chains of various length L with $d = 0.15708$ and $k_S = -0.30$. Spins of the same colour belong to the same sublattice. All spins of unit length.

Figures 5.1 and 5.3 illustrate how anisotropy at the surface greatly affects the spin ordering of the chain. Q changes substantially with changing spin chain length when there is anisotropy at the edges of the chain. We refer to this phenomenon as the *edge effect* [141]. The system's desire for QL/π to be an integer whenever there is surface anisotropy drives the effect.

The variability in Q for nanoparticles of different sizes will affect experimental probes into Q. Raman spectroscopy [111] and terahertz spectroscopy [144] can directly measure Q. These measurements are done on collections of nanoparticles with some variance in size. That variance in size means that there is also a variance in Q. The resultant spectroscopic images will suffer from inhomogeneous broadening of peaks due to the variance in Q.

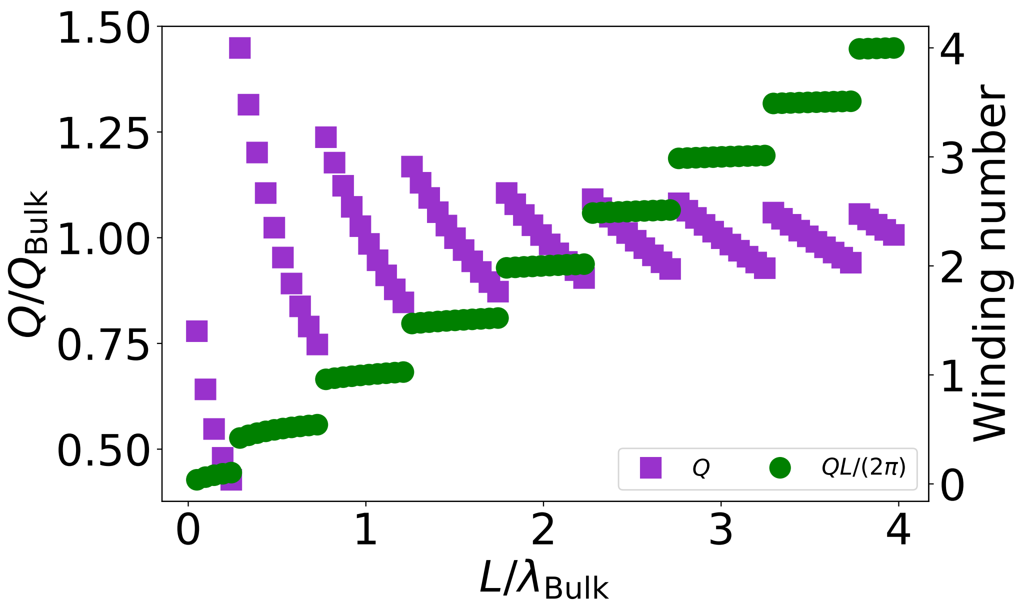

Figure 5.5: Q/Q_{Bulk} and winding number versus spin chain length. $d = 0.31416$ and $k_S = -0.30$. The purple squares are Q/Q_{Bulk} and the green circles represent the winding number.

Figures 5.5 and 5.6 show the spin chain plot of cycloidal wavevector versus chain length for other values of d. Figure 5.5 shows the results for $d = 0.31415$ and $k_S = -0.30$ and Figure 5.6 shows a plot with $d = 0.04724$ and $k_S = -0.30$. These figures show that the locations of the jump discontinuities were independent of d. Figure 5.1 showed that the locations of the jump discontinuities were independent of k_S. Appendix A shows the consistency of results between different values of d and k_S in greater detail.

5.3 Bistability

Another feature of the spin chain with surface anisotropy is the bistability present at the jump discontinuities. There are two Q values at these locations which have the same minimum energy. This is shown in Figure 5.7. The figure plots energy versus Qa at $L = L_0 = \lambda_{\mathrm{bulk}}/4$, the first jump discontinuity. At both $Qa \approx 0.08$ and $Qa \approx 0.23$, the energy is at a minimum.

The presence of the bistability raises the question if there might be some functionality that comes with it. Could the chain, via some impetus, switch between

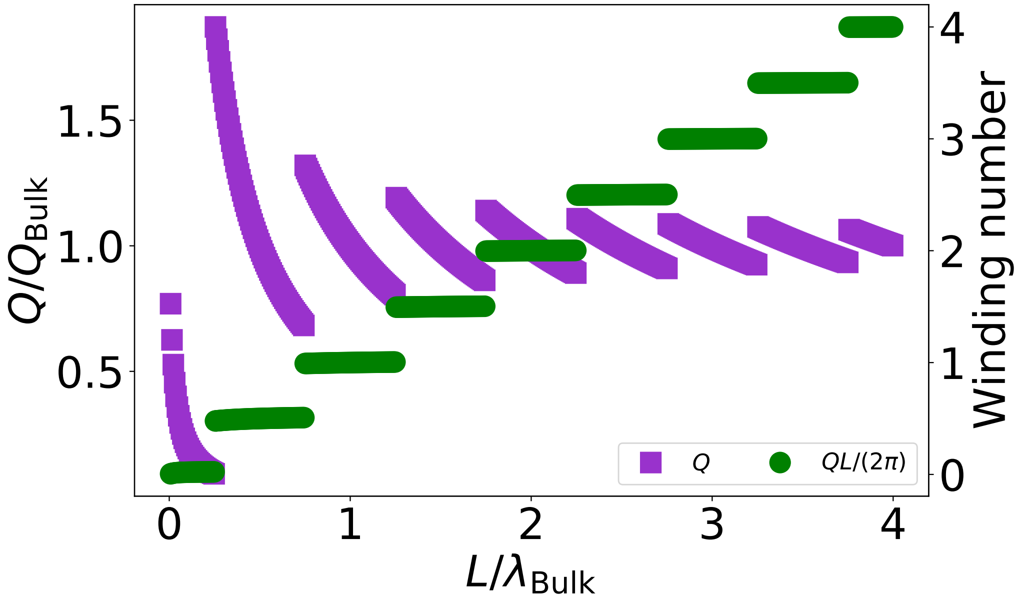

Figure 5.6: Q/Q_{Bulk} and winding number versus spin chain length. $d = 0.04724$ and $k_S = -0.30$. The purple squares are Q/Q_{Bulk} and the green circles represent the winding number.

degenerate ground states and, thus, be used as a memory bit? Chapters 6 and 8 delve a bit into this question.

Figure 5.8 plots energy against Qa for various spin chain lengths where jump discontinuities in Q occur. It is seen that as the length of the chain increases there remains two Qa values with equal energy that are of both minima. There are also more ripples in the energy and more metastable states near the minima.

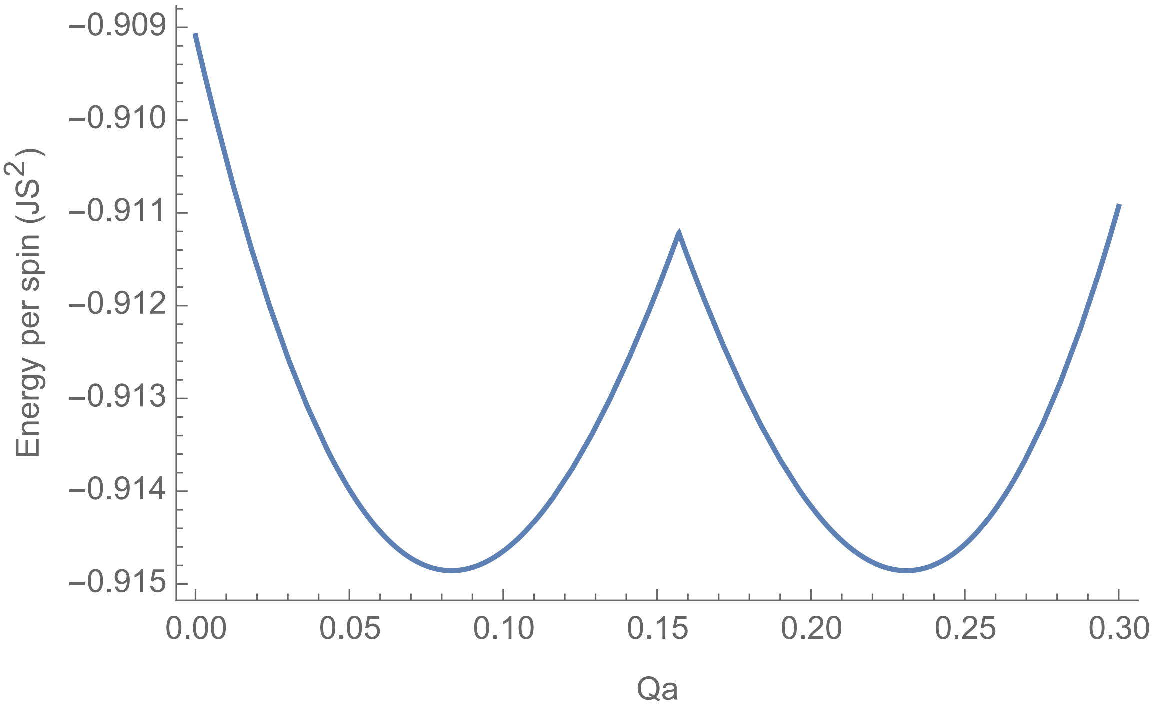

Figure 5.7: Energy per spin versus Qa. $d = 0.15708$, $k_S = 0.10$. The energy at $Qa = 0.08$ and $Qa \approx 0.23$ are equal and minimal.

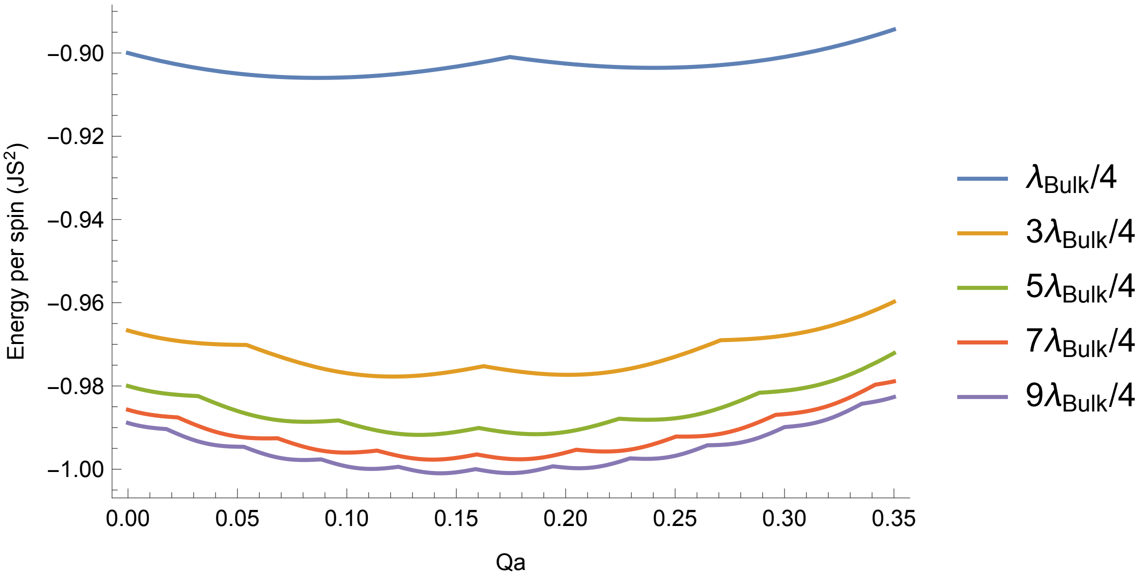

Figure 5.8: Energy versus Qa at various nanoparticle sizes at jump discontinuities in Q. $d = 0.15708$ and $k_S = 0.10$.

Chapter 6

Spin Plaquette

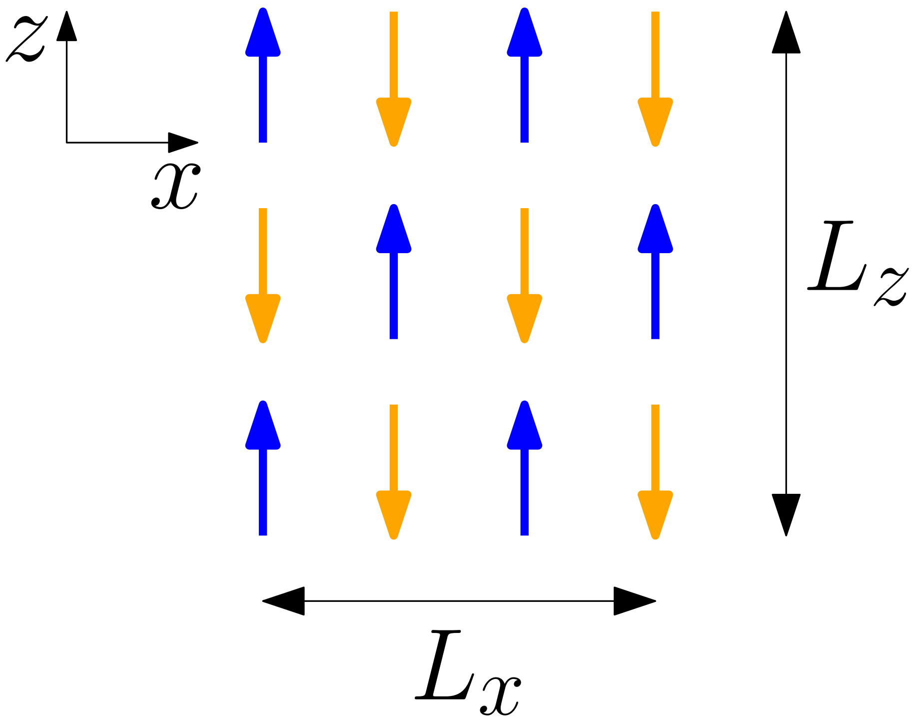

Figure 6.1: Geometry of the investigated spin plaquette. The plaquette is in the xz plane with a size of $L_x \times L_z$, with L_x being the side length in the x direction and L_z being the side length in the z direction. In the figure, the number of spins in the x direction N_x is three and the number of spins in the z direction N_z is four. The blue spins represent spins belonging to one sublattice and the orange spins belonging to the other.

After the research into one-dimensional spin chains was conducted, investigations into two-dimensional spin plaquettes were performed. The motivation being to see what attributes of spin systems found in one dimension were also present in two, and if there were any new features that arose.

For the spin plaquette, spins were in the xz plane with the polarization along the z direction and the cycloid propagation direction along x. With this configuration there are, effectively, spin chains spanning the x direction, stacked on top of each other in the z direction. See Figure 6.1 for the geometry of the problem that was investigated. The size of the plaquette is $L_x \times L_z$, where L_x and L_z are the side lengths in the x and z directions respectively. N_x is the number of spins along the x direction and N_z is the number of spins in the z direction. In the figure, $N_x = 3$ and $N_z = 4$.

The nearest-neighbour spins in the z direction will not experience the Dzyaloshinskii-Moriya interaction because their linking vectors are parallel to the polarization direction. Below we display the full two-dimensional Hamiltonian used to model the spin plaquette:

$$
\begin{aligned}
\mathcal{H} =& J\left(\sum_{i=1}^{N_x-1}\sum_{j=1}^{N_y}\mathbf{S}_{i,j}\cdot\mathbf{S}_{i+1,j}+\sum_{i=1}^{N_x}\sum_{j=1}^{N_y-1}\mathbf{S}_{i,j}\cdot\mathbf{S}_{i,j+1}\right)\\
&+D\Bigg([\hat{\mathbf{z}}\times\hat{\mathbf{x}}]\cdot\sum_{i=1}^{N_x-1}\sum_{j=1}^{N_y}[\mathbf{S}_{i,j}\times\mathbf{S}_{i+1,j}]\\
&+[\hat{\mathbf{z}}\times\hat{\mathbf{z}}]\cdot\sum_{i=1}^{N_x}\sum_{j=1}^{N_y-1}[\mathbf{S}_{i,j}\times\mathbf{S}_{i,j+1}]\Bigg)\\
&-K_S^x\sum_{j=1}^{N_z}\left([\mathbf{S}_{1,j}\cdot\hat{\mathbf{x}}]^2+[\mathbf{S}_{N_x,j}\cdot\hat{\mathbf{x}}]^2\right)\\
&-K_S^z\sum_{i=1}^{N_x}\left([\mathbf{S}_{i,1}\cdot\hat{\mathbf{z}}]^2+[\mathbf{S}_{i,N_z}\cdot\hat{\mathbf{z}}]^2\right)\\
=& J\left(\sum_{i=1}^{N_x-1}\sum_{j=1}^{N_y}\mathbf{S}_{i,j}\cdot\mathbf{S}_{i+1,j}+\sum_{i=1}^{N_x}\sum_{j=1}^{N_y-1}\mathbf{S}_{i,j}\cdot\mathbf{S}_{i,j+1}\right)\\
&+D\sum_{i=1}^{N_x-1}\sum_{j=1}^{N_y}\left(\mathbf{S}_{i,j}\times\mathbf{S}_{i+1,j}\right)_y\\
&-K_S^x\sum_{j=1}^{N_z}\left([\mathbf{S}_{1,j}\cdot\hat{\mathbf{x}}]^2+[\mathbf{S}_{N_x,j}\cdot\hat{\mathbf{x}}]^2\right)
\end{aligned}
$$

$$- K_S^z \sum_{i=1}^{N_x} \left([\mathbf{S}_{i,1} \cdot \hat{\mathbf{z}}]^2 + [\mathbf{S}_{i,N_z} \cdot \hat{\mathbf{z}}]^2 \right) . \tag{6.1}$$

Here N_x and N_z are again the number of spins along the x and z dimension respectively, making for a plaquette of $N_x \times N_z$ spins in total. i is the x index for the spins and j is the z index. For the exchange terms, the first is for spins connected in the x direction and the second for spins linked in the z direction. There are two Dzyaloshinksii-Moriya interaction terms, again one for spins linked in the x direction and one for spins in the z direction. The second of these, the one for spins linked in the z direction, is exactly equal to zero as the polarization direction is parallel to the linkage direction. Thus, there is only a Dzyaloshiskii-Moriya interaction along x. As a result, x is the direction of cycloid propagation.

There are now two surface anisotropy interactions for the plaquette. The K_S^x interaction is the ancestor of the surface anisotropy seen in the spin chain. It acts along the x edges ($x = -L_x/2$ and $x = L_x/2$) or the "sides." Now in two dimensions, all spins on the x surfaces, regardless of row, experience surface anisotropy.

The K_S^z surface anisotropy interaction acts along the z edges, $z = -L_z/2$ and $z = L_z/2$, or the "top" and "bottom" of the plaquette. Again, there is surface anisotropy on all spins on the top and bottom of the nanoparticle.

In most cases considered, $K_S^x = K_S^z$. For an actual nanoparticle, this, of course, would not be the case with the asymmetry of the nanoparticle, surface roughness, missing spins, and the like affecting different surfaces in differing manners.

In all cases considered, the surface anisotropy in the model was equal between opposing ends. This is also not what happens in a real nanoparticle, for the reasons mentioned above. However, there were many qualities to explore for nanoparticles with symmetric ends.

In two dimensions, the spin operator becomes

$$\frac{\mathbf{S}_{i,j}}{S} = \mathbf{s}_{i,j} = (-1)^{i+j} \left(\sin \phi_{i,j} \, \hat{\mathbf{x}} + \cos \phi_{i,j} \, \hat{\mathbf{z}} \right) . \tag{6.2}$$

Spins were again taken to lie in the xz plane, as there is no energy gain from the spins having a component in the y direction. $\phi_{i,j}$ is the angle of the spin at (i, j). Inserting

(6.2) into (6.1) results in

$$\begin{aligned}
\frac{\mathcal{H}}{JS^2} &= -\sum_{i=1}^{N_x-1}\sum_{j=1}^{N_y}\Big(\left[\sin\phi_{i,j}\,\hat{\mathbf{x}}+\cos\phi_{i,j}\,\hat{\mathbf{z}}\right]\cdot\left[\sin\phi_{i+1,j}\,\hat{\mathbf{x}}+\cos\phi_{i+1,j}\,\hat{\mathbf{z}}\right]\Big) \\
&\quad -\sum_{i=1}^{N_x}\sum_{j=1}^{N_y-1}\Big(\left[\sin\phi_{i,j}\,\hat{\mathbf{x}}+\cos\phi_{i,j}\,\hat{\mathbf{z}}\right]\cdot\left[\sin\phi_{i,j+1}\,\hat{\mathbf{x}}+\cos\phi_{i,j+1}\,\hat{\mathbf{z}}\right]\Big) \\
&\quad -d\sum_{i=1}^{N_x-1}\sum_{j=1}^{N_y}\Big(\left[\sin\phi_{i,j}\,\hat{\mathbf{x}}+\cos\phi_{i,j}\,\hat{\mathbf{z}}\right]\times\left[\sin\phi_{i+1,j}\,\hat{\mathbf{x}}+\cos\phi_{i+1,j}\,\hat{\mathbf{z}}\right]\Big)_y \\
&\quad -k_S^x\sum_{j=1}^{N_z}\Big(\left[\left\{\sin\phi_{1,j}\,\hat{\mathbf{x}}+\cos\phi_{1,j}\,\hat{\mathbf{z}}\right\}\cdot\hat{\mathbf{x}}\right]^2+\left[\left\{\sin\phi_{N_x,j}\,\hat{\mathbf{x}}+\cos\phi_{N_x,j}\,\hat{\mathbf{z}}\right\}\cdot\hat{\mathbf{x}}\right]^2\Big) \\
&\quad -k_S^z\sum_{i=1}^{N_x}\Big(\left[\left\{\sin\phi_{i,1}\,\hat{\mathbf{x}}+\cos\phi_{i,1}\,\hat{\mathbf{z}}\right\}\cdot\hat{\mathbf{z}}\right]^2+\left[\left\{\sin\phi_{i,N_z}\,\hat{\mathbf{x}}+\cos\phi_{i,N_z}\,\hat{\mathbf{z}}\right\}\cdot\hat{\mathbf{z}}\right]^2\Big) \\
&= -\sum_{i=1}^{N_x-1}\sum_{j=1}^{N_y}\left(\sin\phi_{i,j}\sin\phi_{i+1,j}+\cos\phi_{i,j}\cos\phi_{i+1,j}\right) \\
&\quad -\sum_{i=1}^{N_x}\sum_{j=1}^{N_y-1}\left(\sin\phi_{i,j}\sin\phi_{i,j+1}+\cos\phi_{i,j}\cos\phi_{i,j+1}\right) \\
&\quad +d\sum_{i=1}^{N_x-1}\sum_{j=1}^{N_y}\left(\sin\phi_{i,j}\cos\phi_{i+1,j}-\cos\phi_{i,j}\sin\phi_{i+1,j}\right) \\
&\quad -k_S^x\sum_{j=1}^{N_z}\left(\sin^2\phi_{1,j}+\sin^2\phi_{N,j}\right)-k_S^z\sum_{i=1}^{N_x}\left(\cos^2\phi_{i,1}+\cos^2\phi_{i,N}\right) \\
&= -\sum_{i=1}^{N_x-1}\sum_{j=1}^{N_y}\cos\left(\phi_{i+1,j}-\phi_{i,j}\right)-\sum_{i=1}^{N_x}\sum_{j=1}^{N_y-1}\cos\left(\phi_{i,j+1}-\phi_{i,j}\right) \\
&\quad -d\sum_{i=1}^{N_x-1}\sum_{j=1}^{N_y}\sin\left(\phi_{i+1,j}-\phi_{i,j}\right)-k_S^x\sum_{j=1}^{N_z}\left(\sin^2\phi_{1,j}+\sin^2\phi_{N_x,j}\right) \\
&\quad -k_S^z\sum_{i=1}^{N_x}\left(\cos^2\phi_{i,1}+\cos^2\phi_{i,N_z}\right). \qquad (6.3)
\end{aligned}$$

In two dimensions $\phi_{i,j}$ is assumed to be

$$\phi_{i,j}=\phi_j+Q_jx_i=\phi_j+\frac{Q_ja\left(2i-N_x-1\right)}{2}, \qquad (6.4)$$

where ϕ_j and Q_j are the phase of the spins and the cycloidal wavevector in the j^{th} row of spins respectively. This is an extension of (5.32) for two dimensions. Here each row is treated as a spin chain with its own Q and phase angle.

In (5.24) we used the identity

$$\sin^2(a-b)+\sin^2(a+b)=1-\cos 2a\cos 2b. \tag{6.5}$$

For the penultimate term in (6.3), we have

$$\begin{aligned}\cos^2(a+b)+\cos^2(c+d)&=\frac{1+\cos\big(2\left[a+b\right]\big)+1+\cos\big(2\left[c+d\right]\big)}{2}\\&=1+\cos(a+b+c+d)\cos(a+b-c-d)\,.\end{aligned} \tag{6.6}$$

This comes from

$$\begin{aligned}&2\cos\left(\frac{a+b}{2}\right)\cos\left(\frac{a-b}{2}\right)\\&=2\left(\cos\left[\frac{a}{2}\right]\cos\left[\frac{b}{2}\right]-\sin\left[\frac{a}{2}\right]\sin\left[\frac{b}{2}\right]\right)\left(\cos\left[\frac{a}{2}\right]\cos\left[\frac{b}{2}\right]+\sin\left[\frac{a}{2}\right]\sin\left[\frac{b}{2}\right]\right)\\&=2\left(\cos^2\left[\frac{a}{2}\right]\cos^2\left[\frac{b}{2}\right]+\cos\left[\frac{a}{2}\right]\cos\left[\frac{b}{2}\right]\sin\left[\frac{a}{2}\right]\sin\left[\frac{b}{2}\right]\right.\\&\quad\left.-\sin\left[\frac{a}{2}\right]\sin\left[\frac{b}{2}\right]\cos\left[\frac{a}{2}\right]\cos\left[\frac{b}{2}\right]-\sin^2\left[\frac{a}{2}\right]\sin^2\left[\frac{b}{2}\right]\right)\\&=2\left(\cos^2\left[\frac{a}{2}\right]\cos^2\left[\frac{b}{2}\right]-\sin^2\left[\frac{a}{2}\right]\sin^2\left[\frac{b}{2}\right]\right)\\&=2\left(\frac{1+\cos a}{2}\frac{1+\cos b}{2}-\frac{1-\cos a}{2}\frac{1-\cos b}{2}\right)\\&=\frac{1+\cos b+\cos a+\cos a\cos b-1+\cos b+\cos a-\cos a\cos b}{2}\\&=\cos a+\cos b.\end{aligned} \tag{6.7}$$

Inserting (6.7) into (6.3) leads to

$$\begin{aligned}\frac{\mathcal{H}}{JS^2}=&-\sum_{i=1}^{N_x-1}\sum_{j=1}^{N_z}\cos\left(Q_ja\right)\\&-\sum_{i=1}^{N_x}\sum_{j=1}^{N_z-1}\cos\left(\phi_{j+1}+\frac{Q_{j+1}a\left[2i-N_x-1\right]}{2}-\phi_j-\frac{Q_ja\left[2i-N_x-1\right]}{2}\right)\end{aligned}$$

$$
\begin{aligned}
&- d \sum_{i=1}^{N_x-1} \sum_{j=1}^{N_z} \sin\left(Q_j a\right) \\
&+ k_S^x \sum_{j=1}^{N_z} \left(\cos\left[2\phi_j\right] \cos\left[Q_j a \left\{N_x - 1\right\}\right] - 1\right) \\
&- k_S^z \sum_{i=1}^{N_x} \left(1 + \cos\left[\phi_1 + \frac{Q_1 a \left\{2i - N_x - 1\right\}}{2} + \phi_N + \frac{Q_N a \left\{2i - N_x - 1\right\}}{2}\right]\right. \\
&\left. \times \cos\left[\phi_1 + \frac{Q_1 a \left\{2i - N_x - 1\right\}}{2} - \phi_N - \frac{Q_N a \left\{2i - N_x - 1\right\}}{2}\right]\right) \\
= &- \sum_{j=1}^{N_z} \left(\left[N_x - 1\right] \sqrt{1 + d^2} \cos\left[Q_j a - \tilde{d}\right]\right. \\
&\left. + k_S^x \left[1 - \cos\left\{2\phi_j\right\} \cos\left\{Q_j a \left(N_x - 1\right)\right\}\right]\right) \\
&- \sum_{i=1}^{N_x} \sum_{j=1}^{N_z-1} \cos\left(\phi_{j+1} - \phi_j + \frac{\left[Q_{j+1} - Q_j\right] a \left[2i - N_x - 1\right]}{2}\right) \\
&- k_S^z \sum_{i=1}^{N_x} \left(1 + \cos\left[\phi_1 + \phi_{N_z} + \frac{\left\{Q_1 + Q_{N_z}\right\} a \left\{2i - N_x - 1\right\}}{2}\right]\right. \\
&\left. \times \cos\left[\phi_1 - \phi_{N_z} + \frac{\left\{Q_1 - Q_{N_z}\right\} a \left\{2i - N_x - 1\right\}}{2}\right]\right). \qquad (6.8)
\end{aligned}
$$

This Hamiltonian was used to evaluate the spin configuration for the minimum energy state as the nanoparticle size and surface anisotropy were varied. The NMinimize function was used in *Mathematica* with the Nelder-Mead algorithm. Multiple results were attained from different, randomly-selected starting points. These were all compared against each other with the ultimate minimum amongst these taken to be the minimum energy value. Those results were then compared to results obtained in *Python* using the L-BFGS-B method from the SciPy optimization library.

The starting points used in that minimization method were $Q_j = d \approx Q_{\text{bulk}}$ and $\phi_j = 0.7\pi$. The intent of using $Q_j = d$ was to start the Q_j's near their bulk values and then allow the algorithm to improve upon the bulk results as necessary. ϕ_j's were initially set to be worth 0.7π due to the observation that the ϕ_j's frequently took values of either $\pi/2$ or π. Setting the ϕ_j's to somewhere near the midpoint was an attempt to not have the system become stuck in a metastable point at either $\pi/2$ or π.

6.1 Electric field due to spin current

The spin-current interaction in one dimension is

$$\mathcal{H}_{SC} = D \sum_{i=1}^{N-1} (\mathbf{P} \times \hat{\mathbf{x}}) \cdot (\mathbf{S}_i \times \mathbf{S}_{i+1}) \,. \tag{6.9}$$

Rewriting this to look like an energy term due to a polarization dotted with an electric field leads to

$$\begin{aligned}\mathcal{H}_{SC} =& D \sum_{i=1}^{N-1} (\mathbf{P} \times \hat{\mathbf{x}}) \cdot (\mathbf{S}_i \times \mathbf{S}_{i+1}) \\ =& D \sum_{i=1}^{N-1} \mathbf{P} \cdot (\hat{\mathbf{x}} \times [\mathbf{S}_i \times \mathbf{S}_{i+1}]) \\ =& \mathbf{P} \cdot \frac{D}{P} \sum_{i=1}^{N-1} (\hat{\mathbf{x}} \times [\mathbf{S}_i \times \mathbf{S}_{i+1}]) \\ =& -a^3 \mathbf{P} \cdot \mathbf{E}_{\text{spin}} ,\end{aligned} \tag{6.10}$$

where

$$\mathbf{E}_{\text{spin}} = -\frac{D}{Pa^3} \sum_{i=1}^{N-1} (\hat{\mathbf{x}} \times [\mathbf{S}_i \times \mathbf{S}_{i+1}]) \,. \tag{6.11}$$

With spins in the xz plane, only the z component in (6.11) will be non-zero. Looking at it,

$$\begin{aligned}E_{\text{spin},z} =& -\frac{D}{Pa^3} \sum_{i=1}^{N-1} (\hat{\mathbf{x}} \times [\mathbf{S}_i \times \mathbf{S}_{i+1}])_z \\ =& -\frac{D}{Pa^3} \sum_{i=1}^{N-1} (\mathbf{S}_i \times \mathbf{S}_{i+1})_y \\ =& \frac{D}{Pa^3} \sum_{i=1}^{N-1} (S_{i,x} S_{i+1,z} - S_{i,z} S_{i+1,x}) \,.\end{aligned} \tag{6.12}$$

Inserting (5.1), (5.31), and (5.32) into (6.12),

$$E_{\text{spin},z} = \frac{DS^2}{Pa^3} \sum_{i=1}^{N-1} \left[(-1)^i \sin\phi_i \, (-1)^{i+1} \cos\phi_{i+1} - (-1)^i \cos\phi_i \, (-1)^{i+1} \sin\phi_{i+1} \right]$$

$$
\begin{aligned}
&= \frac{DS^2}{Pa^3}\sum_{i=1}^{N-1}\left[\cos\phi_i \sin\phi_{i+1} - \sin\phi_i \cos\phi_{i+1}\right] \\
&= \frac{DS^2}{Pa^3}\sum_{i=1}^{N-1}\sin\left(\phi_{i+1} - \phi_i\right) \\
&= \frac{DS^2}{Pa^3}\sum_{i=1}^{N-1}\sin\left(Q\left[x_{i+1} - x_i\right]\right) \\
&= \frac{DS^2}{Pa^3}\sum_{i=1}^{N-1}\sin\left(Qa\right) \\
&= \frac{D\left(N-1\right)S^2}{Pa^3}\sin\left(Qa\right). \qquad (6.13)
\end{aligned}
$$

The electric field in the spin-current interaction is proportional to the size of the system and is dependent on the cycloid wavevector. This means that at points of bistability in Q, the electric field itself is bistable with a discontinuity.

In two dimensions with spins along the x and z directions, the spin-current interaction becomes

$$\mathcal{H}_{SC} = D\sum_{i=1}^{N_x-1}\sum_{j=1}^{N_z}\left(\mathbf{P}\times\hat{\mathbf{x}}\right)\cdot\left(\mathbf{S}_{i,j}\times\mathbf{S}_{i+1,j}\right). \qquad (6.14)$$

The term for spins connected in the z direction was omitted here because the polarization will be taken to be along the z direction, leading to no contribution from this term. Rearranging terms, as before, to get $\mathcal{H}_{SC} = -a^3\mathbf{P}\cdot\mathbf{E}_{\text{spin}}$, leads to

$$\mathbf{E}_{\text{spin}} = -\frac{D}{Pa^3}\sum_{i=1}^{N_x-1}\sum_{j=1}^{N_z}\left(\hat{\mathbf{x}}\times\left[\mathbf{S}_i\times\mathbf{S}_{i+1}\right]\right). \qquad (6.15)$$

Substituting (6.2) and (6.4) into (6.15) and taking the z component (the other two components are zero) leads to

$$E_{\text{spin},z} = \frac{D\left(N_x-1\right)S^2}{Pa^3}\sum_{j=1}^{N_z}\sin\left(Q_j a\right). \qquad (6.16)$$

The field again depends on system size and will have a discontinuity at a point of bistability.

This change in the electric field will change the polarization of the system as well. The change in the polarization will be $\mathbf{P}_{\text{spin}} = \chi\mathbf{E}_{\text{spin}}$, where χ is an electric susceptibility. From this the z component of the $\mathbf{P}_{\text{spin}}$ can be determined:

$$P_{\text{spin},z} = \frac{D\chi\left(N_x - 1\right)S^2}{Pa^3}\sum_{j=1}^{N_z}\sin\left(Q_j a\right). \tag{6.17}$$

Returning to (6.14), if we do not assume that the polarization is along the z direction, then the spin-current interaction term is

$$\mathcal{H}_{SC} = \frac{D}{2}\sum_{i,\hat{\mathbf{v}}}\left(\mathbf{P}\times\hat{\mathbf{v}}\right)\cdot\left(\mathbf{S}_i\times\mathbf{S}_{i+\hat{\mathbf{v}}}\right). \tag{6.18}$$

The summation is now over all sites i with the $1/2$ coefficient to account for the double counting. $\hat{\mathbf{v}} = \pm\,\hat{\mathbf{x}}$ gives (6.14) and $\hat{\mathbf{v}} = \pm\,\hat{\mathbf{y}}$ does not apply as we have assumed that the plaquette lies in the xz plane. $\hat{\mathbf{v}} = \pm\,\hat{\mathbf{z}}$ does provide another term so that

$$\begin{aligned}
\mathcal{H}_{SC} =& D\left(\sum_{i=1}^{N_x-1}\sum_{j=1}^{N_z}\left[\mathbf{P}\times\hat{\mathbf{x}}\right]\cdot\left[\mathbf{S}_{i,j}\times\mathbf{S}_{i+1,j}\right]\right.\\
&\left.+\sum_{i=1}^{N_x}\sum_{j=1}^{N_z-1}\left[\mathbf{P}\times\hat{\mathbf{z}}\right]\cdot\left[\mathbf{S}_{i,j}\times\mathbf{S}_{i,j+1}\right]\right)\\
=& D\,\mathbf{P}\cdot\left(\sum_{i=1}^{N_x-1}\sum_{j=1}^{N_z}\left[\hat{\mathbf{x}}\times\left\{\mathbf{S}_{i,j}\times\mathbf{S}_{i+1,j}\right\}\right]\right.\\
&\left.+\sum_{i=1}^{N_x}\sum_{j=1}^{N_z-1}\left[\hat{\mathbf{z}}\times\left\{\mathbf{S}_{i,j}\times\mathbf{S}_{i,j+1}\right\}\right]\right)\\
=& -a^3\mathbf{P}\cdot\mathbf{E}_{\text{spin}}.
\end{aligned} \tag{6.19}$$

This means that $\mathbf{E}_{\text{spin}}$ is

$$\begin{aligned}
\mathbf{E}_{\text{spin}} =& -\frac{D}{Pa^3}\left(\sum_{i=1}^{N_x-1}\sum_{j=1}^{N_z}\left[\hat{\mathbf{x}}\times\left\{\mathbf{S}_{i,j}\times\mathbf{S}_{i+1,j}\right\}\right]\right.\\
&\left.+\sum_{i=1}^{N_x}\sum_{j=1}^{N_z-1}\left[\hat{\mathbf{z}}\times\left\{\mathbf{S}_{i,j}\times\mathbf{S}_{i,j+1}\right\}\right]\right),
\end{aligned} \tag{6.20}$$

and $\mathbf{P}_{\text{spin}}$ is

$$\begin{aligned}
\mathbf{P}_{\text{spin}} =& -\frac{D\chi}{Pa^3}\left(\sum_{i=1}^{N_x-1}\sum_{j=1}^{N_z}\left[\hat{\mathbf{x}}\times\{\mathbf{S}_{i,j}\times\mathbf{S}_{i+1,j}\}\right]\right.\\
&\left.+\sum_{i=1}^{N_x}\sum_{j=1}^{N_z-1}\left[\hat{\mathbf{z}}\times\{\mathbf{S}_{i,j}\times\mathbf{S}_{i,j+1}\}\right]\right)\\
=& -\frac{D\chi S^2}{Pa^3}\left([1-N_x]\sum_{j=1}^{N_z}\sin\left[Q_j a\right]\hat{\mathbf{z}}\right.\\
&\left.+\sum_{i=1}^{N_x}\sum_{j=1}^{N_z-1}\left[\hat{\mathbf{z}}\times\sin\left\{\phi_{i,j}-\phi_{i,j+1}\right\}\hat{\mathbf{y}}\right]\right)\\
=&\frac{D\chi S^2}{Pa^3}\left([N_x-1]\sum_{j=1}^{N_z}\sin\left[Q_j a\right]\hat{\mathbf{z}}\right.\\
&+\sum_{i=1}^{N_x}\sum_{j=1}^{N_z-1}\sin\left[\phi_j+\frac{Q_j a\left\{2i-N_x-1\right\}}{2}\right.\\
&\left.\left.-\ \phi_{j+1}-\frac{Q_{j+1}a\left\{2i-N-1\right\}}{2}\right]\hat{\mathbf{x}}\right)\\
=&\frac{D\chi S^2}{Pa^3}\left([N_x-1]\sum_{j=1}^{N_z}\sin\left[Q_j a\right]\hat{\mathbf{z}}\right.\\
&\left.-\sum_{i=1}^{N_x}\sum_{j=1}^{N_z-1}\sin\left[\phi_{j+1}-\phi_j+\frac{\left\{Q_{j+1}-Q_j\right\}a\left\{2i-N_x-1\right\}}{2}\right]\hat{\mathbf{x}}\right). \qquad (6.21)
\end{aligned}$$

The magnitude of (6.21) is

$$\begin{aligned}
|\mathbf{P}_{\text{spin}}| =&\frac{D\chi S^2}{Pa^3}\left(\left[\left\{N_x-1\right\}\sum_{j=1}^{N_z}\sin\left\{Q_j a\right\}\right]^2\right.\\
&\left.+\left[\sum_{i=1}^{N_x}\sum_{j=1}^{N_z-1}\sin\left\{\phi_{j+1}-\phi_j+\frac{\left(Q_{j+1}-Q_j\right)a\left(2i-N_x-1\right)}{2}\right\}\right]^2\right)^{1/2}. \qquad (6.22)
\end{aligned}$$

While the x component of (6.21) does not contribute to the spin-current energy when the inherent polarization is along z, it is still present in $\mathbf{P}_{\text{spin}}$.

6.2 Spin-canting-induced magnetization

The second Dzyaloshinskii-Moriya interaction, the one responsible for the weak ferromagnetism in BFO takes the form of

$$\mathcal{H}_{\mathrm{WFM}} = \frac{D'}{2} \sum_{i,\mathbf{v}} (-1)^{\sum_\alpha i_\alpha} \, \hat{\mathbf{P}} \cdot \left(\mathbf{S}_i \times \mathbf{S}_{i+\mathbf{v}} \right), \tag{6.23}$$

where i sums over all lattice sites and $\mathbf{v}$ assumes all nearest-neighbour directions (ie. $\mathbf{v} \in [\pm\hat{\mathbf{x}}, \pm\hat{\mathbf{y}}, \pm\hat{\mathbf{z}}]$). The weak ferromagnetism Dzyaloshinskii-Moriya interaction can be rewritten as

$$\mathcal{H}_{\mathrm{WFM}} = D' \, \hat{\mathbf{P}} \cdot \left(\mathbf{M} \times \mathbf{L} \right), \tag{6.24}$$

where $\mathbf{M}$ is the magnetization vector and $\mathbf{L}$ is the Néel vector [17].

The Néel vector can be written as

$$\mathbf{L} = \frac{1}{\prod\limits_\alpha N_\alpha} \sum_i (-1)^{\sum_\alpha i_\alpha} \, \mathbf{S}_i, \tag{6.25}$$

where N_α is the number of spins in the α direction ($\alpha = x, y, \ldots$) and $(-1)^{\sum_\alpha i_\alpha}$ is either 1 or -1 depending on the spin location. The value of $(-1)^{\sum_\alpha i_\alpha}$ for nearest neighbours is -1. Minimizing the energy in the Hamiltonian leads to

$$\mathbf{M} = \frac{D'}{J} \hat{\mathbf{z}} \times \mathbf{L} = \frac{D'}{J \prod\limits_\alpha N_\alpha} \sum_i (-1)^{\sum_\alpha i_\alpha} \, \hat{\mathbf{z}} \times \mathbf{S}_i. \tag{6.26}$$

It should be emphasized that the energy minimizations were performed with $D' = 0$. Increasing D' from zero leads to a correction of order $(D')^2$ in the energy. The weak magnetization is in turn linear in D' [refer to (6.26)]. When $D'/J \ll 1$ (e.g. for BFO) it makes sense to minimize the energy with $D' = 0$ and calculate the resulting magnetization using (6.26). This is equivalent to including the effect of D' in first-order perturbation theory. Any present magnetization was not due to canting from the Dzyaloshinskii-Moriya interaction, but to size effects and the surface anisotropy. In the bulk case, with $L \gg \lambda_{\mathrm{bulk}}$ the magnetization in the presence of the weak ferromagnetism is zero because the direction of the ferromagnetism changes along the cycloid and is cancelled over a full period. In the smaller systems studied here that cancellation cannot fully occur.

In two dimensions, assuming the spins are in the xz plane, then the magnetization is

$$\begin{aligned}\mathbf{M} =&\frac{D'S}{JN_xN_z}\sum_{i=1}^{N_x}\sum_{j=1}^{N_z}(-1)^{i+j}\,\hat{\mathbf{z}}\times(-1)^{i+j}\left(\sin\left[\phi_j+Q_jx_i\right]\hat{\mathbf{x}}+\cos\left[\phi_j+Q_jx_i\right]\hat{\mathbf{z}}\right)\\ =&\frac{D'S}{JN_xN_z}\sum_{i=1}^{N_x}\sum_{j=1}^{N_z}\sin\left(\phi_j+Q_jx_i\right)\hat{\mathbf{y}}\\ =&\frac{D'S}{JN_xN_z}\sum_{i=1}^{N_x}\sum_{j=1}^{N_z}\sin\left(\phi_j+\frac{Q_ja\left[2i-N_x-1\right]}{2}\right)\hat{\mathbf{y}}.\end{aligned} \tag{6.27}$$

It can be seen from (6.27) that when there is a jump in the Q_j values then there will potentially be a jump in the value of $\mathbf{M}$, as well. These jumps would occur at the points of bistability, just as the jumps in the polarization do. Simultaneous jumps in the polarization and magnetization in multiferroic nanoparticles may be used as a four-state memory, with two possible values of $\mathbf{M}$ and two possible values of $\mathbf{P}$, all degenerate in energy (note that for each stable value of Q there are two states connected by time reversal, S and $-S$). The weak magnetization $\mathbf{M}$ is linear in S, while $\mathbf{P}_{\text{spin}}$ is proportional to S^2. The four states could potentially be electrically written and magnetically read.

6.3 Surface anisotropy on side edges

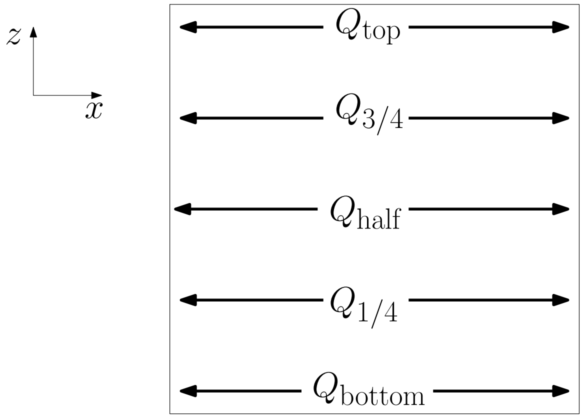

Figure 6.2: Location of various Q's within the plaquette nanoparticle.

Minimizations were done on systems with surface anisotropy along the x edges ($x = -L_x/2$ and $x = L_x/2$) at first to mimic the one dimensional spin problem

($K_S^z = 0$). In addition to the methods mentioned above, the values for Q and ϕ_0 from the corresponding one-dimensional spin chain were assigned to all Q_j and ϕ_j respectively, and this energy was compared to the optimization methods, with the minimal energy state at each nanoparticle size taken to be the global minimum. Figure 6.2 illustrates the location of the different reported Q's in the spin plaquette. Q_{top} and Q_{bottom} refer to the cycloidal wavevectors at $z = L/2$ and $z = -L/2$ respectively. The other Q's are in between these end Q's with $Q_{3/4}$ being near three quarters the way up the plaquette, $Q_{1/2}$ in the middle of the plaquette and $Q_{1/4}$ one quarter of the way up the plaquette. If the rows are indexed one through N, then the special rows are determined as follows:

$$\text{Row}_{\text{top}} = N, \tag{6.28a}$$

$$\text{Row}_{3/4} = N - \text{Round}\left(\frac{N}{4}\right) + 1, \tag{6.28b}$$

$$\text{Row}_{1/2} = \text{Round}\left(\frac{N}{2}\right), \tag{6.28c}$$

$$\text{Row}_{1/4} = \text{Round}\left(\frac{N}{4}\right), \tag{6.28d}$$

$$\text{Row}_{\text{bottom}} = 1. \tag{6.28e}$$

$\text{Round}\,(x)$ is again a function that rounds its argument to the nearest integer. The choice of $\text{Row}_{3/4}$ allows for the row to be equidistant from the surface as $\text{Row}_{1/4}$.

In Figure 6.3 the Q's listed above are plotted against the side length of the plaquette nanoparticle. In the figure, $d = 0.15708$, $k_S^x = -0.30$ and $k_S^z = 0$. As seen in Figure 6.3, the values for all Q's were the same as they were in the spin chain, as was expected, with no additional interactions on the chains, other than exchange. The reason for this can be seen from (6.1). With no Dzyaloshinskii-Moriya interaction and $K_S^z = 0$, the plaquette was effectively a collection of identical (up to the antiferromagnetic exchange) spin chains stacked upon each other. With no top or bottom surface anisotropy, all of the Q's throughout the plaquette were of the same value.

Figure 6.4 looks like Figure 6.3, but instead of $k_S^x = -0.30$, $k_S^x = 0.30$. Figure 6.4 shows the same pattern as Figure A.14, illustrating that the matching Q's between the one-dimensional results and two-dimensional results are independent of k_S^x.

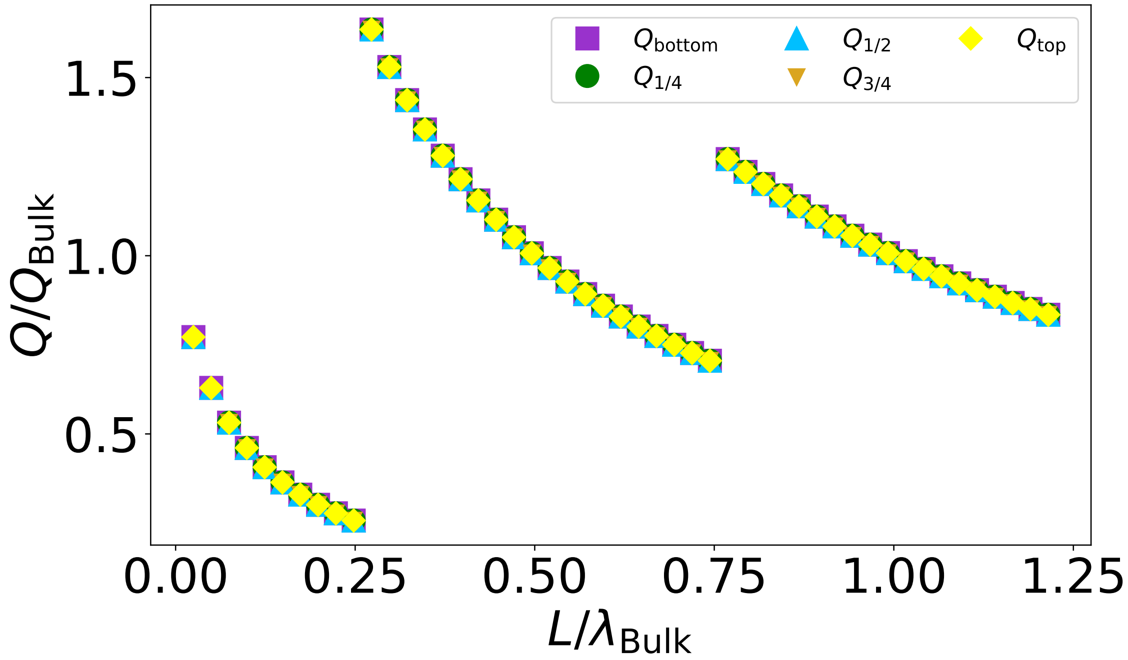

Figure 6.3: Q/Q_{bulk} versus nanoparticle side length L. $d = 0.15708, k_S^x = -0.30, k_S^z = 0$.

6.4 Surface anisotropy on all surfaces

Nanoparticles with equal surface anisotropy, $K_S^x = K_S^z$, on all ends were also analyzed. With there being a non-zero K_S^z term, the symmetry in the z direction present before in Section 6.3 is absent. It would not be expected that all of the Q_j values would be equal any longer as spins in different rows are not equidistant from the top and bottom rows where all spins have surface anisotropy.

In Figure 6.5, a plot of various Q_j values versus nanoparticle side length L is shown. The nanoparticles were square plaquettes of size $L \times L$. Additionally, the spin-canting-induced magnetization of nanoparticle versus nanoparticle length is also shown in units of $D'S/J$. In the figure, the Q's initially rise before dropping off in value. There is a point of bistability at $Q/Q_{\text{bulk}} \approx 0.75$. At the jump discontinuity, not only is Q_j bistable, but consequently, so is $|\mathbf{M}|$. From (6.27) it can be seen why this occurs. The Q_j's have a sudden change in their values at the bistability, which changes all of the $\sin(Q_j)$ values. This leads to the jump in $|\mathbf{M}|$.

The initial rise of the Q's in two dimensions with surface anisotropy suggests that the nanoparticle was trying to immediately move into the one-half winding number

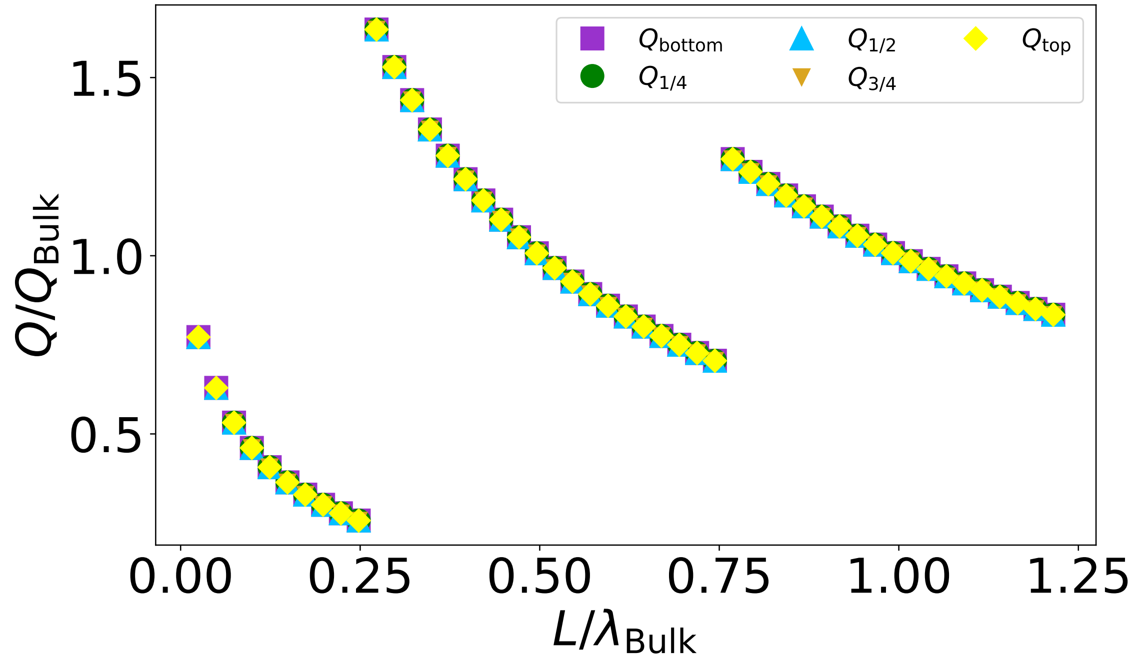

Figure 6.4: $Q/Q_{\rm bulk}$ versus nanoparticle side length L. $d = 0.15708, k_S^x = 0.30, k_S^z = 0$.

level, as opposed to filling the zero winding number as occurred in the one-dimensional spin chain. The difference in two dimensions was the surface anisotropy on the top and bottom surfaces. Top and bottom surfaces compete with the side surfaces to control the spin texture. Ultimately, this discourages the formation of a homogeneous state.

As can be seen in Figure 6.5, different Q_j had different values. Q_j's nearer to the surface of the nanoparticle were lesser than those near the centre. There is evidently an effect from having the surface anisotropy on the top and bottom surfaces. This effect will be referred to as the proximity effect.

The difference in the Q_j's for larger nanoparticles, those to the right of the jump, was less than that for smaller nanoparticles. $Q_{1/2}$ was approximately equal to $Q_{1/4}$ and $Q_{3/4}$ after the jump, indicating that the proximity effect lessens for larger nanoparticles.

Another noteworthy observation from Figure 6.5 is that $Q_{\rm top}$ and $Q_{\rm bottom}$ took the same value at each nanoparticle size, as did $Q_{1/4}$ and $Q_{3/4}$. The symmetric surface anisotropy on the top and bottom surfaces led to symmetry in the cycloidal wavevectors. Wavevectors that were of equal distance from the top or bottom of the plaquette were equal. Figure 6.6 shows the spin configuration for four different sizes.

After the jump discontinuity the Q_j values increase, but $|\mathbf{M}|$ goes to zero. The

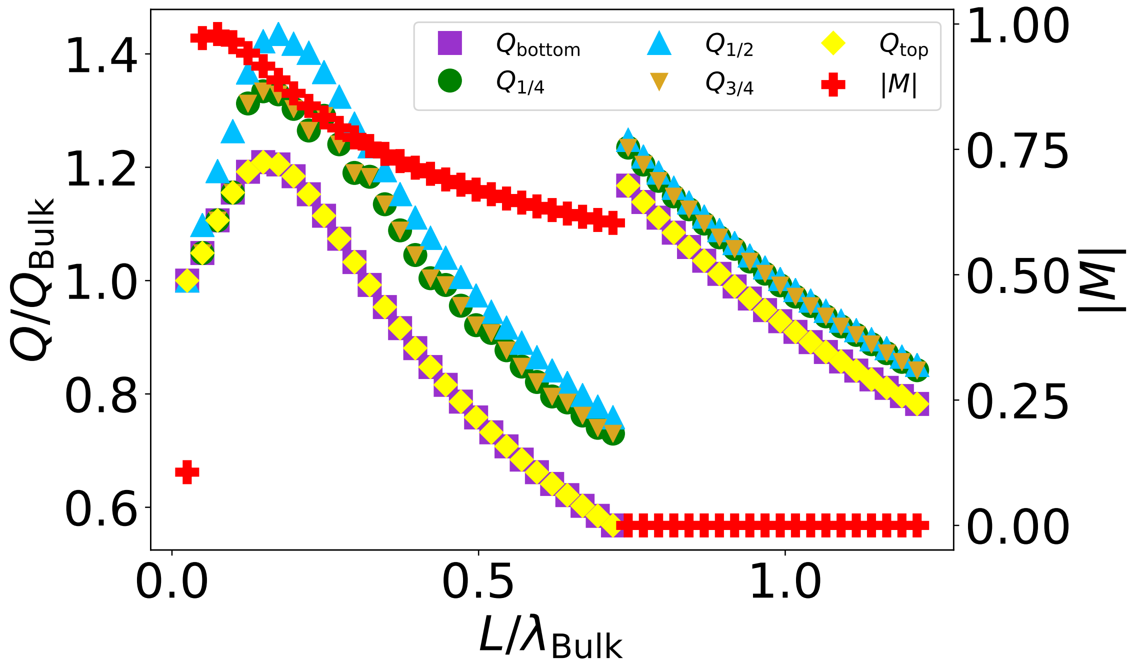

Figure 6.5: Q/Q_{bulk} and spin-canting-induced magnetization versus nanoparticle side length L. $d = 0.15708$, $k_S^x = k_S^z = -0.10$ (easy-plane surface anisotropy). Magnetization is in units of $D'S/J$.

magnetization is proportional to the x component of the Néel vector. In smaller nanoparticles there was not an entire revolution of the cycloid (see Figure 6.6) and $|\mathbf{L} \cdot \hat{\mathbf{x}}| \neq 0$. Here $\mathbf{L}$ is the average Néel vector from (6.25). However, after the jump in the cycloid wavevectors, close to a full revolution of the cycloid can be completed and $|\mathbf{L} \cdot \hat{\mathbf{x}}| \to 0$ and thus $|\mathbf{M}| \to 0$.

At even larger nanoparticle sizes, for instance, when the winding number for the cycloids is 1.5, there may be a non-zero magnetization due to an odd number of sections and a non-zero x component of the Néel vector. This argument holds for any half-integer winding number level, but as the nanoparticle increases in size, the uncompensated segment of the nanoparticle will comprise less of the whole nanoparticle than in smaller ones and $|\mathbf{M}|$ will be less than what it was for smaller nanoparticles.

It should also be noted that the spin-canting-induced magnetization before the jump was proportional to $1/L$. As the plaquette's size grew, the effect of the canting diminished.

That the spin plaquette nanoparticle has a point of bistability is noteworthy. In the spin chain, the bistability point came about because adding or removing a half-

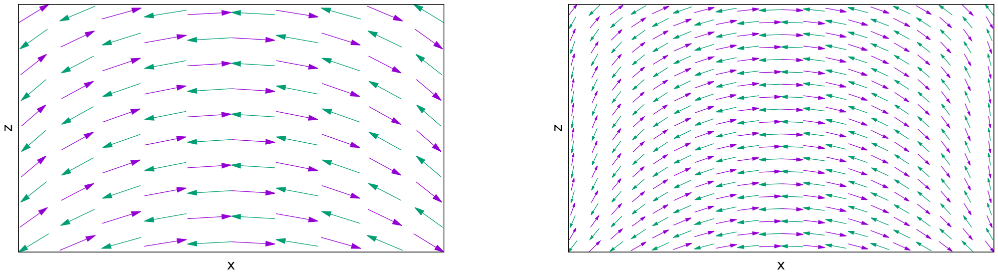

(a) $L = 0.22\lambda_{\text{bulk}}$ (b) $L = 0.47\lambda_{\text{bulk}}$

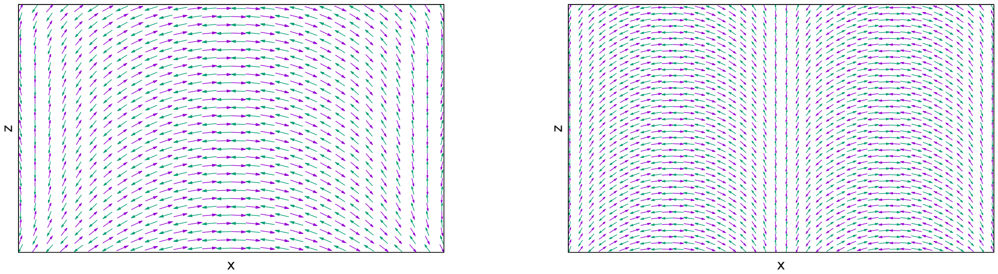

(c) $L = 0.72\lambda_{\text{bulk}}$ (d) $L = 0.97\lambda_{\text{bulk}}$

Figure 6.6: Nanoparticles of different sizes with the same number of spins in each of the two magnetic sublattice (spins purple and green), with $d = 0.15708$ and $k_S^x = k_S^z = -0.10$. Spins of the same colour belong to the same sublattice. The size of the nanoparticles is $L \times L$.

integer winding number became energetically favourable at certain lengths. But with varying Q's throughout the nanoparticle, there is no single length at which there can be a transition to a higher winding number for all Q's. Yet, there is a bistability point, probably related to the average Q in the structure.

Figure 6.7 shows the same information as Figure 6.5, but with $k_S^x = k_z^S = 0.10$ (easy-axis surface anisotropy). The most striking difference between the plots is in the magnetization, which is near zero for all nanoparticle side lengths with $k_S^x = k_S^z = 0.10$. In Figure 6.8, the average Néel vector points along the z direction. As the spin-canting-induced magnetization is a function of the x component of the Néel vector, the magnetization is near zero for the easy-axis surface anisotropy case.

Figure 6.9 shows the cycloidal wavevectors and magnetization versus nanoparticle side length for $d = 0.15708$ and $k_S^x = k_S^z = 0$. This case, like its one-dimensional analogue, resembles the bulk situation. All of the wavevectors throughout the plaquette had the same value, as when there was no top or bottom surface anisotropy. The noisiness of the magnetization versus side length curve occurred due to the freedom in choosing the pinning phase ϕ_j in (6.4). Without anisotropy the phase ϕ_j is arbitrary,

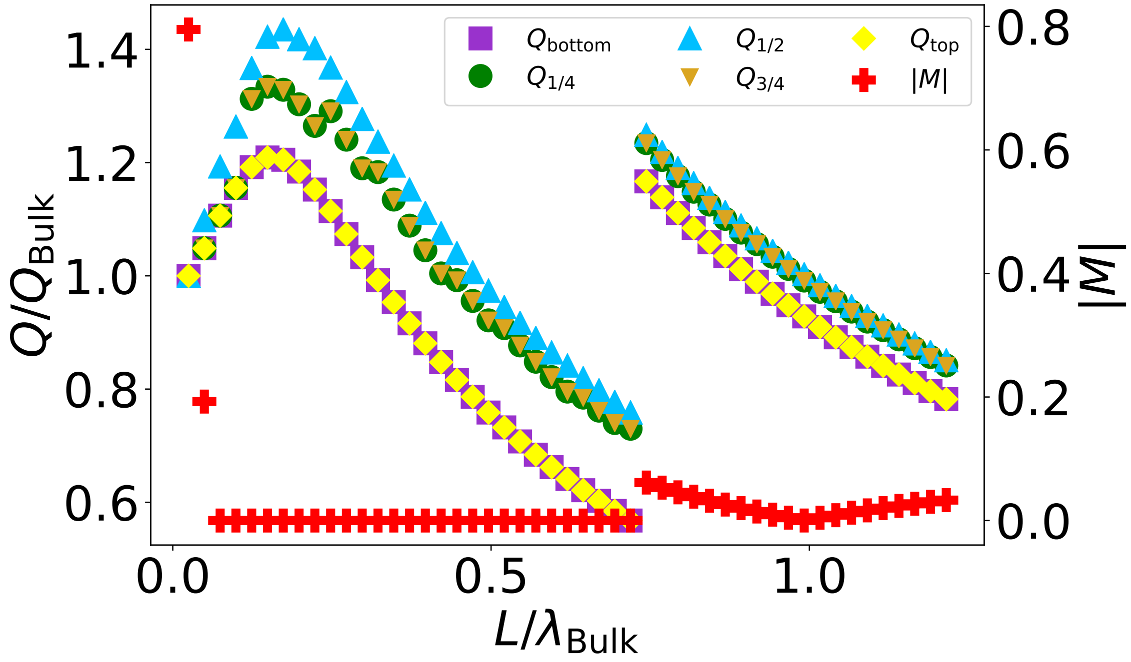

Figure 6.7: Q/Q_{bulk} and spin-canting-induced magnetization versus nanoparticle side length L. $d = 0.15708$, $k_S^x = k_S^z = 0.10$ (easy-axis surface anisotropy). Magnetization is in units of $D'S/J$.

so $\mathbf{M}$ varies in a band of values with $|\mathbf{M}| \lesssim 1/L$.

Without any anisotropy on the sides of the plaquette, the necessity for the spins of the nanoparticle to be symmetric in the x direction was no longer required. This lack of symmetry is seen in Figure 6.10. The winding number versus side length with no surface anisotropy continually increased, with no jumps, as in the spin chain with zero anisotropy.

Other results for the plaquette nanoparticle are displayed in Appendix B. Different values of $k_S^x = k_S^z = k_S$ are displayed there. It should be noted that as $|k_S|$ increased, the location of the jump discontinuity generally increased. As there was no difference seen in the location of the jumps when there was just surface anisotropy on the x ends, we conclude that competition with the surface anisotropy on the top and bottom surfaces is responsible for the varying position of the bistability.

The spin-canting-induced magnetization for all of the easy-axis surface anisotropy cases ($K_S > 0$) was near zero for all sizes of the plaquette nanoparticle, whereas the easy-plane surface anisotropy cases ($K_S < 0$) all had non-zero magnetization at plaquette sizes smaller than the size at which the bistability occurred. Figures 6.6 and

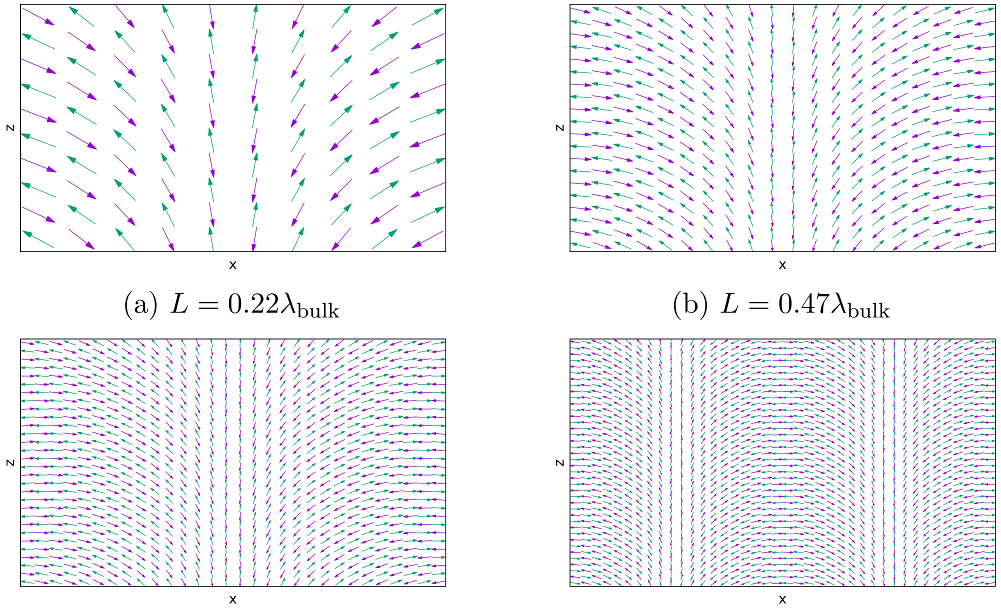

(a) $L = 0.22\lambda_{\text{bulk}}$

(b) $L = 0.47\lambda_{\text{bulk}}$

(c) $L = 0.72\lambda_{\text{bulk}}$

(d) $L = 0.97\lambda_{\text{bulk}}$

Figure 6.8: Nanoparticles of different sizes with $d = 0.15708$ and $k_S^x = k_S^z = 0.10$. Spins of the same colour belong to the same sublattice. The size of the nanoparticles is $L \times L$.

6.8 illustrate why that was so. The spin configurations for plaquettes with easy-plane anisotropy, as in Figure 6.6, had the average Néel vectors pointing along x leading to $\mathbf{M} \propto \hat{z} \times \mathbf{L} \parallel \hat{y}$. In contrast, the easy-axis plaquettes (Figure 6.8) had their average Néel vectors pointing along z, leading to $\mathbf{M} \propto \hat{z} \times \mathbf{L} = 0$. The reason that the spins in the easy-plane plaquettes have a Néel vector component along x is that the system appears to favour minimizing the anisotropy energy for the top and bottom surfaces versus those on the sides. This priority would appear to come from the spin-current Dzyaloshinksii-Moriya interaction not having a component in the z direction. With no component in that direction, the only means by which to minimize the energy of spins on the top and bottom surfaces is to minimize the anisotropy energy. Spins on the sides of the plaquette can have their energy lowered by adjusting Q so that they point parallel to the surface.

6.5 Phase diagrams

With the minimization results generated for the spin plaquettes, phase diagrams showing the magnetically-induced electric polarization and the spin-canting-induced mag-

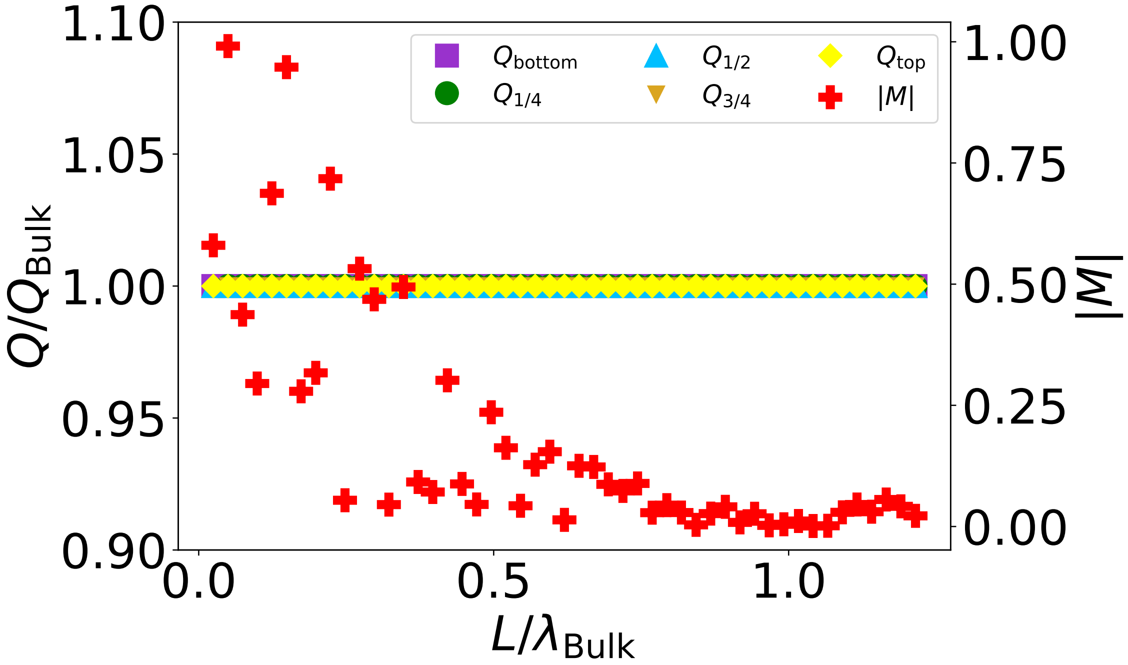

Figure 6.9: Q/Q_{bulk} and spin-canting-induced magnetization versus nanoparticle side length L. $d = 0.15708$, $k_S^x = k_S^z = 0$. Magnetization is in units of $D'S/J$.

netization were created. Figure 6.11 shows the phase diagram for the magnetically-induced polarization $P_{\text{spin},z}$ in units of $D\chi\left(N-1\right)NS^2/\left(Pa^3\right)$. The plaquettes are square, so $N_x = N_z = N$. Specifically, it shows (6.17) for various surface anisotropies and plaquette sizes. The surface anisotropy was equal on all edges of the plaquette, $K_S^x = K_S^z = K_S$. The plaquettes were squares of size $L \times L$. The z component of the spin-induced polarization can be measured as an additional contribution to the inherent polarization $\mathbf{P}$.

Figure 6.11 shows $\sum_{j=1}^{N} \sin\left(Q_j a\right)/N$. From (6.17), this is equal to

$$\frac{1}{N}\sum_{j=1}^{N} \sin\left(Q_j a\right) = \frac{P_{\text{spin},z} P a^3}{D\chi\left(N-1\right)NS^2}. \tag{6.29}$$

Therefore, assuming a small Q, the phase diagram is showing something that is proportional to the average value of Q in the plaquette. The black line in the figure indicates the locations of jump discontinuities. A drastic colour change across this line indicates that the jump discontinuity was not merely in the Q_j's, it was also in

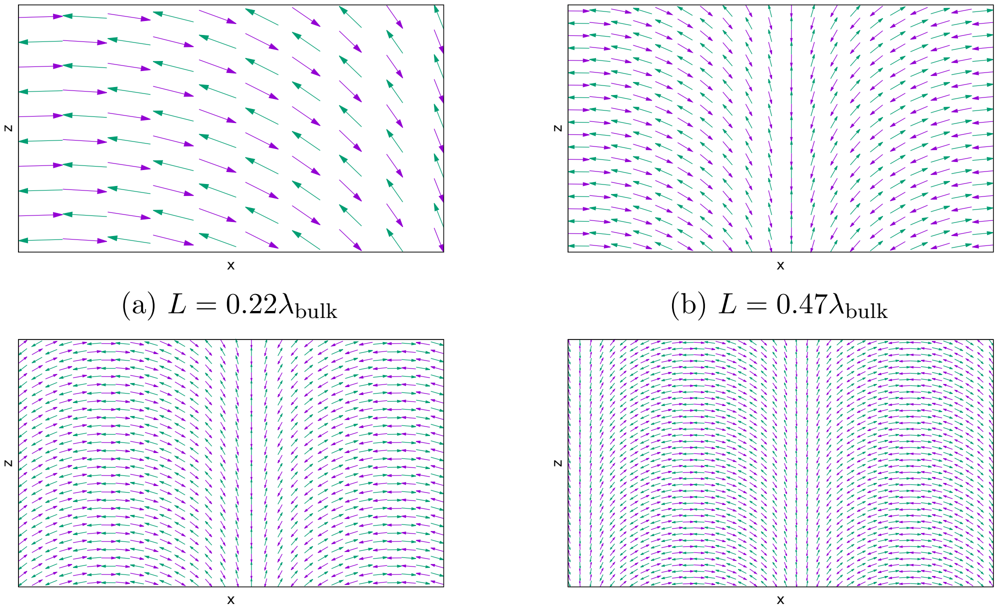

(a) $L = 0.22\lambda_{\text{bulk}}$ (b) $L = 0.47\lambda_{\text{bulk}}$

(c) $L = 0.72\lambda_{\text{bulk}}$ (d) $L = 0.97\lambda_{\text{bulk}}$

Figure 6.10: Nanoparticles of different sizes with $d = 0.15708$ and $k_S^x = k_S^z = 0$. Spins of the same colour belong to the same sublattice. The size of the nanoparticles is $L \times L$.

$P_{\text{spin},z}$. (6.29) shows why that was so: the jumps in the Q_j's change the value of $P_{\text{spin},z}$, resulting in the jump.

A figure was also generated considering the complete electric polarization from the spin-current interaction, not just the z component. The magnitude of the total spin-induced electric polarization is given by (6.22). The figure shows

$$\begin{aligned} &\frac{1}{N^2}\left(\left[\{N-1\}\sum_{j=1}^{N}\sin\{Q_j a\}\right]^2\right. \\ &\left.+\left[\sum_{i=1}^{N}\sum_{j=1}^{N-1}\sin\left\{\phi_{j+1}-\phi_j+\frac{(Q_{j+1}-Q_j)\,a\,(2i-N-1)}{2}\right\}\right]^2\right)^{1/2} \\ &=\frac{|\mathbf{P}_{\text{spin}}|\,Pa^3}{D\chi\,(NS)^2}. \end{aligned} \tag{6.30}$$

Figure 6.12 looks quite similar to Figure 6.11 with a slightly narrower spread of values. This leads to the conclusion that the x component of $\mathbf{P}_{\text{spin}}$ does not contribute much to the polarization's magnitude in comparison with the z component.

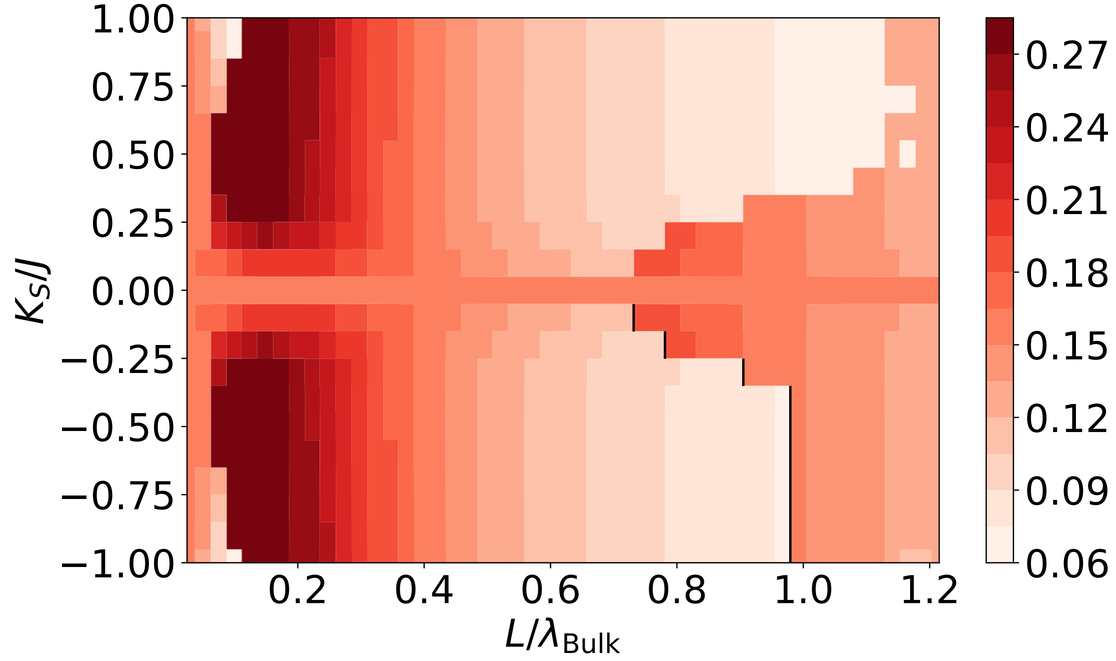

Figure 6.11: Phase diagram of the magnetically-induced electric polarization $P_{\text{spin},z}$ for a plaquette of size $L \times L$ with equal surface anisotropy on all edges ($K_S^x = K_S^z = K_S$). In units of $D\chi\,(N-1)\,NS^2/\left(Pa^3\right)$.

Both Figures 6.11 and 6.12 show a high degree of symmetry about $k_S = 0$ for nanoparticle side lengths less than λ_{bulk}. For $k_S = 0$, there were no jumps in the Q_j's and, consequently, there were no jumps in the spin-induced polarization. In fact, at $k_S = 0$, all of the Q_j's were equal to Q_{bulk}, as seen in Figure 6.9. The lack of change in the Q_j's can be seen in Figure 6.11, where for $k_S = 0$ there is a single band of red for the entire set of side lengths explored. The same single band is not seen in Figure 6.12, since the x component of the spin-induced polarization is dependent on phase angles, which did change for different side lengths at $k_S = 0$. (Note that even with $k_S = 0$ the plaquette has finite size effects, since spins at the surface are interacting with a reduced number of neighbours; hence Q can be slightly different than Q_{bulk}.)

Figure 6.13 shows the spin-canting-induced magnetization phase diagram with the same axes as Figures 6.11 and 6.12. The diagram shows $|\mathbf{M}|$ in units of $D'S/J$. From

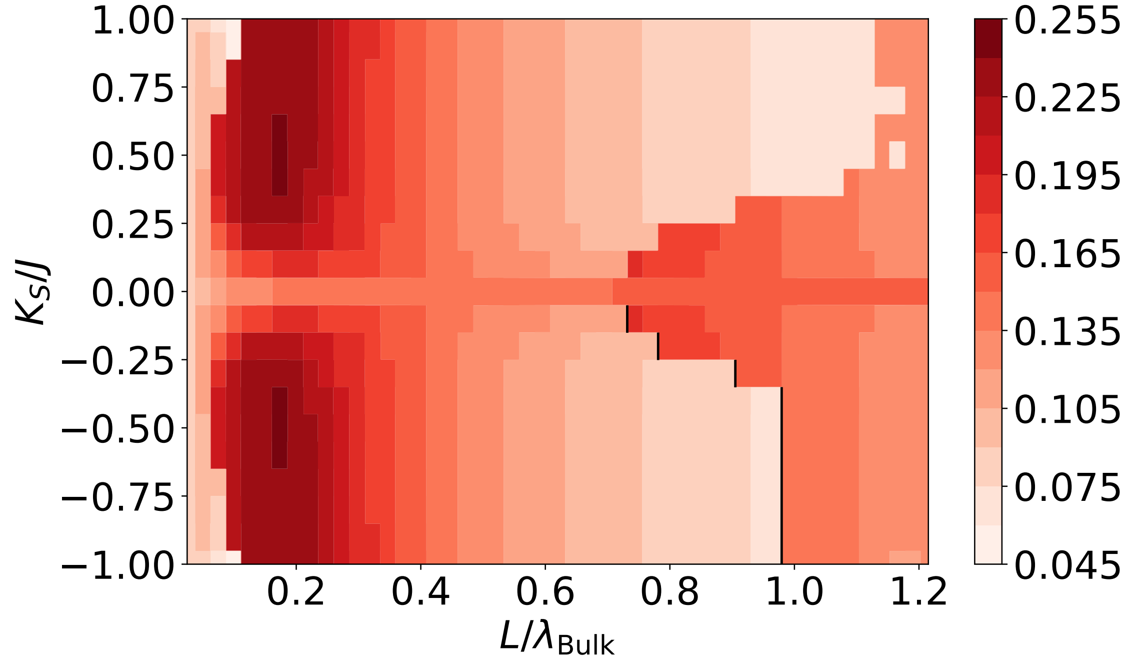

Figure 6.12: Phase diagram of the magnetically-induced electric polarization $|\mathbf{P}_{\text{spin}}|$ for a plaquette of size $L \times L$ with equal surface anisotropy on all edges $(K_S^x = K_S^z = K_S)$. In units of $D\chi\,(NS)^2 / \left(Pa^3\right)$.

(6.27), what is plotted is

$$\frac{1}{N^2}\left|\sum_{i=1}^{N}\sum_{j=1}^{N}\sin\left(\phi_j + \frac{Q_j a\,[2i-N-1]}{2}\right)\right| = \frac{J\,|\mathbf{M}|}{D'S}. \tag{6.31}$$

Like Figures 6.11 and 6.12, the black lines on the phase diagram indicate the locations of jump discontinuities. The jump discontinuities for both the spin-induced electric polarization and spin-canting-induced magnetization occurred at the same nanoparticle sizes and surface anisotropies, indicating that the polarization and magnetization were simultaneously bistable. This raises the prospect that a magnetoelectric memory can be devised from this system. The spin-induced electric polarization could be switched from one state to the other, which would then cause the spin-canting-induced magnetization to switch. That magnetization could then be read.

It is important to note that the bistability only exists for the spin-induced electric polarization, not the inherent electric polarization. An applied electric field meant to switch the bistable spin-induced electric polarization could potentially also switch the inherent polarization. To determine that, one would have to examine the dynamics

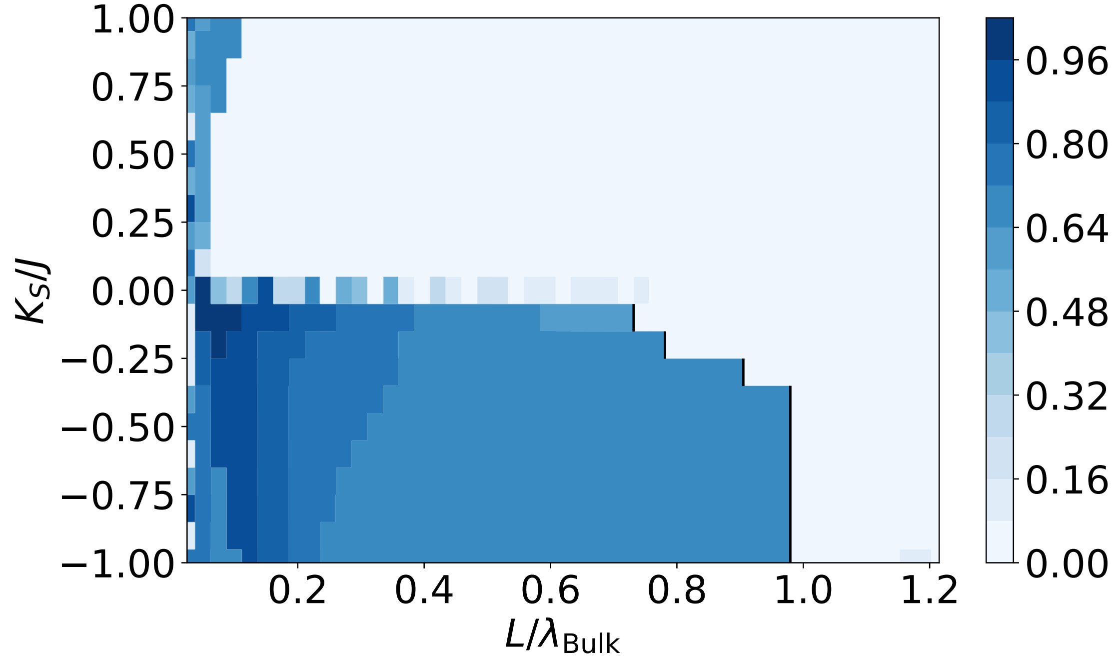

Figure 6.13: Phase diagram of the spin-canting-induced magnetization $|\mathbf{M}|$ for a plaquette of size $L \times L$ with equal surface anisotropy on all edges ($K_S^x = K_S^z = K_S$). In units of $D'S/J$.

of the switching process. The direction and strength of the applied field would factor into whether the inherent polarization was switched.

Unlike the polarization figures, Figure 6.13 does not exhibit symmetry about $k_S = 0$. Section 6.4 explored why that is. The easy-axis surface anisotropy plaquettes did not have spin-canting-induced magnetization because the x component of the Néel vector, responsible for the magnetization, was near zero for those systems.

Chapter 7

Spin Cube

Investigations into three-dimensional nanoparticles were also conducted. Cubic nanoparticles were used in the studies. It should be noted that for easy-axis surface anisotropy on all surfaces, the model of chains along the cubic directions with a single Q breaks down. With spins lowering their energies by having components in all three directions and taking the proximity effect into consideration, the cycloidal wavevector would no longer point in the x direction for a polarization along the z direction. There would be some twisting in the direction of propagation which the model used to date would not be able to replicate. For these reasons, we shall focus our three-dimensional calculations on the case of easy-plane anisotropy.

Maintaining the spins in the xz plane for easy-plane surface anisotropy allows for there to be no surface anisotropy energy from the y faces of the cube. Therefore, a solution with rows of spins with a single Q is admissible for the easy-plane case. Such a solution was explored for the spin cube.

In three dimensions, the Hamiltonian with surface anisotropy on all surfaces becomes

$$\begin{aligned}\mathcal{H} =& J\left(\sum_{i=1}^{N_x-1}\sum_{j=1}^{N_y}\sum_{\ell=1}^{N_z}\mathbf{S}_{i,j,\ell}\cdot\mathbf{S}_{i+1,j,\ell}+\sum_{i=1}^{N_x}\sum_{j=1}^{N_y-1}\sum_{\ell=1}^{N_z}\mathbf{S}_{i,j,\ell}\cdot\mathbf{S}_{i,j+1,\ell}\right.\\ &\left.+\sum_{i=1}^{N_x}\sum_{j=1}^{N_y}\sum_{\ell=1}^{N_z-1}\mathbf{S}_{i,j,\ell}\cdot\mathbf{S}_{i,j,\ell+1}\right)\\ &+D\left(\sum_{i=1}^{N_x-1}\sum_{j=1}^{N_y}\sum_{\ell=1}^{N_z}[\hat{\mathbf{z}}\times\hat{\mathbf{x}}]\cdot[\mathbf{S}_{i,j,\ell}\times\mathbf{S}_{i+1,j,\ell}]\right.\end{aligned}$$

$$\begin{aligned}
&+\sum_{i=1}^{N_x}\sum_{j=1}^{N_y-1}\sum_{\ell=1}^{N_z}[\hat{\mathbf{z}}\times\hat{\mathbf{y}}]\cdot[\mathbf{S}_{i,j,\ell}\times\mathbf{S}_{i,j+1,\ell}] \\
&+\sum_{i=1}^{N_x}\sum_{j=1}^{N_y}\sum_{\ell=1}^{N_z-1}[\hat{\mathbf{z}}\times\hat{\mathbf{z}}]\cdot[\mathbf{S}_{i,j,\ell}\times\mathbf{S}_{i,j,\ell+1}]\Bigg) \\
&-K_S^x\sum_{j=1}^{N_y}\sum_{\ell=1}^{N_z}\left([\mathbf{S}_{1,j,\ell}\cdot\hat{\mathbf{x}}]^2+[\mathbf{S}_{N,j,\ell}\cdot\hat{\mathbf{x}}]^2\right) \\
&-K_S^y\sum_{i=1}^{N_x}\sum_{\ell=1}^{N_z}\left([\mathbf{S}_{i,1,\ell}\cdot\hat{\mathbf{y}}]^2+[\mathbf{S}_{i,N,\ell}\cdot\hat{\mathbf{y}}]^2\right) \\
&-K_S^z\sum_{i=1}^{N_x}\sum_{j=1}^{N_y}\left([\mathbf{S}_{i,j,1}\cdot\hat{\mathbf{z}}]^2+[\mathbf{S}_{i,j,N}\cdot\hat{\mathbf{z}}]^2\right). \qquad (7.1)
\end{aligned}$$

Here $S_{i,j,\ell}$ is a spin at the site (i,j,ℓ). i is the index for the x dimension, j the y dimension index and ℓ is the index for the z dimension. With the spins kept in the xz plane, the spins can be described by

$$\frac{\mathbf{S}_{i,j,\ell}}{S}=(-1)^{i+j+\ell}\,\mathbf{s}_{i,j,\ell}=(-1)^{i+j+\ell}\left(\sin\phi_{i,j,\ell}\,\hat{\mathbf{x}}+\cos\phi_{i,j,\ell}\,\hat{\mathbf{z}}\right). \qquad (7.2)$$

Substituting (7.2) into (7.1) results in

$$\begin{aligned}
\frac{\mathcal{H}}{JS^2}=&-\sum_{i=1}^{N_x-1}\sum_{j=1}^{N_y}\sum_{\ell=1}^{N_z}\left(\sin\phi_{i,j,\ell}\sin\phi_{i+1,j,\ell}+\cos\phi_{i,j,\ell}\cos\phi_{i+1,j,\ell}\right) \\
&-\sum_{i=1}^{N_x}\sum_{j=1}^{N_y-1}\sum_{\ell=1}^{N_z}\left(\sin\phi_{i,j,\ell}\sin\phi_{i,j+1,\ell}+\cos\phi_{i,j,\ell}\cos\phi_{i,j+1,\ell}\right) \\
&-\sum_{i=1}^{N_x}\sum_{j=1}^{N_y}\sum_{\ell=1}^{N_z-1}\left(\sin\phi_{i,j,\ell}\sin\phi_{i,j,\ell+1}+\cos\phi_{i,j,\ell}\cos\phi_{i,j,\ell+1}\right) \\
&+d\sum_{i=1}^{N_x-1}\sum_{j=1}^{N_y}\sum_{\ell=1}^{N_z}\left(\sin\phi_{i,j,\ell}\cos\phi_{i+1,j,\ell}-\cos\phi_{i,j,\ell}\sin\phi_{i+1,j,\ell}\right) \\
&-k_S^x\sum_{j=1}^{N_y}\sum_{\ell=1}^{N_z}\left(\sin^2\phi_{1,j,\ell}+\sin^2\phi_{N_x,j,\ell}\right) \\
&-k_S^z\sum_{i=1}^{N_x}\sum_{j=1}^{N_y}\left(\cos^2\phi_{i,j,1}+\cos^2\phi_{i,j,N_z}\right)
\end{aligned}$$

$$
\begin{aligned}
&= - \sum_{i=1}^{N_x-1} \sum_{j=1}^{N_y} \sum_{\ell=1}^{N_z} \cos\left(\phi_{i+1,j,\ell} - \phi_{i,j,\ell}\right) \\
&- \sum_{i=1}^{N_x} \sum_{j=1}^{N_y-1} \sum_{\ell=1}^{N_z} \cos\left(\phi_{i,j+1,\ell} - \phi_{i,j,\ell}\right) \\
&- \sum_{i=1}^{N_x} \sum_{j=1}^{N_y} \sum_{\ell=1}^{N_z-1} \cos\left(\phi_{i,j,\ell+1} - \phi_{i,j,\ell}\right) \\
&+ d \sum_{i=1}^{N_x-1} \sum_{j=1}^{N_y} \sum_{\ell=1}^{N_z} \sin\left(\phi_{i,j,\ell} - \phi_{i+1,j,\ell}\right) \\
&- k_S^x \sum_{j=1}^{N_y} \sum_{\ell=1}^{N_z} \left(\sin^2 \phi_{1,j,\ell} + \sin^2 \phi_{N_x,j,\ell}\right) \\
&- k_S^z \sum_{i=1}^{N_x} \sum_{j=1}^{N_y} \left(\cos^2 \phi_{i,j,1} + \cos^2 \phi_{i,j,N_z}\right). \qquad (7.3)
\end{aligned}
$$

Due to the direction of the polarization being along the z direction, the Dzyaloshinskii-Moriya interaction for spins along the z axis is zero, as it was in the spin plaquette. In addition, the Dzyaloshinskii-Moriya interaction for spins connected along the y direction ends up being zero due to the spins being in the xz plane. The y faces of the cube end up not contributing to the anisotropy energy of the system, as mentioned above, because there is no y spin component. This ends up being similar to the two-dimensional spin plaquette with additional exchange coupling in the y direction.

The angle $\phi_{i,j,\ell}$ in three dimensions takes the form

$$\phi_{i,j,\ell} = \phi_{j,\ell} + \frac{Q_{j,\ell} a \left(2i - N_x - 1\right)}{2}. \qquad (7.4)$$

With the direction of propagation for the cycloid taken to be along the x direction, each row in the z direction in a certain y layer has its own $Q_{j,\ell}$ and $\phi_{j,\ell}$. Inserting (7.4) into (7.3) leads to

$$
\begin{aligned}
\frac{\mathcal{H}}{JS^2} = &- \sum_{i=1}^{N_x-1} \sum_{j=1}^{N_y} \sum_{\ell=1}^{N_z} \cos\Bigg(\phi_{j,\ell} + \frac{Q_{j,\ell} a \left[2\left\{i+1\right\} - N_x - 1\right]}{2} \\
&-\phi_{j,\ell} - \frac{Q_{j,\ell} a \left[2i - N_x - 1\right]}{2}\Bigg)
\end{aligned}
$$

$$
\begin{aligned}
&-\sum_{i=1}^{N_x}\sum_{j=1}^{N_y-1}\sum_{\ell=1}^{N_z}\cos\left(\phi_{j+1,\ell}+\frac{Q_{j+1,\ell}a\left[2i-N_x-1\right]}{2}\right.\\
&\left.-\phi_{j,\ell}-\frac{Q_{j,\ell}a\left[2i-N_x-1\right]}{2}\right)\\
&-\sum_{i=1}^{N_x}\sum_{j=1}^{N_y}\sum_{\ell=1}^{N_z-1}\cos\left(\phi_{j,\ell+1}+\frac{Q_{j,\ell+1}a\left[2i-N_x-1\right]}{2}\right.\\
&\left.-\phi_{j,\ell}-\frac{Q_{j,\ell}a\left[2i-N_x-1\right]}{2}\right)\\
&+d\sum_{i=1}^{N_x-1}\sum_{j=1}^{N_y}\sum_{\ell=1}^{N_z}\sin\left(\phi_{j,\ell}+\frac{Q_{j,\ell}a\left[2i-N_x-1\right]}{2}\right.\\
&\left.-\phi_{j,\ell}-\frac{Q_{j,\ell}a\left[2\left\{i+1\right\}-N_x-1\right]}{2}\right)\\
&-k_S^x\sum_{j=1}^{N_y}\sum_{\ell=1}^{N_z}\left(\sin^2\left[\phi_{j,\ell}+\frac{Q_{j,\ell}a\left\{2-N_x-1\right\}}{2}\right]\right.\\
&\left.+\sin^2\left[\phi_{j,\ell}+\frac{Q_{j,\ell}a\left\{2N_x-N_x-1\right\}}{2}\right]\right)\\
&-k_S^z\sum_{i=1}^{N_x}\sum_{j=1}^{N_y}\left(\cos^2\left[\phi_{j,1}+\frac{Q_{j,1}a\left\{2i-N_x-1\right\}}{2}\right]\right.\\
&\left.+\cos^2\left[\phi_{j,N_z}+\frac{Q_{j,N_z}a\left\{2i-N_x-1\right\}}{2}\right]\right)\\
=&-\sum_{i=1}^{N_x-1}\sum_{j=1}^{N_y}\sum_{\ell=1}^{N_z}\cos\left(Q_{j,\ell}a\right)\\
&-\sum_{i=1}^{N_x}\sum_{j=1}^{N_y-1}\sum_{\ell=1}^{N_z}\cos\left(\phi_{j+1,\ell}-\phi_{j,\ell}+\frac{\left[Q_{j+1,\ell}-Q_{j,\ell}\right]a\left[2i-N_x-1\right]}{2}\right)\\
&-\sum_{i=1}^{N_x}\sum_{j=1}^{N_y}\sum_{\ell=1}^{N_z-1}\cos\left(\phi_{j,\ell+1}-\phi_{j,\ell}+\frac{\left[Q_{j,\ell+1}-Q_{j,\ell}\right]a\left[2i-N_x-1\right]}{2}\right)\\
&-d\sum_{i=1}^{N_x-1}\sum_{j=1}^{N_y}\sum_{\ell=1}^{N_z}\sin\left(Q_{j,\ell}a\right)\\
&-k_S^x\sum_{j=1}^{N_y}\sum_{\ell=1}^{N_z}\left(\sin^2\left[\phi_{j,\ell}+\frac{Q_{j,\ell}a\left\{1-N_x\right\}}{2}\right]+\sin^2\left[\phi_{j,\ell}+\frac{Q_{j,\ell}a\left\{N_x-1\right\}}{2}\right]\right)
\end{aligned}
$$

$$
\begin{aligned}
&- k_S^z \sum_{i=1}^{N_x} \sum_{j=1}^{N_y} \left(\cos^2 \left[\phi_{j,1} + \frac{Q_{j,1} a \left\{ 2i - N_x - 1 \right\}}{2} \right] \right. \\
&\left. + \cos^2 \left[\phi_{j,N_z} + \frac{Q_{j,N_z} a \left\{ 2i - N_x - 1 \right\}}{2} \right] \right) \\
= &- \sum_{j=1}^{N_y} \sum_{\ell=1}^{N_z} \left(\left[N_x - 1 \right] \sqrt{1 + d^2} \cos \left[Q_{j,\ell} a - \tilde{d} \right] \right. \\
&\left. + k_S^x \left[1 - \cos \left\{ 2 \phi_{j,\ell} \right\} \cos \left\{ Q_{j,\ell} a \left(N_x - 1 \right) \right\} \right] \right) \\
&- \sum_{i=1}^{N_x} \sum_{j=1}^{N_y - 1} \sum_{\ell=1}^{N_z} \cos \left(\phi_{j+1,\ell} - \phi_{j,\ell} + \frac{\left[Q_{j+1,\ell} - Q_{j,\ell} \right] a \left[2i - N_x - 1 \right]}{2} \right) \\
&- \sum_{i=1}^{N_x} \sum_{j=1}^{N_y} \sum_{\ell=1}^{N_z - 1} \cos \left(\phi_{j,\ell+1} - \phi_{j,\ell} + \frac{\left[Q_{j,\ell+1} - Q_{j,\ell} \right] a \left[2i - N_x - 1 \right]}{2} \right) \\
&- k_S^z \sum_{i=1}^{N_x} \sum_{j=1}^{N_y} \left(1 + \cos \left[\phi_{j,1} + \phi_{j,N_z} + \frac{\left\{ Q_{j,1} + Q_{j,N_z} \right\} a \left\{ 2i - N_x - 1 \right\}}{2} \right] \right. \\
&\left. \times \cos \left[\phi_{j,1} - \phi_{j,N_z} + \frac{\left\{ Q_{j,1} - Q_{j,N_z} \right\} a \left\{ 2i - N_x - 1 \right\}}{2} \right] \right) . \qquad (7.5)
\end{aligned}
$$

The last step comes from (6.8), with $\tilde{d} = \arctan(d)$ as before. Whilst the numbers N_x, N_y, and N_z were used here to denote the number of spins along the x, y, and z edges of a spin rectangle, only cubes with $N_x = N_y = N_z = N$ were used in the minimizations for three dimensions.

Scaling to three dimensions proved challenging in terms of computing resources. *Mathematica* was unable to minimize systems with more than twelve spins on a side in a timely fashion. A cube with more than twelve spins per side took beyond a day to do with NMinimize and the Nelder-Mead method. As such, attempts to use *Mathematica* in three dimensions were abandoned.

Python was used exclusively to optimize the Hamiltonian using the L-BFGS-B method. The starting points used in one set of minimizations of $Q_{j,\ell}$ and $\phi_{j,\ell}$ were d and 0.7π respectively, as was done in two dimensions. These minimizations were compared to others done with the starting points of $Q_{j,\ell} = Q_\ell$ and $\phi_{j,\ell} = \phi_\ell$, where Q_ℓ and ϕ_ℓ are the final answers for the two-dimensional plaquette for a given z row, ℓ, and for the same d and k_S. The lowest energy configurations were taken from these minimizations to be the minimum energy spin configurations for the given parameters.

7.1 Polarization due to spins

The polarization induced from the spins that was explored in Section 6.1 also appears in three dimensions. Its form is similar to that in two dimensions. The Dzyaloshinskii-Moriya interaction responsible for the induced polarization takes the form in three dimensions of

$$\begin{aligned}\mathcal{H}_{\text{SC}} =& D\left(\sum_{i=1}^{N_x-1}\sum_{j=1}^{N_y}\sum_{\ell=1}^{N_z}[\mathbf{P}\times\hat{\mathbf{x}}]\cdot[\mathbf{S}_{i,j,\ell}\times\mathbf{S}_{i+1,j,\ell}]\right.\\ &+\sum_{i=1}^{N_x}\sum_{j=1}^{N_y-1}\sum_{\ell=1}^{N_z}[\mathbf{P}\times\hat{\mathbf{y}}]\cdot[\mathbf{S}_{i,j,\ell}\times\mathbf{S}_{i,j+1,\ell}]\\ &\left.+\sum_{i=1}^{N_x}\sum_{j=1}^{N_y}\sum_{\ell=1}^{N_z-1}[\mathbf{P}\times\hat{\mathbf{z}}]\cdot[\mathbf{S}_{i,j,\ell}\times\mathbf{S}_{i,j,\ell+1}]\right)\\ =& D\,\mathbf{P}\cdot\left(\sum_{i=1}^{N_x-1}\sum_{j=1}^{N_y}\sum_{\ell=1}^{N_z}[\hat{\mathbf{x}}\times\{\mathbf{S}_{i,j,\ell}\times\mathbf{S}_{i+1,j,\ell}\}]\right.\\ &+\sum_{i=1}^{N_x}\sum_{j=1}^{N_y-1}\sum_{\ell=1}^{N_z}[\hat{\mathbf{y}}\times\{\mathbf{S}_{i,j,\ell}\times\mathbf{S}_{i,j+1,\ell}\}]\\ &\left.+\sum_{i=1}^{N_x}\sum_{j=1}^{N_y}\sum_{\ell=1}^{N_z-1}[\hat{\mathbf{z}}\times\{\mathbf{S}_{i,j,\ell}\times\mathbf{S}_{i,j,\ell+1}\}]\right)\\ =& -a^3\mathbf{P}\cdot\mathbf{E}_{\text{spin}}. \end{aligned}\tag{7.6}$$

That means that the induced electric polarization $\mathbf{P}_{\text{spin}} = \chi\mathbf{E}_{\text{spin}}$ due to the spins is

$$\begin{aligned}\mathbf{P}_{\text{spin}} =& -\frac{D\chi}{Pa^3}\left(\sum_{i=1}^{N_x-1}\sum_{j=1}^{N_y}\sum_{\ell=1}^{N_z}[\hat{\mathbf{x}}\times\{\mathbf{S}_{i,j,\ell}\times\mathbf{S}_{i+1,j,\ell}\}]\right.\\ &+\sum_{i=1}^{N_x}\sum_{j=1}^{N_y-1}\sum_{\ell=1}^{N_z}[\hat{\mathbf{y}}\times\{\mathbf{S}_{i,j,\ell}\times\mathbf{S}_{i,j+1,\ell}\}]\\ &\left.+\sum_{i=1}^{N_x}\sum_{j=1}^{N_y}\sum_{\ell=1}^{N_z-1}[\hat{\mathbf{z}}\times\{\mathbf{S}_{i,j,\ell}\times\mathbf{S}_{i,j,\ell+1}\}]\right). \end{aligned}\tag{7.7}$$

Inserting (7.2) and (7.4) into (7.7) results in

$$\begin{aligned}
\mathbf{P}_{\text{spin}} =& -\frac{D\chi S^2}{Pa^3}\left(\sum_{i=1}^{N_x-1}\sum_{j=1}^{N_y}\sum_{\ell=1}^{N_z}\left[\hat{\mathbf{x}}\times\left\{\sin\phi_{i,j,\ell}\cos\phi_{i+1,j,\ell}-\cos\phi_{i,j,\ell}\sin\phi_{i+1,j,\ell}\right\}\hat{\mathbf{y}}\right]\right.\\
&+\sum_{i=1}^{N_x}\sum_{j=1}^{N_y-1}\sum_{\ell=1}^{N_z}\left[\hat{\mathbf{y}}\times\left\{\sin\phi_{i,j,\ell}\cos\phi_{i,j+1,\ell}-\cos\phi_{i,j,\ell}\sin\phi_{i,j+1,\ell}\right\}\hat{\mathbf{y}}\right]\\
&\left.+\sum_{i=1}^{N_x}\sum_{j=1}^{N_y}\sum_{\ell=1}^{N_z-1}\left[\hat{\mathbf{z}}\times\left\{\sin\phi_{i,j,\ell}\cos\phi_{i,j,\ell+1}-\cos\phi_{i,j,\ell}\sin\phi_{i,j,\ell+1}\right\}\hat{\mathbf{y}}\right]\right)\\
=& -\frac{D\chi S^2}{Pa^3}\left(\sum_{i=1}^{N_x-1}\sum_{j=1}^{N_y}\sum_{\ell=1}^{N_z}\sin\left[\phi_{i,j,\ell}-\phi_{i+1,j,\ell}\right]\hat{\mathbf{z}}\right.\\
&\left.-\sum_{i=1}^{N_x}\sum_{j=1}^{N_y}\sum_{\ell=1}^{N_z-1}\sin\left[\phi_{i,j,\ell}-\phi_{i,j,\ell+1}\right]\hat{\mathbf{x}}\right)\\
=& -\frac{D\chi S^2}{Pa^3}\left(\sum_{i=1}^{N_x-1}\sum_{j=1}^{N_y}\sum_{\ell=1}^{N_z}\sin\left[\phi_{j,\ell}+\frac{Q_{j,\ell}a\left\{2i-N_x-1\right\}}{2}\right.\right.\\
&\left.-\phi_{j,\ell}-\frac{Q_{j,\ell}a\left\{2\left(i+1\right)-N_x-1\right\}}{2}\right]\hat{\mathbf{z}}\\
&-\sum_{i=1}^{N_x}\sum_{j=1}^{N_y}\sum_{\ell=1}^{N_z-1}\sin\left[\phi_{j,\ell}+\frac{Q_{j,\ell}a\left\{2i-N_x-1\right\}}{2}\right.\\
&\left.\left.-\phi_{j,\ell+1}-\frac{Q_{j,\ell+1}a\left\{2i-N_x-1\right\}}{2}\right]\hat{\mathbf{x}}\right)\\
=&\frac{D\chi S^2}{Pa^3}\left(\left[N_x-1\right]\sum_{j=1}^{N_y}\sum_{\ell=1}^{N_z}\sin\left[Q_{j,\ell}a\right]\hat{\mathbf{z}}\right.\\
&\left.-\sum_{i=1}^{N_x}\sum_{j=1}^{N_y}\sum_{\ell=1}^{N_z-1}\sin\left[\phi_{j,\ell+1}-\phi_{j,\ell}+\frac{\left\{Q_{j,\ell+1}-Q_{j,\ell}\right\}a\left\{2i-N_x-1\right\}}{2}\right]\hat{\mathbf{x}}\right).
\end{aligned}\tag{7.8}$$

The absolute value of the polarization is

$$\left|\mathbf{P}_{\text{spin}}\right| =\frac{D\chi S^2}{Pa^3}\left(\left[\left\{N_x-1\right\}\sum_{j=1}^{N_y}\sum_{\ell=1}^{N_z}\sin\left\{Q_{j,\ell}a\right\}\right]^2\right.$$

$$+\left[\sum_{i=1}^{N_x}\sum_{j=1}^{N_y}\sum_{\ell=1}^{N_z-1}\sin\left\{\phi_{j,\ell+1}-\phi_{j,\ell}+\frac{\left(Q_{j,\ell+1}-Q_{j,\ell}\right)a\left(2i-N_x-1\right)}{2}\right\}\right]^2\Bigg)^{1/2}. \tag{7.9}$$

This is just like (6.22) but with a summation over the spins along the y direction included.

7.2 Magnetization due to spin canting

The magnetization due to the canting of the spins that was tracked in two dimensions was also tracked in three dimensions. Following fron (6.26), in three dimensions, the magnetization takes the form of

$$\begin{aligned}\mathbf{M} =&\frac{D'S}{JN_xN_yN_z}\sum_{i=1}^{N_x}\sum_{j=1}^{N_y}\sum_{\ell=1}^{N_z}\left(-1\right)^{i+j+\ell}\hat{\mathbf{z}}\\ &\times\left(-1\right)^{i+j+\ell}\left(\sin\left[\phi_{j,\ell}+Q_{j,\ell}x_i\right]\hat{\mathbf{x}}+\cos\left[\phi_{j,\ell}+Q_{j,\ell}x_i\right]\hat{\mathbf{z}}\right)\\ =&\frac{D'S}{JN_xN_yN_z}\sum_{i=1}^{N_x}\sum_{j=1}^{N_y}\sum_{\ell=1}^{N_z}\sin\left(\phi_{j,\ell}+Q_{j,\ell}x_i\right)\hat{\mathbf{y}}\\ =&\frac{D'S}{JN_xN_yN_z}\sum_{i=1}^{N_x}\sum_{j=1}^{N_y}\sum_{\ell=1}^{N_z}\sin\left(\phi_{j,\ell}+\frac{Q_{j,\ell}a\left[2i-N_x-1\right]}{2}\right)\hat{\mathbf{y}},\end{aligned} \tag{7.10}$$

which is quite similar to (6.27).

7.3 Optimization results

Minimizations in three dimensions were all done with equal surface anisotropy on all sides: $k_S^x = k_S^y = k_S^z = k_S$. $Q_{j,\ell}$ and $\phi_{j,\ell}$ were optimized. Various $Q_{j,\ell}$'s were plotted, similar to the spin plaquette case (see Figure 7.1). For the cube, the labels refer to multiple $Q_{j,\ell}$'s. Q_{top} refers to Q's at the top of the cube ($z = L/2$) with $\ell = N$. There are N Q_{top}'s for the N different y layers. Q_{bottom} refers to Q's at the bottom of the cube ($z = -L/2$) with $\ell = 1$. Q_u, where u is a fraction, refers to a set of Q's that are u of the way up the cube (for example the $Q_{1/4}$ wavevectors are one quarter of way up the cube). That means that for every Q type (top, bottom, 3/4, etc.) at each L, there were N Q's plotted corresponding to N values of the y-layer index j.

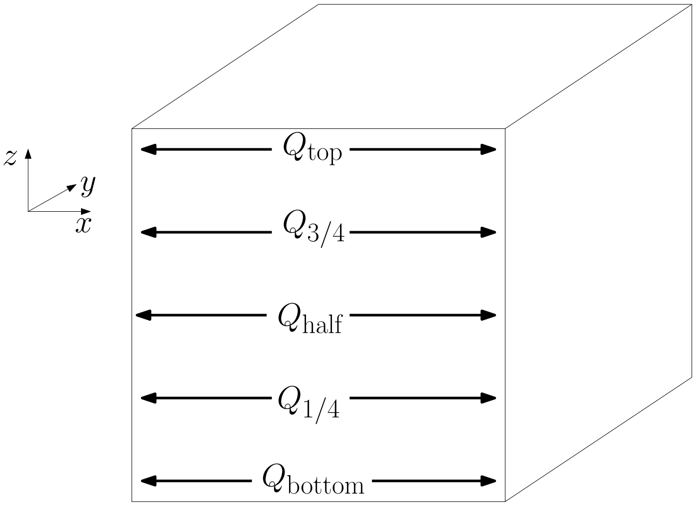

Figure 7.1: Diagram showing the position of the various labelled Q's in the spin cube.

Figure 7.2 shows the results for $k_S = -0.10$ and $d = 0.15708$. It plots Q/Q_{bulk} versus relative side length, L/λ_{bulk}, as well as magnetization versus relative side length. The cubes were sized $L \times L \times L$. The first thing to notice is that all of the Q's of the same type for a given L were equal. There was no change in $Q_{j,\ell}$ for different j's. There was again a jump discontinuity in the plot just as there was in one and two dimensions. Thus, bistability is present in three dimensions. Compared with Figure 6.5, which is the two-dimensional analogue of Figure 7.2, the plots are identical. Each y layer of the spin cube exhibits the same spin texture found on the spin plaquette, with neighbouring y layers antiferromagnetically aligned to each other. There are additional results for three dimensional cubic nanoparticles displayed in Appendix C. They exhibit the same pattern for Q/Q_{bulk} versus relative side length that was seen in $k_S = -0.10$, with the three-dimensional results mirroring the two-dimensional ones. The magnetizations for the two-dimensional and three-dimensional nanoparticles were also identical. With the Q's identical between the two and three dimension systems, by (6.27) and (7.10), this means that the phase angles were also the same for both the plaquettes and the cubes. The conclusion we reached from these studies is that the additional antiferromagnetic interaction between y layers does not compete with surface anisotropy.

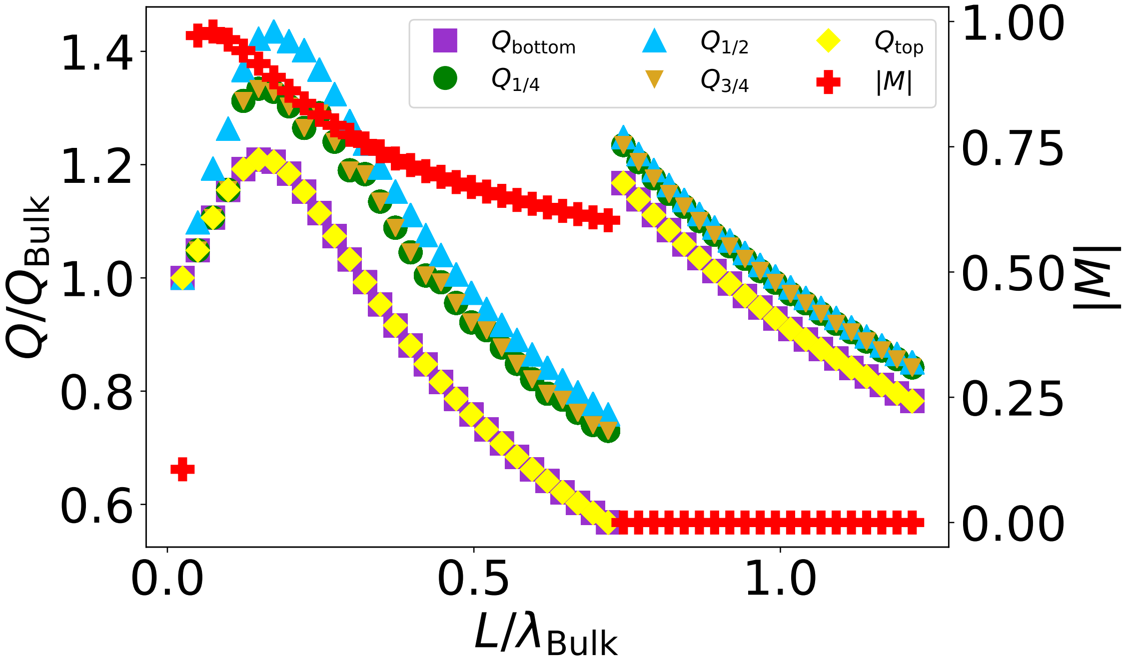

Figure 7.2: Q/Q_{Bulk} versus nanoparticle side length $L/\lambda_{\mathrm{bulk}}$ and magnetization versus nanoparticle side length $L/\lambda_{\mathrm{bulk}}$ for spin cube $(L \times L \times L)$. The magnetization is in units of $D'S/J$. $d = 0.15708$, $k_S = -0.10$.

7.4 Phase diagrams

Phase diagrams were created for the three dimensional results. The induced polarization and magnetization of the systems were studied, as they were in two dimensions.

Figure 7.3 is a phase diagram showing $P_{\mathrm{spin},z}$ at different surface anisotropies and side lengths. The polarization is in units of $D\chi\,(N-1)\,(NS)^2 / \left(Pa^3\right)$. The phase diagram displays $\sum_{j=1}^{N}\sum_{\ell=1}^{N}\sin\left(Q_{j,\ell}a\right)/N^2$. Per (7.8), this is equal to

$$\frac{1}{N^2}\sum_{j=1}^{N}\sum_{\ell=1}^{N}\sin\left(Q_{j,\ell}a\right) = \frac{P_{\mathrm{spin},z}Pa^3}{D\chi\,(N-1)\,(NS)^2}. \tag{7.11}$$

The black lines in the phase diagram describe where the points of bistability are. Comparing Figure 7.3 to the lower half of Figure 6.11, they are identical. Again, the two-dimensional plaquette acts as if it was one layer of the spin cube.

Figure 7.4 shows the phase diagram of the magnitude of the spin-induced electric polarization $|\mathbf{P}_{\mathrm{spin}}|$. This is in units of $D\chi N^3 S^2/\left(Pa^3\right)$. From (7.9), the precise

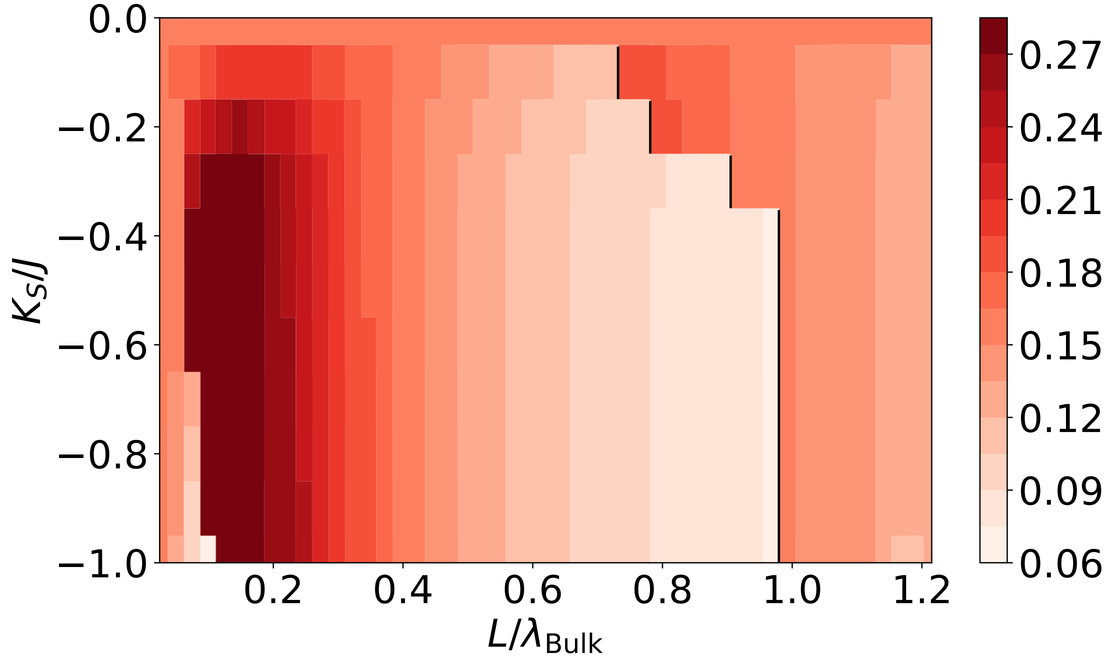

Figure 7.3: Phase diagram of the spin-induced electric polarization $P_{\mathrm{spin},z}$ in a cubic nanoparticle of side length L. $d = 0.15708$. In units of $D\chi\left(N-1\right)\left(NS\right)^2 / \left(Pa^3\right)$.

object plotted is

$$\begin{aligned}&\frac{1}{N^3}\left(\left[\{N-1\}\sum_{j=1}^{N}\sum_{\ell=1}^{N}\sin\{Q_{j,\ell}a\}\right]^2\right.\\&\left.+\left[\sum_{i=1}^{N}\sum_{j=1}^{N}\sum_{\ell=1}^{N-1}\sin\left\{\phi_{j,\ell+1}-\phi_{j,\ell}+\frac{\left(Q_{j,\ell+1}-Q_{j,\ell}\right)a\left(2i-N-1\right)}{2}\right\}\right]^2\right)^{1/2}\\&=\frac{\left|\mathbf{P}_{\mathrm{spin}}\right|Pa^3}{D\chi N^3S^2}.\end{aligned} \tag{7.12}$$

It looks quite similar to Figure 7.3, which is just the z component of the polarization. Figure 7.4 and the bottom half of Figure 6.12 are identical, as were the z components of the polarization in Figure 7.3 and the bottom half of Figure 6.11.

The spin-canting-induced magnetization was also displayed in a phase diagram as a function of surface anisotropy and cubic nanoparticle side length. Using (7.10), the

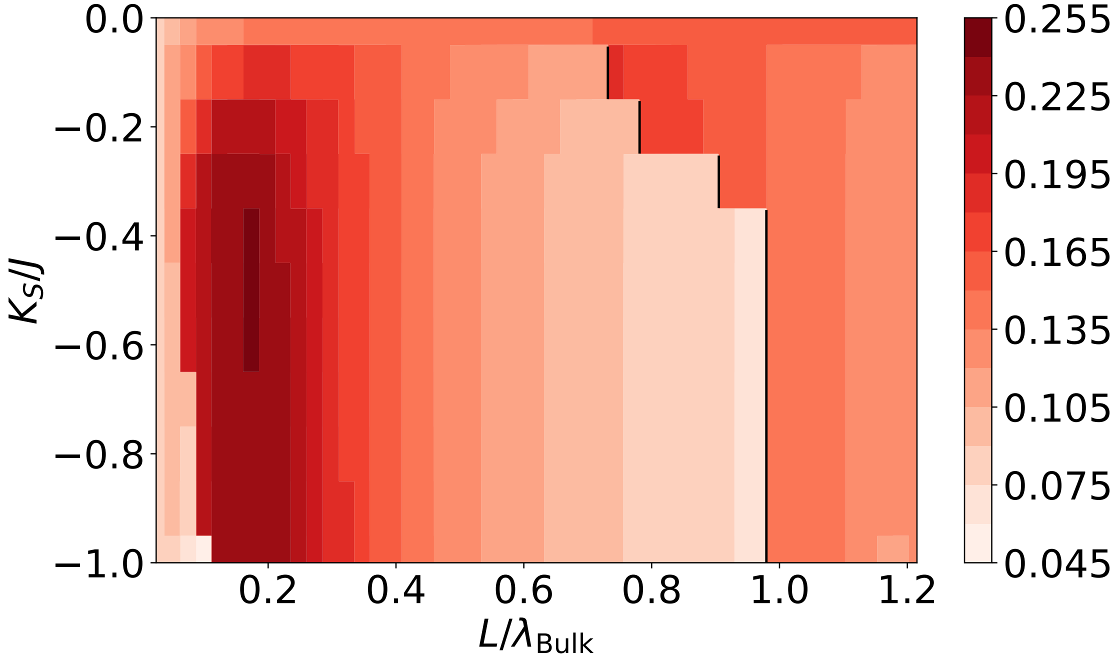

Figure 7.4: Phase diagram of the spin-induced electric polarization $|\mathbf{P}_{\text{spin}}|$ in a cubic nanoparticle of side length L. $d = 0.15708$. In units of $D\chi N^3S^2/\left(Pa^3\right)$.

object plotted was

$$\frac{1}{N^3}\left|\sum_{i=1}^{N}\sum_{j=1}^{N}\sum_{\ell=1}^{N}\sin\left(\phi_{j,\ell}+\frac{Q_{j,\ell}a\left[2i-N-1\right]}{2}\right)\right| = \frac{J\left|\mathbf{M}\right|}{D'S}. \tag{7.13}$$

The magnetization has units of $D'S/J$. The black lines noting the bistability points matched those in Figures 7.3 and 7.4, showing that in three dimensions, as well as two, there is simultaneous bistability in polarization and magnetization. This property could be of use if the multiferroic nanoparticle was to be integrated into a memory element. Figure 7.5 matches the bottom half of Figure 6.13, as would be expected, considering the similarity between (7.13) and (6.31) (the three-dimensional equation sums over spins in the y direction, but the wavevectors and phases are equal for different y layers) and that the cycloidal wavevectors and phases were the same in two and three dimensions.

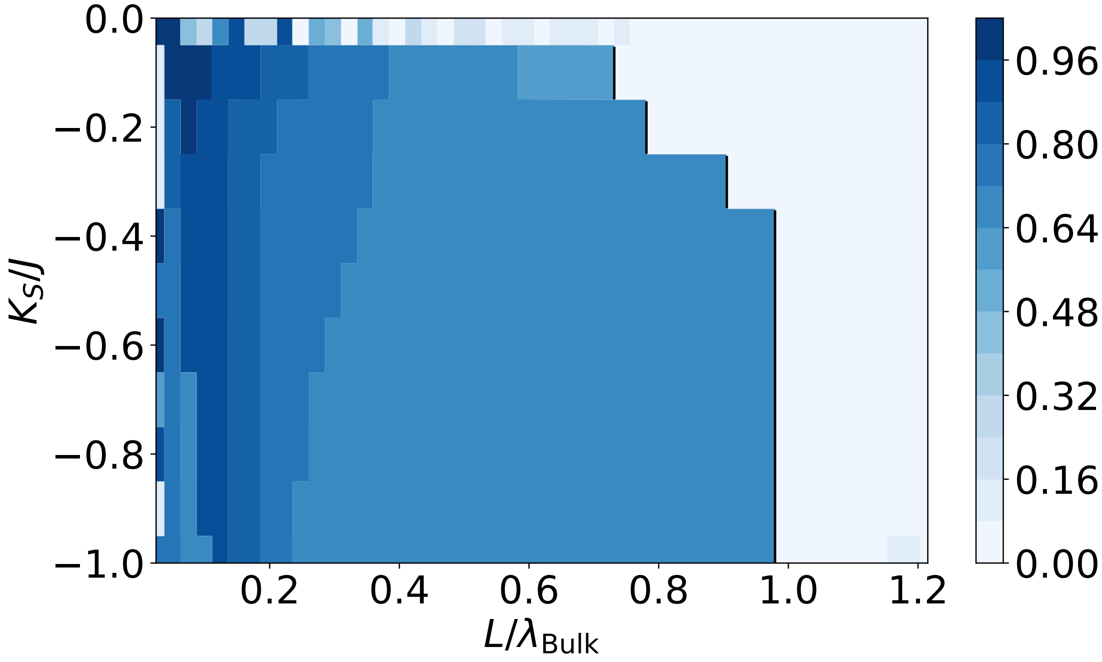

Figure 7.5: Phase diagram of the spin-current-induced magnetization $|\mathbf{M}|$ in a cubic nanoparticle of side length L. $d = 0.15708$. In units of $D'S/J$.

Chapter 8

Discussion of Results

It has been shown in Chapters 5, 6, and 7 that there are sizes of multiferroic nanoparticles at which bistability in the cycloidal wavevectors occurs. This bistability could potentially be of use in devices. The origins of the bistability were explored in Chapter 5 and will be further analyzed in this chapter.

The presence of bistability is most easily explained by looking at the one-dimensional spin chain with infinite surface anisotropy. The lowest energy spin configuration in this case necessarily has $Q = n\pi/L$, where n is a non-negative integer, so that the surface anisotropy energy is exactly equal to zero. The winding angle, QL, is an integer multiple of π. This comes from the minimization of the surface anisotropy energy. The value of n is determined by L; the lattice parameter, a; the exchange interaction strength, J; and the Dzyaloshinskii-Moriya interaction strength, D. Because n must be an integer, small changes in L, a, J, or D may not affect n. However, there will eventually be a threshold when the change in one of those interaction parameters causes n to jump to the next integer. In the modelling, a, J, and D were held constant during a trial, with only L changing. When L changed by enough to alter n, this caused the cycloidal wavevector to jump in value. The energy is the same for the two $Q(n)$'s at the critical length, and the system is bistable.

Our numerical calculations showed that the locations of bistability, L_{bist}, were independent of $d = D/J$ and $k_S = K_S/J$ (see Figure 5.1). As a result, the critical sizes, L_{bist}, can be found by solving the problem exactly for the particular case of $k_S = \infty$. This was done in Section 5.1, leading to

$$Q_{\text{min}} = \frac{\pi}{L}\text{Round}\left(\frac{dL}{\pi a}\right). \tag{8.1}$$

The jumps in Q occur when the argument of the round function in (8.1) is near a half-integer value:

$$\frac{dL_{\text{bist}}}{\pi a} = \frac{2n'+1}{2} \quad \text{for } n' = 0, 1, 2, \ldots \tag{8.2}$$

Thus, for $k_S = \infty$ the bistability occurs at

$$L_{\text{bist}} = \left(\frac{2n'+1}{2}\right)\left(\frac{\pi a}{d}\right) \approx \left(\frac{2n'+1}{4}\right)\left(\frac{2\pi a}{\arctan\left[d\right]}\right) = \left(\frac{2n'+1}{4}\right)\lambda_{\text{bulk}}. \tag{8.3}$$

Our numerical calculations show that for $k_S < \infty$ the bistability remains at the same values described by (8.3). There is a reason for this: Recall that $Q = Q_{\text{bulk}}$ minimizes the combined exchange and spin-current energy. However, when $L = L_{\text{bist}}$, $Q = Q_{\text{bulk}}$ would make the edge spins exactly perpendicular to each other, making it impossible to minimize the surface anisotropy energy at both edges. As a result, the system has two choices: It either increases Q (in order to approximately align edge spins) or decreases Q (in order to approximately anti-align the edge spins). Both cases can be achieved with the same energy cost, leading to bistability independent of k_S (however, the value of the energy cost and the change in Q does depend on k_S as can be seen in Figure 5.1).

Any potential patterns in the jumps in higher dimensions could not be determined in part because the side lengths L were much shorter for two and three dimensions than they were for one dimension due to computing limitations, so we could not determine whether the bistabilities in higher dimensions were evenly spaced in L. What was seen in higher dimensions was that the locations of bistability changed with k_S, which did not occur for the one-dimensional chains. The proximity effect, again, may explain this. Depending on the value of k_S, the average value of Q in the structure gets reduced so that $\langle Q\rangle L/2\pi$ half-integer values occur for larger L in a k_S-dependent fashion.

Figure 5.8 illustrated that at longer lengths the points of bistability had many metastable Q's which were of similar energy to the global minima. The energy wells also became shallower at longer lengths. As seen in figures in Chapter 5, the jumps in Q became less dramatic as the length of the spin chain increased. As the chain lengthened, the system was tending to its bulk value for Q. It is assumed that for even longer spin chains the jumps in Q would become less distinct and eventually for some chain of a certain length, imperceptible.

The lessening of the effect of the surface anisotropy as the chain lengthens is understandable as an ever-decreasing ratio of the spins are near the surface. The surface anisotropy acts as a form of pinning for the surface spins and that affects neighbouring spins. As more spins are added and the surface anisotropy energy is reduced in its contribution to the total energy of the chain, the system increasingly behaves as if there was no surface anisotropy present.

An open question is what is the length scale of the proximity effect. This is an area where future work could be done to understand the phenomenon. The only natural length scale in the problem is λ_{bulk}, so the range where there is attenuation on Q must be of the order of λ_{bulk}. There is also the question of whether the attenuation of Q is related to magnitude of K_S. Also, if there was asymmetric surface anisotropy on the surfaces, that might affect how the proximity effect behaved. The attenuation of Q would likely be greater near the surface with the larger magnitude surface anisotropy than the surface with smaller magnitude surface anisotropy.

It should be emphasized again that the presence of bistability in higher dimensions is rather remarkable. The proximity effect influences what Q is for neighbouring rows, and as such, there is no critical length where every row is at the point of transition from one winding number level to the next. Yet, the bistability exists. It may be that spin chains near the surface of the nanoparticle significantly influence at what side length, L, the jump discontinuity occurs. The jumps occur at longer lengths in higher dimensions than for one dimension. The proximity effect, present in higher dimensions, but not one dimension, reduces Q for spin chains near the surface. As a result, the average Q over the sample is reduced, which may lead to an increase of L_{bist}.

The bistability in the spin-induced polarization $\mathbf{P}_{\text{spin}}$ and the spin-canting-induced magnetization $\mathbf{M}$ could be exploited as a memory element. Previous theoretical results suggest that the magnitude of both these features are in the range where they could be switched and read by already-developed devices. $\mathbf{P}_{\text{spin}}$ is approximately 3 μC/cm^2 [145]. At this strength the polarization could be switched by an applied electric field on the order of 10^2 V/cm [9]. The magnitude of the spin-canting-induced magnetization is approximately 0.09 μB/Fe which corresponds to a local magnetic field of 200 G [146].

To read out the magnetization, conventional methods akin to those used in magnetic hard drives could be employed. Alternatively, diamond nitrogen-vacancy (NV) centre magnetometry could be used [147]. In that method, the electronic spin of a diamond NV centre is used to probe the local magnetic field and has enough precision to be able to detect the spin structure of a BFO film. The photoluminescence of the NV centre is dependent upon the spin of the electron of the centre and the electron spin resonance spectrum of the NV centre can be determined. The magnetism of the probed material then shifts the spectrum and from the nature of the shift, the magnetic field of the material is found.

As covered in Section 2.10, thermal fluctuations will affect the magnetization by reducing it. A sufficiently-high reduction in the spin-canting-induced magnetization would make it so any device would not be able to read out the magnetization. There is some threshold value that any magnetometer needs in the magnetization to be able to distinguish between states and it is possible that the thermal fluctuations could lower the magnetization below this. As room temperature is well below T_N, this should not occur in this temperature range. The spin-induced polarization is a function of the Néel vector, which would also be reduced by thermal fluctuations. This would mean that the polarization would also be reduced. A smaller polarization would be easier to switch as a lesser external field would be needed to achieve the switching. This might ensure that the inherent polarization does not switch with the induced polarization. Switching the inherent polarization is not desirable as $\mathbf{Q}$ follows the inherent polarization [7, 71, 148]. That would then change the direction of the spin-canting-induced magnetization. The objective here in switching is to change the magnitude of the magnetization, not change its direction. Readout would be complicated if the magnetization changed directions, as the probe would be oriented to measure the magnetic field in a certain direction and then the magnetic field would switch to mostly being in another direction, where the probe could possibly not distinguish between the two bistable states.

Very small nanoparticles would not be magnetic but superparamagnetic, as discussed in Sections 2.5 and 2.6. Due to the rapid spin flipping in the superparamagnetic regime, the time averages of $\langle \mathbf{M} \rangle$ and $\langle \mathbf{L} \rangle$ equal zero. From that it can be seen that the average spin-induced polarization, dependent on $\langle \mathbf{L} \rangle$, would also be zero. BFO nanoparticles with a radius greater than 7 nm would appear to be stable for any measurement one wanted to take of them. While thermal fluctuations might not be able to switch the magnetization of most nanoparticles on the time scale required to interfere with measurement, they can play a role through the generation of magnons which can lower the magnetization. The magnons, however, do not eliminate the spin-canting-induced magnetization even though the room temperature thermal energy is $k_B T_{\mathrm{RT}} = \left(0.08617 \text{ meV K}^{-1}\right)(300K) \approx 26$ meV and the Dzyaloshinskii-Moriya spin-canting energy is $D' = 0.085$ meV [149]. Returning to Figure 2.14, this can be seen in the nature of the antiferromagnetic magnons. The magnons will produce vibrations in the spin-canting-induced magnetization, but for $T \ll T_N$ these will be small angle vibrations that only reduce the value of the weak ferromagnetic moment by a small amount. As a result, the magnetization and spin-induced polarization magnitudes should decrease somewhat with increasing T, but not be eliminated.

The spin-canting-induced magnetization is derived from the weak ferromagnetism Dzyaloshinskii-Moriya interaction. The model for the optimization did not include the weak ferromagnetism interaction. As pointed out in Section 6.2, it leads to a correction of the order of $(D'/J)^2$ to the minimization energy, which is quite a small effect for BFO [150]. The interaction would be present in nanoparticles; its influence on the spin structure is merely less than the interactions present in the model. For larger D' we would have to include this extra Dzyaloshinskii-Moriya interaction in the energy minimization procedure, and we would expect the canting to become even more pronounced. That canting is present without the weak ferromagnetism interaction demonstrates the unique qualities of nanoparticles.

The three-dimensional results shown in Chapter 7 were identical to the two-dimensional ones from Chapter 6. This was in part because only $K_S \leq 0$ values were explored. For $K_S > 0$, the results would not have been identical to the two-dimensional ones. This is because the easy-axis anisotropy would have favoured a more complicated cycloid with $\mathbf{Q}(\mathbf{R})$ changing direction inside the nanoparticle.

It should be noted that the polarization in BFO is along one of the $\langle 111 \rangle$ directions. In the modelling, the polarization was along [001]. This was done for simplicity and to allow for comparison between results of different dimensions. The principle that explains the existence of bistabilities would still be valid, so the bistabilities would remain. However, the locations of the bistabilities would likely change for a polarization along $\langle 111 \rangle$. With the polarization along one of these directions, the number of spins in one complete cycloid for a given D/J would be different than for $\mathbf{P} \parallel [001]$. Also, depending on the shape of the nanoparticle, adjacent spin chains would not necessarily be of the same length, changing how they interact.

Future work could use a polarization along one of the $\langle 111 \rangle$ directions to see the changes to the cycloidal wavevectors as a function of size and surface anisotropy. This only makes sense to do in three dimensions, as in lesser dimensions it would not be possible to complete a cycloid, assuming that the spins are taken to be along one of the x, y, or z directions in one dimension or in one of the xy, xz, or yz planes for two dimensions. The size of the nanoparticle would affect the relative lengths of the spin chains, which would affect how the proximity effect would be realized. With the polarization along [111], the propagation direction of $\mathbf{Q}$ is one of the $\langle 1\bar{1}0\rangle$ directions [146]. As $0 < \hat{\mathbf{Q}} \cdot \hat{\mathbf{n}} < 1$ for all of these values of $\mathbf{Q}$, the surface anisotropy should affect the spin chains differently than with $\mathbf{Q} \parallel \hat{\mathbf{x}}$ where either $\hat{\mathbf{Q}} \cdot \hat{\mathbf{n}} = 0$ or $\hat{\mathbf{Q}} \cdot \hat{\mathbf{n}} = 1$. With $\hat{\mathbf{Q}} \cdot \hat{\mathbf{n}} = 0$, the spins were not affected by the anisotropy of the surfaces (the y surfaces) or were only affected by the proximity effect (the z surfaces). Those cases cannot occur with $\mathbf{P} \parallel \langle 111\rangle$. All surfaces would play a role in how the edge effect was realized.

A three-dimensional system with easy-axis anisotropy on all ends would not look like its two-dimensional analogue [141]. Assuming the polarization remains along [001], then the easy-axis anisotropy for the x and y surfaces means that the cycloid energy is reduced if spins possess both non-zero x and y components. The assumed form of the cycloid in the xz plane would no longer hold. $\mathbf{Q}$ would be in the xy plane with spins at the intersection of x and y faces wanting to point in or against the $\hat{\mathbf{x}} \pm \hat{\mathbf{y}}$ direction. Spins not at the surface and spins only at one surface would not have this same desire for its spin orientation. This would lead to twisting in $\mathbf{Q}$. The approach used in other cases to find the spin configurations – assuming the the spins lie in the xz plane and optimizing Q and the phase angle – would not work for cubic nanoparticles with easy-axis anisotropy. It is evident that the spins cannot lie in the xz plane, thus a different method of treating the problem would be needed. A future direction could be the development of a new approach suitable for evaluating three-dimensional nanoparticles with easy-axis surface anisotropy.

There is an obvious shape-dependence to the results. The surface anisotropy is a substantial contributor to the orientation of the spins. In all of the data presented, the chains in two and three dimensions were of equal length in square or cubic lattices. With spin chains of differing lengths, the edge effect would produce cycloidal wavevectors of different magnitude for chains near to each other. Combined with the coupling through exchange and the proximity effect, this would lead to spin chains whose Q values would be related to each other in a different way than they were for square and cubic nanoparticles. Future work could look into different shapes and see how the cycloidal wavevectors were affected. The locations of jump discontinuities would likely be different as well.

It is rather unlikely that the surface anisotropy would be equal for all spins. Thus, a direction in which this work could be extended is to evaluate how surfaces with different surface anisotropies affect the spin configuration. For a spin chain with only surface anisotropy on its end spins this could mean that the spin with greater surface anisotropy dictates how the spin configuration would look. This would be due to the greater reduction in energy for satisfying the desires of the spin with greater anisotropy. The situation where opposing surfaces have anisotropy of equal magnitude but differing signs would also be of interest. It is unclear how spins would arrange themselves in such a situation. The system would benefit equally from the surface spins being fully satisfied in terms of their orientation to lower their anisotropy energy, but only a certain Q could allow the system to do this. The symmetry that was present in the results where opposing surfaces always had the same anisotropy energy would be absent for surfaces of unequal of surface anisotropies.

Spin chains where all spins in the chain have surface anisotropy would likely not be affected much by opposing unequal surface anisotropies. The proximity effect would suggest that only in very small nanoparticles would there be a change. Perhaps if the opposing surface had a large enough anisotropy that would not be the case and there would be a change in how the spins arranged on the opposing surface. This returns to the question of the length (and nature) of influence for the proximity effect.

As mentioned in Section 2.7, the depolarization field was not taken into account for the nanoparticles. It would be possible to incorporate the field into calculations. This could be done by changing the value of D from the Dzyaloshinskii-Moriya interaction as a function of size. D is proportional to the polarization, so a reduction in the polarization will be seen in the model as a reduction in D. Selbach *et al.* [92] included a formula for the pseudotetragonality, a property that indicates a loss of ferroelectricity when the ratio c/a becomes equal to one:

$$\left(\frac{c}{a}\right)_d = \left(\frac{c}{a}\right)_\infty - \frac{A}{d - d_c}. \tag{8.4}$$

Here c/a is the pseudotetragonality with $a = a_{\text{hex}}/\sqrt{2}$ and $c = c_{\text{hex}}/\sqrt{12}$ being the reduced lattice parameters with BFO in the hexagonal configuration. $(c/a)_d$ is the pseduotetragonality as a function of d, the nanoparticle size, and $(c/a)_\infty$ is the bulk value. A is a fitting parameter and d_c is value closely related to the critical size for ferroelectricity. The idea would be to use (8.4) with D/J replacing c/a and the fitting parameter multiplied by $(D/J+1)_\infty/(c/a)_\infty$. That would allow for a size-dependent Dzyaloshinskii-Moriya interaction strength, which would incorporate the effect of depolarization into the model.

The inclusion of temperature effects and dynamics would be needed to model superparamagnetism and the loss of weak ferromagnetism in small nanoparticles. Inclusion of temperature effects would allow for an investigation into how the spin arrangements change with temperature. As mentioned in Secton 2.10, the Néel and Curie temperatures being so high above room temperature means that the effects probed at 0 K should produce similar results at room temperature. However, if one wants results for even higher temperatures, the inclusion of temperature in the model and approach taken would become necessary. Monte Carlo methods could be employed to introduce temperature-dependence into the system and analyze the resultant spin structures.

There is the question as to how consistently one would ever be able to manufacture nanoparticles of the same size. The idea of nanoparticles at a particular size being able to switch its polarization and magnetization states relies on the assumption that at some point it will be possible to make nanoparticles with a minimal size spread. To date, that is not the case [90]. However, even nanoparticles with sizes quite different than L_{bist} have metastable states with spin configurations not much different from the most stable state. If these metastable states are long lived, the requirement on size distribution may not be too stringent after all.

Chapter 9

Conclusions

This dissertation has laid out the case of a multiferroic nanoparticle and how its spin configuration is dependent on its size and surface anisotropy. It was seen that a bistability in the cycloidal wavevector occurs for certain sizes and surface anisotropies. That bistability is responsible for the bistability present in the spin-induced polarization and spin-canting-induced magnetization. Because the bistabilities have the same origin, they are coupled. That suggests that if an external stimulus was applied to drive the system to its other stable Q value, then the corresponding magnetic and electric moments would follow along in being switched. In this way the magnetic ordering could be altered electrically or the electric ordering magnetically. From the viewpoint of potential applications of this magnetoelectric effect, a low-power means to change the magnetic moment of a material is a long-desired attribute in the hard drive industry. Electrically switching the weak magnetization in multiferroics would be a way to achieve this. There has been evidence that it is possible to read spin-induced moments of the magnitude produced in the results [147].

The fact that nanoparticles of similar size can have much different cycloidal wavevectors is a challenge to experiments that intend to probe the magnetic structure of these nanoparticles. When nanoparticles are prepared there is a range of sizes produced. When these collections are analyzed by Raman or terahertz spectroscopy, the responses for the different sizes will be varied. The result is inhomogeneous broadening in the peaks of the signal. Too much broadening could lead to a loss of signal.

These results indicate the powerful impact that anisotropy can have on spin textures. The application of surface anisotropy of one-tenth the strength of the exchange interaction to a one-dimensional chain resulted in drastic changes to the cycloidal wavevector. By making it so advantageous for the surface spins to have a particular alignment, the anisotropy is a significant factor in determining Q via the edge effect. With the surface spins desiring a certain arrangement, the interior spins have to have an angle between themselves that allows the surface spins to reduce their anisotropy energy.

The proximity effect, where the spins chains nearer to the surface have reduced cycloidal wavevectors relative to those near the middle of the nanoparticle, was witnessed in two- and three-dimensional nanoparticles. This was seen for both easy-axis and easy-plane anisotropy. Spin chains at the surface have all of their spins experiencing surface anisotropy. A reduced Q is then ideal for these chains as they all want to be (anti)parallel or perpendicular to the same axis. Adjacent spin chains are coupled through the exchange interaction, which means that chains next to surface spin chains would benefit in having a reduced Q to match the surface spin chains to lower their exchange energy. This argument persists as one plunges deeper into the nanoparticle. While the argument holds as one moves into the nanoparticle, the effect is reduced towards the centre of the nanoparticle. The length scale over which the proximity effect acts is of the order of λ_{bulk}.

Three-dimensional results for easy-plane cases were provided. With easy-plane anisotropy, the layers of the nanoparticle cube in the y direction could be stacked in an antiferromagnetic fashion with each layer resembling a two-dimensional nanoparticle with easy-plane anisotropy. This allowed for there to be no additional surface anisotropy energy for spins on the y faces of the cube. The cycloidal wavevectors for the cubic nanoparticle were identical to their two-dimensional analogues.

The presence of bistability in dimensions greater than one is noteworthy. The picture for the jump discontinuities and bistabilities is quite clear in one dimension. The size confinement and surface anisotropy mean that there is a particular Q that satisfies the end spins' desire to point along or orthogonal to a certain axis. There comes a point where increasing Q lowers the exchange and Dzyaloshinskii-Moriya energy while still maintaining a low anisotropy energy for nanoparticles of increasing size. There is a jump in Q at this point. The proximity effect in higher dimensions means that spin chains have different Q's. That there is a length at which all of the chains can agree to have a jump in Q is surprising as the desire to fit a new Q should occur at different lengths for different Q's. We believe the presence of bistability in two and three dimensions is related to the space average of Q adjusting itself to minimize the surface anisotropy energy.

The novel effects seen in multiferroic nanoparticles in this work illustrate how size and surface anisotropy can greatly affect spin ordering. The results detailed how sensitive nanoparticles are to these variables and that there may be a means to put that sensitivity to use in a device. From a broader scope, the phase diagrams explored show that finite size has a profound effect on multiferroic order. The physics of multiferroics does not just lie in the bulk. Systems of reduced size have much to offer in our understanding of an already compelling class of materials.

Appendix A

Additional Spin Chain Results

The proceeding figures are results additional minimization results for the spin chain. Results are shown for three different values of d, illustrating that the minimizations characteristics are independent of d. The jump discontinuites occured at the same positions for all d and k_S values explored.

Below are additional results for $d = 0.15708$. Figure A.1 shows Q/Q_{bulk} versus spin chain length for multiple values of $k_S : -1.00, -0.10, 0.10$, and 1.00. They show the similarity in Q for different k_S. Figures A.2–A.21 show Q/Q_{bulk} versus spin chain length and winding number versus spin chain length.

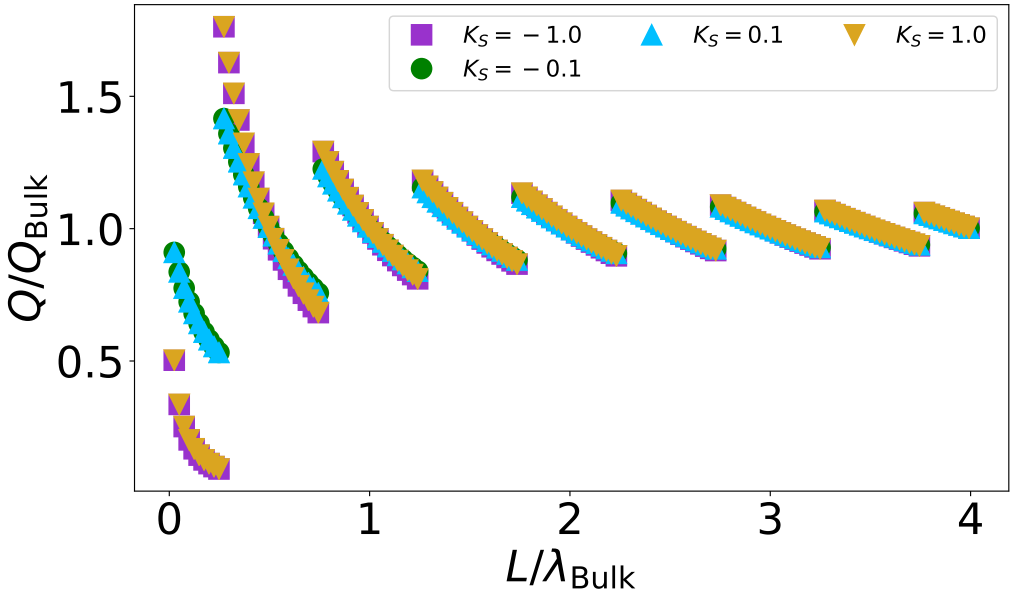

Figure A.1: Q/Q_{Bulk} versus spin chain length. $d = 0.15708$ and $k_S = -1.00$, -0.10, 0.10, and 1.00.

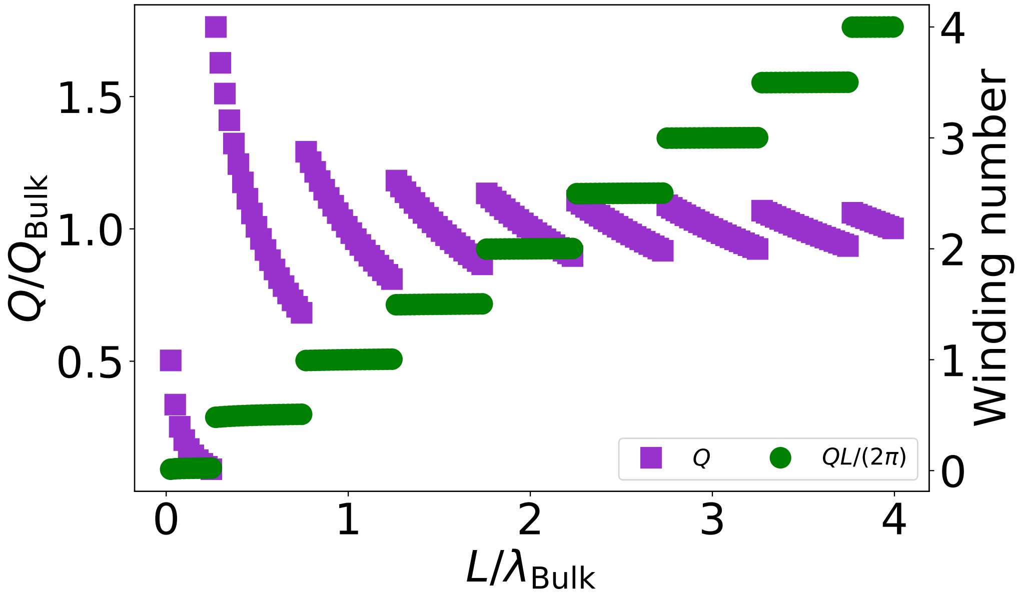

Figure A.2: Q/Q_{Bulk} and winding number versus spin chain length. $d = 0.15708$ and $k_S = -1.00$. The purple squares are Q/Q_{Bulk} and the green circles represent the winding number.

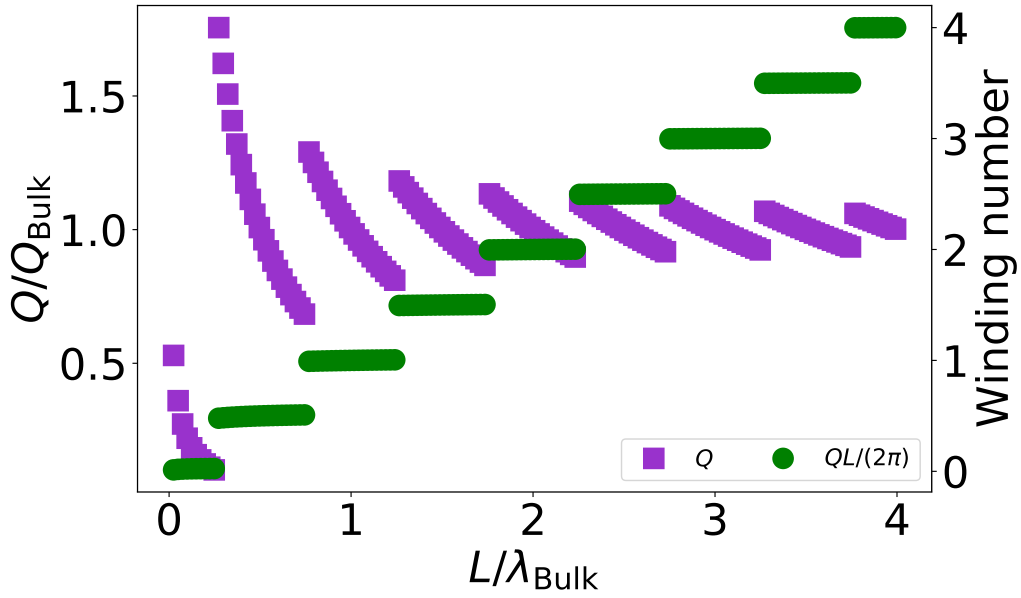

Figure A.3: Q/Q_{Bulk} and winding number versus spin chain length. $d = 0.15708$ and $k_S = -0.90$. The purple squares are Q/Q_{Bulk} and the green circles represent the winding number.

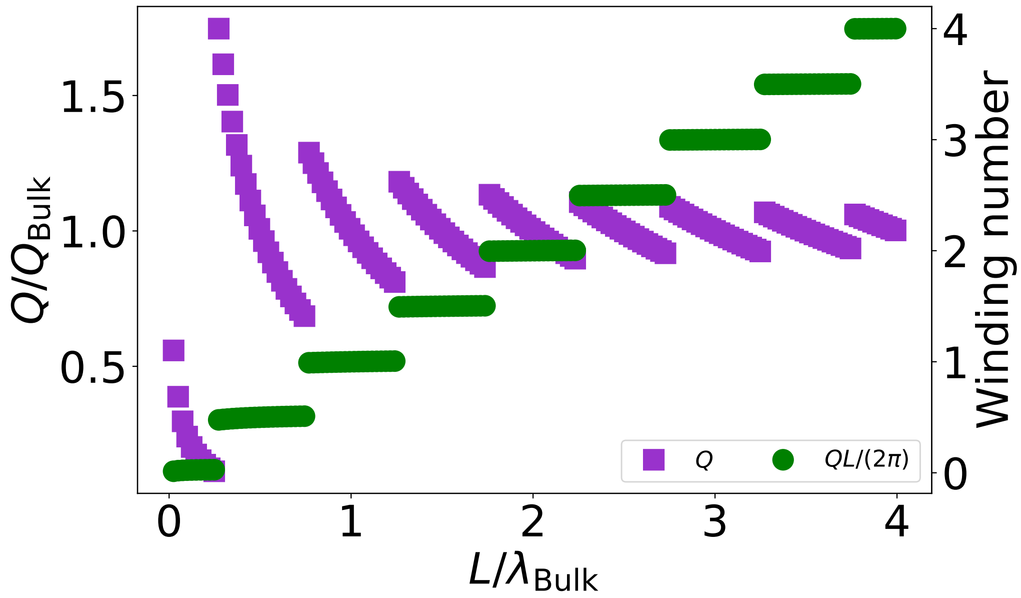

Figure A.4: Q/Q_{Bulk} and winding number versus spin chain length. $d = 0.15708$ and $k_S = -0.80$. The purple squares are Q/Q_{Bulk} and the green circles represent the winding number.

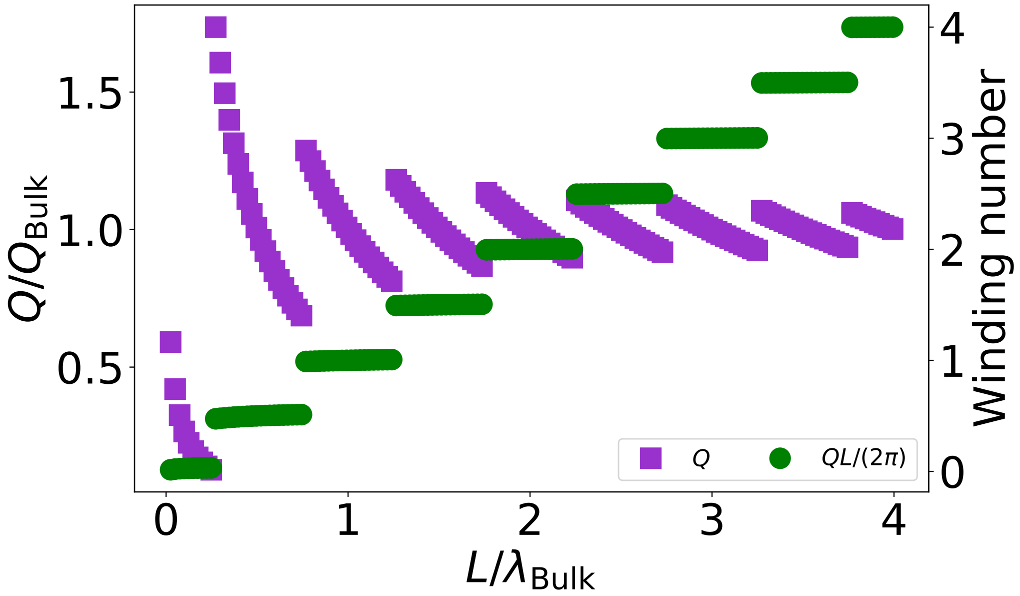

Figure A.5: Q/Q_{Bulk} and winding number versus spin chain length. $d = 0.15708$ and $k_S = -0.70$. The purple squares are Q/Q_{Bulk} and the green circles represent the winding number.

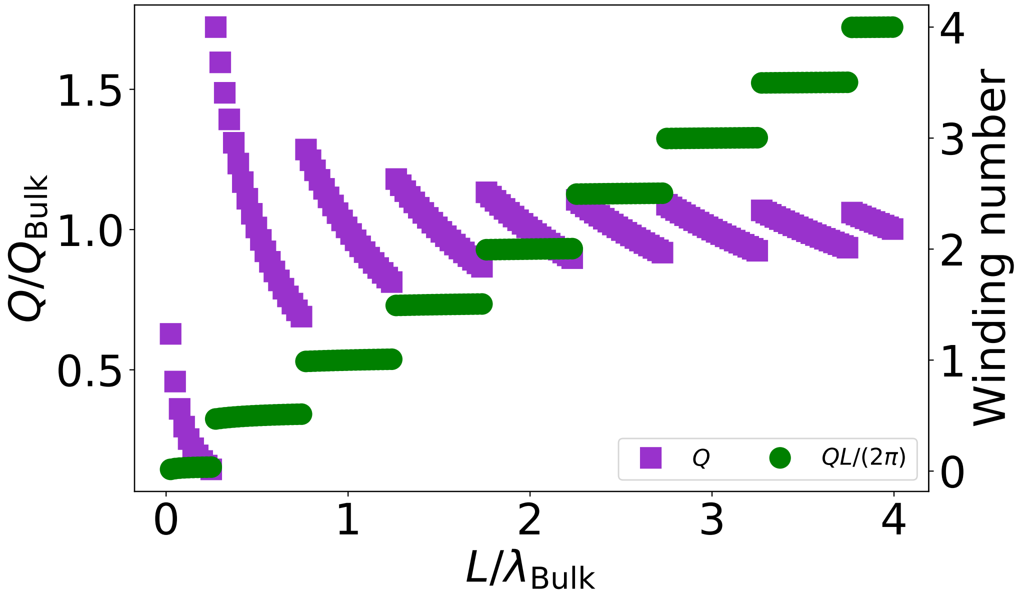

Figure A.6: Q/Q_{Bulk} and winding number versus spin chain length. $d = 0.15708$ and $k_S = -0.60$. The purple squares are Q/Q_{Bulk} and the green circles represent the winding number.

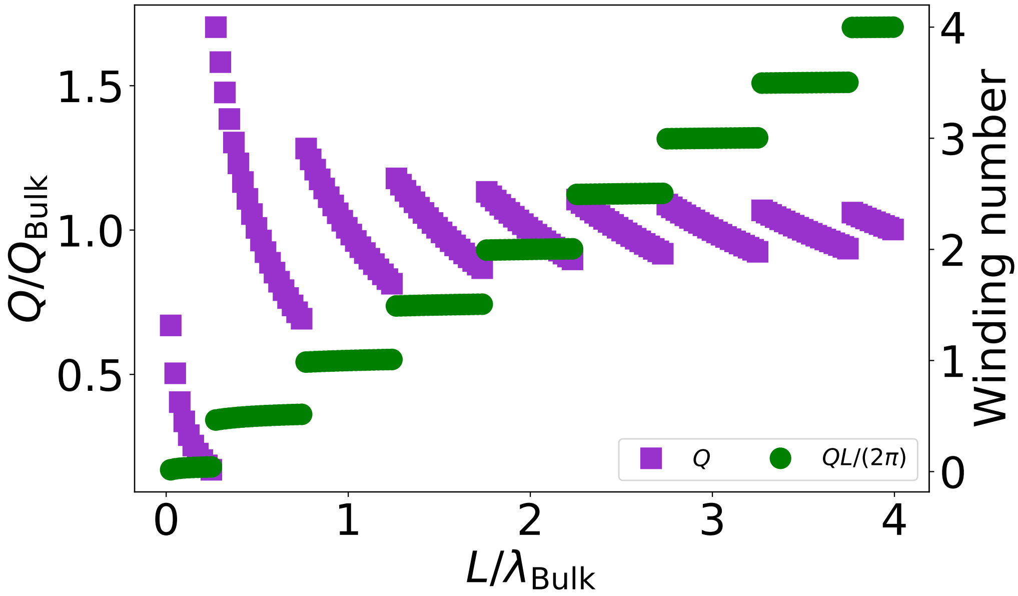

Figure A.7: Q/Q_{Bulk} and winding number versus spin chain length. $d = 0.15708$ and $k_S = -0.50$. The purple squares are Q/Q_{Bulk} and the green circles represent the winding number.

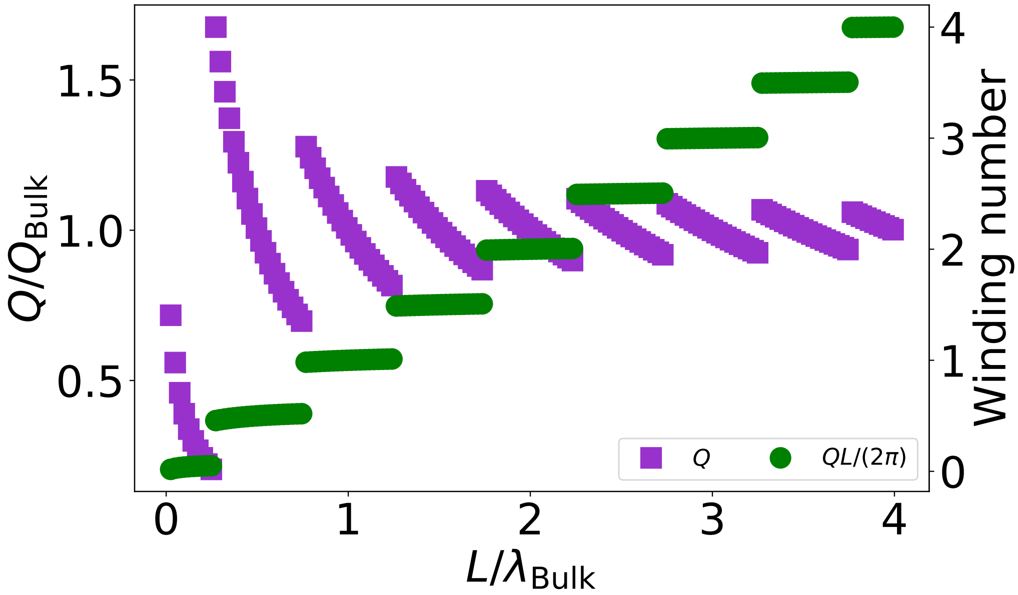

Figure A.8: Q/Q_{Bulk} and winding number versus spin chain length. $d = 0.15708$ and $k_S = -0.40$. The purple squares are Q/Q_{Bulk} and the green circles represent the winding number.

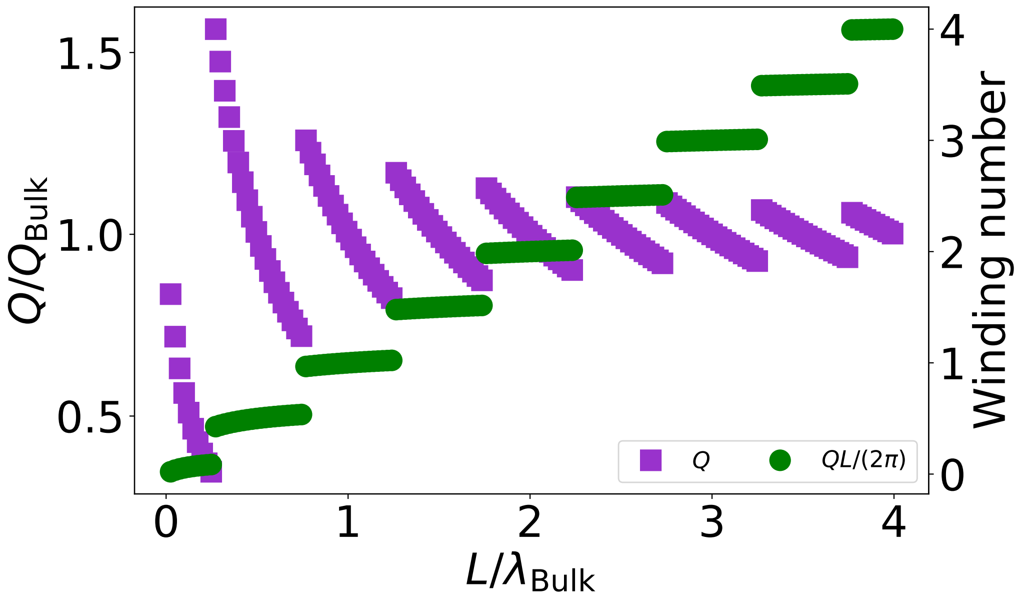

Figure A.9: Q/Q_{Bulk} and winding number versus spin chain length. $d = 0.15708$ and $k_S = -0.20$. The purple squares are Q/Q_{Bulk} and the green circles represent the winding number.

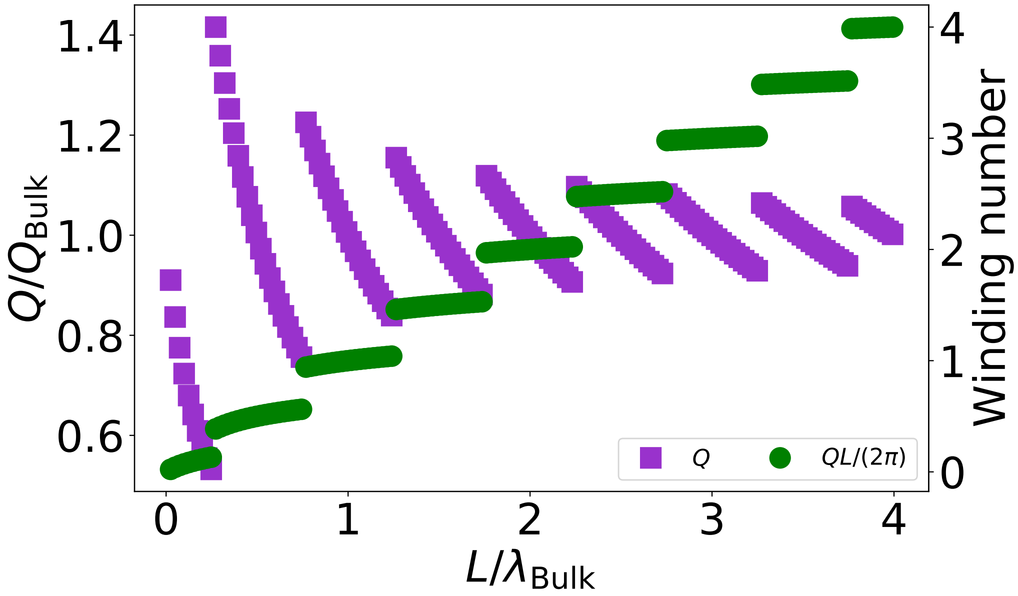

Figure A.10: Q/Q_{Bulk} and winding number versus spin chain length. $d = 0.15708$ and $k_S = -0.10$. The purple squares are Q/Q_{Bulk} and the green circles represent the winding number.

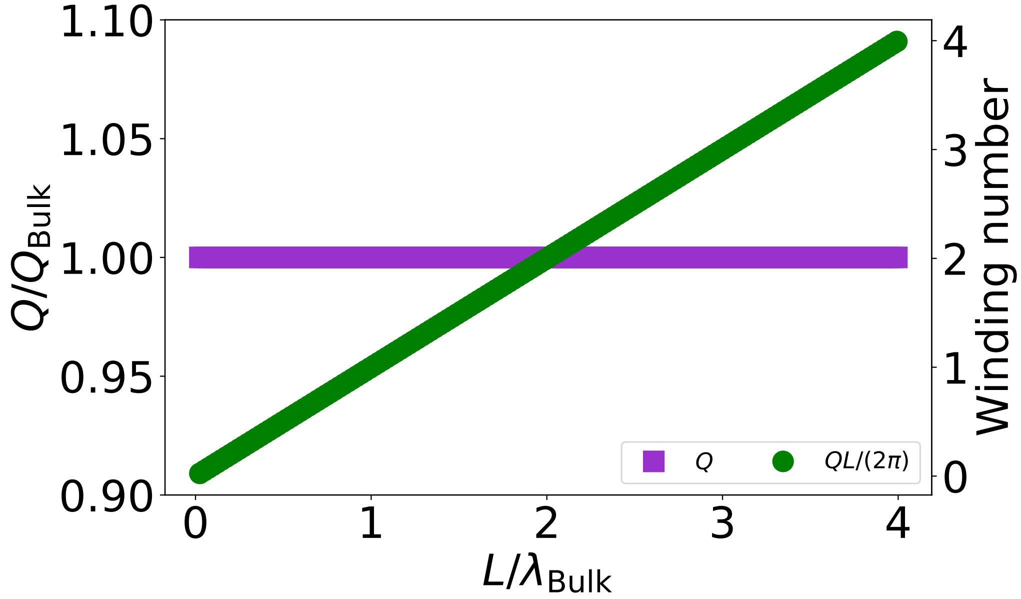

Figure A.11: Q/Q_{Bulk} and winding number versus spin chain length. $d = 0.15708$ and $k_S = 0$. The purple squares are Q/Q_{Bulk} and the green circles represent the winding number.

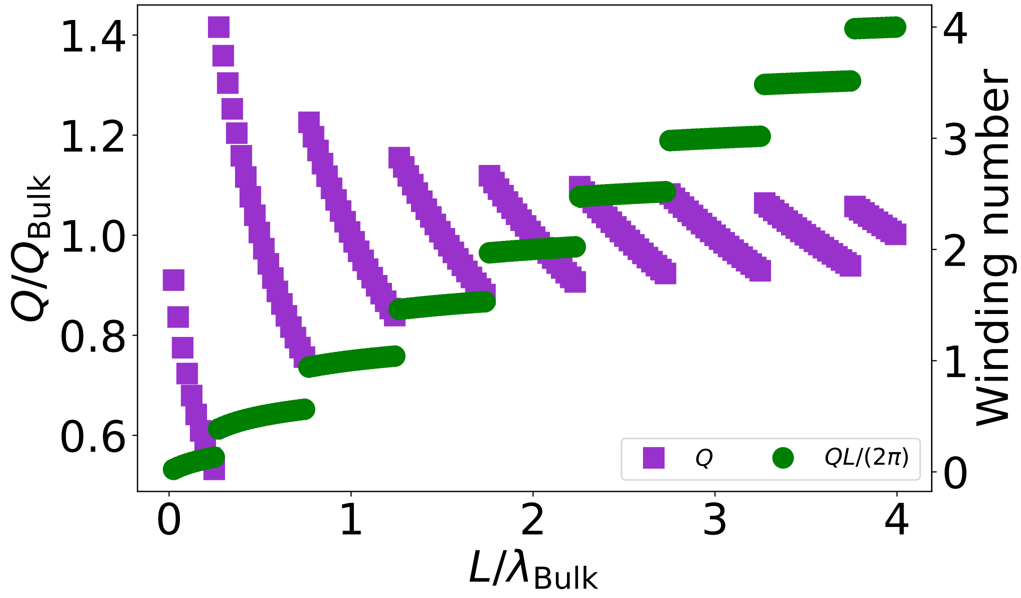

Figure A.12: Q/Q_{Bulk} and winding number versus spin chain length. $d = 0.15708$ and $k_S = 0.10$. The purple squares are Q/Q_{Bulk} and the green circles represent the winding number.

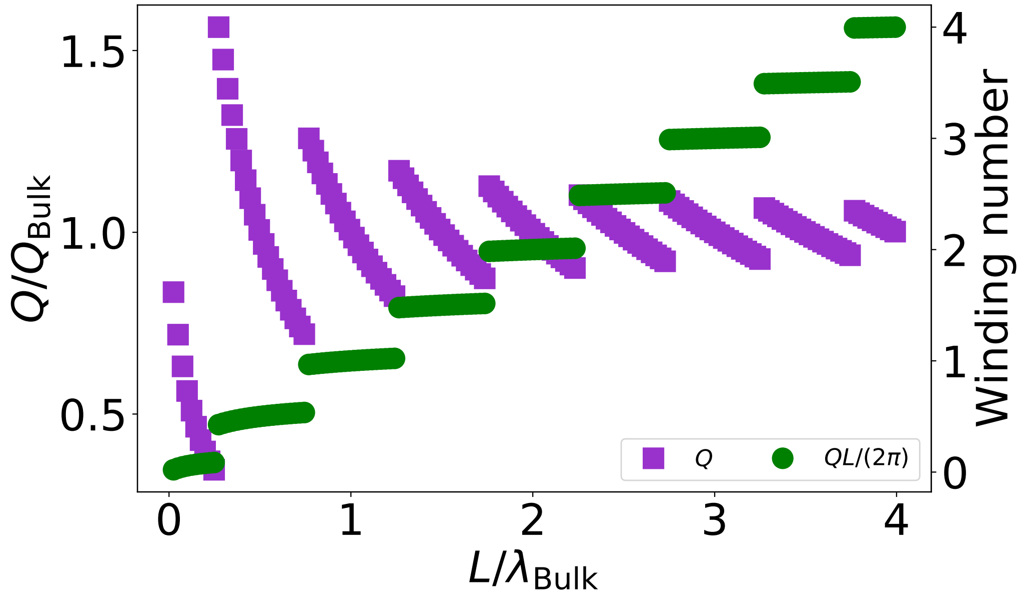

Figure A.13: Q/Q_{Bulk} and winding number versus spin chain length. $d = 0.15708$ and $k_S = 0.20$. The purple squares are Q/Q_{Bulk} and the green circles represent the winding number.

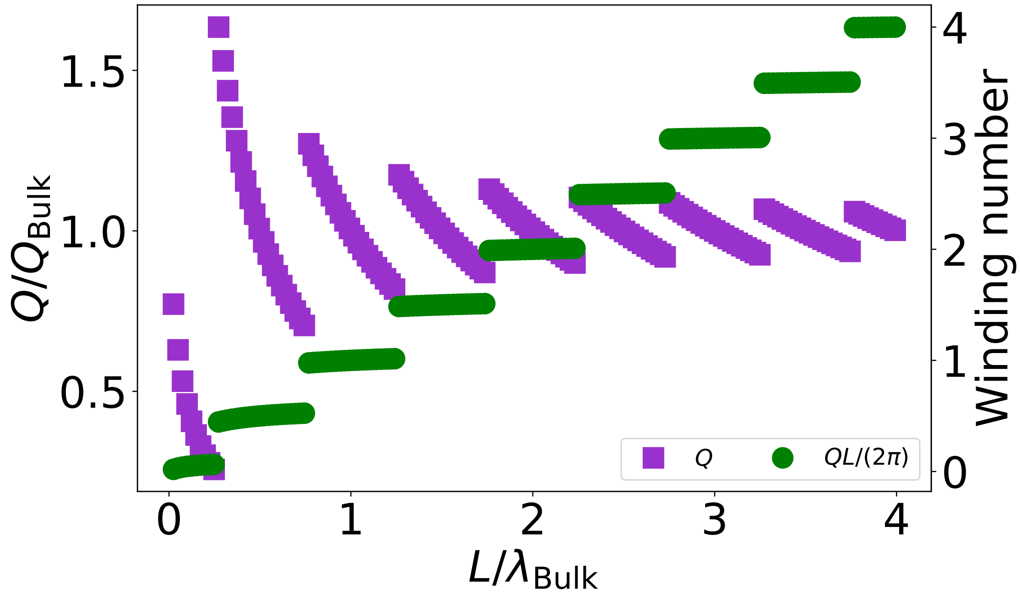

Figure A.14: Q/Q_{Bulk} and winding number versus spin chain length. $d = 0.15708$ and $k_S = 0.30$. The purple squares are Q/Q_{Bulk} and the green circles represent the winding number.

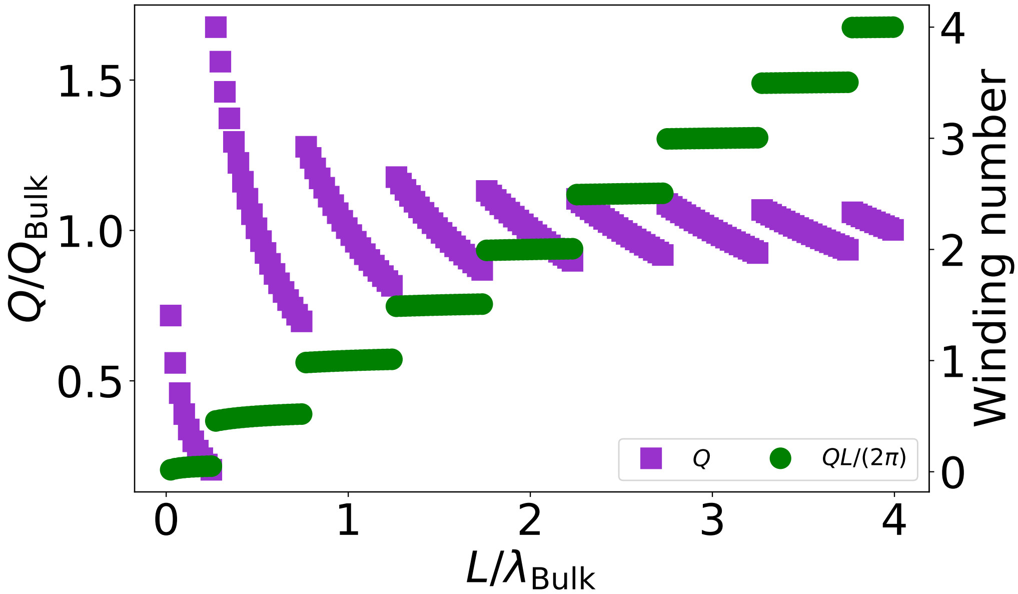

Figure A.15: Q/Q_{Bulk} and winding number versus spin chain length. $d = 0.15708$ and $k_S = 0.40$. The purple squares are Q/Q_{Bulk} and the green circles represent the winding number.

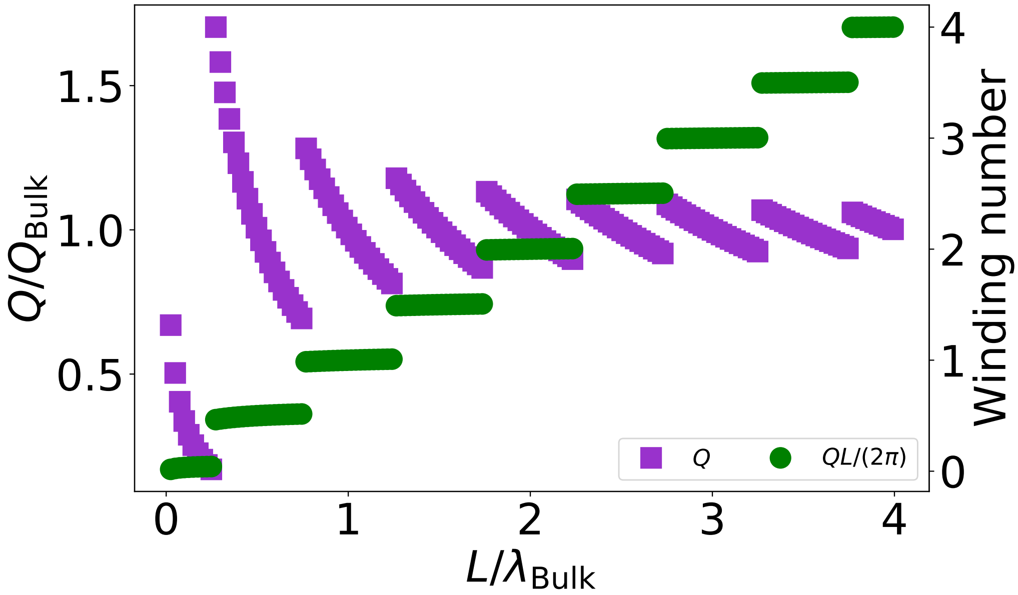

Figure A.16: Q/Q_{Bulk} and winding number versus spin chain length. $d = 0.15708$ and $k_S = 0.50$. The purple squares are Q/Q_{Bulk} and the green circles represent the winding number.

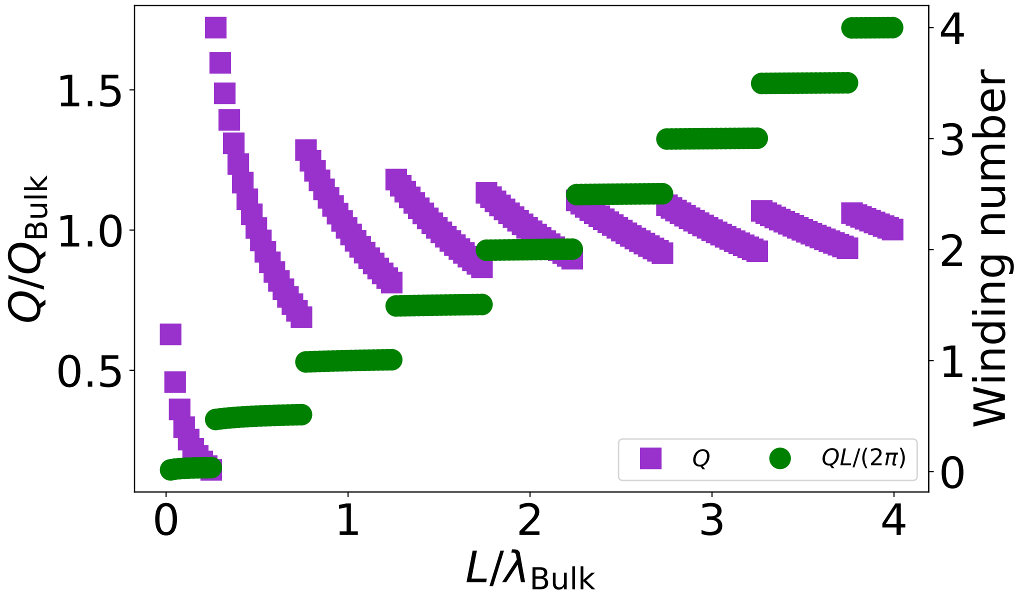

Figure A.17: Q/Q_{Bulk} and winding number versus spin chain length. $d = 0.15708$ and $k_S = 0.60$. The purple squares are Q/Q_{Bulk} and the green circles represent the winding number.

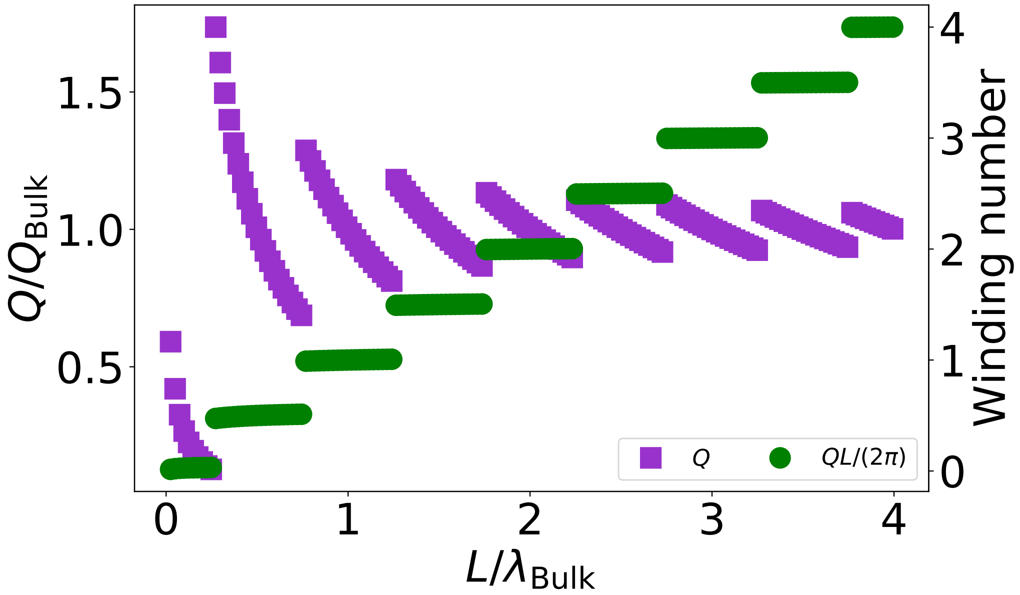

Figure A.18: Q/Q_{Bulk} and winding number versus spin chain length. $d = 0.15708$ and $k_S = 0.70$. The purple squares are Q/Q_{Bulk} and the green circles represent the winding number.

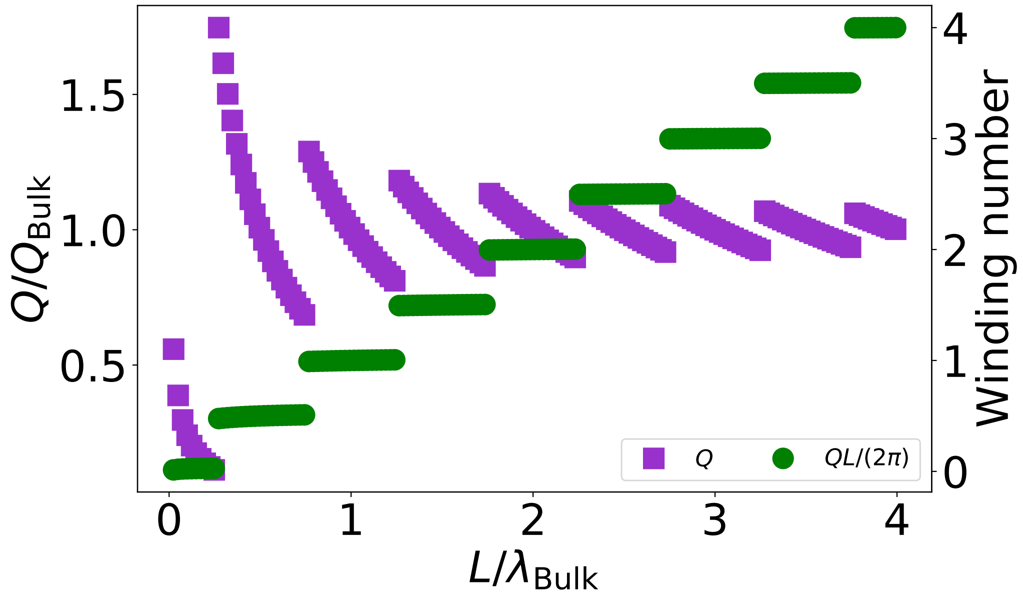

Figure A.19: Q/Q_{Bulk} and winding number versus spin chain length. $d = 0.15708$ and $k_S = 0.80$. The purple squares are Q/Q_{Bulk} and the green circles represent the winding number.

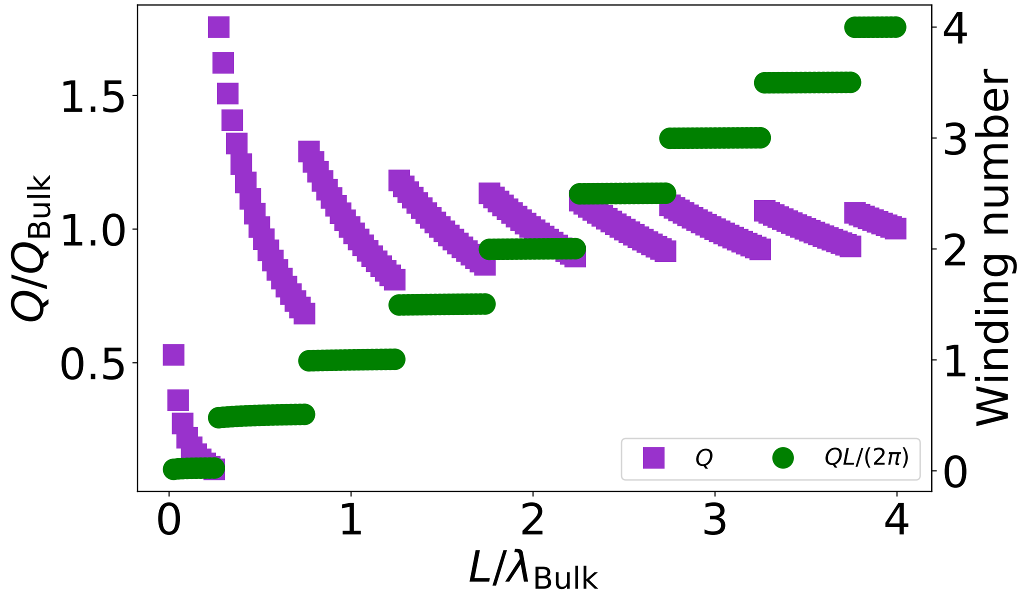

Figure A.20: Q/Q_{Bulk} and winding number versus spin chain length. $d = 0.15708$ and $k_S = 0.90$. The purple squares are Q/Q_{Bulk} and the green circles represent the winding number.

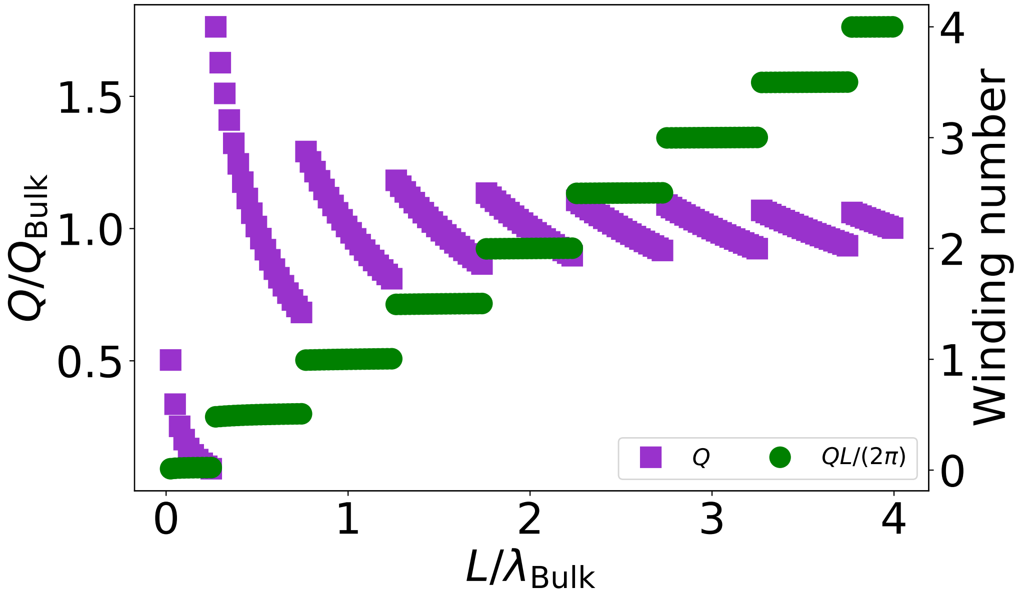

Figure A.21: Q/Q_{Bulk} and winding number versus spin chain length. $d = 0.15708$ and $k_S = 1.00$. The purple squares are Q/Q_{Bulk} and the green circles represent the winding number.

The following figures are for $d = 0.31416$. Figure A.22 plots Q/Q_{Bulk} versus spin chain length for multiple k_S values. Figures A.23 to A.42 plot Q/Q_{Bulk} and winding number versus spin chain length.

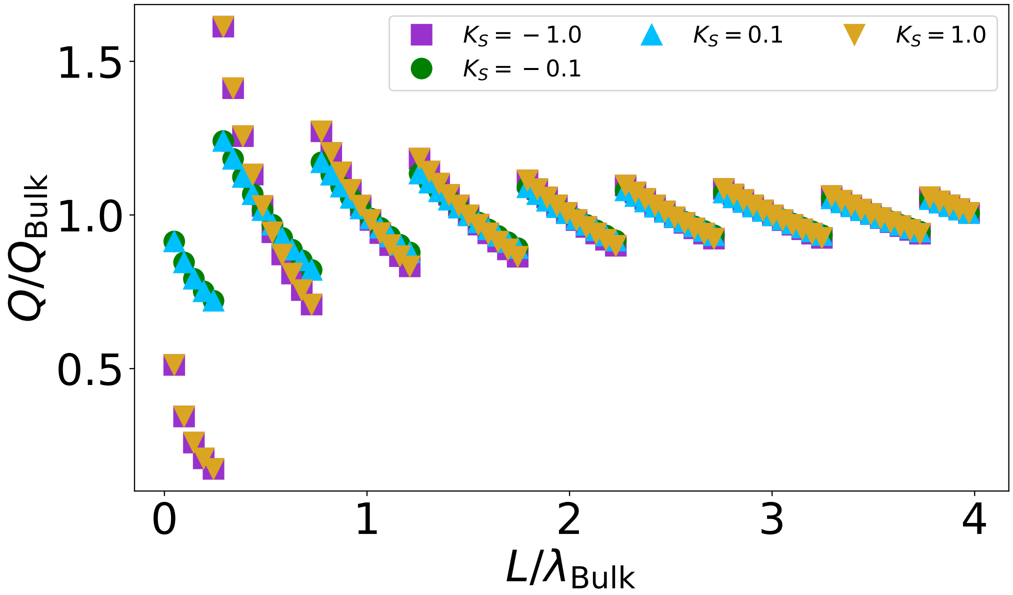

Figure A.22: Q/Q_{Bulk} versus spin chain length. $d = 0.31416$ and $k_S = -1.00$, -0.10, 0.10, and 1.00.

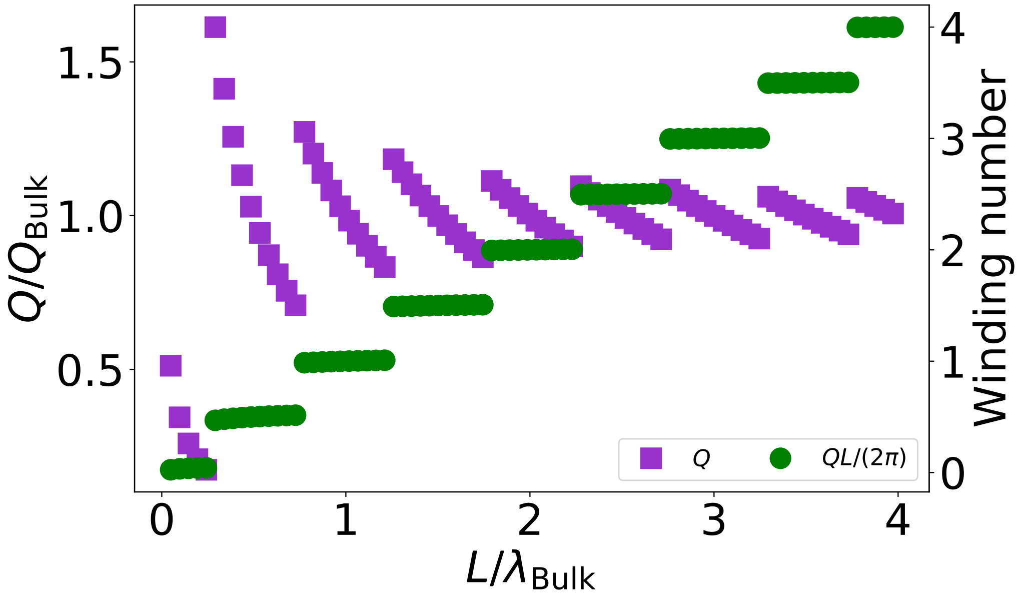

Figure A.23: Q/Q_{Bulk} and winding number versus spin chain length. $d = 0.31416$ and $k_S = -1.00$. The purple squares are Q/Q_{Bulk} and the green circles represent the winding number.

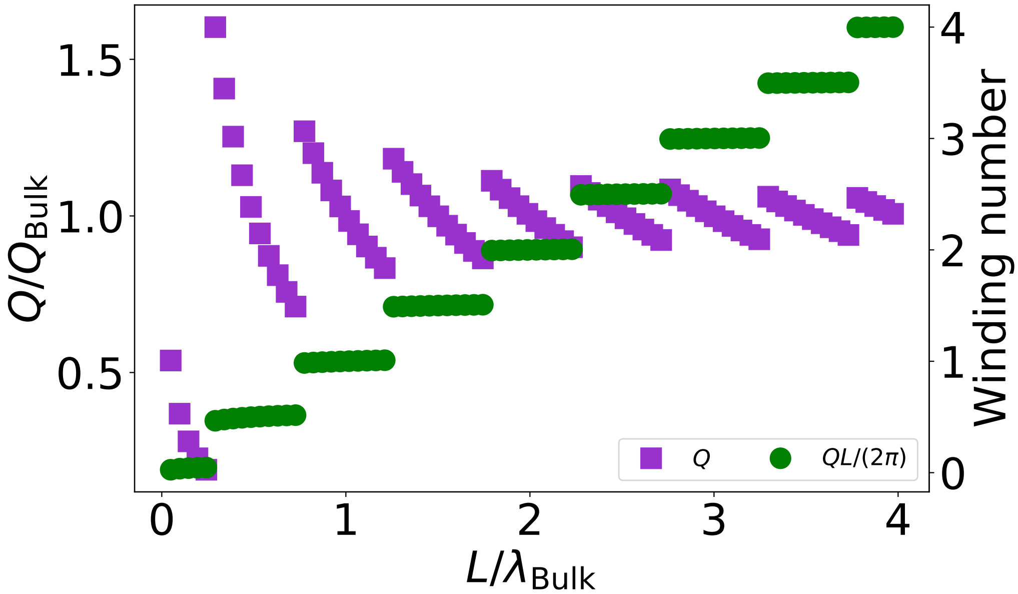

Figure A.24: Q/Q_{Bulk} and winding number versus spin chain length. $d = 0.31416$ and $k_S = -0.90$. The purple squares are Q/Q_{Bulk} and the green circles represent the winding number.

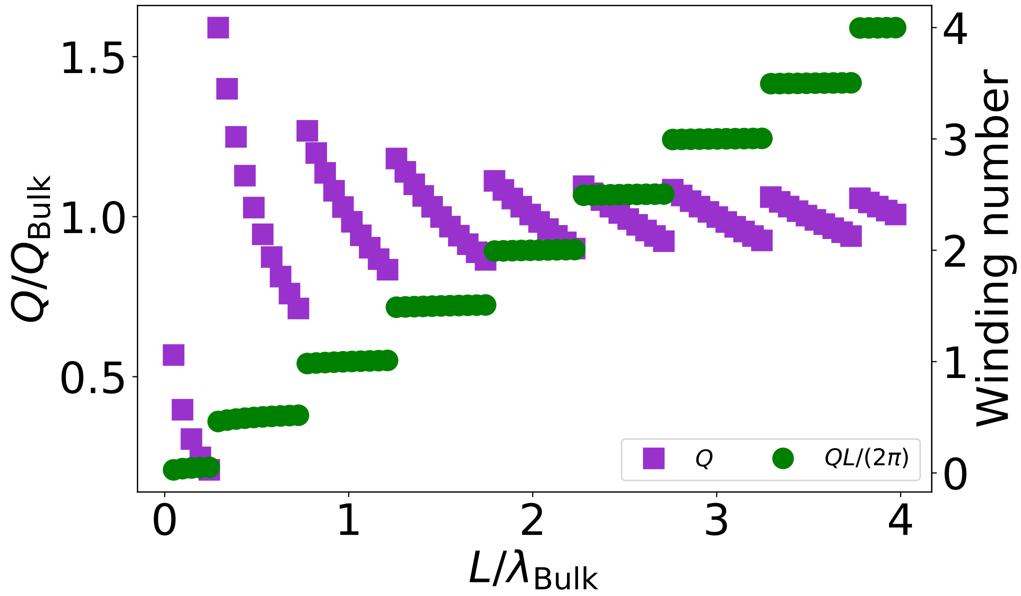

Figure A.25: Q/Q_{Bulk} and winding number versus spin chain length. $d = 0.31416$ and $k_S = -0.80$. The purple squares are Q/Q_{Bulk} and the green circles represent the winding number.

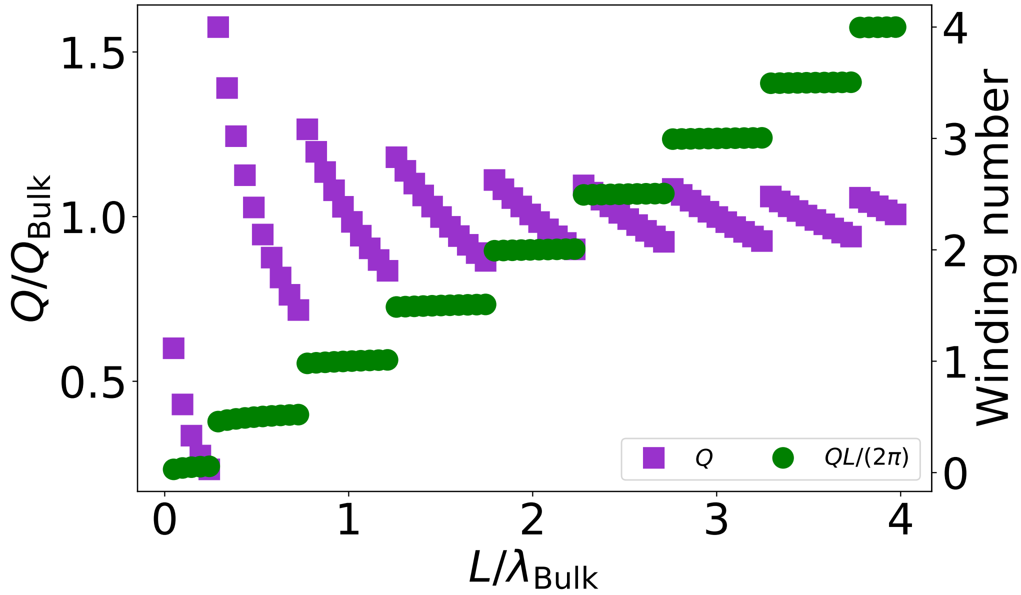

Figure A.26: Q/Q_{Bulk} and winding number versus spin chain length. $d = 0.31416$ and $k_S = -0.70$. The purple squares are Q/Q_{Bulk} and the green circles represent the winding number.

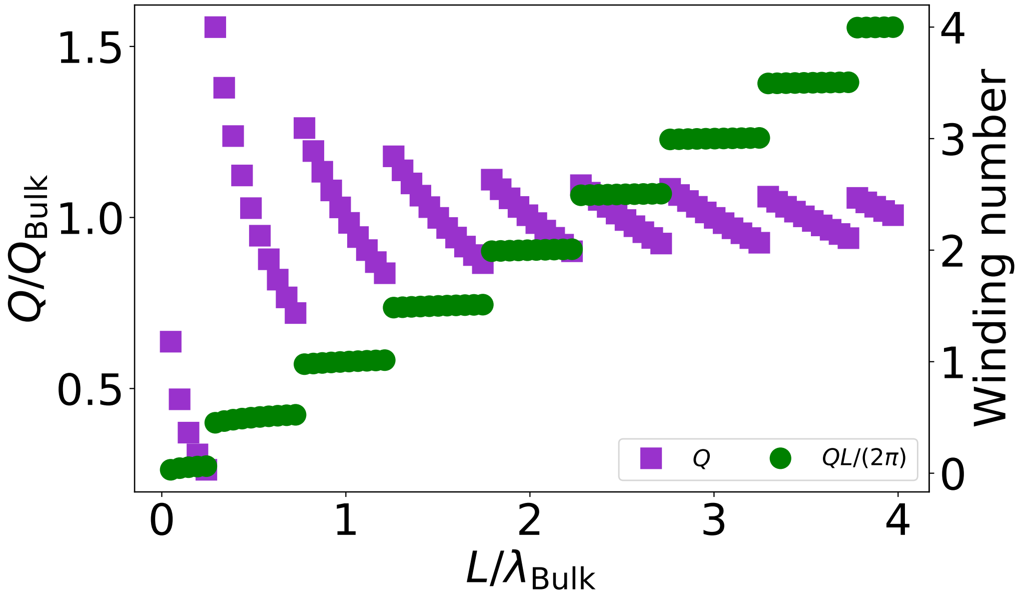

Figure A.27: Q/Q_{Bulk} and winding number versus spin chain length. $d = 0.31416$ and $k_S = -0.60$. The purple squares are Q/Q_{Bulk} and the green circles represent the winding number.

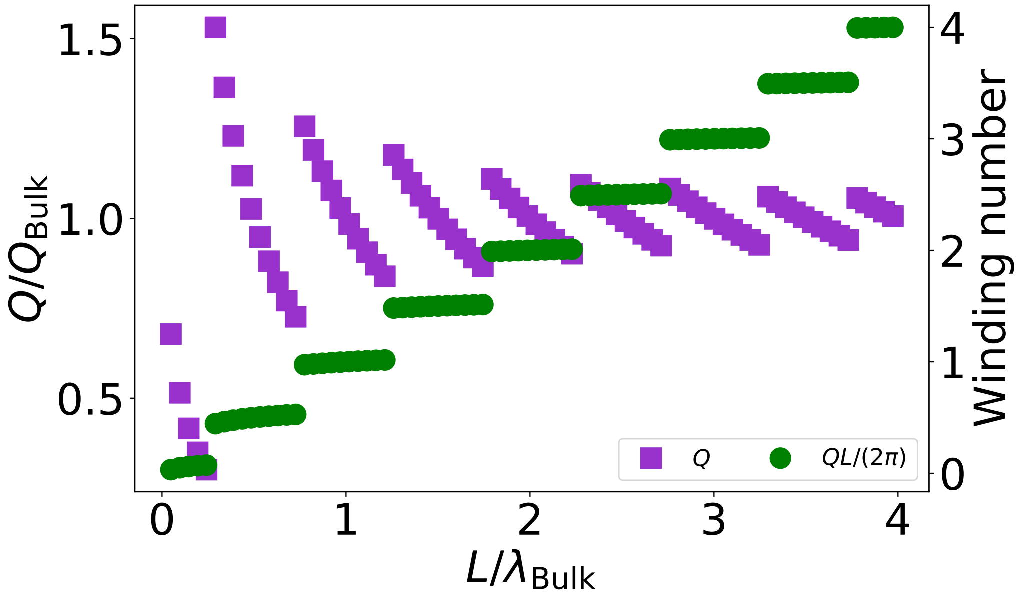

Figure A.28: Q/Q_{Bulk} and winding number versus spin chain length. $d = 0.31416$ and $k_S = -0.50$. The purple squares are Q/Q_{Bulk} and the green circles represent the winding number.

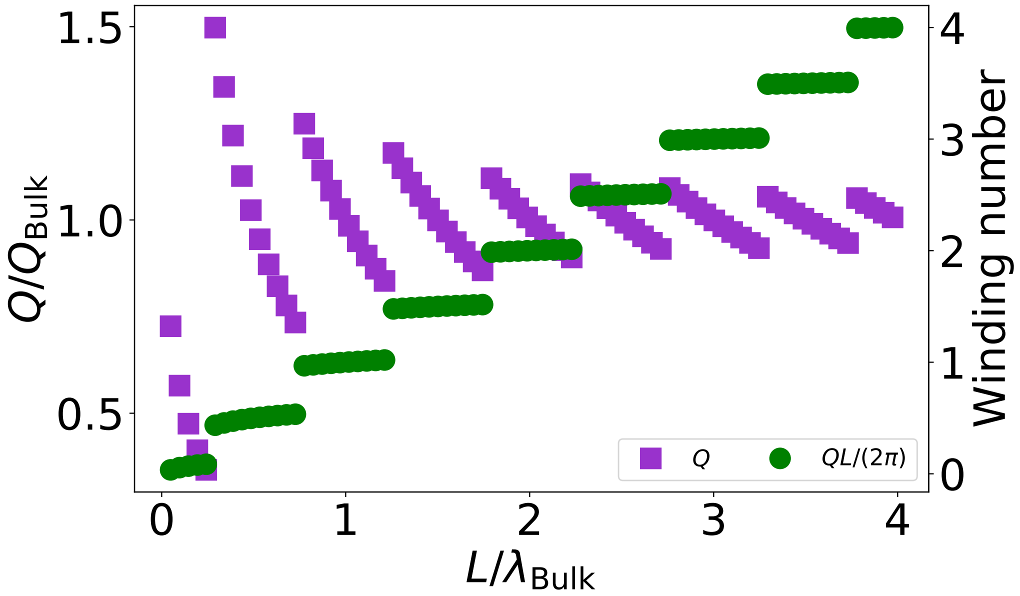

Figure A.29: Q/Q_{Bulk} and winding number versus spin chain length. $d = 0.31416$ and $k_S = -0.40$. The purple squares are Q/Q_{Bulk} and the green circles represent the winding number.

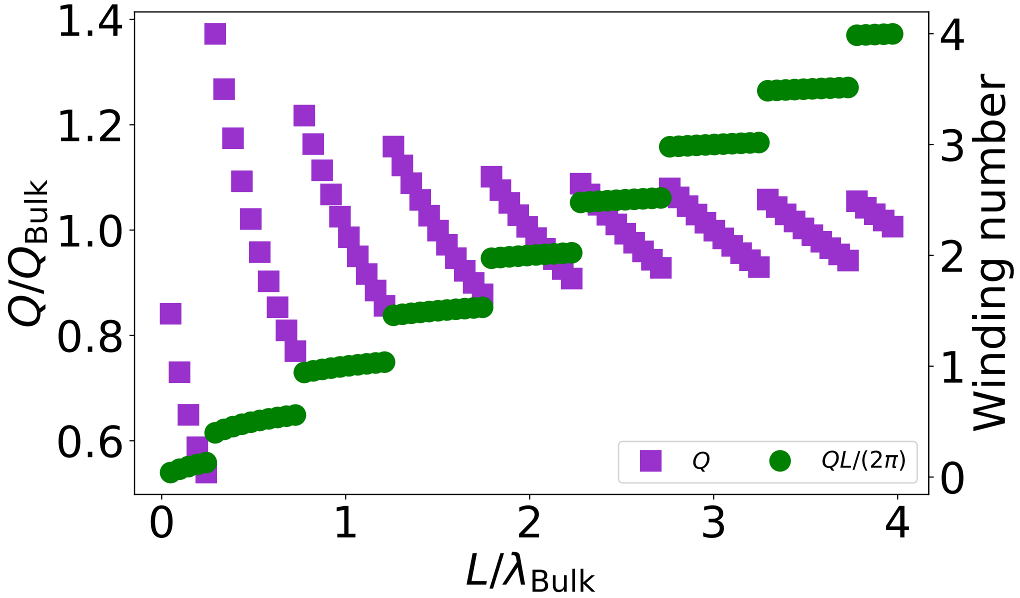

Figure A.30: Q/Q_{Bulk} and winding number versus spin chain length. $d = 0.31416$ and $k_S = -0.20$. The purple squares are Q/Q_{Bulk} and the green circles represent the winding number.

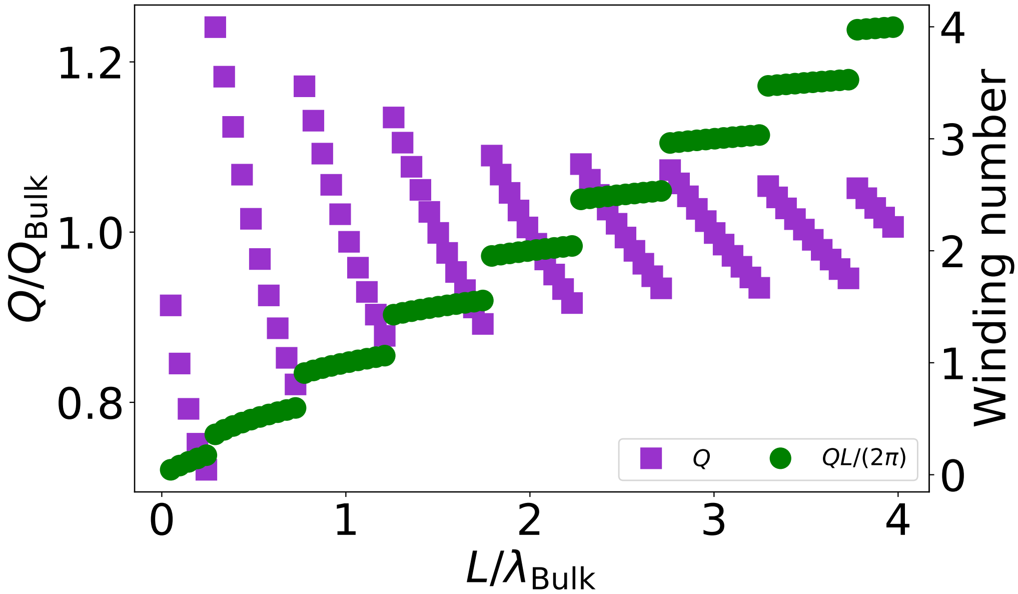

Figure A.31: Q/Q_{Bulk} and winding number versus spin chain length. $d = 0.31416$ and $k_S = -0.10$. The purple squares are Q/Q_{Bulk} and the green circles represent the winding number.

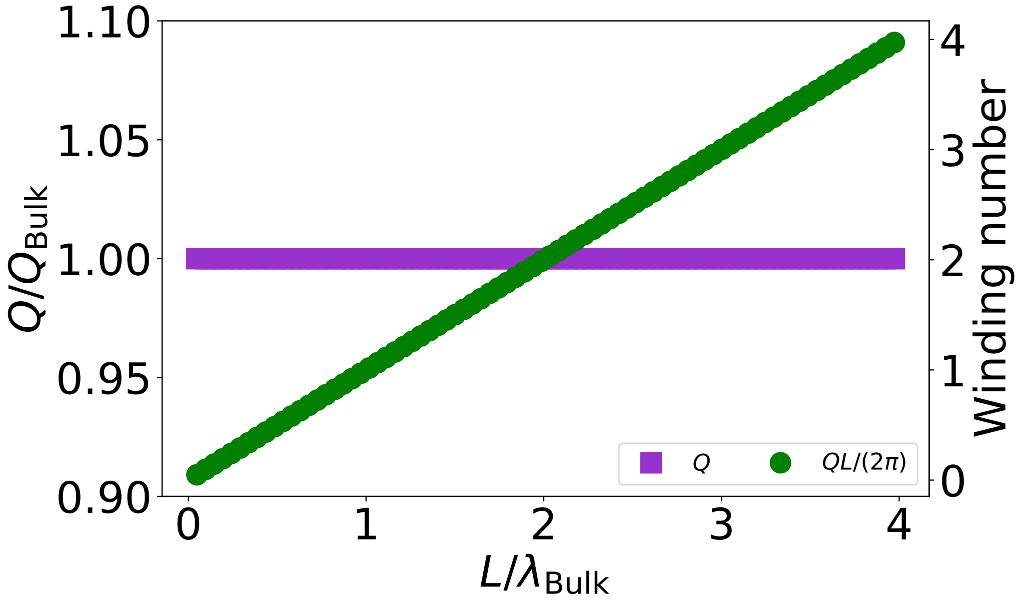

Figure A.32: Q/Q_{Bulk} and winding number versus spin chain length. $d = 0.31416$ and $k_S = 0$. The purple squares are Q/Q_{Bulk} and the green circles represent the winding number.

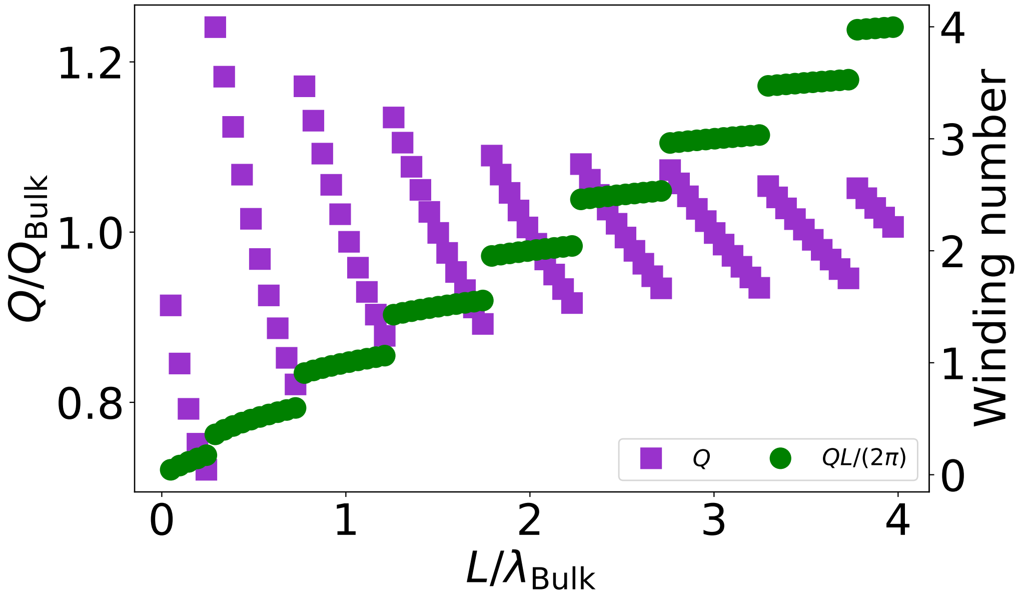

Figure A.33: Q/Q_{Bulk} and winding number versus spin chain length. $d = 0.31416$ and $k_S = 0.10$. The purple squares are Q/Q_{Bulk} and the green circles represent the winding number.

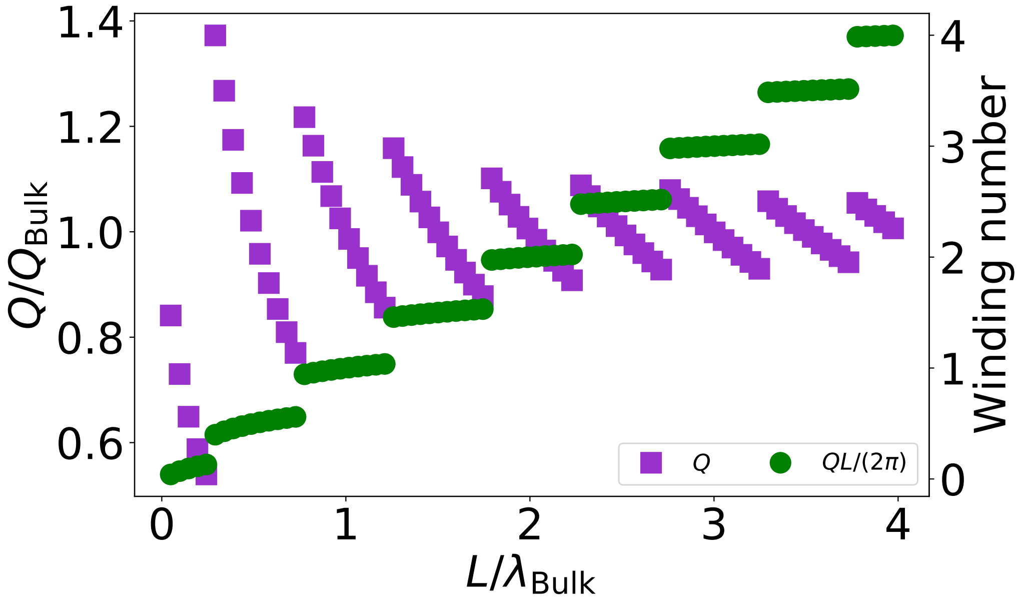

Figure A.34: Q/Q_{Bulk} and winding number versus spin chain length. $d = 0.31416$ and $k_S = 0.20$. The purple squares are Q/Q_{Bulk} and the green circles represent the winding number.

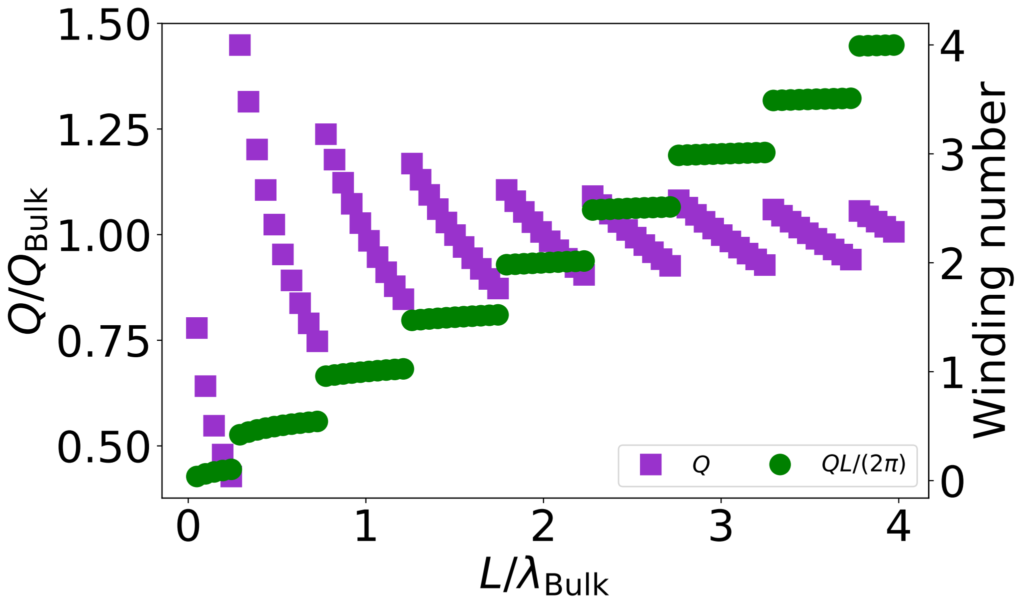

Figure A.35: Q/Q_{Bulk} and winding number versus spin chain length. $d = 0.31416$ and $k_S = 0.30$. The purple squares are Q/Q_{Bulk} and the green circles represent the winding number.

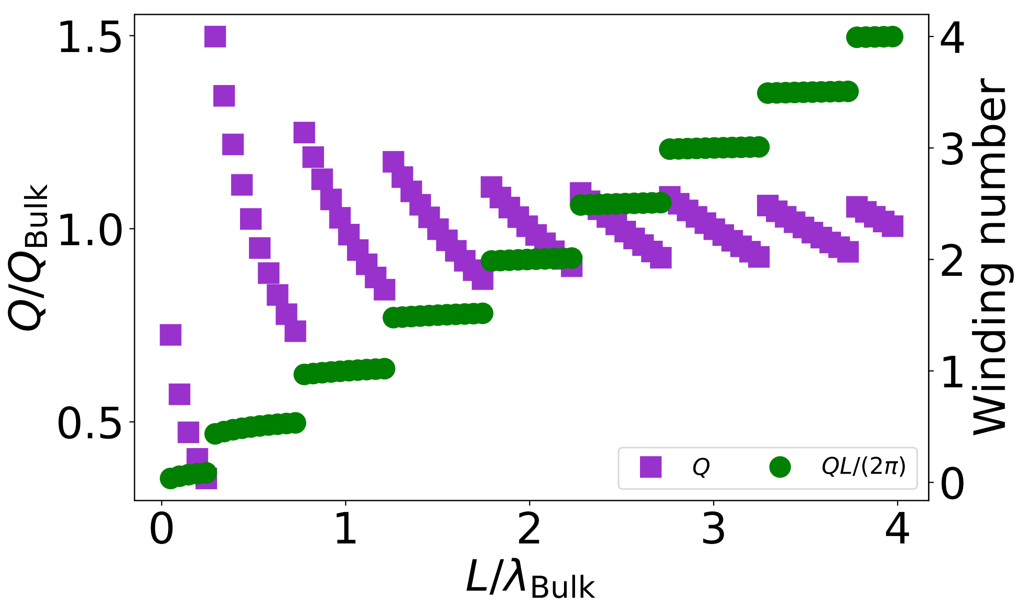

Figure A.36: Q/Q_{Bulk} and winding number versus spin chain length. $d = 0.31416$ and $k_S = 0.40$. The purple squares are Q/Q_{Bulk} and the green circles represent the winding number.

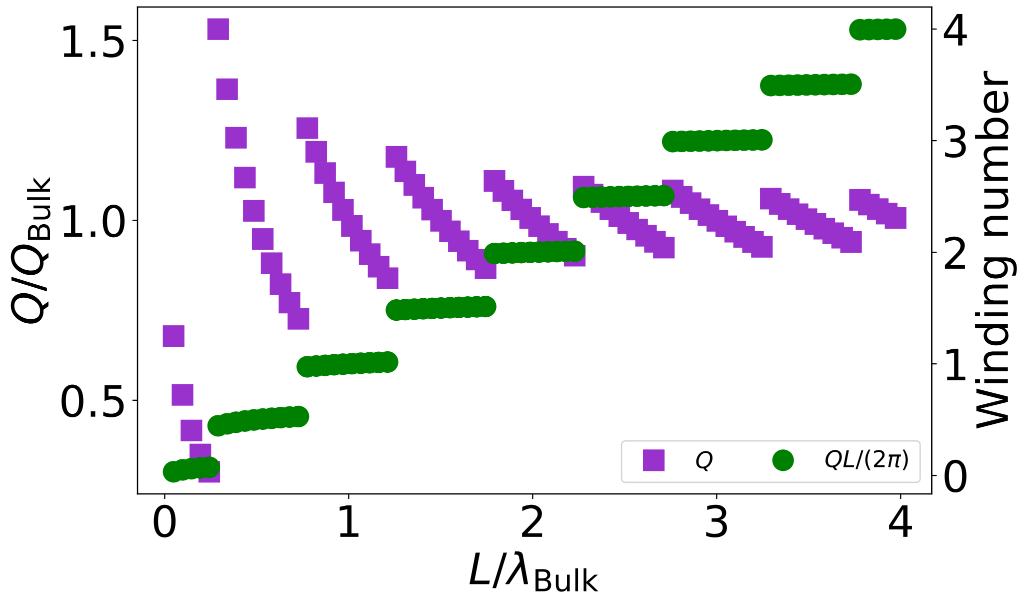

Figure A.37: Q/Q_{Bulk} and winding number versus spin chain length. $d = 0.31416$ and $k_S = 0.50$. The purple squares are Q/Q_{Bulk} and the green circles represent the winding number.

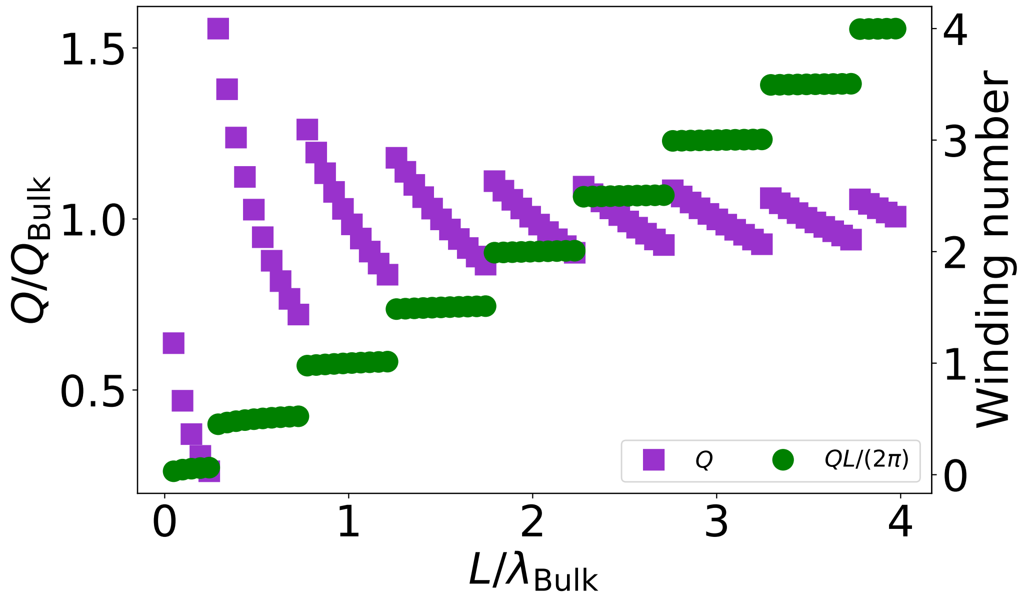

Figure A.38: Q/Q_{Bulk} and winding number versus spin chain length. $d = 0.31416$ and $k_S = 0.60$. The purple squares are Q/Q_{Bulk} and the green circles represent the winding number.

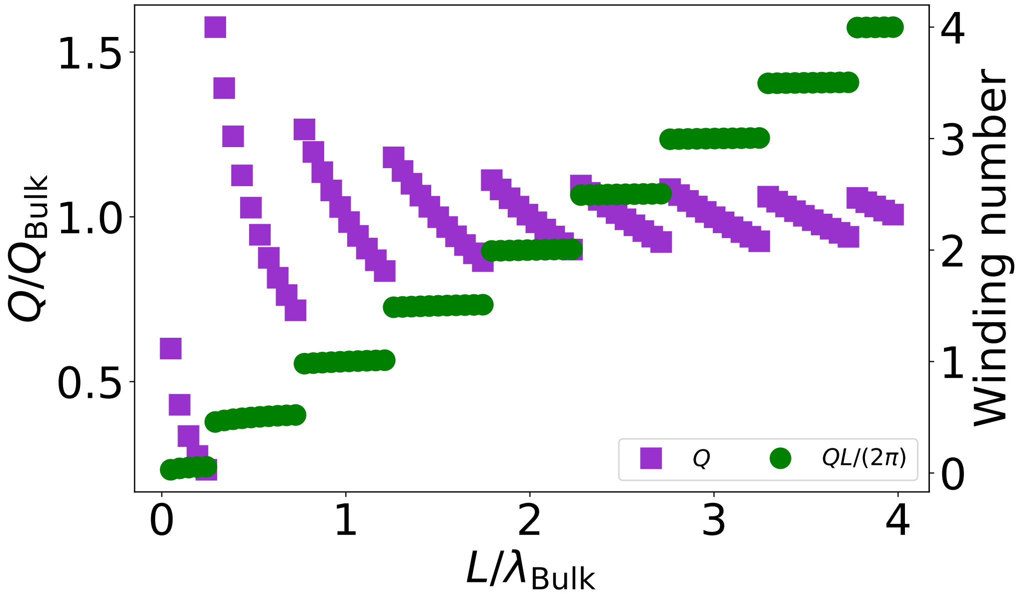

Figure A.39: Q/Q_{Bulk} and winding number versus spin chain length. $d = 0.31416$ and $k_S = 0.70$. The purple squares are Q/Q_{Bulk} and the green circles represent the winding number.

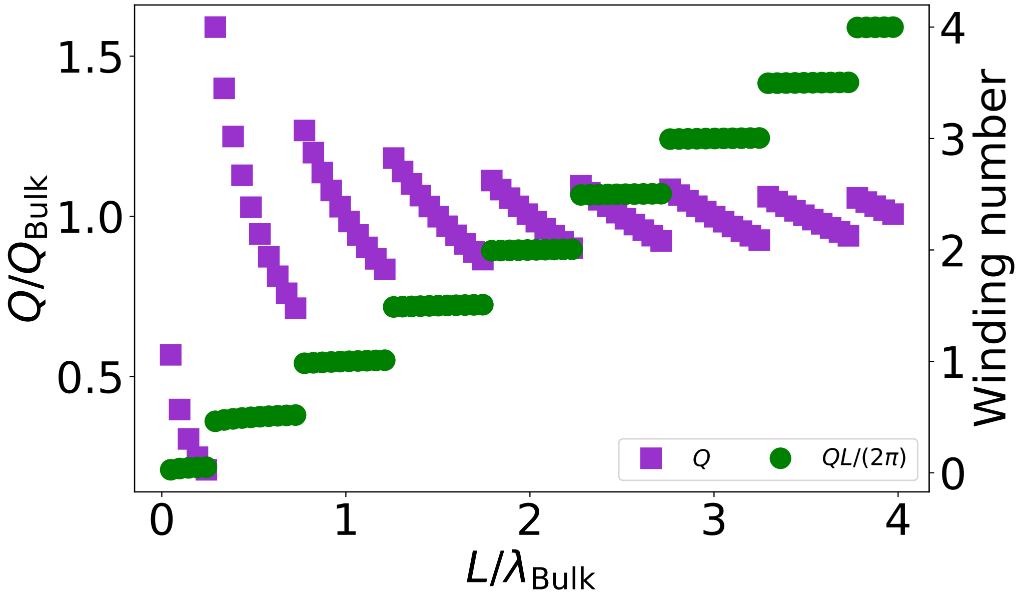

Figure A.40: Q/Q_{Bulk} and winding number versus spin chain length. $d = 0.31416$ and $k_S = 0.80$. The purple squares are Q/Q_{Bulk} and the green circles represent the winding number.

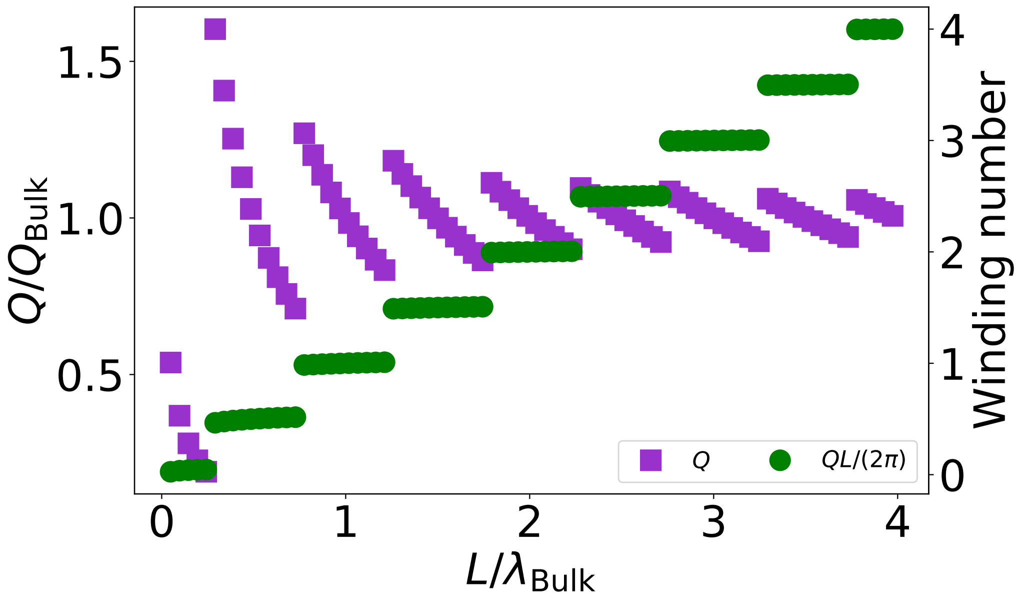

Figure A.41: Q/Q_{Bulk} and winding number versus spin chain length. $d = 0.31416$ and $k_S = 0.90$. The purple squares are Q/Q_{Bulk} and the green circles represent the winding number.

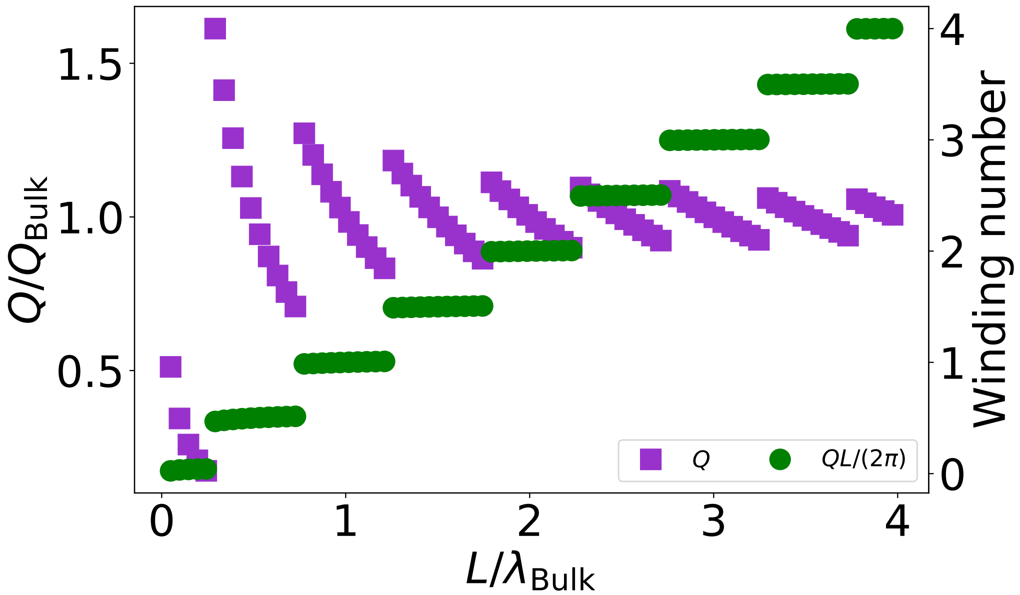

Figure A.42: Q/Q_{Bulk} and winding number versus spin chain length. $d = 0.31416$ and $k_S = 1.00$. The purple squares are Q/Q_{Bulk} and the green circles represent the winding number.

$d = 0.04724$ for the proceeding plots. Figure A.43 plots Q/Q_{Bulk} versus spin chain length for multiple k_S values. Figures A.44 to A.63 plot Q/Q_{Bulk} and winding number versus spin chain length. Again, for all values of k_S, the jump discontinuities occur at the same chain lengths.

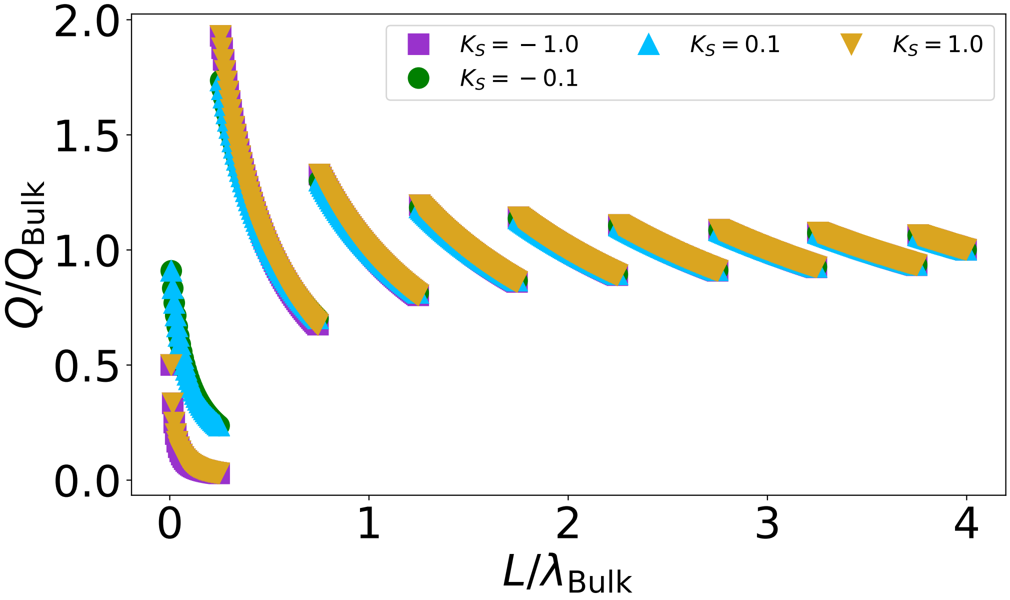

Figure A.43: Q/Q_{Bulk} versus spin chain length. $d = 0.04724$ and $k_S = -1.00$, -0.10, 0.10, and 1.00.

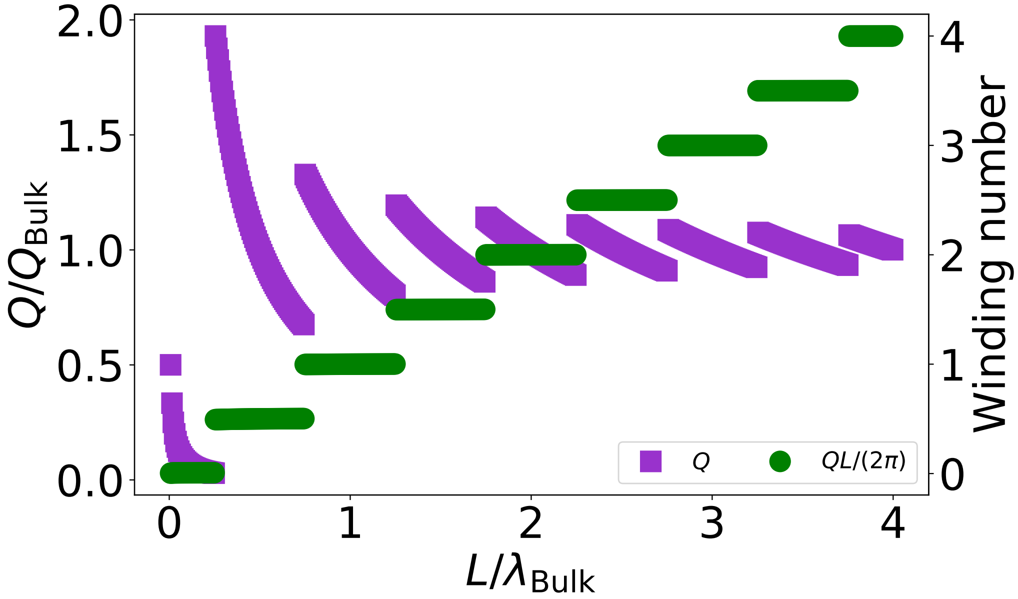

Figure A.44: Q/Q_{Bulk} and winding number versus spin chain length. $d = 0.04724$ and $k_S = -1.00$. The purple squares are Q/Q_{Bulk} and the green circles represent the winding number.

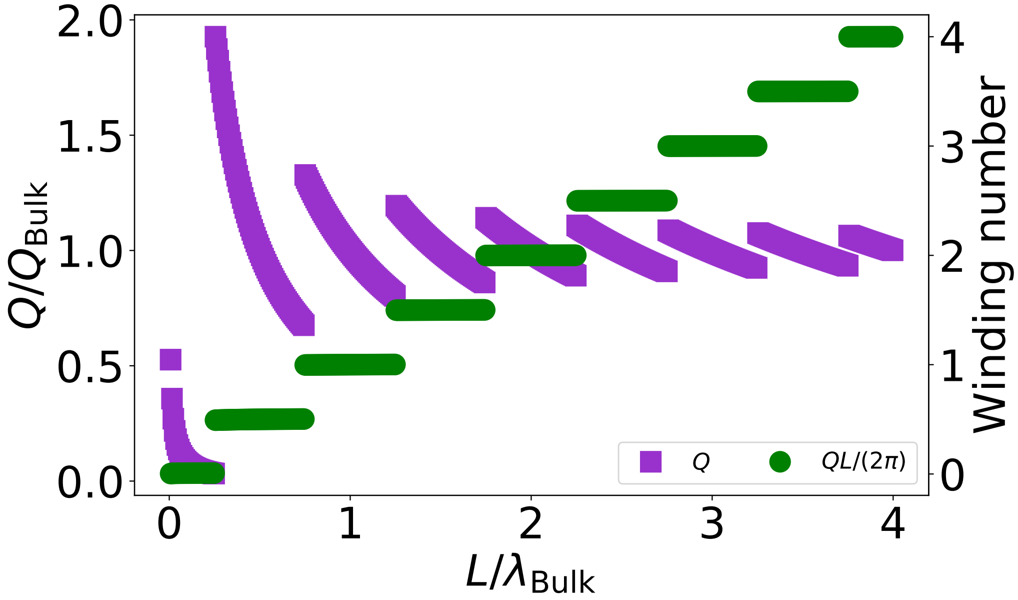

Figure A.45: Q/Q_{Bulk} and winding number versus spin chain length. $d = 0.04724$ and $k_S = -0.90$. The purple squares are Q/Q_{Bulk} and the green circles represent the winding number.

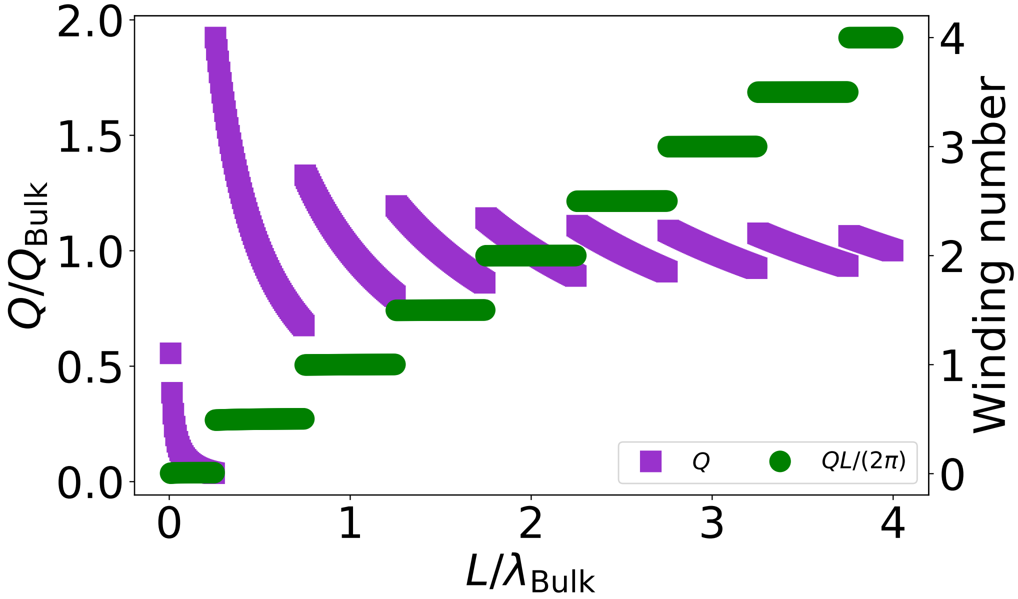

Figure A.46: Q/Q_{Bulk} and winding number versus spin chain length. $d = 0.04724$ and $k_S = -0.80$. The purple squares are Q/Q_{Bulk} and the green circles represent the winding number.

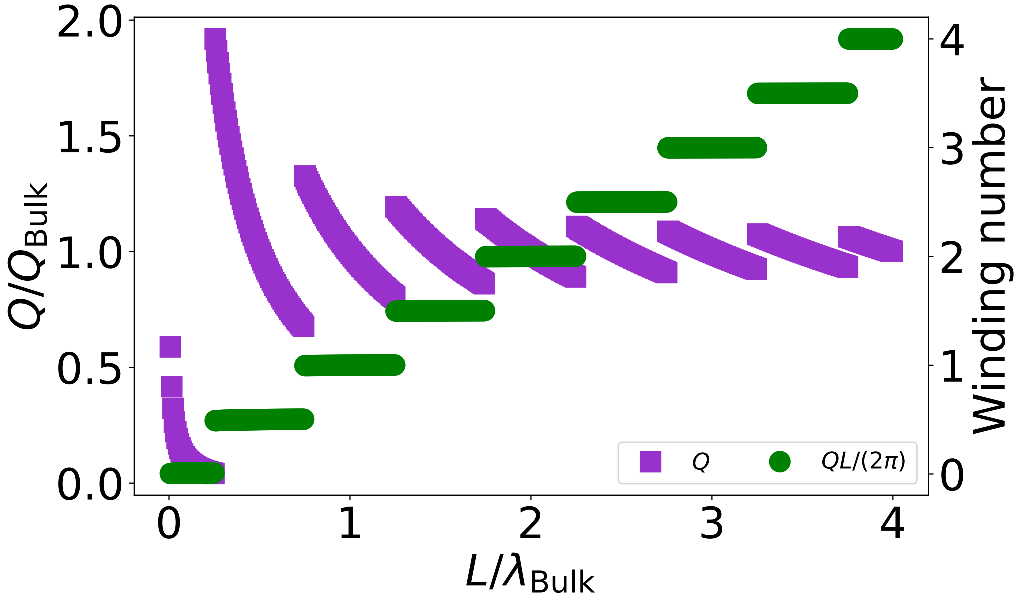

Figure A.47: Q/Q_{Bulk} and winding number versus spin chain length. $d = 0.04724$ and $k_S = -0.70$. The purple squares are Q/Q_{Bulk} and the green circles represent the winding number.

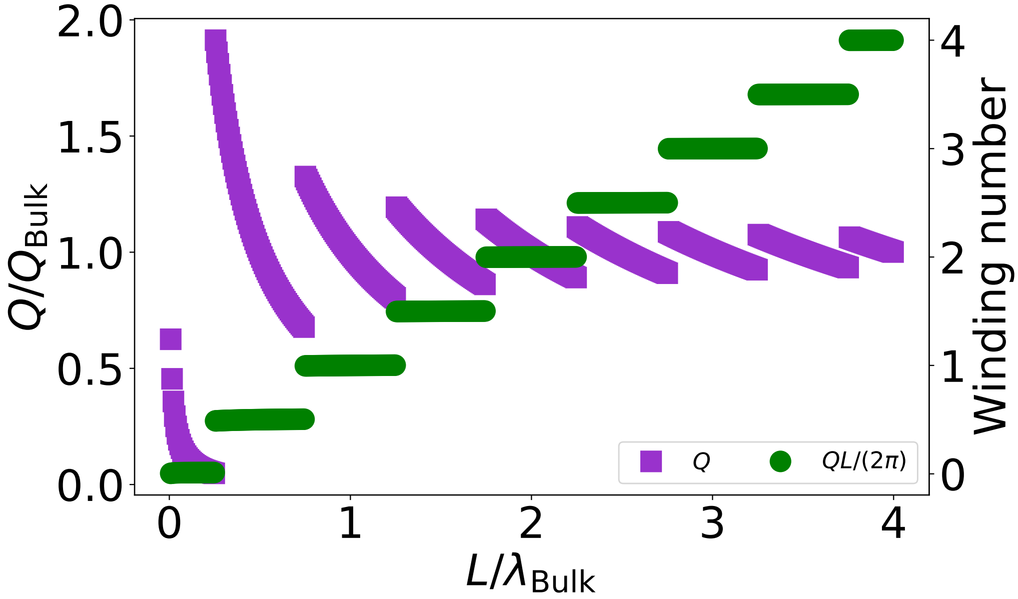

Figure A.48: Q/Q_{Bulk} and winding number versus spin chain length. $d = 0.04724$ and $k_S = -0.60$. The purple squares are Q/Q_{Bulk} and the green circles represent the winding number.

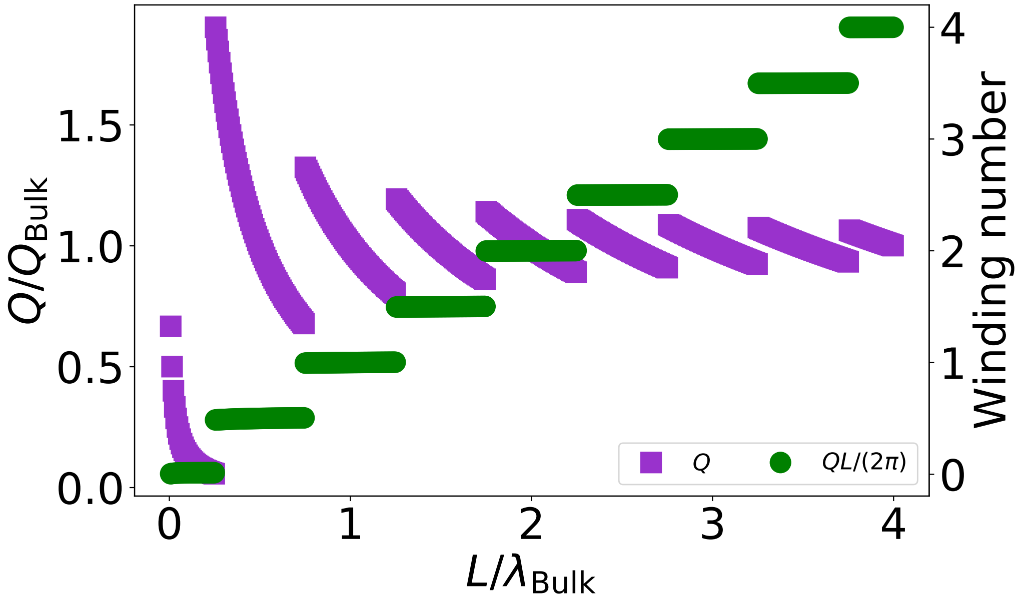

Figure A.49: Q/Q_{Bulk} and winding number versus spin chain length. $d = 0.04724$ and $k_S = -0.50$. The purple squares are Q/Q_{Bulk} and the green circles represent the winding number.

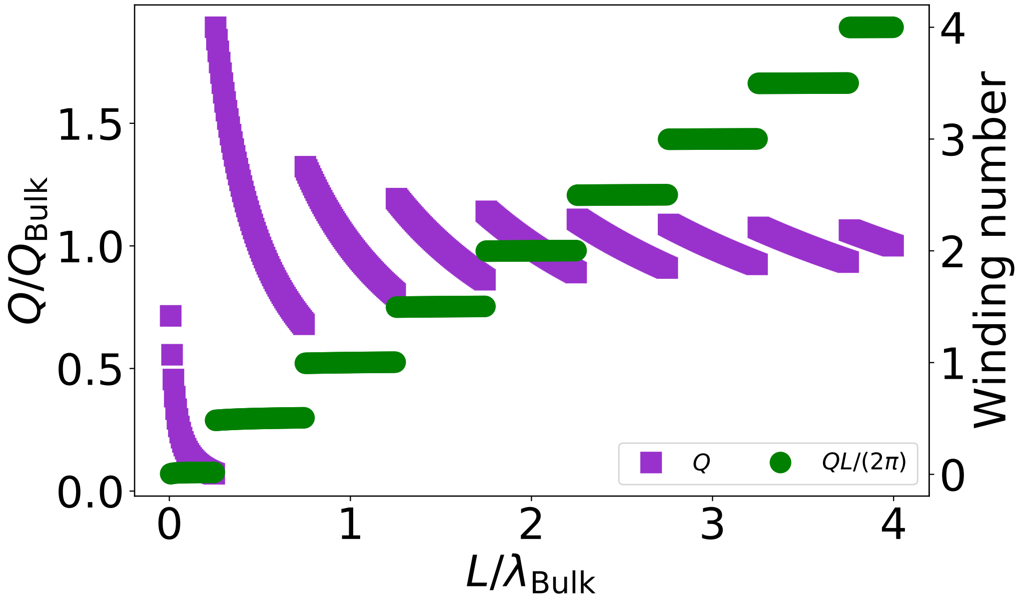

Figure A.50: Q/Q_{Bulk} and winding number versus spin chain length. $d = 0.04724$ and $k_S = -0.40$. The purple squares are Q/Q_{Bulk} and the green circles represent the winding number.

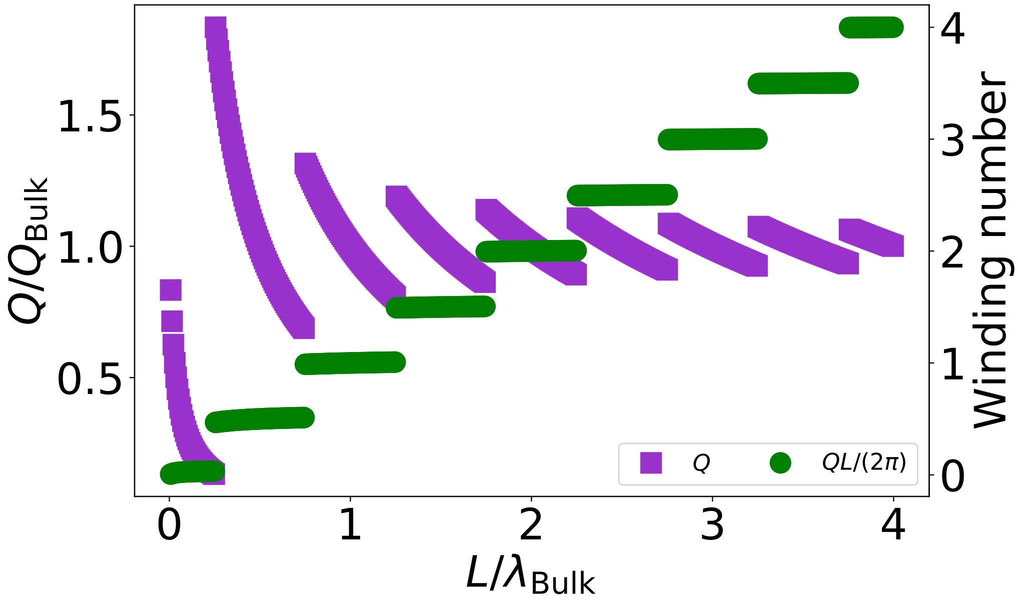

Figure A.51: Q/Q_{Bulk} and winding number versus spin chain length. $d = 0.04724$ and $k_S = -0.20$. The purple squares are Q/Q_{Bulk} and the green circles represent the winding number.

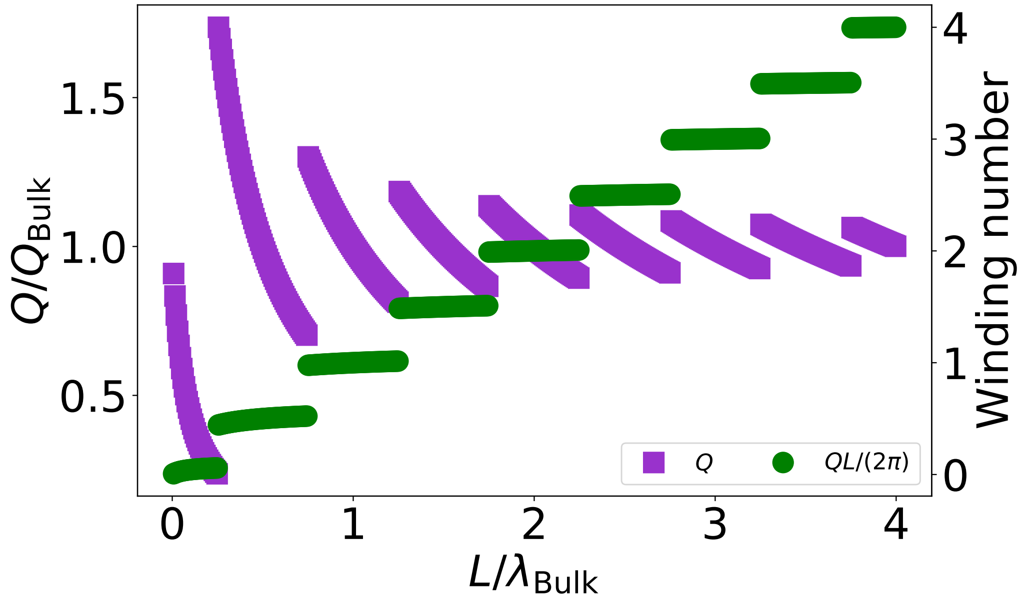

Figure A.52: Q/Q_{Bulk} and winding number versus spin chain length. $d = 0.04724$ and $k_S = -0.10$. The purple squares are Q/Q_{Bulk} and the green circles represent the winding number.

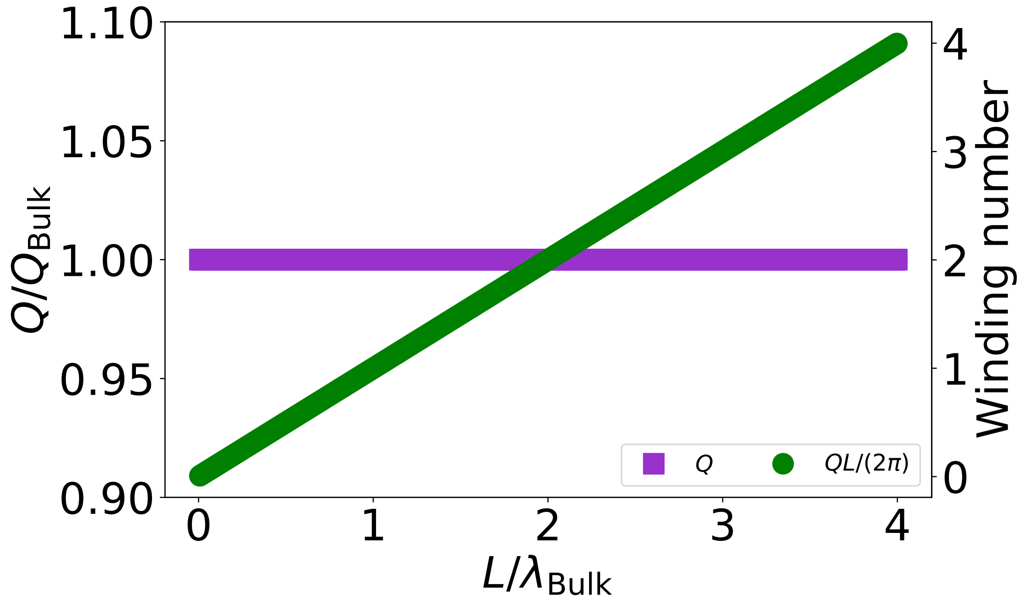

Figure A.53: Q/Q_{Bulk} and winding number versus spin chain length. $d = 0.04724$ and $k_S = 0$. The purple squares are Q/Q_{Bulk} and the green circles represent the winding number.

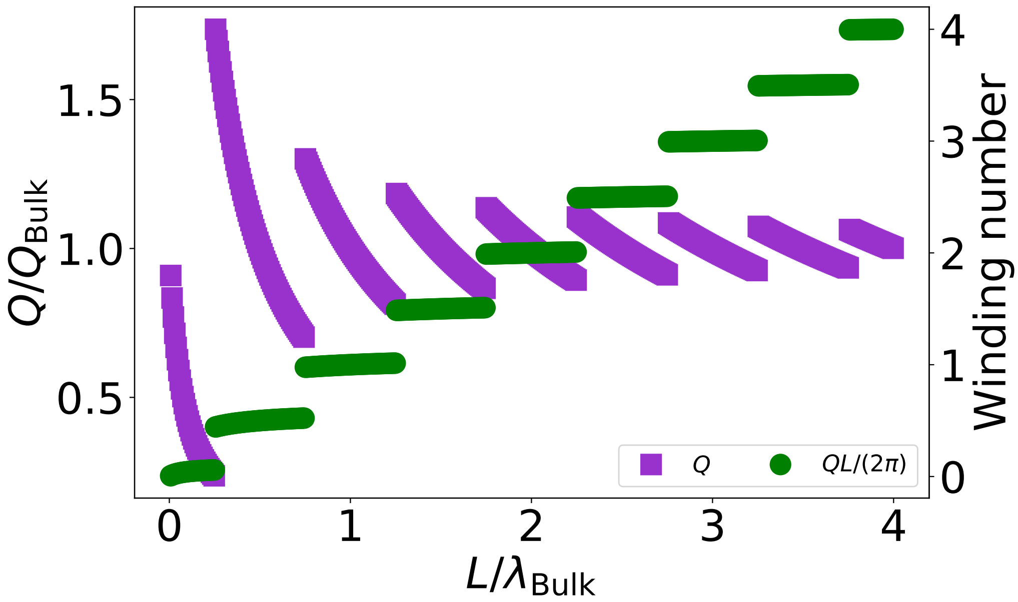

Figure A.54: Q/Q_{Bulk} and winding number versus spin chain length. $d = 0.04724$ and $k_S = 0.10$. The purple squares are Q/Q_{Bulk} and the green circles represent the winding number.

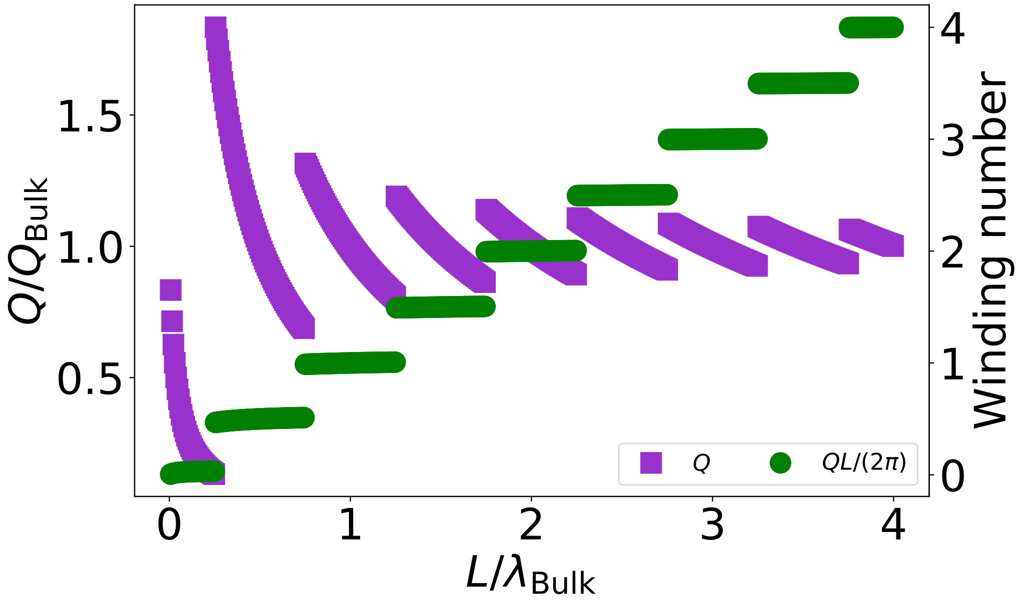

Figure A.55: Q/Q_{Bulk} and winding number versus spin chain length. $d = 0.04724$ and $k_S = 0.20$. The purple squares are Q/Q_{Bulk} and the green circles represent the winding number.

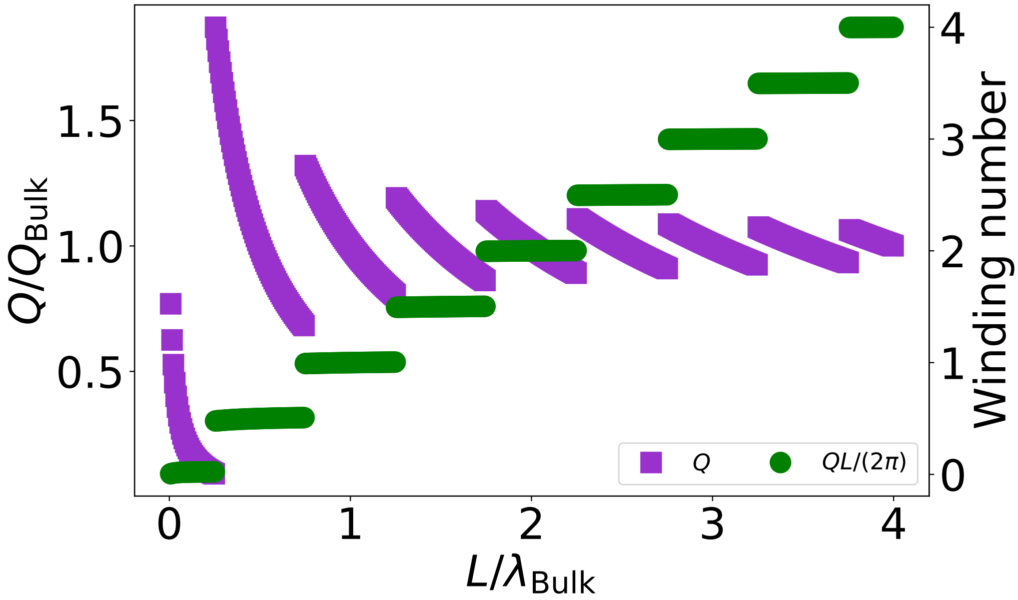

Figure A.56: Q/Q_{Bulk} and winding number versus spin chain length. $d = 0.04724$ and $k_S = 0.30$. The purple squares are Q/Q_{Bulk} and the green circles represent the winding number.

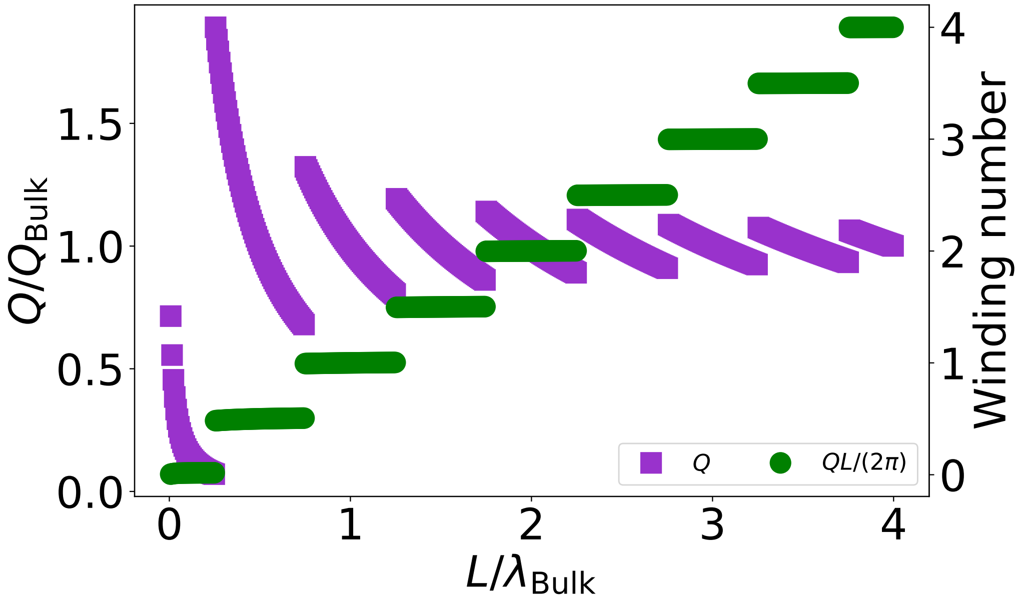

Figure A.57: Q/Q_{Bulk} and winding number versus spin chain length. $d = 0.04724$ and $k_S = 0.40$. The purple squares are Q/Q_{Bulk} and the green circles represent the winding number.

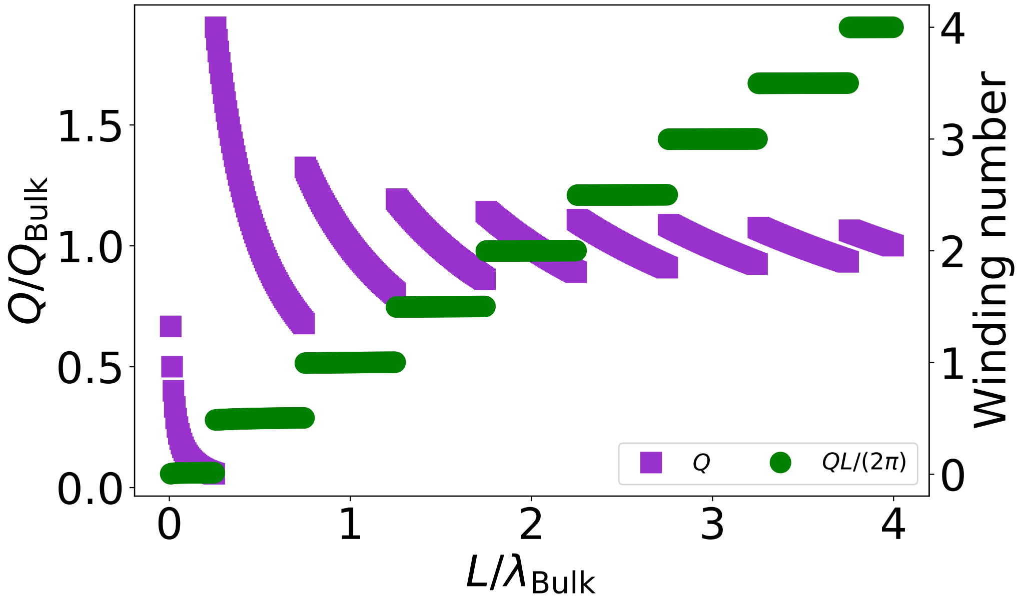

Figure A.58: Q/Q_{Bulk} and winding number versus spin chain length. $d = 0.04724$ and $k_S = 0.50$. The purple squares are Q/Q_{Bulk} and the green circles represent the winding number.

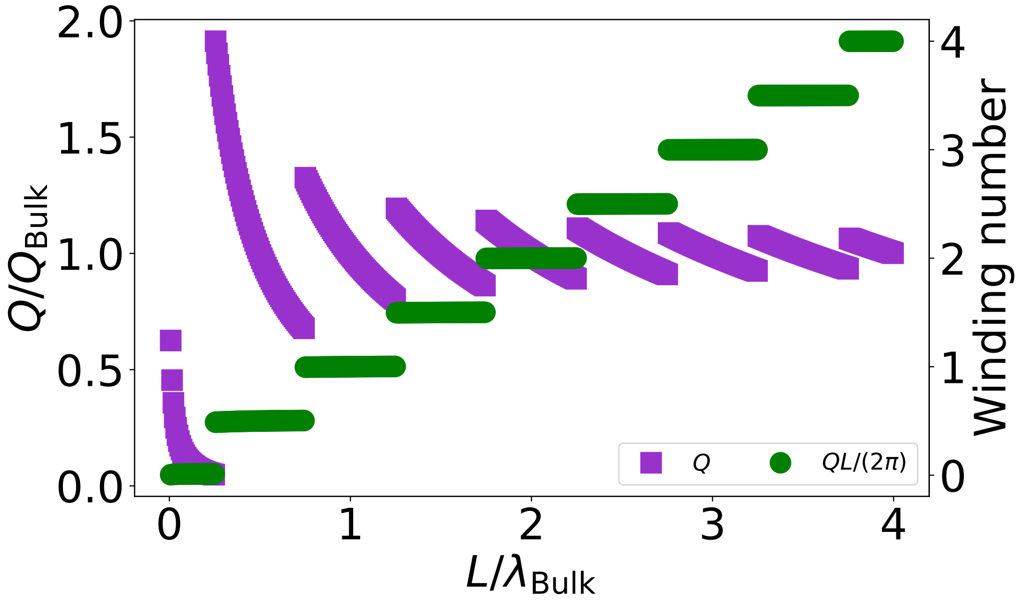

Figure A.59: Q/Q_{Bulk} and winding number versus spin chain length. $d = 0.04724$ and $k_S = 0.60$. The purple squares are Q/Q_{Bulk} and the green circles represent the winding number.

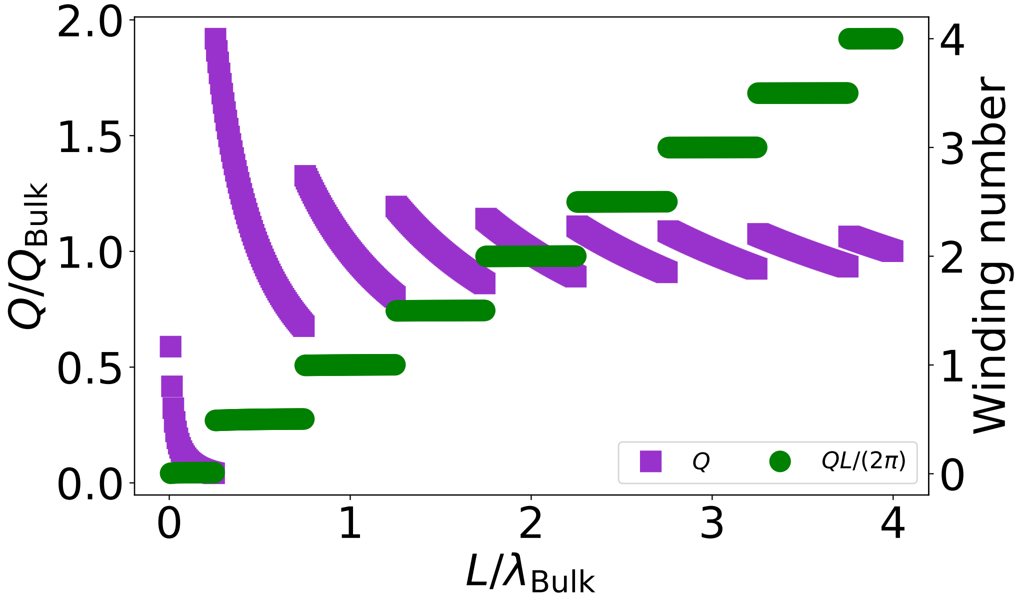

Figure A.60: Q/Q_{Bulk} and winding number versus spin chain length. $d = 0.04724$ and $k_S = 0.70$. The purple squares are Q/Q_{Bulk} and the green circles represent the winding number.

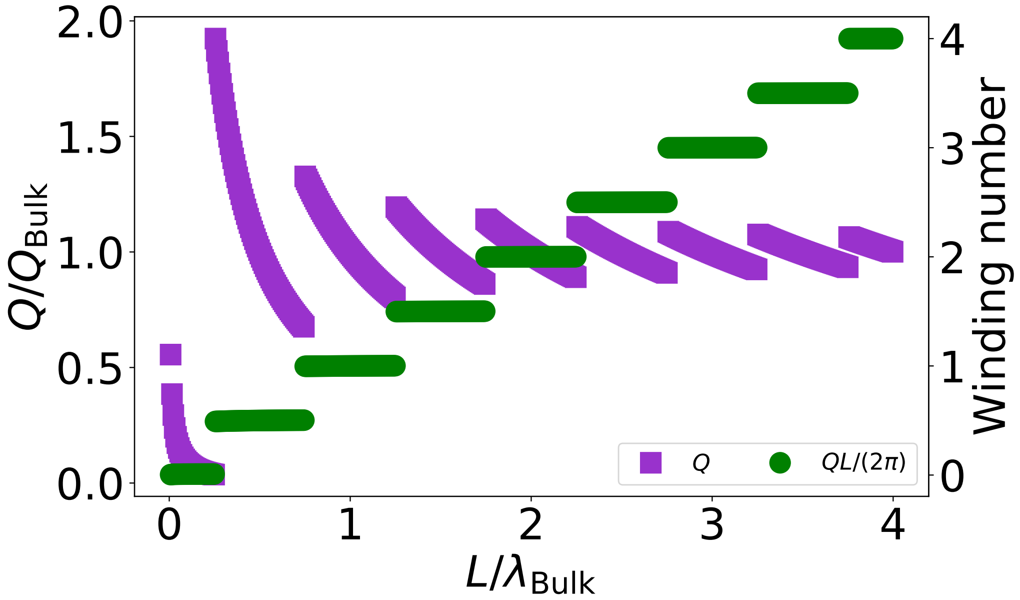

Figure A.61: Q/Q_{Bulk} and winding number versus spin chain length. $d = 0.04724$ and $k_S = 0.80$. The purple squares are Q/Q_{Bulk} and the green circles represent the winding number.

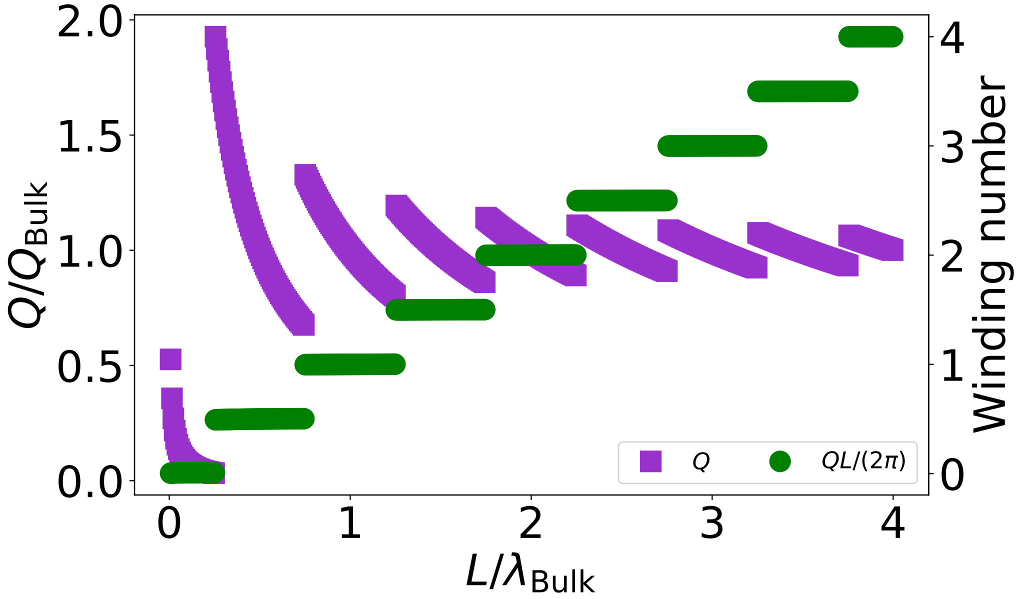

Figure A.62: Q/Q_{Bulk} and winding number versus spin chain length. $d = 0.04724$ and $k_S = 0.90$. The purple squares are Q/Q_{Bulk} and the green circles represent the winding number.

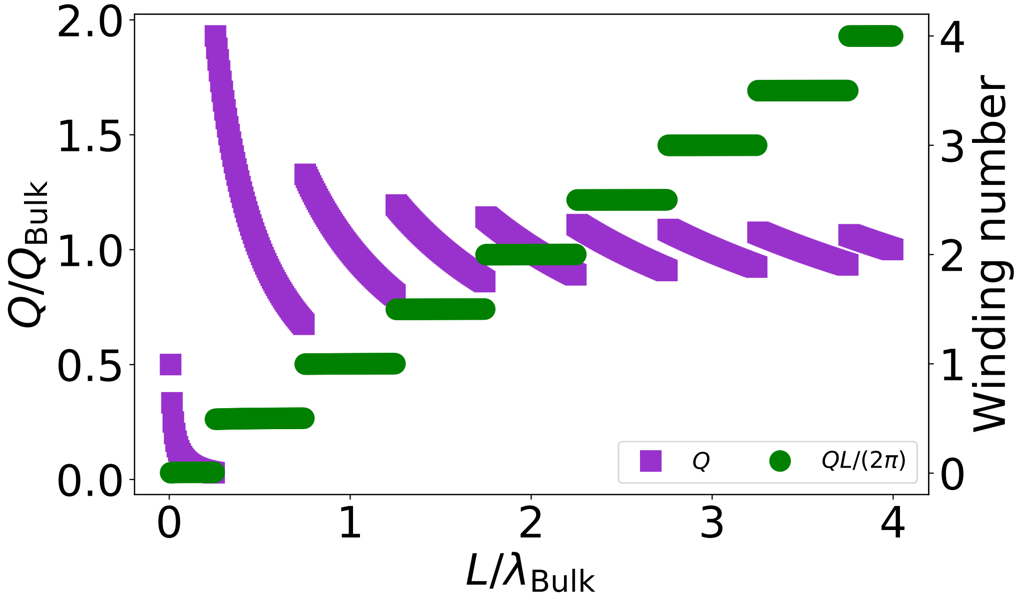

Figure A.63: Q/Q_{Bulk} and winding number versus spin chain length. $d = 0.04724$ and $k_S = 1.00$. The purple squares are Q/Q_{Bulk} and the green circles represent the winding number.

Appendix B

Additional Spin Plaquette Results

The following plots are of minimizations from spin plaquettes. There was equal anisotropy on all surfaces ($k_S^x = k_S^z = k_S$). For all plots, $d = 0.15708$. k_S varies between -1.00 and 1.00. The plots show Q/Q_{bulk} versus the side length of the plaquette nanoparticle, as well as the magnetization versus side length. The magnetization had units of $D'S/J$. Accompanying the plots are spin configurations for plaquettes of select sizes for the various values of k_S.

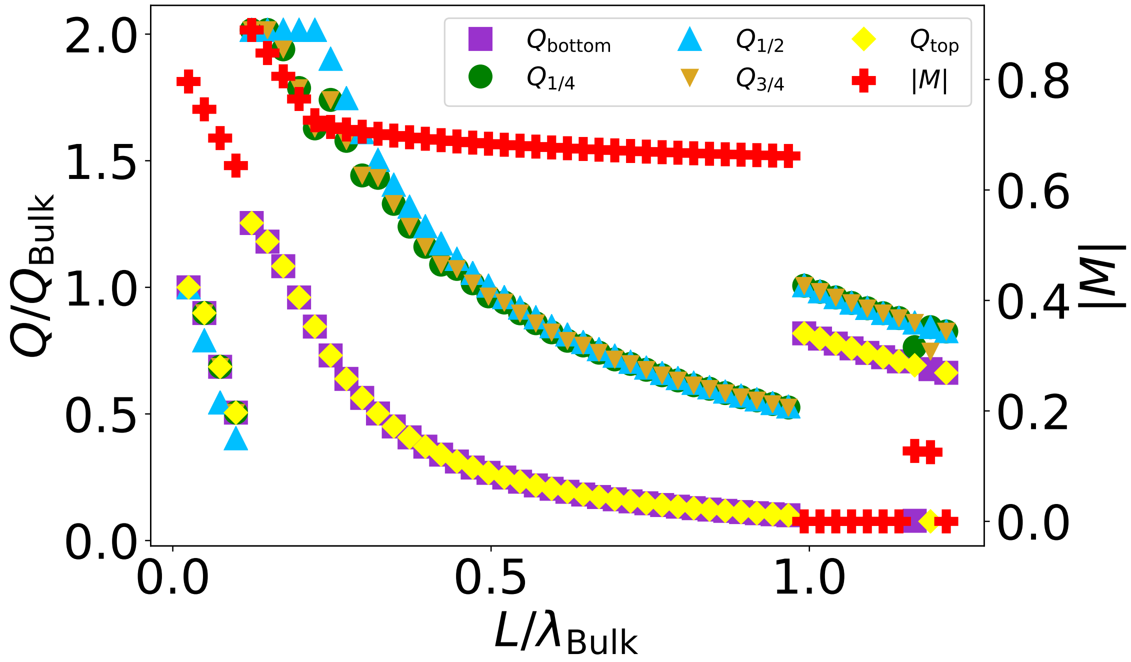

Figure B.1: Q/Q_{bulk} and spin-canting-induced magnetization versus nanoparticle length. $d = 0.15708$, $k_S = -1.00$. Magnetization is in units of $D'S/J$.

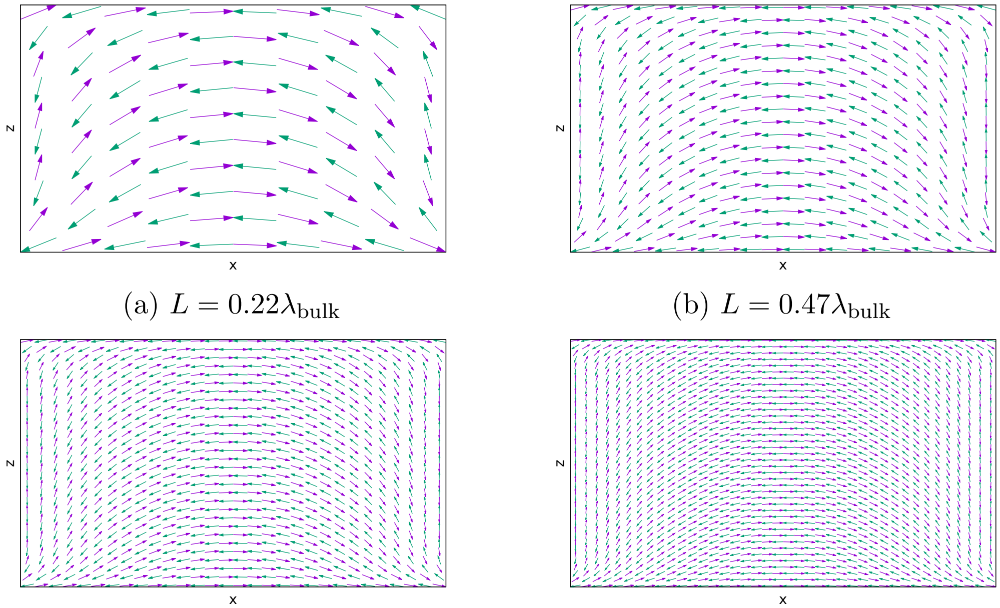

(a) $L = 0.22\lambda_{\text{bulk}}$

(b) $L = 0.47\lambda_{\text{bulk}}$

(c) $L = 0.72\lambda_{\text{bulk}}$

(d) $L = 0.97\lambda_{\text{bulk}}$

Figure B.2: Nanoparticles of different sizes with $d = 0.15708$ and $k_S = -1.00$. Spins of the same colour belong to the same sublattice. The size of the nanoparticles is $L \times L$.

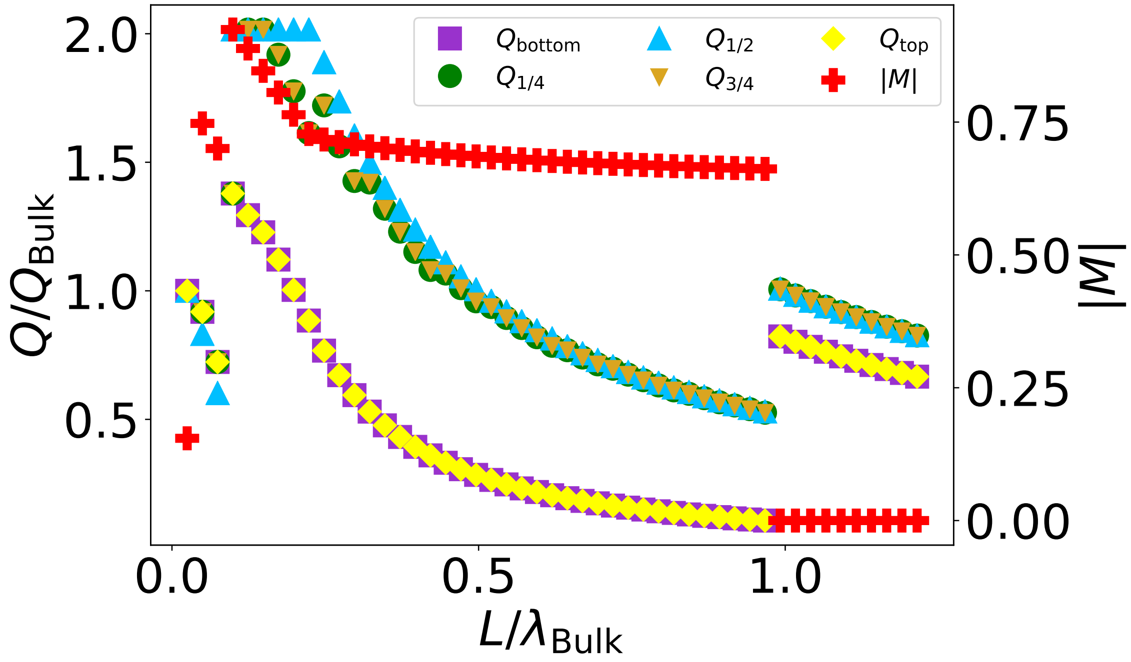

Figure B.3: Q/Q_{bulk} and spin-canting-induced magnetization versus nanoparticle length. $d = 0.15708$, $k_S = -0.90$. Magnetization is in units of $D'S/J$.

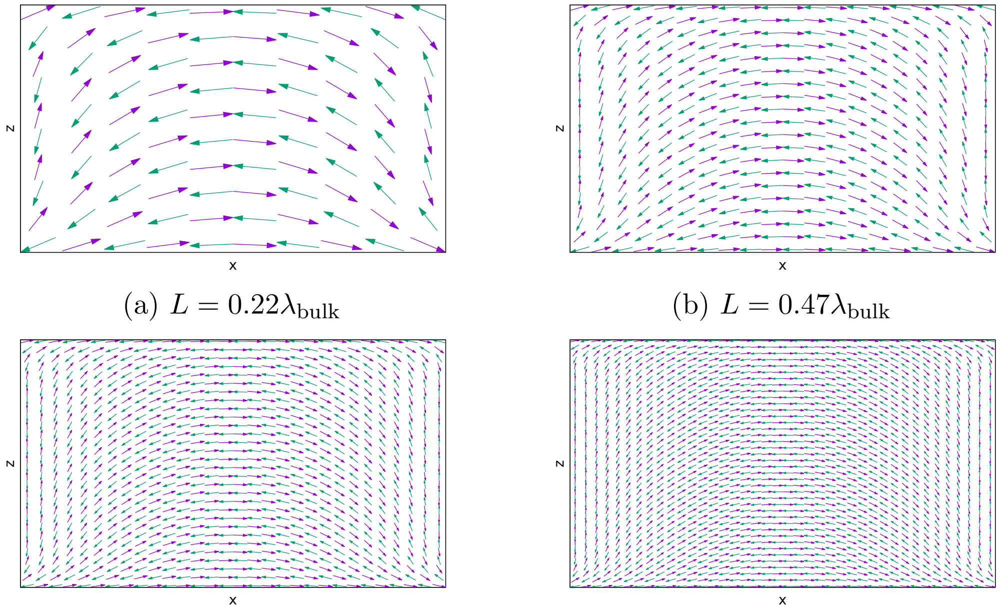

(a) $L = 0.22\lambda_{\text{bulk}}$ (b) $L = 0.47\lambda_{\text{bulk}}$

(c) $L = 0.72\lambda_{\text{bulk}}$ (d) $L = 0.97\lambda_{\text{bulk}}$

Figure B.4: Nanoparticles of different sizes with $d = 0.15708$ and $k_S = -0.90$. Spins of the same colour belong to the same sublattice. The size of the nanoparticles is $L \times L$.

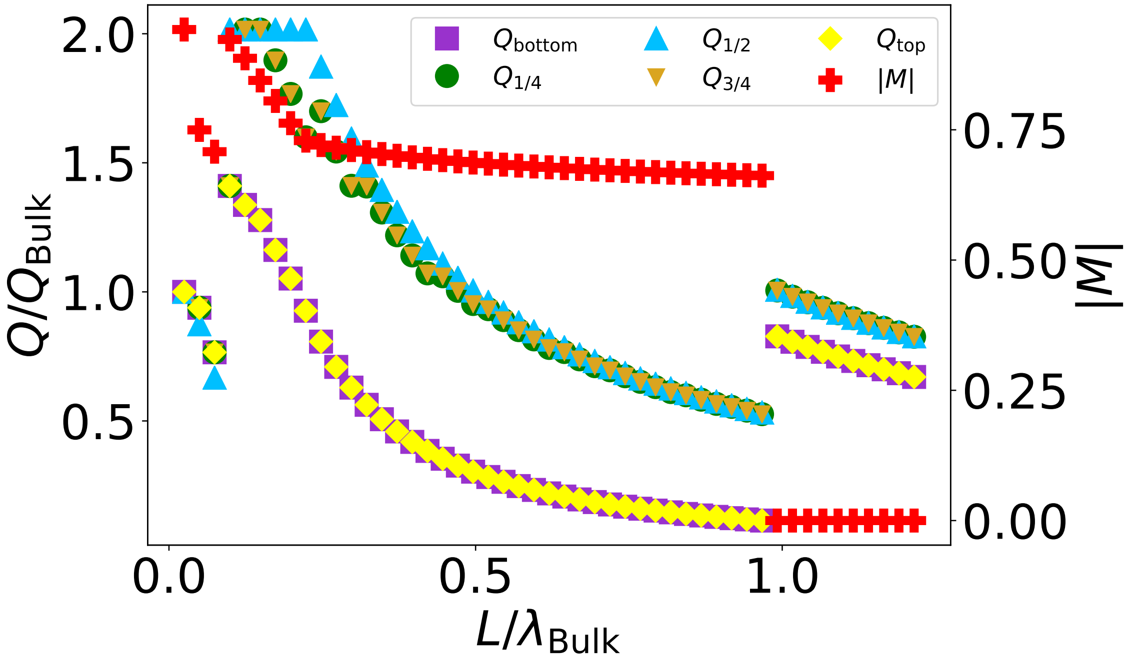

Figure B.5: Q/Q_{bulk} and spin-canting-induced magnetization versus nanoparticle length. $d = 0.15708$, $k_S = -0.80$. Magnetization is in units of $D'S/J$.

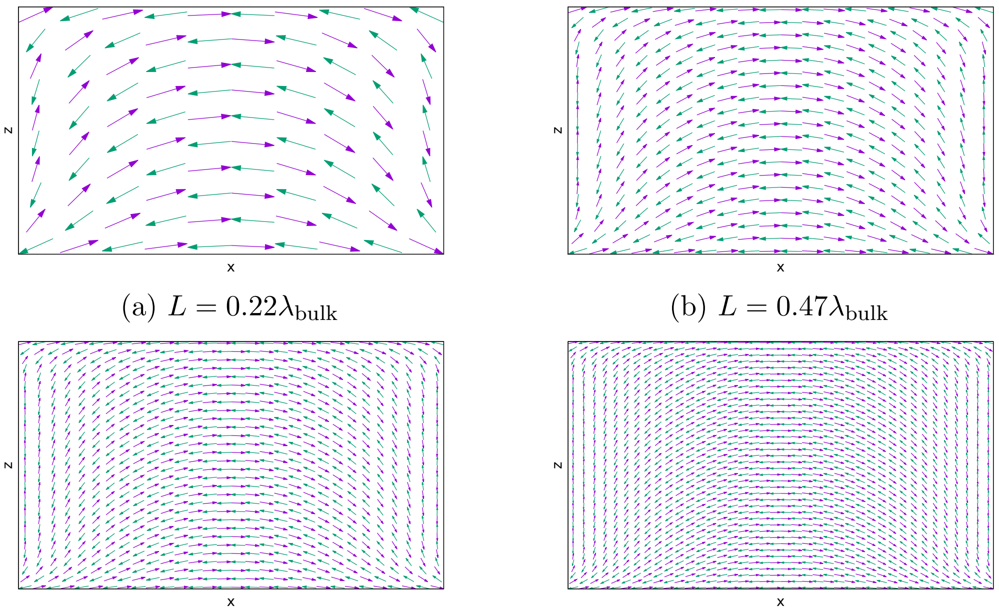

(a) $L = 0.22\lambda_{\text{bulk}}$

(b) $L = 0.47\lambda_{\text{bulk}}$

(c) $L = 0.72\lambda_{\text{bulk}}$

(d) $L = 0.97\lambda_{\text{bulk}}$

Figure B.6: Nanoparticles of different sizes with $d = 0.15708$ and $k_S = -0.80$. Spins of the same colour belong to the same sublattice. The size of the nanoparticles is $L \times L$.

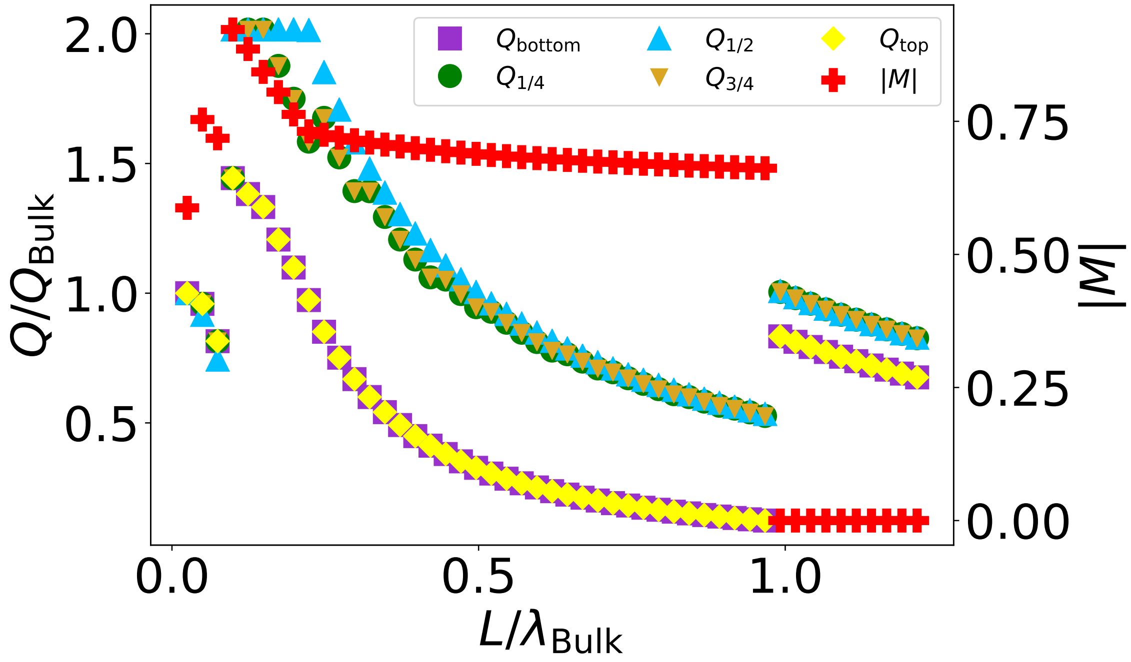

Figure B.7: Q/Q_{bulk} and spin-canting-induced magnetization versus nanoparticle length. $d = 0.15708$, $k_S = -0.70$. Magnetization is in units of $D'S/J$.

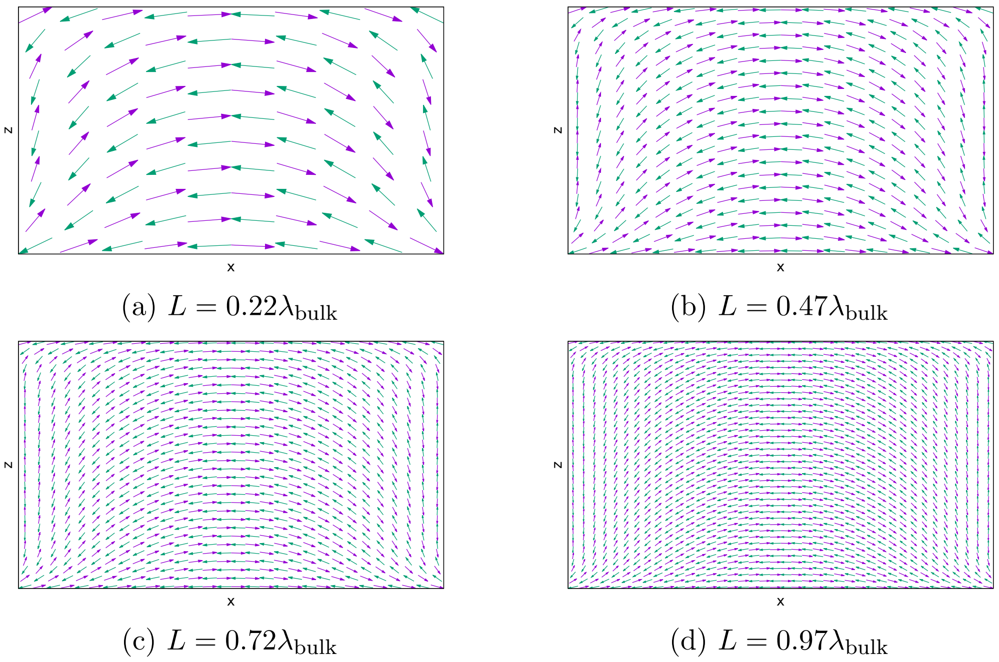

(a) $L = 0.22\lambda_{\text{bulk}}$ (b) $L = 0.47\lambda_{\text{bulk}}$

(c) $L = 0.72\lambda_{\text{bulk}}$ (d) $L = 0.97\lambda_{\text{bulk}}$

Figure B.8: Nanoparticles of different sizes with $d = 0.15708$ and $k_S = -0.70$. Spins of the same colour belong to the same sublattice. The size of the nanoparticles is $L \times L$.

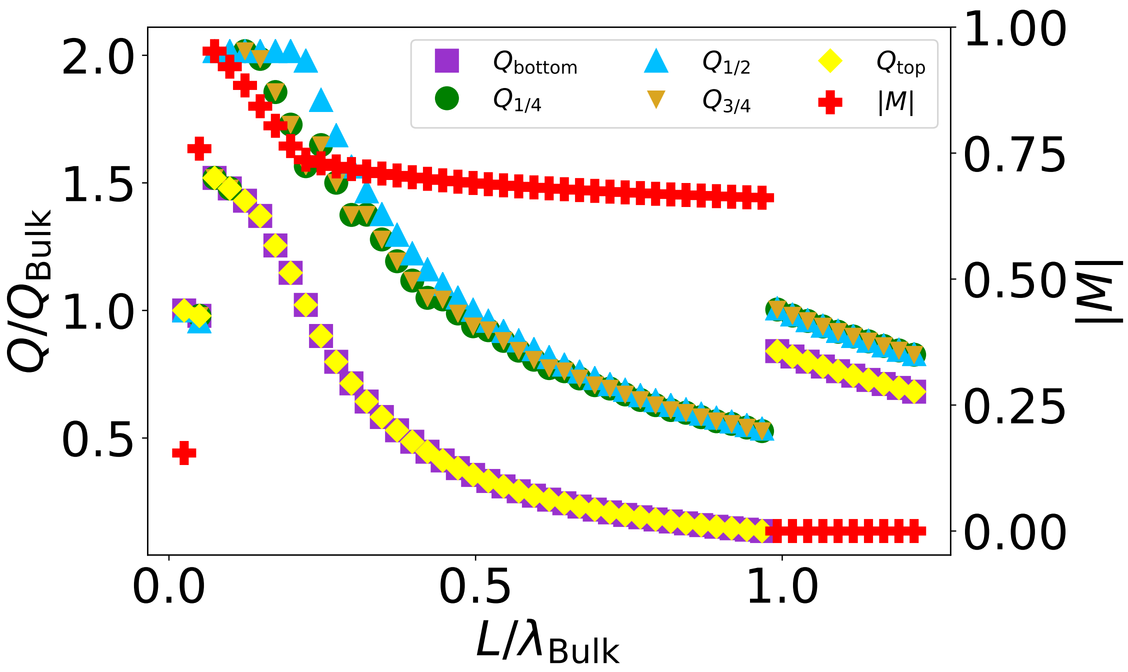

Figure B.9: Q/Q_{bulk} and spin-canting-induced magnetization versus nanoparticle length. $d = 0.15708$, $k_S = -0.60$. Magnetization is in units of $D'S/J$.

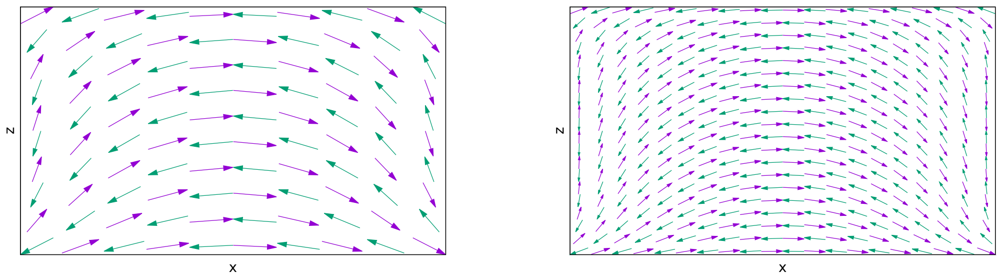

(a) $L = 0.22\lambda_{\text{bulk}}$ (b) $L = 0.47\lambda_{\text{bulk}}$

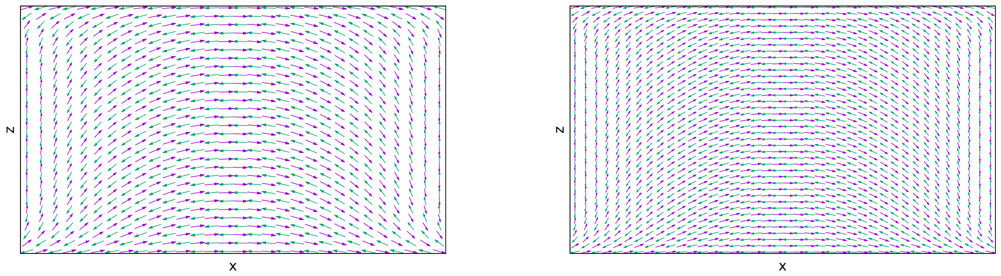

(c) $L = 0.72\lambda_{\text{bulk}}$ (d) $L = 0.97\lambda_{\text{bulk}}$

Figure B.10: Nanoparticles of different sizes with $d = 0.15708$ and $k_S = -0.60$. Spins of the same colour belong to the same sublattice. The size of the nanoparticles is $L \times L$.

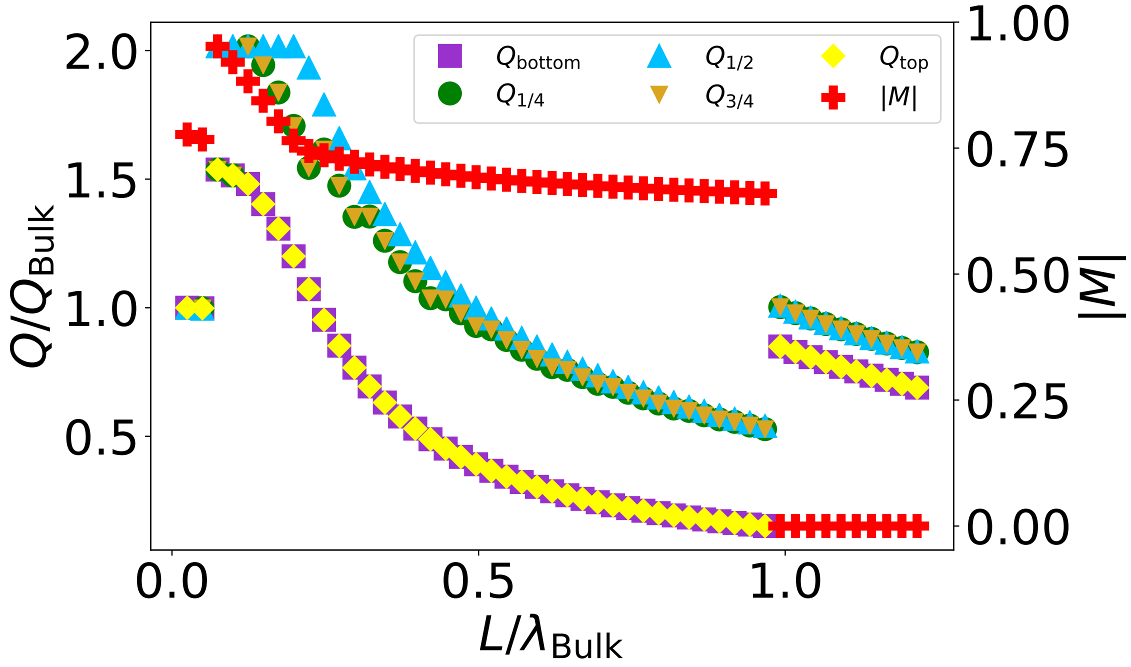

Figure B.11: Q/Q_{bulk} and spin-canting-induced magnetization versus nanoparticle length. $d = 0.15708$, $k_S = -0.50$. Magnetization is in units of $D'S/J$.

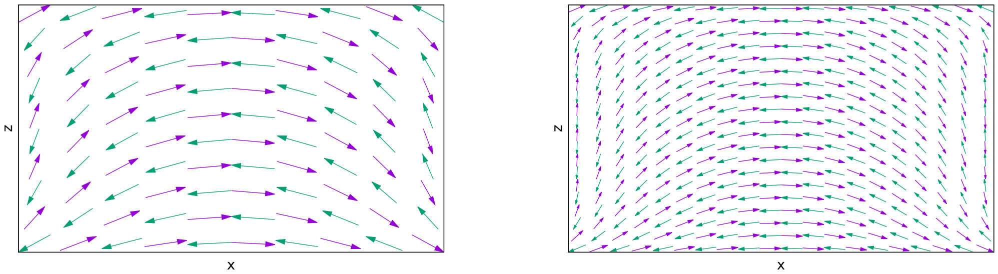

(a) $L = 0.22\lambda_{\text{bulk}}$ (b) $L = 0.47\lambda_{\text{bulk}}$

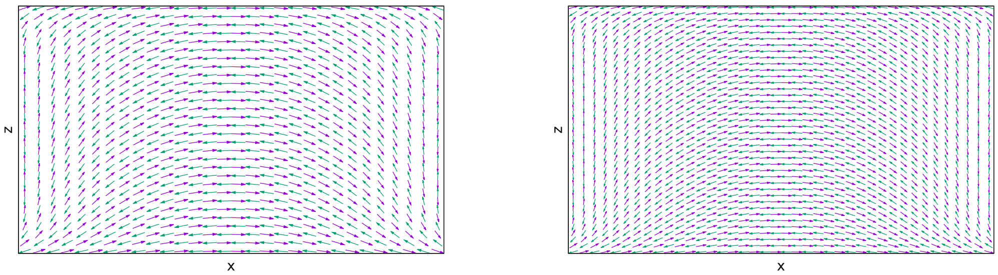

(c) $L = 0.72\lambda_{\text{bulk}}$ (d) $L = 0.97\lambda_{\text{bulk}}$

Figure B.12: Nanoparticles of different sizes with $d = 0.15708$ and $k_S = -0.50$. Spins of the same colour belong to the same sublattice. The size of the nanoparticles is $L \times L$.

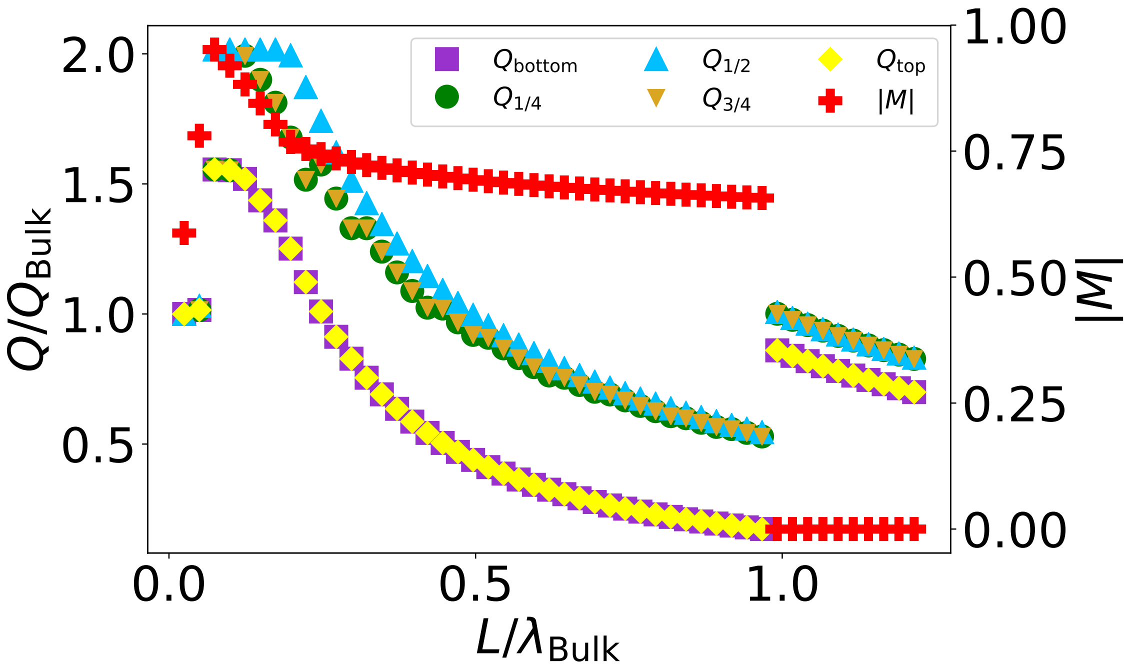

Figure B.13: Q/Q_{bulk} and spin-canting-induced magnetization versus nanoparticle length. $d = 0.15708$, $k_S = -0.40$. Magnetization is in units of $D'S/J$.

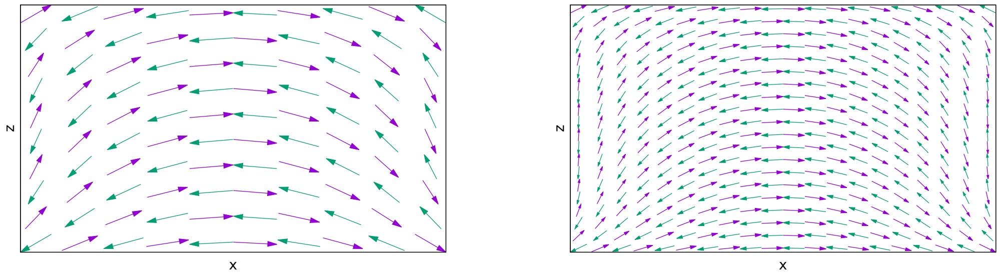

(a) $L = 0.22\lambda_{\mathrm{bulk}}$ (b) $L = 0.47\lambda_{\mathrm{bulk}}$

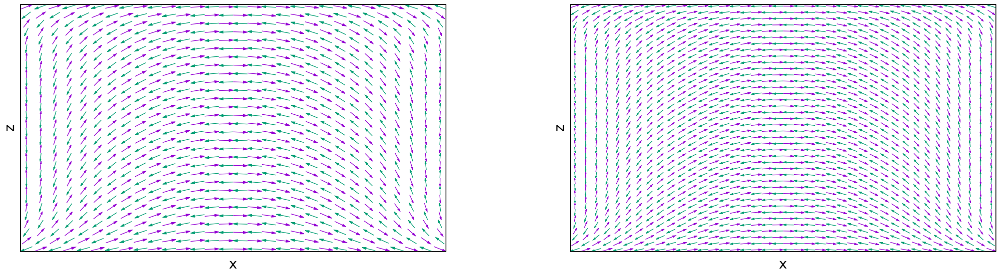

(c) $L = 0.72\lambda_{\mathrm{bulk}}$ (d) $L = 0.97\lambda_{\mathrm{bulk}}$

Figure B.14: Nanoparticles of different sizes with $d = 0.15708$ and $k_S = -0.40$. Spins of the same colour belong to the same sublattice. The size of the nanoparticles is $L \times L$.

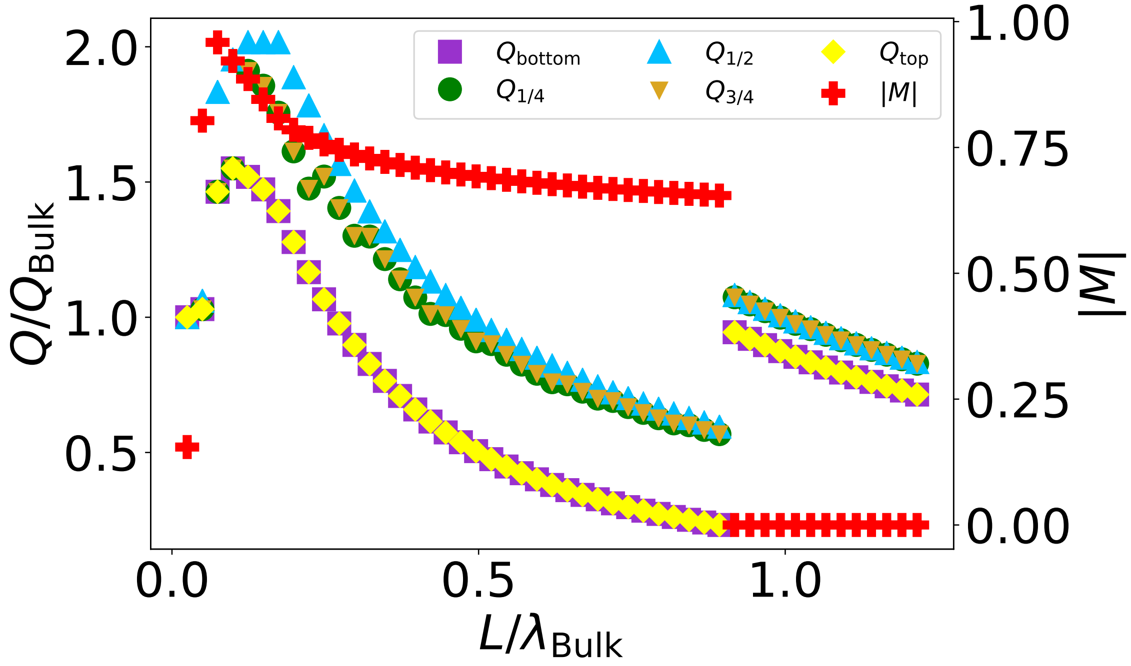

Figure B.15: Q/Q_{bulk} and spin-canting-induced magnetization versus nanoparticle length. $d = 0.15708$, $k_S = -0.30$. Magnetization is in units of $D'S/J$.

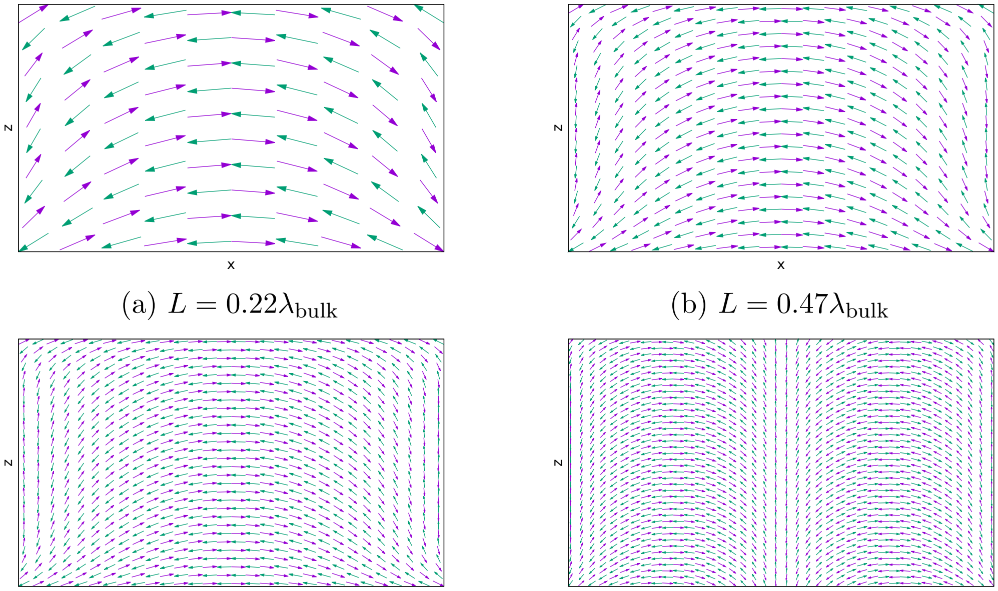

(a) $L = 0.22\lambda_{\mathrm{bulk}}$

(b) $L = 0.47\lambda_{\mathrm{bulk}}$

(c) $L = 0.72\lambda_{\mathrm{bulk}}$

(d) $L = 0.97\lambda_{\mathrm{bulk}}$

Figure B.16: Nanoparticles of different sizes with $d = 0.15708$ and $k_S = -0.30$. Spins of the same colour belong to the same sublattice. The size of the nanoparticles is $L \times L$.

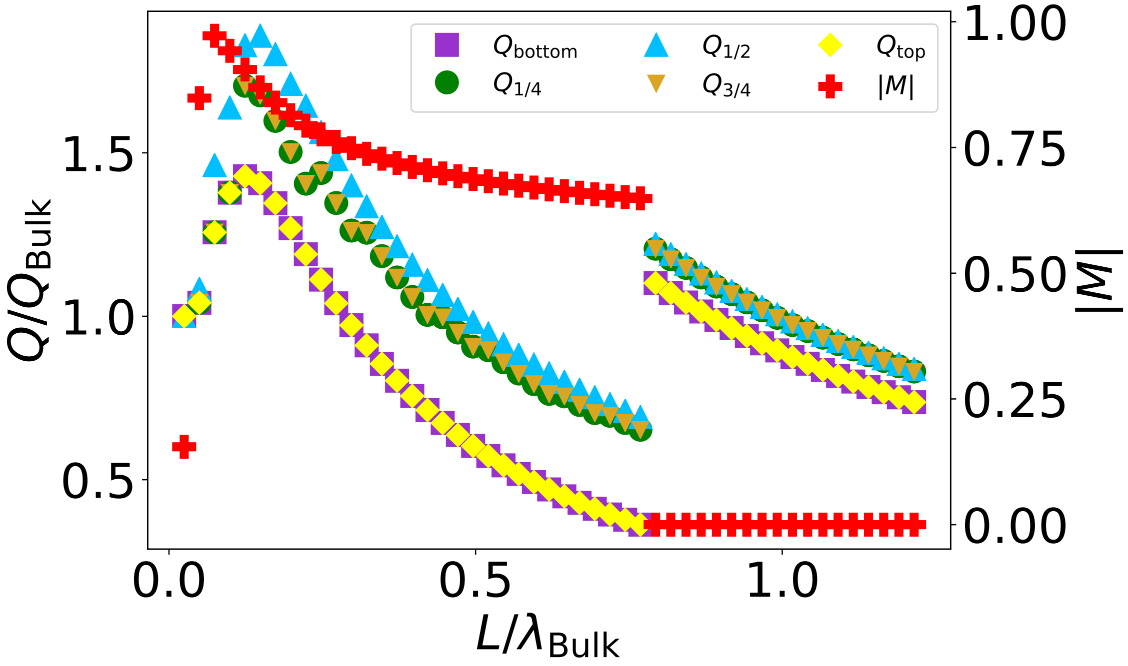

Figure B.17: Q/Q_{bulk} and spin-canting-induced magnetization versus nanoparticle length. $d = 0.15708$, $k_S = -0.20$. Magnetization is in units of $D'S/J$.

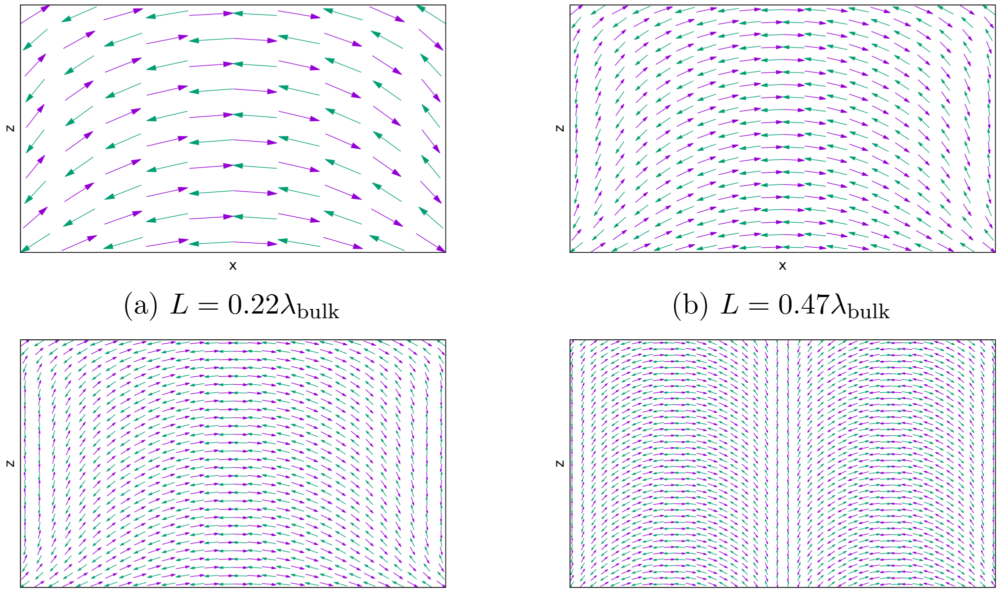

(a) $L = 0.22\lambda_{\text{bulk}}$
(b) $L = 0.47\lambda_{\text{bulk}}$
(c) $L = 0.72\lambda_{\text{bulk}}$
(d) $L = 0.97\lambda_{\text{bulk}}$

Figure B.18: Nanoparticles of different sizes with $d = 0.15708$ and $k_S = -0.20$. Spins of the same colour belong to the same sublattice. The size of the nanoparticles is $L \times L$.

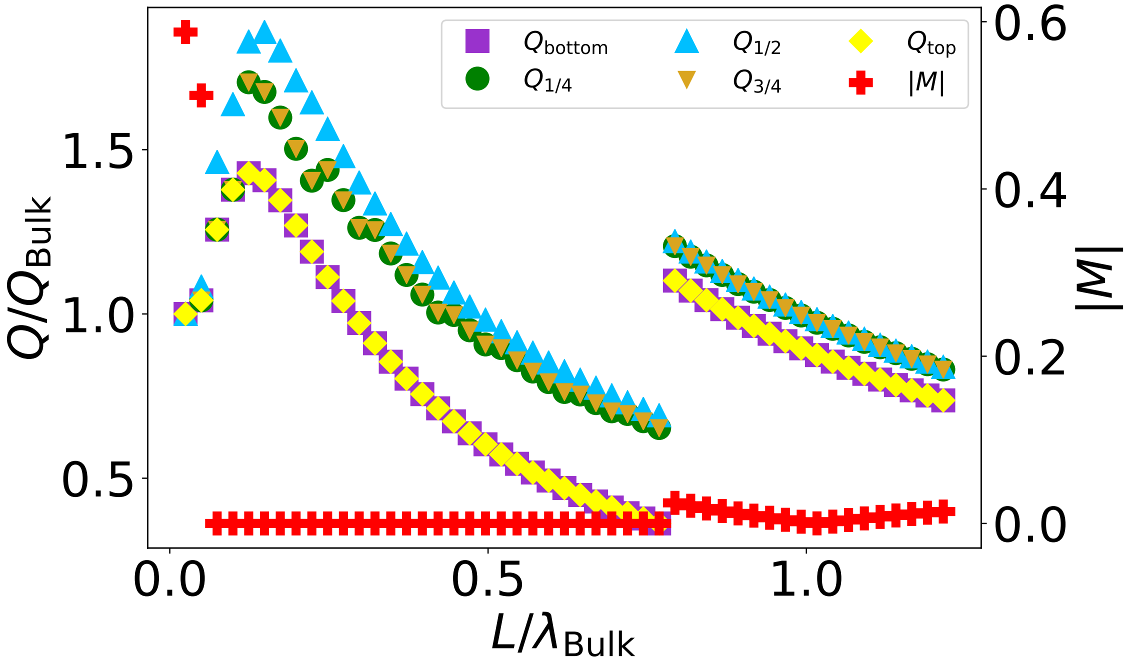

Figure B.19: Q/Q_{bulk} and spin-canting-induced magnetization versus nanoparticle length. $d = 0.15708$, $k_S = 0.20$. Magnetization is in units of $D'S/J$.

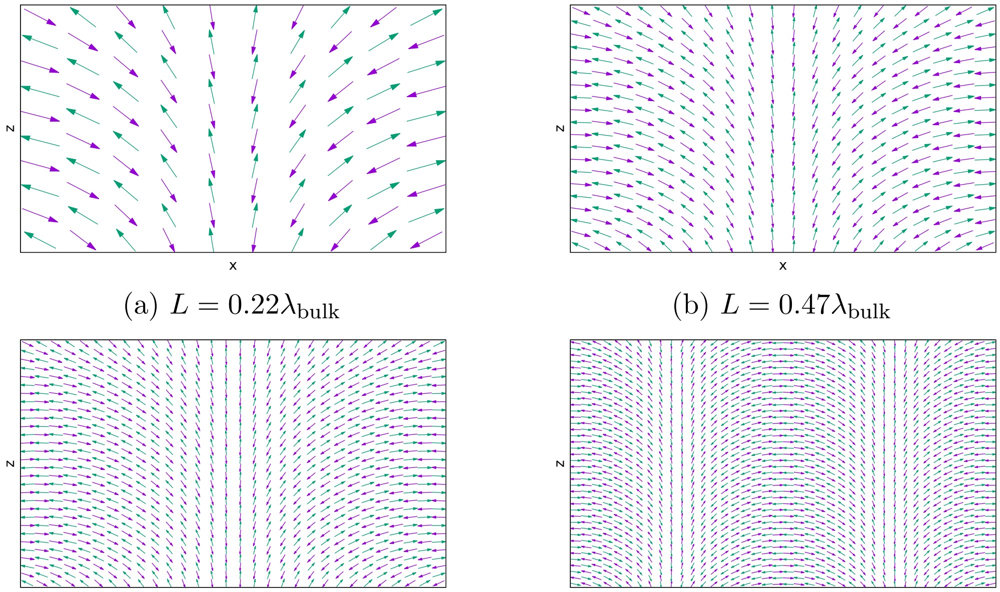

(a) $L = 0.22\lambda_{\text{bulk}}$

(b) $L = 0.47\lambda_{\text{bulk}}$

(c) $L = 0.72\lambda_{\text{bulk}}$

(d) $L = 0.97\lambda_{\text{bulk}}$

Figure B.20: Nanoparticles of different sizes with $d = 0.15708$ and $k_S = 0.20$. Spins of the same colour belong to the same sublattice. The size of the nanoparticles is $L \times L$.

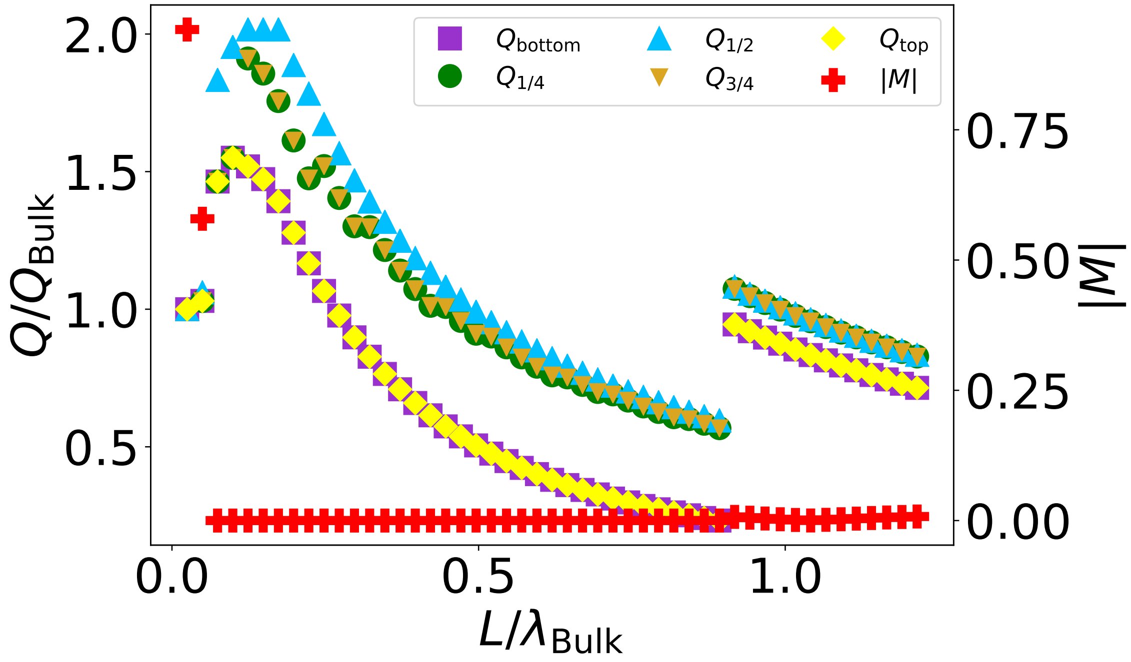

Figure B.21: Q/Q_{bulk} and spin-canting-induced magnetization versus nanoparticle length. $d = 0.15708$, $k_S = 0.30$. Magnetization is in units of $D'S/J$.

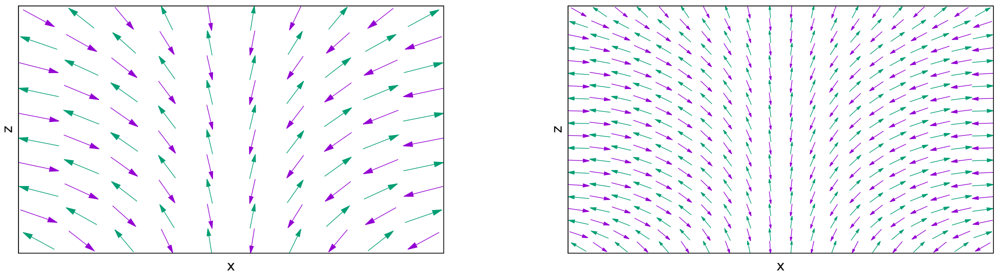

(a) $L = 0.22\lambda_{\text{bulk}}$ (b) $L = 0.47\lambda_{\text{bulk}}$

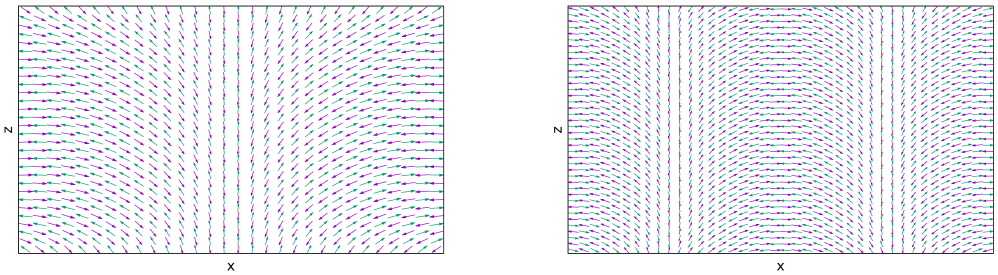

(c) $L = 0.72\lambda_{\text{bulk}}$ (d) $L = 0.97\lambda_{\text{bulk}}$

Figure B.22: Nanoparticles of different sizes with $d = 0.15708$ and $k_S = 0.30$. Spins of the same colour belong to the same sublattice. The size of the nanoparticles is $L \times L$.

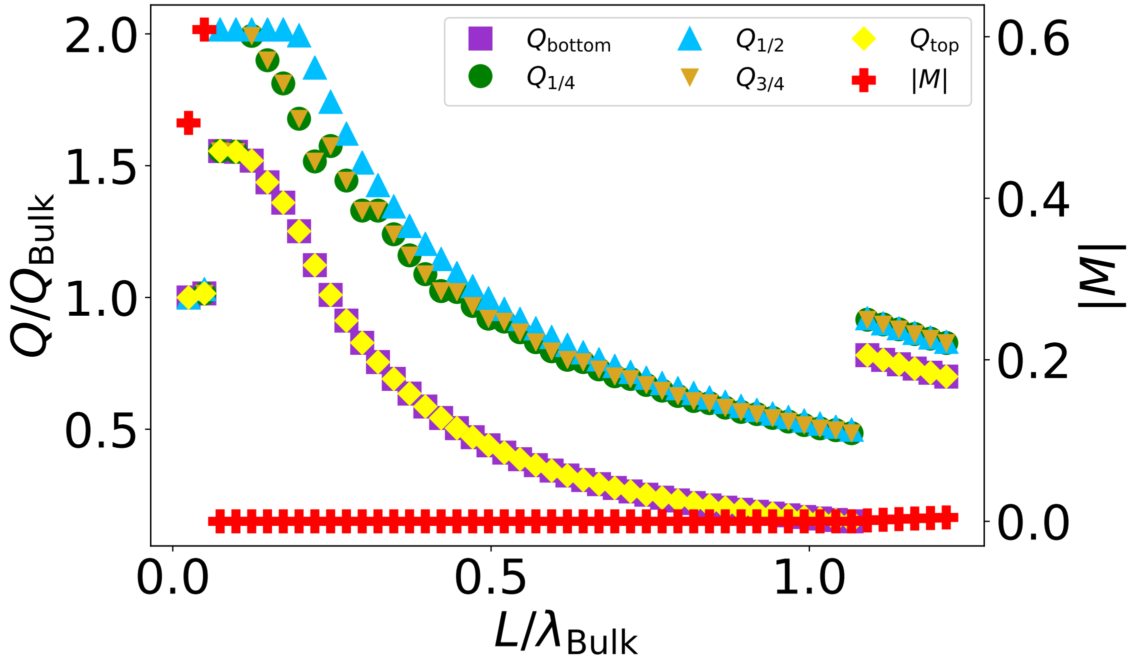

Figure B.23: Q/Q_{bulk} and spin-canting-induced magnetization versus nanoparticle length. $d = 0.15708$, $k_S = 0.40$. Magnetization is in units of $D'S/J$.

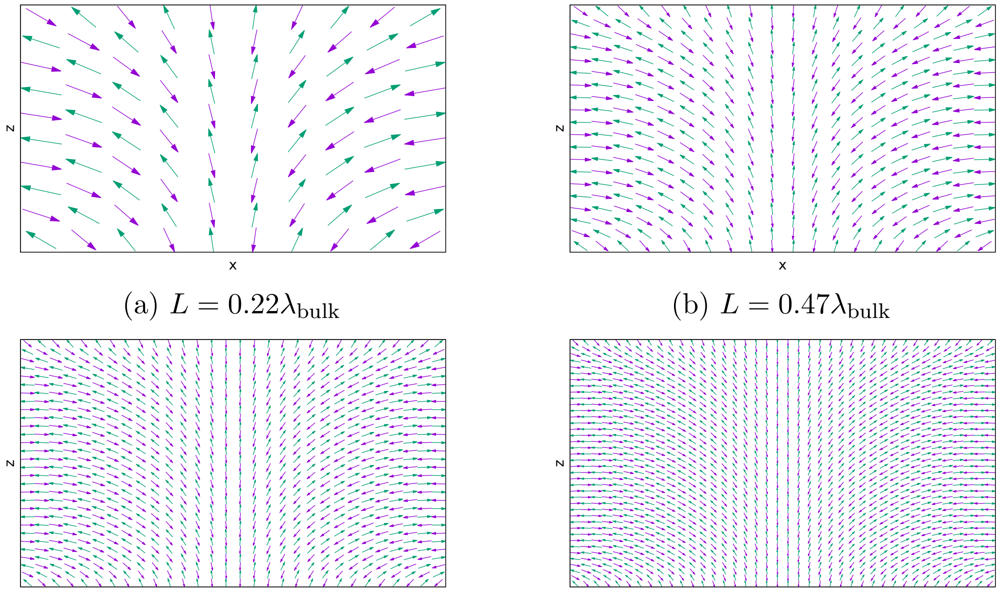

(a) $L = 0.22\lambda_{\text{bulk}}$ (b) $L = 0.47\lambda_{\text{bulk}}$

(c) $L = 0.72\lambda_{\text{bulk}}$ (d) $L = 0.97\lambda_{\text{bulk}}$

Figure B.24: Nanoparticles of different sizes with $d = 0.15708$ and $k_S = 0.40$. Spins of the same colour belong to the same sublattice. The size of the nanoparticles is $L \times L$.

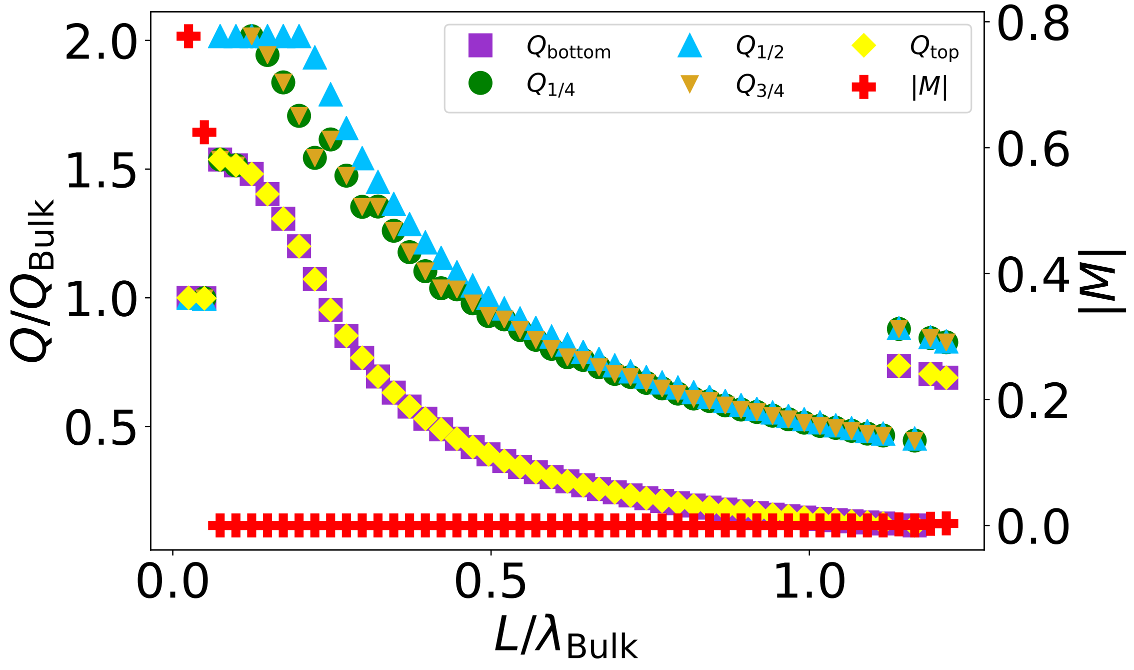

Figure B.25: Q/Q_{bulk} and spin-canting-induced magnetization versus nanoparticle length. $d = 0.15708$, $k_S = 0.50$. Magnetization is in units of $D'S/J$.

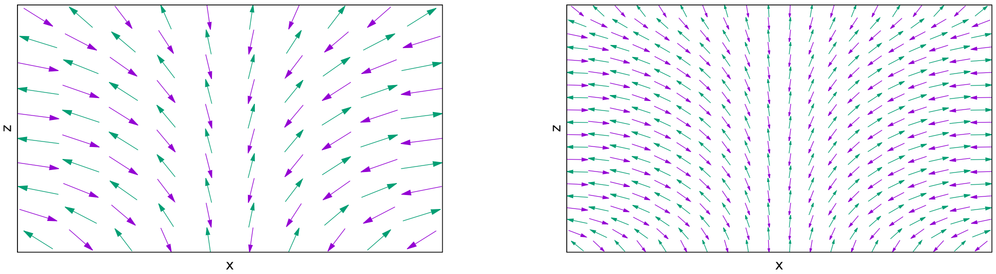

(a) $L = 0.22\lambda_{\text{bulk}}$ (b) $L = 0.47\lambda_{\text{bulk}}$

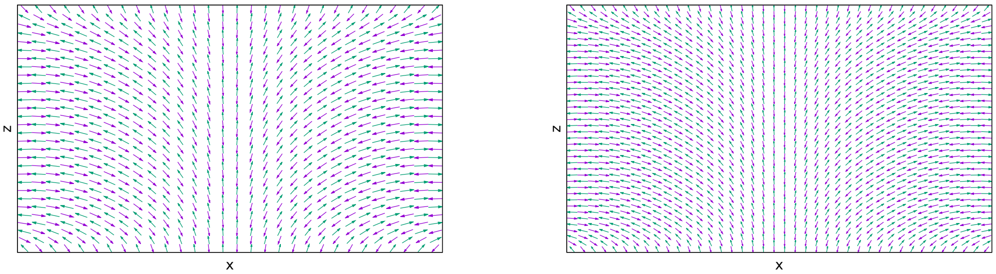

(c) $L = 0.72\lambda_{\text{bulk}}$ (d) $L = 0.97\lambda_{\text{bulk}}$

Figure B.26: Nanoparticles of different sizes with $d = 0.15708$ and $k_S = 0.50$. Spins of the same colour belong to the same sublattice. The size of the nanoparticles is $L \times L$.

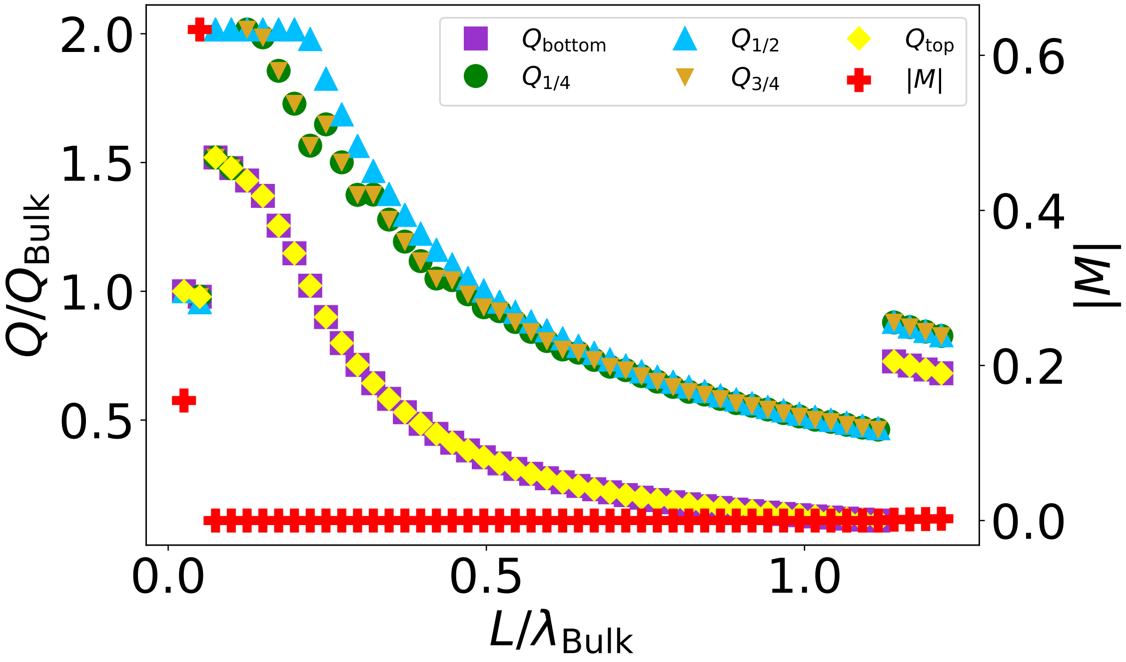

Figure B.27: Q/Q_{bulk} and spin-canting-induced magnetization versus nanoparticle length. $d = 0.15708$, $k_S = 0.60$. Magnetization is in units of $D'S/J$.

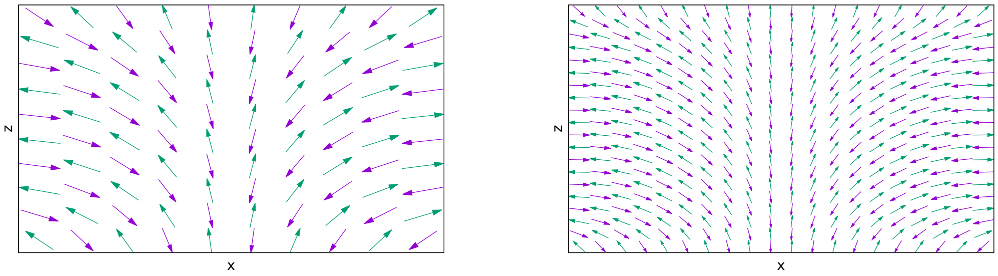

(a) $L = 0.22\lambda_{\text{bulk}}$ (b) $L = 0.47\lambda_{\text{bulk}}$

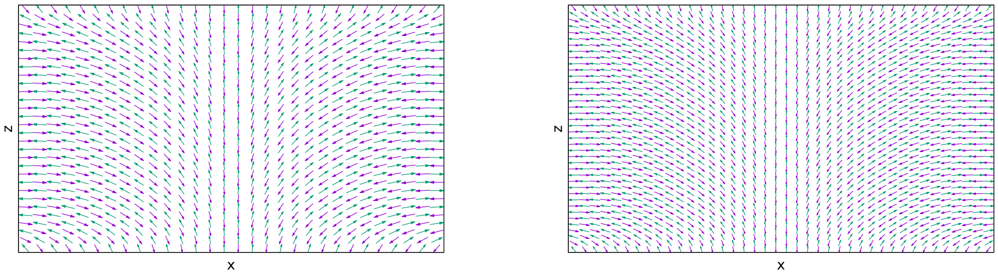

(c) $L = 0.72\lambda_{\text{bulk}}$ (d) $L = 0.97\lambda_{\text{bulk}}$

Figure B.28: Nanoparticles of different sizes with $d = 0.15708$ and $k_S = 0.60$. Spins of the same colour belong to the same sublattice. The size of the nanoparticles is $L \times L$.

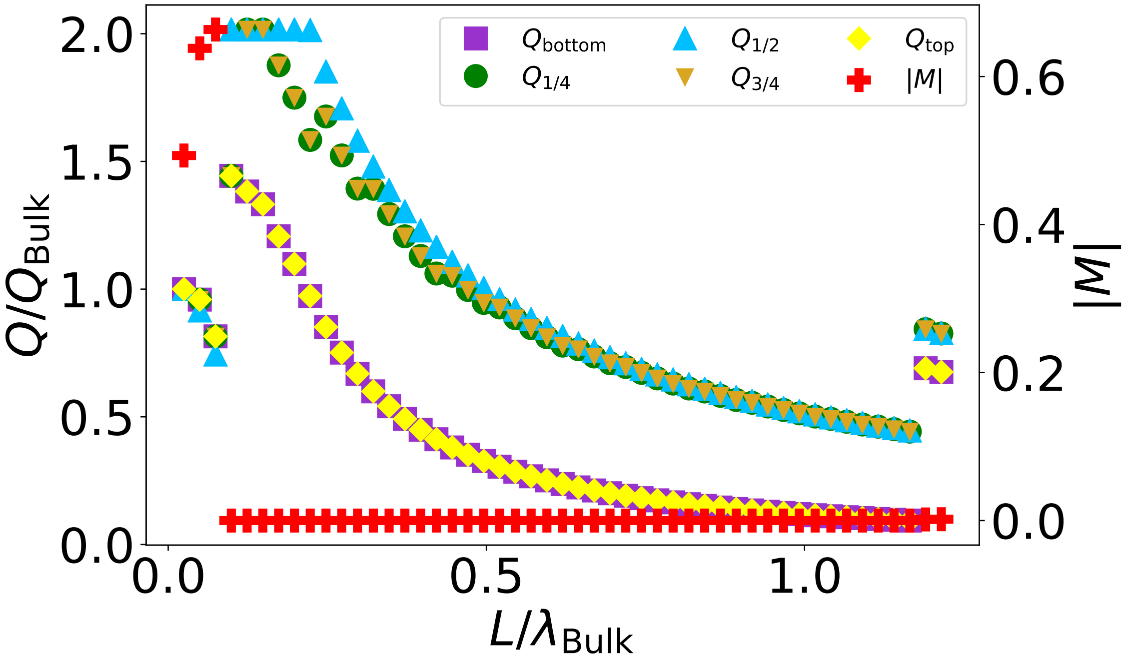

Figure B.29: Q/Q_{bulk} and spin-canting-induced magnetization versus nanoparticle length. $d = 0.15708$, $k_S = 0.70$. Magnetization is in units of $D'S/J$.

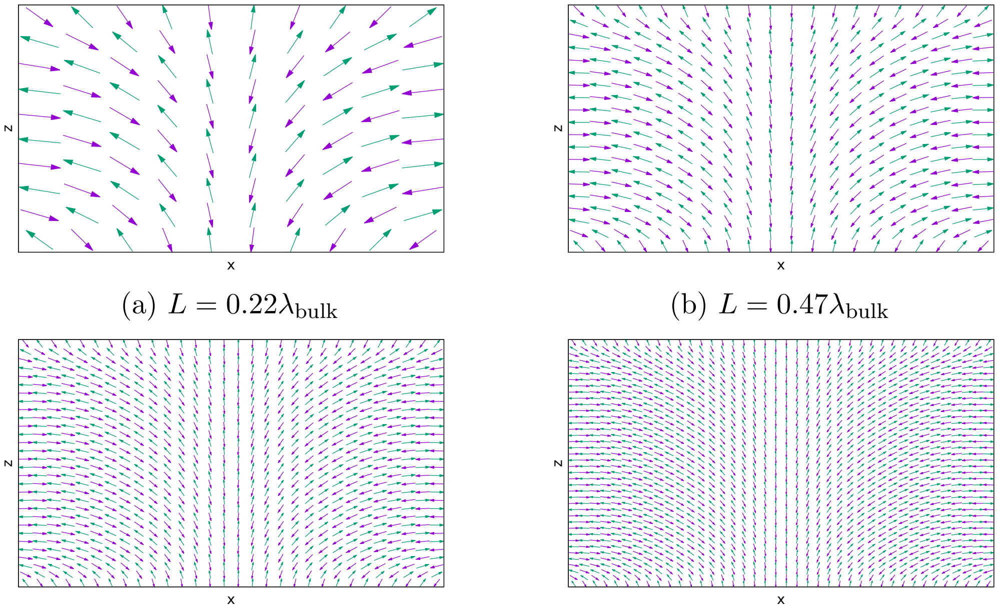

(a) $L = 0.22\lambda_{\text{bulk}}$ (b) $L = 0.47\lambda_{\text{bulk}}$

(c) $L = 0.72\lambda_{\text{bulk}}$ (d) $L = 0.97\lambda_{\text{bulk}}$

Figure B.30: Nanoparticles of different sizes with $d = 0.15708$ and $k_S = 0.70$. Spins of the same colour belong to the same sublattice. The size of the nanoparticles is $L \times L$.

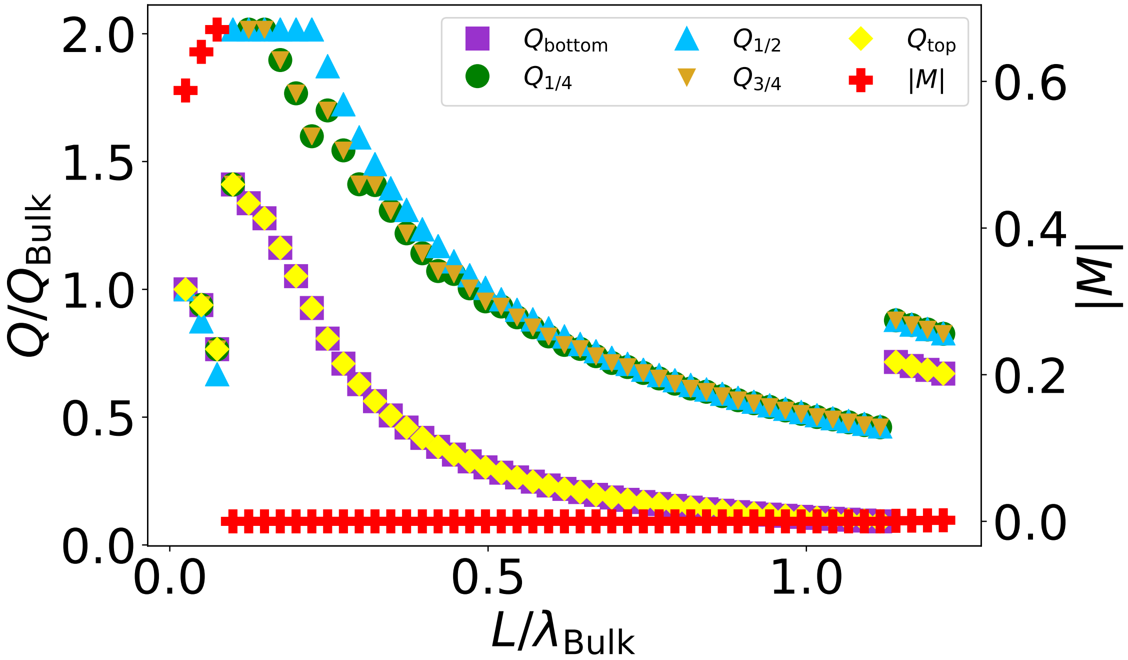

Figure B.31: Q/Q_{bulk} and spin-canting-induced magnetization versus nanoparticle length. $d = 0.15708$, $k_S = 0.80$. Magnetization is in units of $D'S/J$.

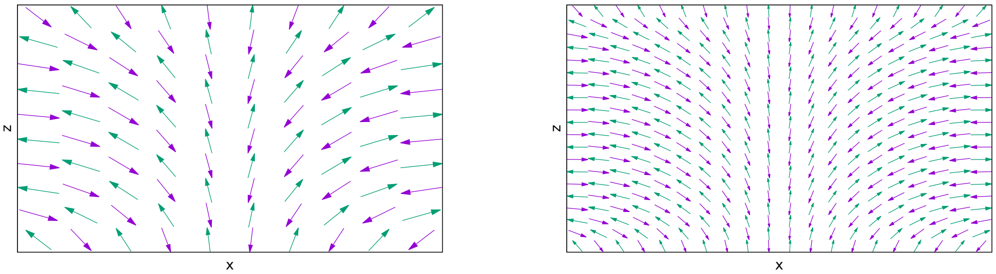

(a) $L = 0.22\lambda_{\text{bulk}}$ (b) $L = 0.47\lambda_{\text{bulk}}$

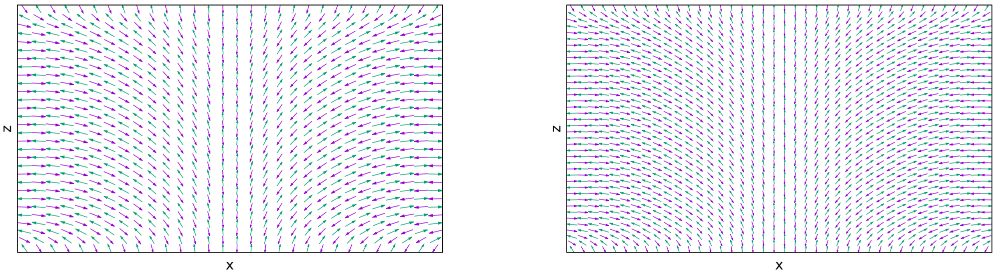

(c) $L = 0.72\lambda_{\text{bulk}}$ (d) $L = 0.97\lambda_{\text{bulk}}$

Figure B.32: Nanoparticles of different sizes with $d = 0.15708$ and $k_S = 0.80$. Spins of the same colour belong to the same sublattice. The size of the nanoparticles is $L \times L$.

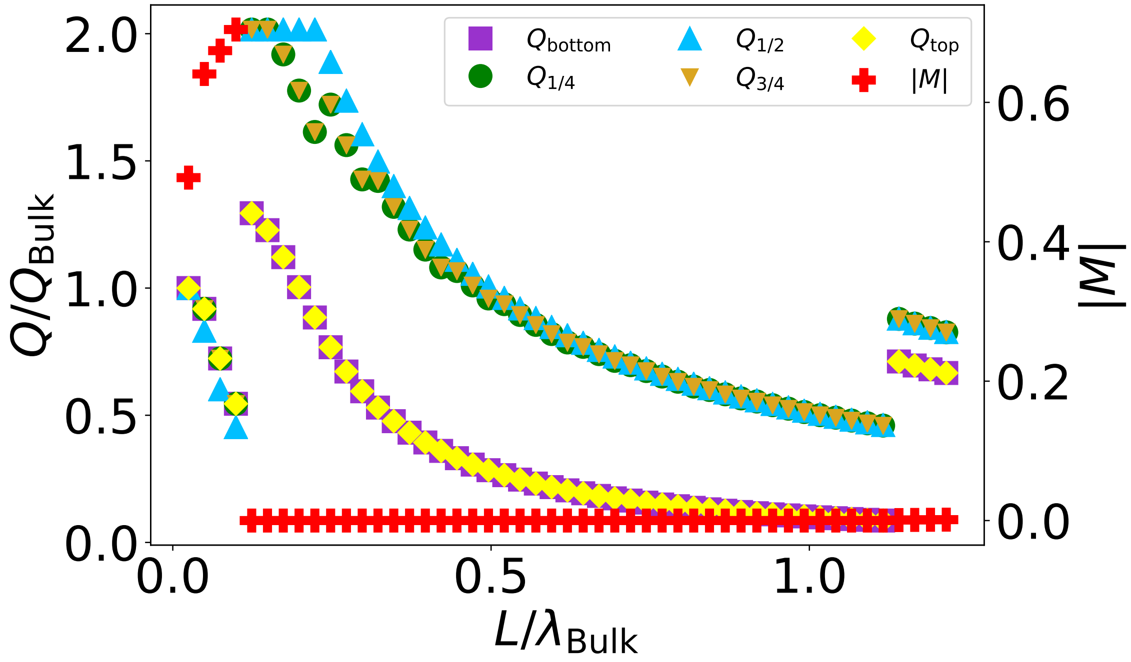

Figure B.33: Q/Q_{bulk} and spin-canting-induced magnetization versus nanoparticle length. $d = 0.15708$, $k_S = 0.90$. Magnetization is in units of $D'S/J$.

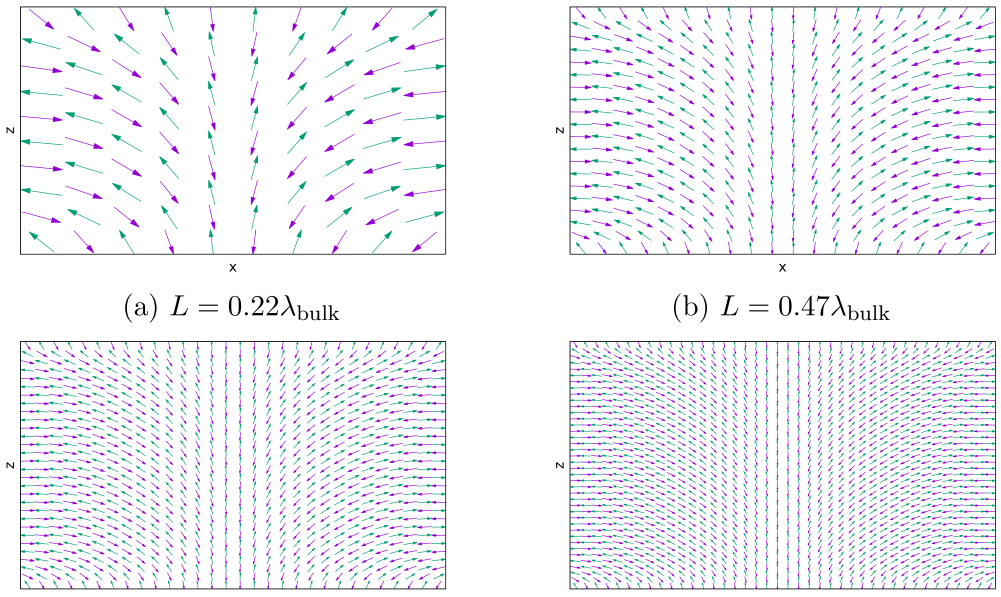

(a) $L = 0.22\lambda_{\text{bulk}}$

(b) $L = 0.47\lambda_{\text{bulk}}$

(c) $L = 0.72\lambda_{\text{bulk}}$

(d) $L = 0.97\lambda_{\text{bulk}}$

Figure B.34: Nanoparticles of different sizes with $d = 0.15708$ and $k_S = 0.90$. Spins of the same colour belong to the same sublattice. The size of the nanoparticles is $L \times L$.

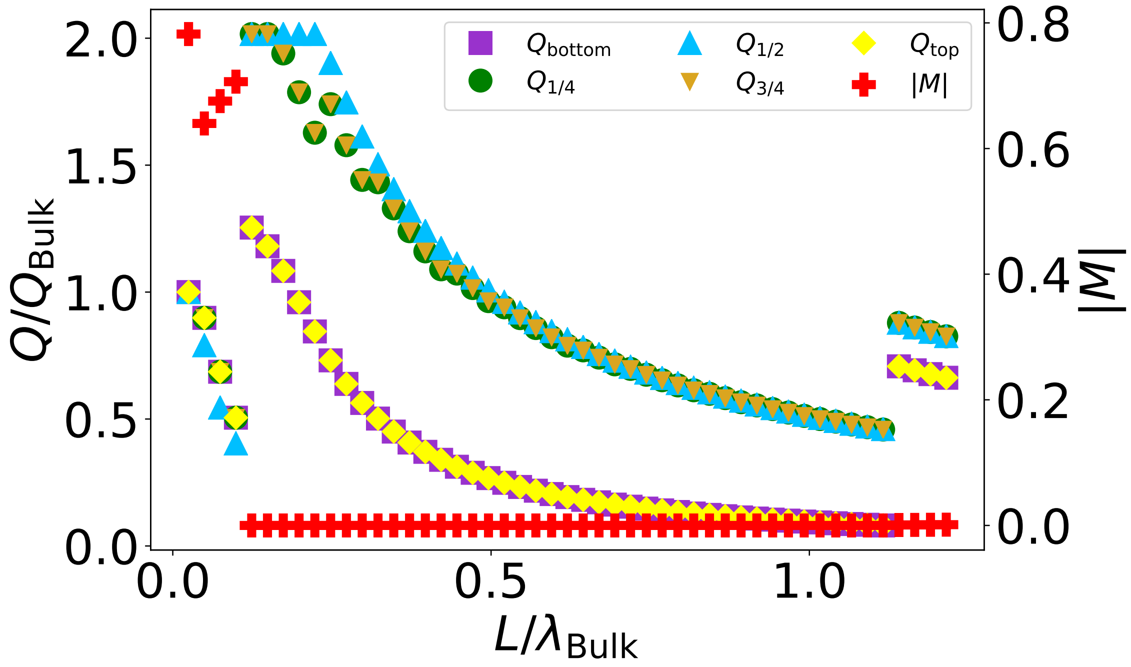

Figure B.35: Q/Q_{bulk} and spin-canting-induced magnetization versus nanoparticle length. $d = 0.15708$, $k_S = 1.00$. Magnetization is in units of $D'S/J$.

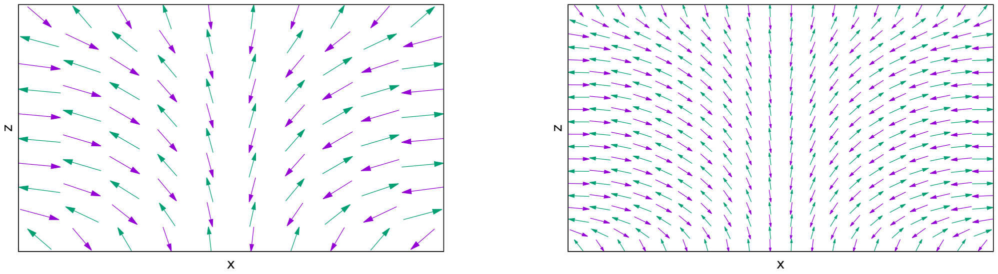

(a) $L = 0.22\lambda_{\text{bulk}}$ (b) $L = 0.47\lambda_{\text{bulk}}$

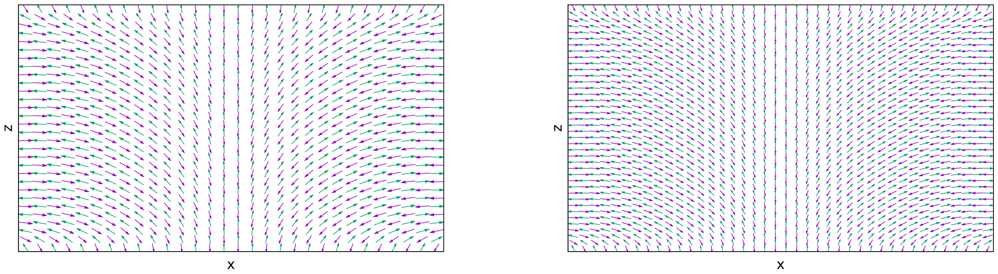

(c) $L = 0.72\lambda_{\text{bulk}}$ (d) $L = 0.97\lambda_{\text{bulk}}$

Figure B.36: Nanoparticles of different sizes with $d = 0.15708$ and $k_S = 1.00$. Spins of the same colour belong to the same sublattice. The size of the nanoparticles is $L \times L$.

Appendix C

Additional Spin Cube Results

Below are additional minimization plots for the spin cube. There was equal anisotropy on all surfaces ($k_S^x = k_S^y = k_S^z = k_S$). k_S values varied from -1.00 to 0.00. $d = 0.15708$ in all figures. Figures C.1 to C.10 show Q/Q_{Bulk} and magnetization versus nanoparticle side length $L/\lambda_{\mathrm{bulk}}$. The magnetization is in units $D'S/J$.

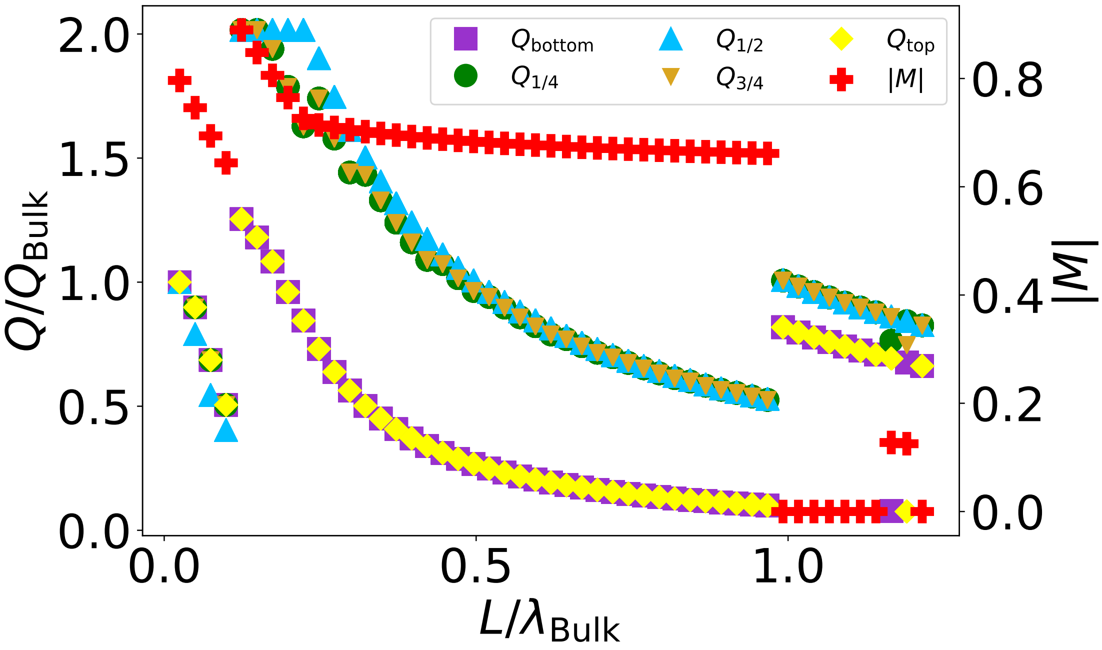

Figure C.1: Q/Q_{Bulk} versus nanoparticle side length L/λ_{bulk} and magnetization versus nanoparticle side length L/λ_{bulk} for spin cube ($L \times L \times L$). The magnetization is in units of $D'S/J$. $d = 0.15708$, $k_S = -1.00$.

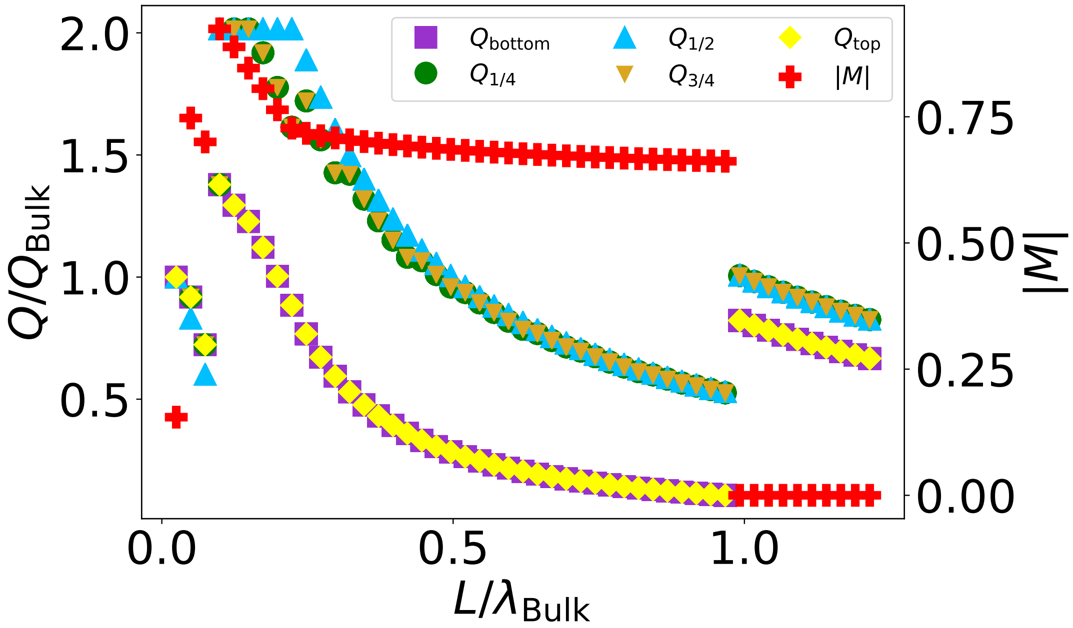

Figure C.2: Q/Q_{Bulk} versus nanoparticle side length L/λ_{bulk} and magnetization versus nanoparticle side length L/λ_{bulk} for spin cube ($L \times L \times L$). The magnetization is in units of $D'S/J$. $d = 0.15708$, $k_S = -0.90$.

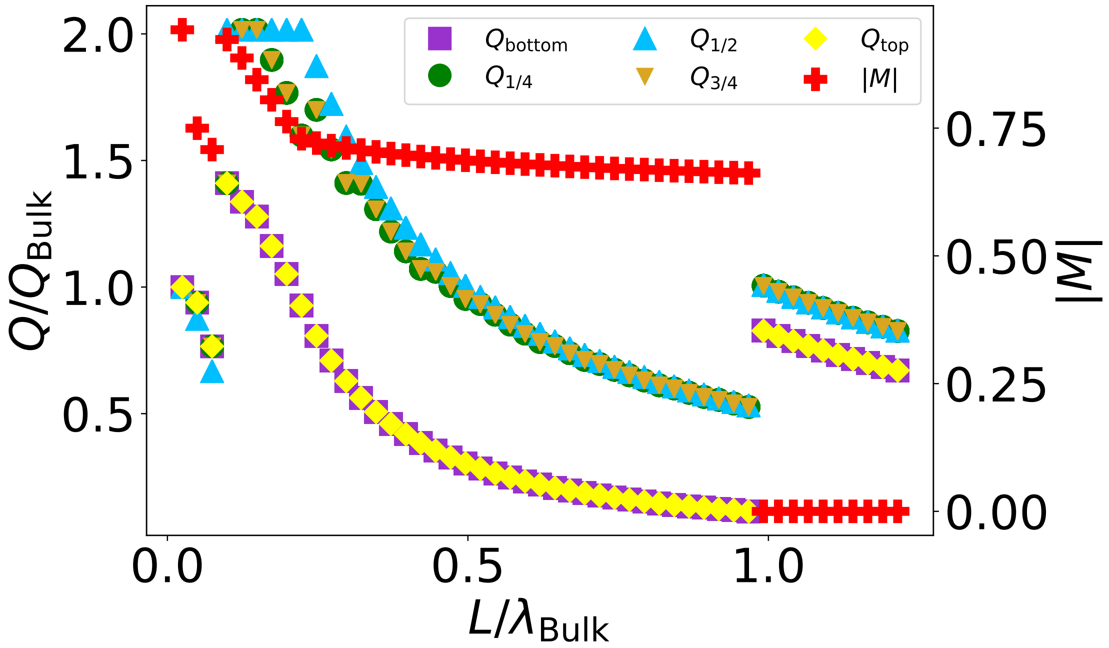

Figure C.3: Q/Q_{Bulk} versus nanoparticle side length L/λ_{bulk} and magnetization versus nanoparticle side length L/λ_{bulk} for spin cube $(L \times L \times L)$. The magnetization is in units of $D'S/J$. $d = 0.15708$, $k_S = -0.80$.

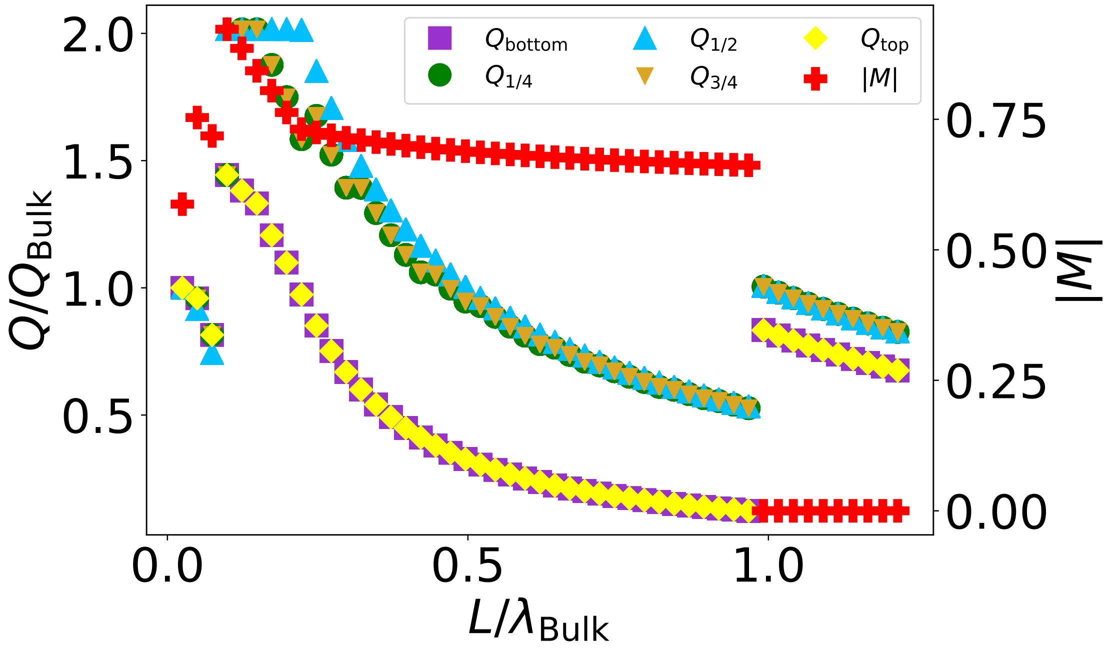

Figure C.4: Q/Q_{Bulk} versus nanoparticle side length L/λ_{bulk} and magnetization versus nanoparticle side length L/λ_{bulk} for spin cube $(L \times L \times L)$. The magnetization is in units of $D'S/J$. $d = 0.15708$, $k_S = -0.70$.

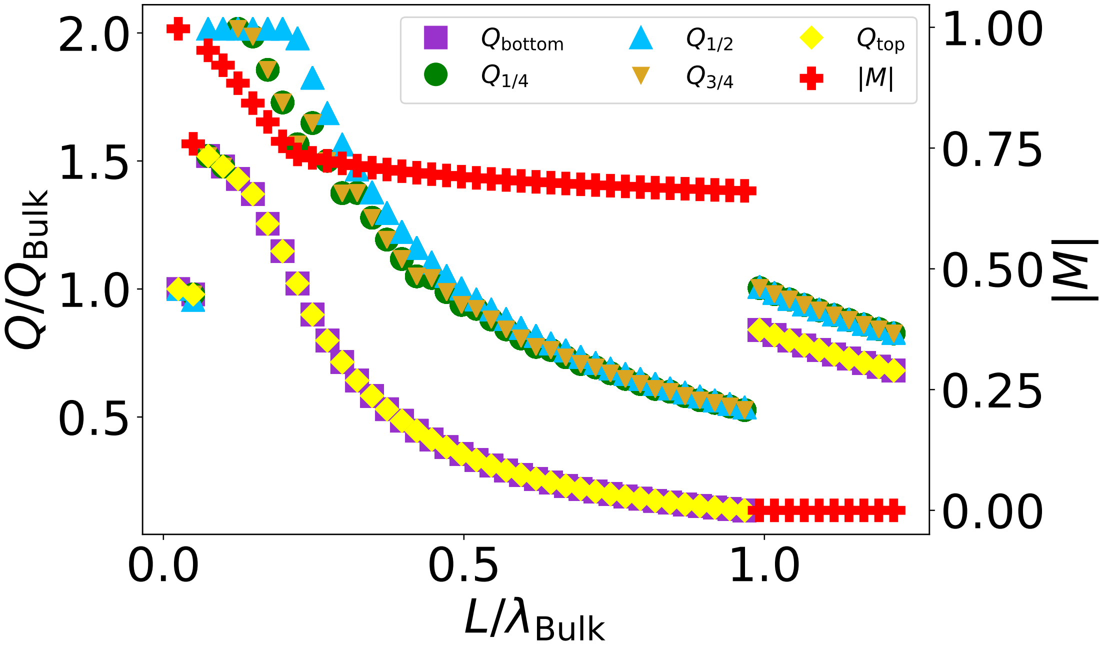

Figure C.5: Q/Q_{Bulk} versus nanoparticle side length $L/\lambda_{\mathrm{bulk}}$ and magnetization versus nanoparticle side length $L/\lambda_{\mathrm{bulk}}$ for spin cube ($L \times L \times L$). The magnetization is in units of $D'S/J$. $d = 0.15708$, $k_S = -0.60$.

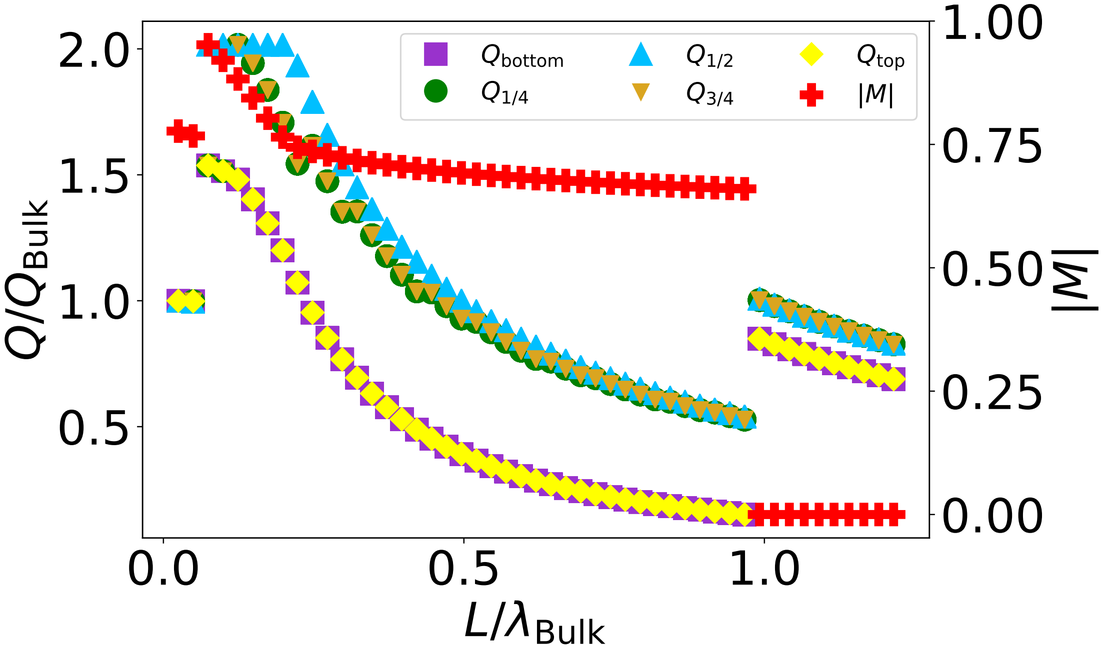

Figure C.6: Q/Q_{Bulk} versus nanoparticle side length $L/\lambda_{\mathrm{bulk}}$ and magnetization versus nanoparticle side length $L/\lambda_{\mathrm{bulk}}$ for spin cube ($L \times L \times L$). The magnetization is in units of $D'S/J$. $d = 0.15708$, $k_S = -0.50$.

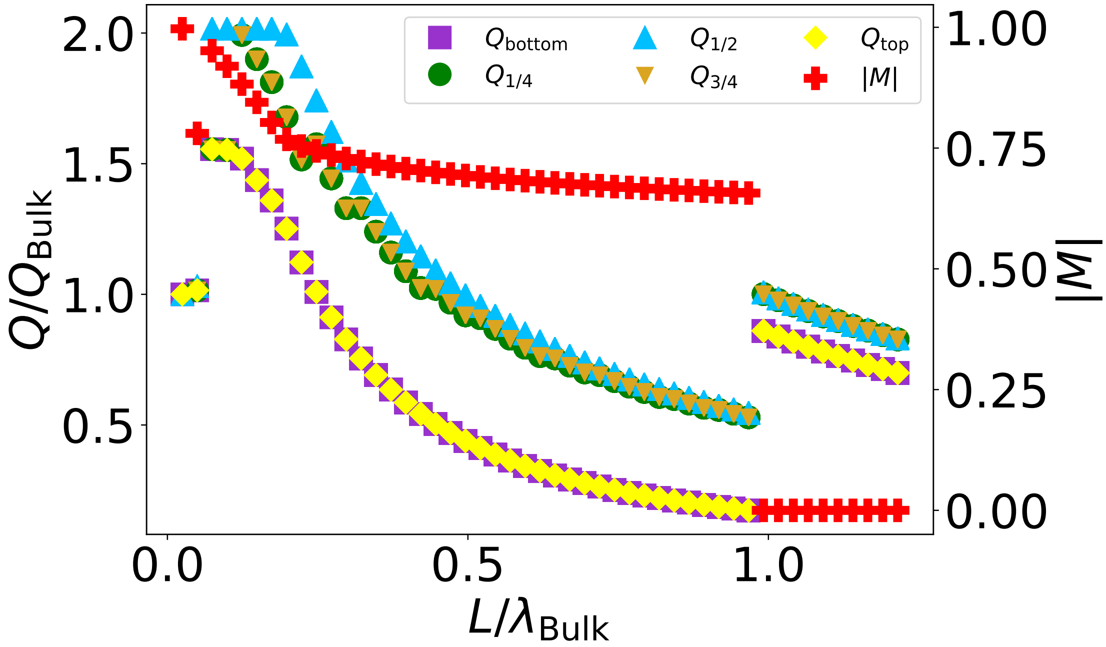

Figure C.7: Q/Q_{Bulk} versus nanoparticle side length $L/\lambda_{\mathrm{bulk}}$ and magnetization versus nanoparticle side length $L/\lambda_{\mathrm{bulk}}$ for spin cube $(L \times L \times L)$. The magnetization is in units of $D'S/J$. $d = 0.15708$, $k_S = -0.40$.

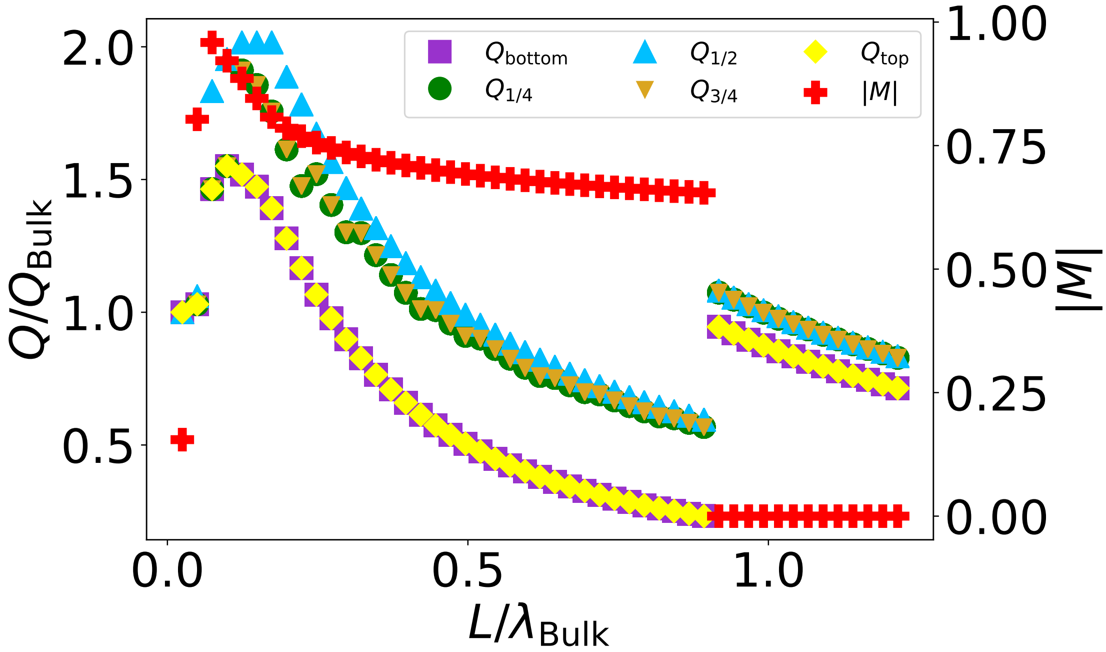

Figure C.8: Q/Q_{Bulk} versus nanoparticle side length $L/\lambda_{\mathrm{bulk}}$ and magnetization versus nanoparticle side length $L/\lambda_{\mathrm{bulk}}$ for spin cube $(L \times L \times L)$. The magnetization is in units of $D'S/J$. $d = 0.15708$, $k_S = -0.30$.

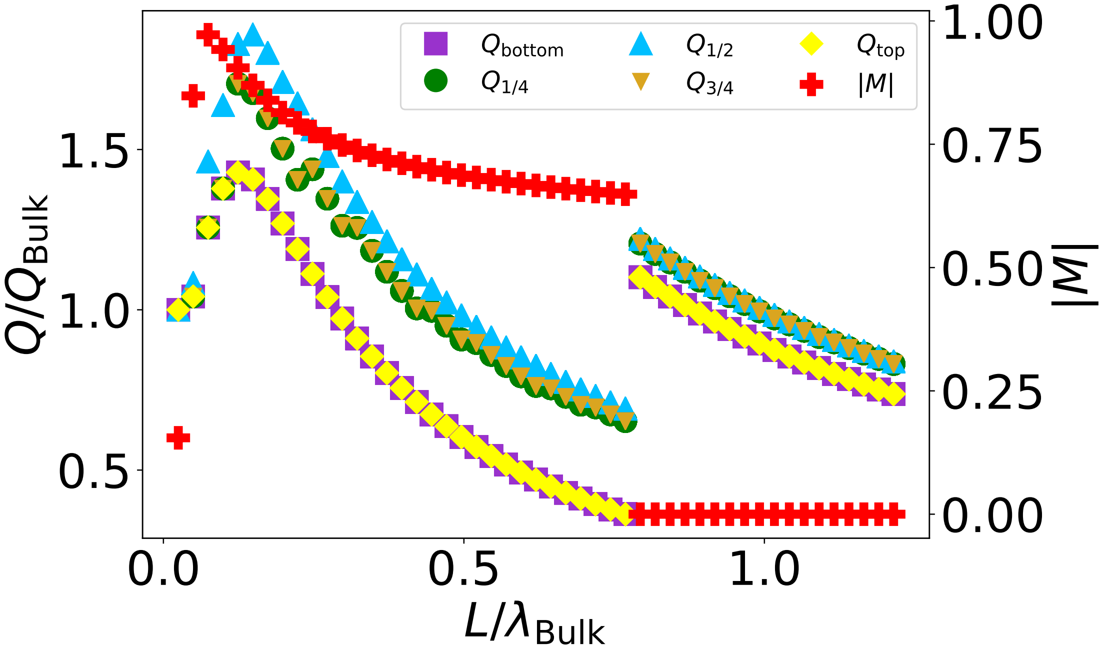

Figure C.9: Q/Q_{Bulk} versus nanoparticle side length L/λ_{bulk} and magnetization versus nanoparticle side length L/λ_{bulk} for spin cube ($L \times L \times L$). The magnetization is in units of $D'S/J$. $d = 0.15708$, $k_S = -0.20$.

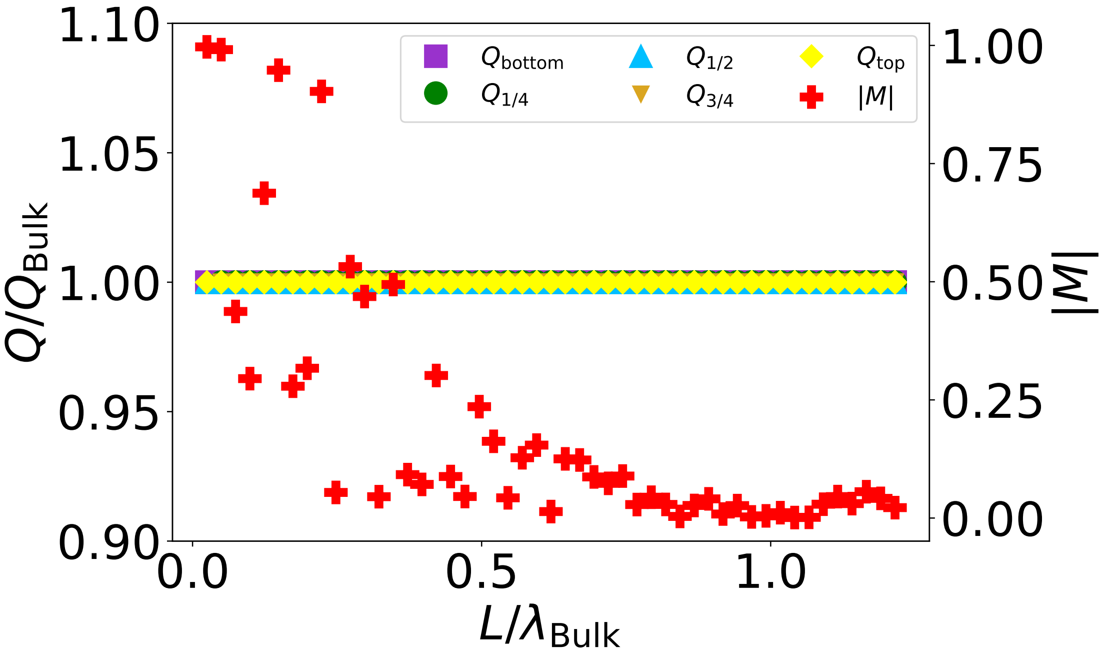

Figure C.10: Q/Q_{Bulk} versus nanoparticle side length $L/\lambda_{\mathrm{bulk}}$ and magnetization versus nanoparticle side length $L/\lambda_{\mathrm{bulk}}$ for spin cube $(L \times L \times L)$. The magnetization is in units of $D'S/J$. $d = 0.15708$, $k_S = 0$.

Bibliography

[1] G. Catalan and J. F. Scott, “Physics and Applications of Bismuth Ferrite”, Advanced Materials **21**, 2463 (2009).

[2] R. de Sousa, “The ‘Holy Grail’ of Multiferroic Physics”, Physics in Canada **72**, 57 (2016).

[3] J. F. Scott, “Data storage: Multiferroic memories”, Nature Materials **6**, 256 (2007).

[4] K. Ashraf, S. Smith, and S. Salahuddin, “Electric field induced magnetic switching at room temperature: Switching speed, device scaling and switching energy”, in 2012 International Electron Devices Meeting (Dec. 2012), 26.5.1.

[5] J.-G. Park, M. D. Le, J. Jeong, and S. Lee, “Structure and spin dynamics of multiferroic $BiFeO_3$”, Journal of Physics: Condensed Matter **26**, 433202 (2014).

[6] T. Zhao, A. Scholl, F. Zavaliche, K. Lee, M. Barry, A. Doran, M. P. Cruz, Y. H. Chu, C. Ederer, N. A. Spaldin, R. R. Das, D. M. Kim, S. H. Baek, C. B. Eom, and R. Ramesh, “Electrical control of antiferromagnetic domains in multiferroic $BiFeO_3$ films at room temperature”, Nature Materials **5**, 823 (2006).

[7] Y.-H. Chu, L. W. Martin, M. B. Holcomb, M. Gajek, S.-J. Han, Q. He, N. Balke, C.-H. Yang, D. Lee, W. Hu, Q. Zhan, P.-L. Yang, A. Fraile-Rodríguez, A. Scholl, S. X. Wang, and R. Ramesh, “Electric-field control of local ferromagnetism using a magnetoelectric multiferroic”, Nature Materials **7**, 478 (2008).

[8] D. Lebeugle, A. Mougin, M. Viret, D. Colson, and L. Ranno, “Electric Field Switching of the Magnetic Anisotropy of a Ferromagnetic Layer Exchange Coupled to the Multiferroic Compound $BiFeO_3$”, Physical Review Letters **103**, 257601 (2009).

[9] R. de Sousa, M. Allen, and M. Cazayous, “Theory of Spin-Orbit Enhanced Electric-Field Control of Magnetism in Multiferroic BiFeO$_3$”, Physical Review Letters **110**, 267202 (2013).

[10] P. Rovillain, R. de Sousa, Y. Gallais, A. Sacuto, M. A. Méasson, D. Colson, A. Forget, M. Bibes, A. Barthélémy, and M. Cazayous, “Electric-field control of spin waves at room temperature in multiferroic BiFeO$_3$”, Nature Materials **9**, 975 (2010).

[11] R. Mazumder, S. Ghosh, P. Mondal, D. Bhattacharya, S. Dasgupta, N. Das, A. Sen, A. K. Tyagi, M. Sivakumar, T. Takami, and H. Ikuta, “Particle size dependence of magnetization and phase transition near T_N in multiferroic BiFeO$_3$”, Journal of Applied Physics **100**, 033908 (2006).

[12] V. Annapu Reddy, N. P. Pathak, and R. Nath, “Particle size dependent magnetic properties and phase transitions in multiferroic BiFeO$_3$ nano-particles”, Journal of Alloys and Compounds **543**, 206 (2012).

[13] F. Huang, Z. Wang, X. Lu, J. Zhang, K. Min, W. Lin, R. Ti, T. Xu, J. He, C. Yue, and J. Zhu, “Peculiar magnetism of BiFeO$_3$ nanoparticles with size approaching the period of the spiral spin structure”, Scientific Reports **3**, 2907 (2013).

[14] M. Bibes and A. Barthelemy, “Multiferroics: Towards a magnetoelectric memory”, Nature Materials **7**, 425 (2008).

[15] D. Sando, A. Barthélémy, and M. Bibes, “BiFeO$_3$ epitaxial thin films and devices: past, present and future”, Journal of Physics: Condensed Matter **26**, 473201 (2014).

[16] C. Weingart, N. Spaldin, and E. Bousquet, “Noncollinear magnetism and single-ion anisotropy in multiferroic perovskites”, Physical Review B **86**, 094413 (2012).

[17] R. de Sousa, “Electric-field control of magnetism in an insulator at room temperature: the case of multiferroic BiFeO$_3$”, in Spintronics VI, Vol. 8813 (2013), 88131L.

[18] M. Fiebig, “Revival of the magnetoelectric effect”, Journal of Physics D: Applied Physics **38**, R123 (2005).

[19] L. D. Landau, E. M. Lifshitz, and L. P. Pitaevskiĭ, *Electrodynamics of Continuous Media*, Second edition, Vol. 8, Course of Theoretical Physics (Pergamon, Oxford; New York, 1984).

[20] W. C. Röntgen, “Ueber die durch Bewegung eines im homogenen electrischen Felde befindlichen Dielectricums hervorgerufene electrodynamische Kraft”, Annalen der Physik **271**, 264 (1888).

[21] P. Curie, “Sur la symétrie dans les phénomènes physiques, symétrie d’un champ électrique et d’un champ magnétique”, Journal de Physique Théorique et Appliquée **3**, 393 (1894).

[22] T. H. O’Dell, *The Electrodynamics of Magneto-Electric Media*, Vol. XI, Series of Monographs on Selected Topics in Solid State Physics (North-Holland Pub. Co.; American Elsevier Pub. Co, Amsterdam, New York, 1970).

[23] I. E. Dzyaloshinskii, “On The Magneto-Electrical Effect in Antiferromagnets”, Soviet Physics JETP **10**, 628 (1960).

[24] D. N. Astrov, “The Magnetoelectric Effect in Antiferromagnetics”, Soviet Physics JETP **11**, 708 (1960).

[25] T. H. O’Dell, “The field invariants in a magneto-electric medium”, Philosophical Magazine **8**, 411 (1963).

[26] W. Eerenstein, N. D. Mathur, and J. F. Scott, “Multiferroic and magnetoelectric materials”, Nature **442**, 759 (2006).

[27] N. A. Hill, “Why Are There so Few Magnetic Ferroelectrics?”, Journal of Physical Chemistry B **104**, 6694 (2000).

[28] J. H. Lee, L. Fang, E. Vlahos, X. Ke, Y. W. Jung, L. F. Kourkoutis, J.-W. Kim, P. J. Ryan, T. Heeg, M. Roeckerath, V. Goian, M. Bernhagen, R. Uecker, P. C. Hammel, K. M. Rabe, S. Kamba, J. Schubert, J. W. Freeland, D. A. Muller, C. J. Fennie, P. Schiffer, V. Gopalan, E. Johnston-Halperin, and D. G. Schlom, “A strong ferroelectric ferromagnet created by means of spin–lattice coupling”, Nature **466**, 954 (2010).

[29] H. Katsura, N. Nagaosa, and A. V. Balatsky, “Spin Current and Magnetoelectric Effect in Noncollinear Magnets”, Physical Review Letters **95**, 057205 (2005).

[30] S.-W. Cheong and M. Mostovoy, “Multiferroics: a magnetic twist for ferroelectricity”, Nature Materials **6**, 13 (2007).

[31] N. A. Spaldin, S.-W. Cheong, and R. Ramesh, “Multiferroics: Past, present, and future”, Physics Today **63**(10), 38 (2010).

[32] M. Fiebig, T. Lottermoser, D. Meier, and M. Trassin, “The evolution of multiferroics”, Nature Reviews Materials **1**, 16046 (2016).

[33] N. A. Spaldin and R. Ramesh, “Advances in magnetoelectric multiferroics”, Nature Materials **18**, 203 (2019).

[34] M. Mostovoy, “Ferroelectricity in Spiral Magnets”, Physical Review Letters **96**, 067601 (2006).

[35] M. S. Senn, J. P. Wright, and J. P. Attfield, “Charge order and three-site distortions in the Verwey structure of magnetite”, Nature **481**, 173 (2012).

[36] P. Lunkenheimer, J. Müller, S. Krohns, F. Schrettle, A. Loidl, B. Hartmann, R. Rommel, M. de Souza, C. Hotta, J. A. Schlueter, and M. Lang, “Multiferroicity in an organic charge-transfer salt that is suggestive of electric-dipole-driven magnetism”, Nature Materials **11**, 755 (2012).

[37] J. F. Scott, “Room-temperature multiferroic magnetoelectrics”, NPG Asia Materials **5**, e72 (2013).

[38] R. Nechache, C. Harnagea, A. Pignolet, F. Normandin, T. Veres, L.-P. Carignan, and D. Ménard, “Growth, structure, and properties of epitaxial thin films of first-principles predicted multiferroic Bi_2FeCrO_6”, Applied Physics Letters **89**, 102902 (2006).

[39] A. Kumar, I. Rivera, R. S. Katiyar, and J. F. Scott, “Multiferroic $Pb\,(Fe_{0.66}W_{0.33})_{0.80}\,Ti_{0.20}O_3$ thin films: A room-temperature relaxor ferroelectric and weak ferromagnetic”, Applied Physics Letters **92**, 132913 (2008).

[40] Y. C. Yang, C. F. Zhong, X. H. Wang, B. He, S. Q. Wei, F. Zeng, and F. Pan, “Room temperature multiferroic behavior of Cr-doped ZnO films”, Journal of Applied Physics **104**, 064102 (2008).

[41] H. Zhao, H. Kimura, Z. Cheng, X. Wang, and T. Nishida, “Room temperature multiferroic properties of Nd:$BiFeO_3$/Bi_2FeMnO_6 bilayered films”, Applied Physics Letters **95**, 232904 (2009).

[42] S. Dussan, A. Kumar, J. F. Scott, S. Priya, and R. S. Katiyar, “Room temperature multiferroic effects in superlattice nanocapacitors”, Applied Physics Letters **97**, 252902 (2010).

[43] Y. Tokunaga, Y. Kaneko, D. Okuyama, S. Ishiwata, T. Arima, S. Wakimoto, K. Kakurai, Y. Taguchi, and Y. Tokura, “Multiferroic M-Type Hexaferrites with a Room-Temperature Conical State and Magnetically Controllable Spin Helicity”, Physical Review Letters **105**, 257201 (2010).

[44] R. Nechache, C. V. Cojocaru, C. Harnagea, C. Nauenheim, M. Nicklaus, A. Ruediger, F. Rosei, and A. Pignolet, “Epitaxial Patterning of Bi_2FeCrO_6 Double Perovskite Nanostructures: Multiferroic at Room Temperature”, Advanced Materials **23**, 1724 (2011).

[45] S. Valencia, A. Crassous, L. Bocher, V. Garcia, X. Moya, R. O. Cherifi, C. Deranlot, K. Bouzehouane, S. Fusil, A. Zobelli, A. Gloter, N. D. Mathur, A. Gaupp, R. Abrudan, F. Radu, A. Barthélémy, and M. Bibes, “Interface-induced room-temperature multiferroicity in $BaTiO_3$”, Nature Materials **10**, 753 (2011).

[46] H.-L. Cai, Y. Zhang, D.-W. Fu, W. Zhang, T. Liu, H. Yoshikawa, K. Awaga, and R.-G. Xiong, “Above-Room-Temperature Magnetodielectric Coupling in a Possible Molecule-Based Multiferroic: Triethylmethylammonium Tetrabromoferrate(III)”, Journal of the American Chemical Society **134**, 18487 (2012).

[47] L. Keeney, S. Kulkarni, N. Deepak, M. Schmidt, N. Petkov, P. F. Zhang, S. Cavill, S. Roy, M. E. Pemble, and R. W. Whatmore, “Room temperature ferroelectric and magnetic investigations and detailed phase analysis of Aurivillius phase $Bi_5Ti_3Fe_{0.7}Co_{0.3}O_{15}$ thin films”, Journal of Applied Physics **112**, 052010 (2012).

[48] J. Wu, Z. Shi, J. Xu, N. Li, Z. Zheng, H. Geng, Z. Xie, and L. Zheng, “Synthesis and room temperature four-state memory prototype of $Sr_3Co_2Fe_{24}O_{41}$ multiferroics”, Applied Physics Letters **101**, 122903 (2012).

[49] A. Chen, H. Zhou, Z. Bi, Y. Zhu, Z. Luo, A. Bayraktaroglu, J. Phillips, E.-M. Choi, J. L. MacManus-Driscoll, S. J. Pennycook, J. Narayan, Q. Jia, X. Zhang, and H. Wang, “A New Class of Room-Temperature Multiferroic Thin Films with Bismuth-Based Supercell Structure”, Advanced Materials **25**, 1028 (2013).

[50] D. M. Evans, A. Schilling, A. Kumar, D. Sanchez, N. Ortega, M. Arredondo, R. S. Katiyar, J. M. Gregg, and J. F. Scott, “Magnetic switching of ferroelectric domains at room temperature in multiferroic PZTFT”, Nature Communications **4**, 1534 (2013).

[51] D. A. Sanchez, N. Ortega, A. Kumar, G. Sreenivasulu, R. S. Katiyar, J. F. Scott, D. M. Evans, M. Arredondo-Arechavala, A. Schilling, and J. M. Gregg, “Room-temperature single phase multiferroic magnetoelectrics: $\mathrm{Pb}\left(\mathrm{Fe},\mathrm{M}\right)_x\left(\mathrm{Zr},\mathrm{Ti}\right)_{(1-x)}\mathrm{O}_3\ \ [\mathrm{M}=\mathrm{Ta},\mathrm{Nb}]$”, Journal of Applied Physics **113**, 074105 (2013).

[52] W. Wang, J. Zhao, W. Wang, Z. Gai, N. Balke, M. Chi, H. N. Lee, W. Tian, L. Zhu, X. Cheng, D. J. Keavney, J. Yi, T. Z. Ward, P. C. Snijders, H. M. Christen, W. Wu, J. Shen, and X. Xu, “Room-Temperature Multiferroic Hexagonal LuFeO_3 Films”, Physical Review Letters **110**, 237601 (2013).

[53] M. Gich, I. Fina, A. Morelli, F. Sánchez, M. Alexe, J. Gàzquez, J. Fontcuberta, and A. Roig, “Multiferroic Iron Oxide Thin Films at Room Temperature”, Advanced Materials **26**, 4645 (2014).

[54] M. D. Glinchuk, E. A. Eliseev, and A. N. Morozovska, “Novel room temperature multiferroics on the base of single-phase nanostructured perovskites”, Journal of Applied Physics **116**, 054101 (2014).

[55] K. S. Pugazhvadivu, L. Balakrishnan, G. M. Rao, and K. Tamilarasan, “Room temperature ferromagnetic and ferroelectric properties of $\mathrm{Bi}_{1-x}\mathrm{Ca}_x\mathrm{MnO}_3$ thin films”, AIP Advances **4**, 117105 (2014).

[56] S. Sun, Y. Huang, G. Wang, J. Wang, Z. Fu, R. Peng, R. J. Knize, and Y. Lu, “Nanoscale structural modulation and enhanced room-temperature multiferroic properties”, Nanoscale **6**, 13494 (2014).

[57] L. F. Henrichs, O. Cespedes, J. Bennett, J. Landers, S. Salamon, C. Heuser, T. Hansen, T. Helbig, O. Gutfleisch, D. C. Lupascu, H. Wende, W. Kleemann, and A. J. Bell, “Multiferroic Clusters: A New Perspective for Relaxor-Type Room-Temperature Multiferroics”, Advanced Functional Materials **26**, 2111 (2016).

[58] J. A. Mundy, C. M. Brooks, M. E. Holtz, J. A. Moyer, H. Das, A. F. Rébola, J. T. Heron, J. D. Clarkson, S. M. Disseler, Z. Liu, A. Farhan, R. Held, R. Hovden, E. Padgett, Q. Mao, H. Paik, R. Misra, L. F. Kourkoutis, E. Arenholz, A. Scholl, J. A. Borchers, W. D. Ratcliff, R. Ramesh, C. J. Fennie, P. Schiffer, D. A. Muller, and D. G. Schlom, "Atomically engineered ferroic layers yield a room-temperature magnetoelectric multiferroic", Nature **537**, 523 (2016).

[59] C. Zhang, M. Shang, M. Liu, T. Zhang, L. Ge, H. Yuan, and S. Feng, "Multiferroicity in $SmFeO_3$ synthesized by hydrothermal method", Journal of Alloys and Compounds **665**, 152 (2016).

[60] E. Gradauskaite, J. Gardner, R. M. Smith, F. D. Morrison, S. L. Lee, R. S. Katiyar, and J. F. Scott, "Lead palladium titanate: A room-temperature multiferroic", Physical Review B **96**, 104104 (2017).

[61] M. Mishra, A. Roy, A. Garg, R. Gupta, and S. Mukherjee, "Room temperature multiferroism in polycrystalline thin films of gallium ferrite", Journal of Alloys and Compounds **721**, 593 (2017).

[62] T. Katayama, S. Yasui, Y. Hamasaki, T. Shiraishi, A. Akama, T. Kiguchi, and M. Itoh, "Ferroelectric and Magnetic Properties in Room-Temperature Multiferroic $Ga_xMn_{2-x}O_3$ Epitaxial Thin Films", Advanced Functional Materials **28**, 1704789 (2018).

[63] K. Zhai, D.-S. Shang, Y.-S. Chai, G. Li, J.-W. Cai, B.-G. Shen, and Y. Sun, "Room-Temperature Nonvolatile Memory Based on a Single-Phase Multiferroic Hexaferrite", Advanced Functional Materials **28**, 1705771 (2018).

[64] G. Zhong, Y. Bitla, J. Wang, X. Zhong, F. An, Y.-Y. Chin, Y. Zhang, W. Gao, Y. Zhang, A. Eshghinejad, E. N. Esfahani, Q. Zhu, C. Tan, X. Meng, H.-J. Lin, X. Pan, S. Xie, Y.-H. Chu, and J. Li, "Tuning Fe concentration in epitaxial gallium ferrite thin films for room temperature multiferroic properties", Acta Materialia **145**, 488 (2018).

[65] D. Lebeugle, D. Colson, A. Forget, and M. Viret, "Very large spontaneous electric polarization in $BiFeO_3$ single crystals at room temperature and its evolution under cycling fields", Applied Physics Letters **91**, 022907 (2007).

[66] A. Janner and T. Janssen, "Symmetry of incommensurate crystal phases. I. Commensurate basic structures", Acta Crystallographica Section A: Crystal Physics, Diffraction, Theoretical and General Crystallography **36**, 399 (1980).

[67] P. Bak, “Commensurate phases, incommensurate phases and the devil’s staircase”, Reports on Progress in Physics **45**, 587 (1982).

[68] F. Bai, J. Wang, M. Wuttig, J. Li, N. Wang, A. P. Pyatakov, A. K. Zvezdin, L. E. Cross, and D. Viehland, “Destruction of spin cycloid in $(111)_c$-oriented $BiFeO_3$ thin films by epitiaxial constraint: Enhanced polarization and release of latent magnetization”, Applied Physics Letters **86**, 032511 (2005).

[69] P. Chen, Ö. Günaydın-Şen, W. J. Ren, Z. Qin, T. V. Brinzari, S. McGill, S.-W. Cheong, and J. L. Musfeldt, “Spin cycloid quenching in Nd^{3+}-substituted $BiFeO_3$”, Physical Review B **86**, 014407 (2012).

[70] Y. F. Popov, A. K. Zvezdin, G. P. Vorob’ev, A. M. Kadomtseva, V. A. Murashev, and D. N. Rakov, “Linear magnetoelectric effect and phase transitions in bismuth ferrite $BiFeO_3$”, Soviet Journal of Experimental and Theoretical Physics Letters **57**, 69 (1993).

[71] D. Lebeugle, D. Colson, A. Forget, M. Viret, A. M. Bataille, and A. Gukasov, “Electric-Field-Induced Spin Flop in $BiFeO_3$ Single Crystals at Room Temperature”, Physical Review Letters **100**, 227602 (2008).

[72] J. T. Heron, J. L. Bosse, Q. He, Y. Gao, M. Trassin, L. Ye, J. D. Clarkson, C. Wang, J. Liu, S. Salahuddin, D. C. Ralph, D. G. Schlom, J. Íñiguez, B. D. Huey, and R. Ramesh, “Deterministic switching of ferromagnetism at room temperature using an electric field”, Nature **516**, 370 (2014).

[73] S. Blundell, *Magnetism in Condensed Matter*, Oxford Master Series in Condensed Matter Physics (Oxford University Press, Oxford; New York, 2001).

[74] R. C. O’Handley, *Modern Magnetic Materials: Principles and Applications* (Wiley, New York, 2000).

[75] N. Spaldin, *Magnetic Materials: Fundamentals and Applications*, Second edition (Cambridge University Press, Cambridge; New York, 2011).

[76] J. J. Sakurai and J. Napolitano, *Modern Quantum Mechanics*, Second edition (Addison-Wesley, Boston, 2011).

[77] J. D. Jackson, *Classical Electrodynamics*, Third edition (Wiley, New York, 1999).

[78] R. H. Kodama and A. E. Berkowitz, “Atomic-scale magnetic modeling of oxide nanoparticles”, Physical Review B **59**, 6321 (1999).

[79] L. Néel, "Anisotropie magnétique superficielle et surstructures d'orientation", Journal de Physique et le Radium **15**, 225 (1954).

[80] E. Winkler, R. D. Zysler, and D. Fiorani, "Surface and magnetic interaction effects in Mn_3O_4 nanoparticles", Physical Review B **70**, 174406 (2004).

[81] E. Winkler, R. D. Zysler, M. V. Mansilla, and D. Fiorani, "Surface anisotropy effects in NiO nanoparticles", Physical Review B **72**, 132409 (2005).

[82] J. Buhot, C. Toulouse, Y. Gallais, A. Sacuto, R. de Sousa, D. Wang, L. Bellaiche, M. Bibes, A. Barthélémy, A. Forget, D. Colson, M. Cazayous, and M.-A. Measson, "Driving Spin Excitations by Hydrostatic Pressure in $BiFeO_3$", Physical Review Letters **115**, 267204 (2015).

[83] M. Matsuda, R. S. Fishman, T. Hong, C. H. Lee, T. Ushiyama, Y. Yanagisawa, Y. Tomioka, and T. Ito, "Magnetic Dispersion and Anisotropy in Multiferroic $BiFeO_3$", Physical Review Letters **109**, 067205 (2012).

[84] G. C. Papaefthymiou, "Nanoparticle magnetism", Nano Today **4**, 438 (2009).

[85] M. Respaud, J. M. Broto, H. Rakoto, A. R. Fert, L. Thomas, B. Barbara, M. Verelst, E. Snoeck, P. Lecante, A. Mosset, J. Osuna, T. O. Ely, C. Amiens, and B. Chaudret, "Surface effects on the magnetic properties of ultrafine cobalt particles", Physical Review B **57**, 2925 (1998).

[86] P. Gambardella, S. Rusponi, M. Veronese, S. S. Dhesi, C. Grazioli, A. Dallmeyer, I. Cabria, R. Zeller, P. H. Dederichs, K. Kern, C. Carbone, and H. Brune, "Giant Magnetic Anisotropy of Single Cobalt Atoms and Nanoparticles", Science **300**, 1130 (2003).

[87] F. Bødker, S. Mørup, and S. Linderoth, "Surface effects in metallic iron nanoparticles", Physical Review Letters **72**, 282 (1994).

[88] F. Luis, J. M. Torres, L. M. García, J. Bartolomé, J. Stankiewicz, F. Petroff, F. Fettar, J.-L. Maurice, and A. Vaurès, "Enhancement of the magnetic anisotropy of nanometer-sized Co clusters: Influence of the surface and of interparticle interactions", Physical Review B **65**, 094409 (2002).

[89] N. Pérez, P. Guardia, A. G. Roca, M. P. Morales, C. J. Serna, O. Iglesias, F. Bartolomé, L. M. García, X. Batlle, and A. Labarta, "Surface anisotropy broadening of the energy barrier distribution in magnetic nanoparticles", Nanotechnology **19**, 475704 (2008).

[90] T.-J. Park, G. C. Papaefthymiou, A. J. Viescas, A. R. Moodenbaugh, and S. S. Wong, "Size-Dependent Magnetic Properties of Single-Crystalline Multiferroic $BiFeO_3$ Nanoparticles", Nano Letters **7**, 766 (2007).

[91] R. Mazumder, P. Sujatha Devi, D. Bhattacharya, P. Choudhury, A. Sen, and M. Raja, "Ferromagnetism in nanoscale $BiFeO_3$", Applied Physics Letters **91**, 062510 (2007).

[92] S. M. Selbach, T. Tybell, M.-A. Einarsrud, and T. Grande, "Size-Dependent Properties of Multiferroic $BiFeO_3$ Nanoparticles", Chemistry of Materials **19**, 6478 (2007).

[93] W. Ren and L. Bellaiche, "Size effects in multiferroic $BiFeO_3$ nanodots: A first-principles-based study", Physical Review B **82**, 113403 (2010).

[94] J. Landers, S. Salamon, M. Escobar Castillo, D. C. Lupascu, and H. Wende, "Mössbauer Study of Temperature-Dependent Cycloidal Ordering in $BiFeO_3$ Nanoparticles", Nano Letters **14**, 6061 (2014).

[95] P. S. V. Mocherla, C. Karthik, R. Ubic, M. S. Ramachandra Rao, and C. Sudakar, "Effect of microstrain on the magnetic properties of $BiFeO_3$ nanoparticles", Applied Physics Letters **105**, 132409 (2014).

[96] J. Wu, Z. Fan, D. Xiao, J. Zhu, and J. Wang, "Multiferroic bismuth ferrite-based materials for multifunctional applications: Ceramic bulks, thin films and nanostructures", Progress in Materials Science **84**, 335 (2016).

[97] F. Huang, X. Xu, X. Lu, M. Zhou, H. Sang, and J. Zhu, "The exchange bias behavior of $BiFeO_3$ nanoparticles with natural core-shell structure", Scientific Reports **8**, 2311 (2018).

[98] D. Carranza-Celis, A. Cardona-Rodríguez, J. Narváez, O. Moscoso-Londono, D. Muraca, M. Knobel, N. Ornelas-Soto, A. Reiber, and J. G. Ramírez, "Control of Multiferroic properties in $BiFeO_3$ nanoparticles", Scientific Reports **9**, 3182 (2019).

[99] D. P. Landau, "Finite-size behavior of the simple-cubic Ising lattice", Physical Review B **14**, 255 (1976).

[100] X. Batlle and A. Labarta, "Finite-size effects in fine particles: magnetic and transport properties", Journal of Physics D: Applied Physics **35**, R15 (2002).

[101] H. D. Megaw and C. N. W. Darlington, "Geometrical and structural relations in the rhombohedral perovskites", Acta Crystallographica Section A: Crystal Physics, Diffraction, Theoretical and General Crystallography **31**, 161 (1975).

[102] H. M. Rietveld, "A profile refinement method for nuclear and magnetic structures", Journal of Applied Crystallography **2**, 65 (1969).

[103] P. Fischer, M. Polomska, I. Sosnowska, and M. Szymanski, "Temperature dependence of the crystal and magnetic structures of $BiFeO_3$", Journal of Physics C: Solid State Physics **13**, 1931 (1980).

[104] Planck Collaboration, "Planck 2015 results. XIII. Cosmological parameters", Astronomy & Astrophysics **594**, A13 (2016).

[105] I. Aupiais, P. Hemme, M. Allen, A. M. Scida, X. Lu, C. Ricolleau, Y. Gallais, A. Sacuto, S. S. Wong, R. de Sousa, and M. Cazayous, "Impact of the surface phase transition on magnon and phonon excitations in $BiFeO_3$ nanoparticles", Applied Physics Letters **116**, 172903 (2020).

[106] R. Jarrier, X. Marti, J. Herrero-Albillos, P. Ferrer, R. Haumont, P. Gemeiner, G. Geneste, P. Berthet, T. Schülli, P. Cevc, R. Blinc, S. S. Wong, T.-J. Park, M. Alexe, M. A. Carpenter, J. F. Scott, G. Catalan, and B. Dkhil, "Surface phase transitions in $BiFeO_3$ below room temperature", Physical Review B **85**, 184104 (2012).

[107] W. Y. Shih, W.-H. Shih, and I. A. Aksay, "Size dependence of the ferroelectric transition of small $BaTiO_3$ particles: effect of depolarization", Physical Review B **50**, 15575 (1994).

[108] C. Kittel, *Introduction to Solid State Physics*, Eighth edition (Wiley, Hoboken, NJ, 2005).

[109] Q. Sheng, X. L. Liu, W. J. Chen, W. M. Xiong, G. L. Jiang, and Y. Zheng, "Phase diagrams of magnetic state transformations in multiferroic composites controlled by size, shape and interfacial coupling strain", AIP Advances **7**, 105221 (2017).

[110] R. de Sousa and J. E. Moore, "Optical coupling to spin waves in the cycloidal multiferroic $BiFeO_3$", Physical Review B **77**, 012406 (2008).

[111] M. Cazayous, Y. Gallais, A. Sacuto, R. de Sousa, D. Lebeugle, and D. Colson, "Possible Observation of Cycloidal Electromagnons in $BiFeO_3$", Physical Review Letters **101**, 037601 (2008).

[112] R. de Sousa and J. E. Moore, “Electrical control of magnon propagation in multiferroic $BiFeO_3$ films”, Applied Physics Letters **92**, 022514 (2008).

[113] M. Tokunaga, M. Akaki, A. Miyake, T. Ito, and H. Kuwahara, “High field studies on $BiFeO_3$ single crystals grown by the laser-diode heating floating zone method”, Journal of Magnetism and Magnetic Materials **383**, 259 (2015).

[114] M. Ramazanoglu, W. Ratcliff, Y. J. Choi, S. Lee, S.-W. Cheong, and V. Kiryukhin, “Temperature-dependent properties of the magnetic order in single-crystal $BiFeO_3$”, Physical Review B **83**, 174434 (2011).

[115] I. Sosnowska, T. P. Neumaier, and E. Steichele, “Spiral magnetic ordering in bismuth ferrite”, Journal of Physics C: Solid State Physics **15**, 4835 (1982).

[116] M. A. Allen, “Theoretical determination of electric field-magnetic field phase diagrams of the multiferroic bismuth ferrite”, M.Sc. Thesis (University of Victoria, Victoria, BC, Canada, 2014).

[117] I. Sosnowska and A. Zvezdin, “Origin of the long period magnetic ordering in $BiFeO_3$”, Journal of Magnetism and Magnetic Materials **140–144, Part 1**, 167 (1995).

[118] D. Rahmedov, D. Wang, J. Íñiguez, and L. Bellaiche, “Magnetic Cycloid of $BiFeO_3$ from Atomistic Simulations”, Physical Review Letters **109**, 037207 (2012).

[119] R. S. Fishman, “The microscopic model of $BiFeO_3$”, Physica B: Condensed Matter **536**, 115 (2018).

[120] P. W. Anderson, “Antiferromagnetism. Theory of Superexchange Interaction”, Physical Review **79**, 350 (1950).

[121] J. Rumble, ed., *CRC Handbook of Chemistry and Physics*, 101st edition (CRC Press, London, 2020).

[122] F. Damay, C. Martin, V. Hardy, G. André, S. Petit, and A. Maignan, “Magnetoelastic coupling and unconventional magnetic ordering in the multiferroic triangular lattice $AgCrS_2$”, Physical Review B **83**, 184413 (2011).

[123] A. V. Ushakov, D. A. Kukusta, A. N. Yaresko, and D. I. Khomskii, “Magnetism of layered chromium sulfides MCrS$_2$ (M = Li, Na, K, Ag, and Au): A first-principles study”, Physical Review B **87**, 014418 (2013).

[124] K. Dey, A. Karmakar, A. Indra, S. Majumdar, U. Rütt, O. Gutowski, M. v. Zimmermann, and S. Giri, "Thermally assisted and magnetic field driven isostructural distortion of spinel structure and occurrence of polar order in $CoCr_2S_4$", Physical Review B **92**, 024401 (2015).

[125] A. Ruff, Z. Wang, S. Zherlitsyn, J. Wosnitza, S. Krohns, H.-A. Krug von Nidda, P. Lunkenheimer, V. Tsurkan, and A. Loidl, "Multiferroic spin-superfluid and spin-supersolid phases in $MnCr_2S_4$", Physical Review B **100**, 014404 (2019).

[126] E. O. Wollan and W. C. Koehler, "Neutron Diffraction Study of the Magnetic Properties of the Series of Perovskite-Type Compounds $[(1-x)\mathrm{La}, x\mathrm{Ca}]\mathrm{MnO}_3$", Physical Review **100**, 545 (1955).

[127] I. Dzyaloshinsky, "A thermodynamic theory of 'weak' ferromagnetism of antiferromagnetics", Journal of Physics and Chemistry of Solids **4**, 241 (1958).

[128] T. Moriya, "New Mechanism of Anisotropic Superexchange Interaction", Physical Review Letters **4**, 228 (1960).

[129] T. Moriya, "Anisotropic Superexchange Interaction and Weak Ferromagnetism", Physical Review **120**, 91 (1960).

[130] A. Abragam and B. Bleaney, *Electron Paramagnetic Resonance of Transition Ions* (Oxford University Press, Oxford, 2012).

[131] A. V. Zalessky, A. A. Frolov, T. A. Khimich, A. A. Bush, V. S. Pokatilov, and A. K. Zvezdin, "^{57}Fe NMR study of spin-modulated magnetic structure in $BiFeO_3$", Europhysics Letters **50**, 547 (2000).

[132] W. A. Harrison, *Elementary Electronic Structure*, Revised edition (World Scientific, Singapore; River Edge, NJ, 2004).

[133] P. W. Atkins and R. Friedman, *Molecular Quantum Mechanics*, Fifth edition (Oxford University Press, Oxford; New York, 2011).

[134] Wolfram, *Some Notes on Internal Implementation—Wolfram Language Documentation*, `https://reference.wolfram.com/language/tutorial/SomeNotesOnInternalImplementation.html` (visited on 01/23/2020).

[135] J. Nocedal and S. J. Wright, *Numerical Optimization*, Second edition, Springer Series in Operations Research and Financial Engineering (Springer New York, 2006).

[136] E. W. Weisstein, *Simplex*, `http://mathworld.wolfram.com/Simplex.html` (visited on 01/21/2020).

[137] J. A. Nelder and R. Mead, "A Simplex Method for Function Minimization", The Computer Journal **7**, 308 (1965).

[138] F. Gao and L. Han, "Implementing the Nelder-Mead simplex algorithm with adaptive parameters", Computational Optimization and Applications **51**, 259 (2012).

[139] Wolfram, *Numerical Nonlinear Global Optimization—Wolfram Language Documentation*, `https://reference.wolfram.com/language/tutorial/ConstrainedOptimizationGlobalNumerical.html` (visited on 01/23/2020).

[140] R. H. Byrd, P. Lu, J. Nocedal, and C. Zhu, "A Limited Memory Algorithm for Bound Constrained Optimization", SIAM Journal on Scientific Computing **16**, 1190 (1995).

[141] M. Allen, I. Aupiais, M. Cazayous, and R. de Sousa, "Size-dependent bistability in multiferroic nanoparticles", Physical Review Materials **3**, 084402 (2019).

[142] X. Ke, P. P. Zhang, S. H. Baek, J. Zarestky, W. Tian, and C. B. Eom, "Magnetic structure of epitaxial multiferroic $BiFeO_3$ films with engineered ferroelectric domains", Physical Review B **82**, 134448 (2010).

[143] D. Sando, A. Agbelele, D. Rahmedov, J. Liu, P. Rovillain, C. Toulouse, I. C. Infante, A. P. Pyatakov, S. Fusil, E. Jacquet, C. Carrétéro, C. Deranlot, S. Lisenkov, D. Wang, J.-M. Le Breton, M. Cazayous, A. Sacuto, J. Juraszek, A. K. Zvezdin, L. Bellaiche, B. Dkhil, A. Barthélémy, and M. Bibes, "Crafting the magnonic and spintronic response of $BiFeO_3$ films by epitaxial strain", Nature Materials **12**, 641 (2013).

[144] U. Nagel, R. S. Fishman, T. Katuwal, H. Engelkamp, D. Talbayev, H. T. Yi, S.-W. Cheong, and T. Rõõm, "Terahertz Spectroscopy of Spin Waves in Multiferroic $BiFeO_3$ in High Magnetic Fields", Physical Review Letters **110**, 257201 (2013).

[145] J. H. Lee and R. S. Fishman, "Giant Spin-Driven Ferroelectric Polarization in $BiFeO_3$ at Room Temperature", Physical Review Letters **115**, 207203 (2015).

[146] M. Ramazanoglu, M. Laver, W. Ratcliff, S. M. Watson, W. C. Chen, A. Jackson, K. Kothapalli, S. Lee, S.-W. Cheong, and V. Kiryukhin, "Local Weak Ferromagnetism in Single-Crystalline Ferroelectric $BiFeO_3$", Physical Review Letters **107**, 207206 (2011).

[147] I. Gross, W. Akhtar, V. Garcia, L. J. Martínez, S. Chouaieb, K. Garcia, C. Carrétéro, A. Barthélémy, P. Appel, P. Maletinsky, J.-V. Kim, J. Y. Chauleau, N. Jaouen, M. Viret, M. Bibes, S. Fusil, and V. Jacques, "Real-space imaging of non-collinear antiferromagnetic order with a single-spin magnetometer", Nature **549**, 252 (2017).

[148] J. T. Heron, M. Trassin, K. Ashraf, M. Gajek, Q. He, S. Y. Yang, D. E. Nikonov, Y.-H. Chu, S. Salahuddin, and R. Ramesh, "Electric-Field-Induced Magnetization Reversal in a Ferromagnet-Multiferroic Heterostructure", Physical Review Letters **107**, 217202 (2011).

[149] R. S. Fishman, J. H. Lee, S. Bordács, I. Kézsmárki, U. Nagel, and T. Rõõm, "Spin-induced polarizations and nonreciprocal directional dichroism of the room-temperature multiferroic $BiFeO_3$", Physical Review B **92**, 094422 (2015).

[150] R. S. Fishman, "Field dependence of the spin state and spectroscopic modes of multiferroic $BiFeO_3$", Physical Review B **87**, 224419 (2013).